Applications of New X-ray Imaging Modalities in Food- and Medical Science

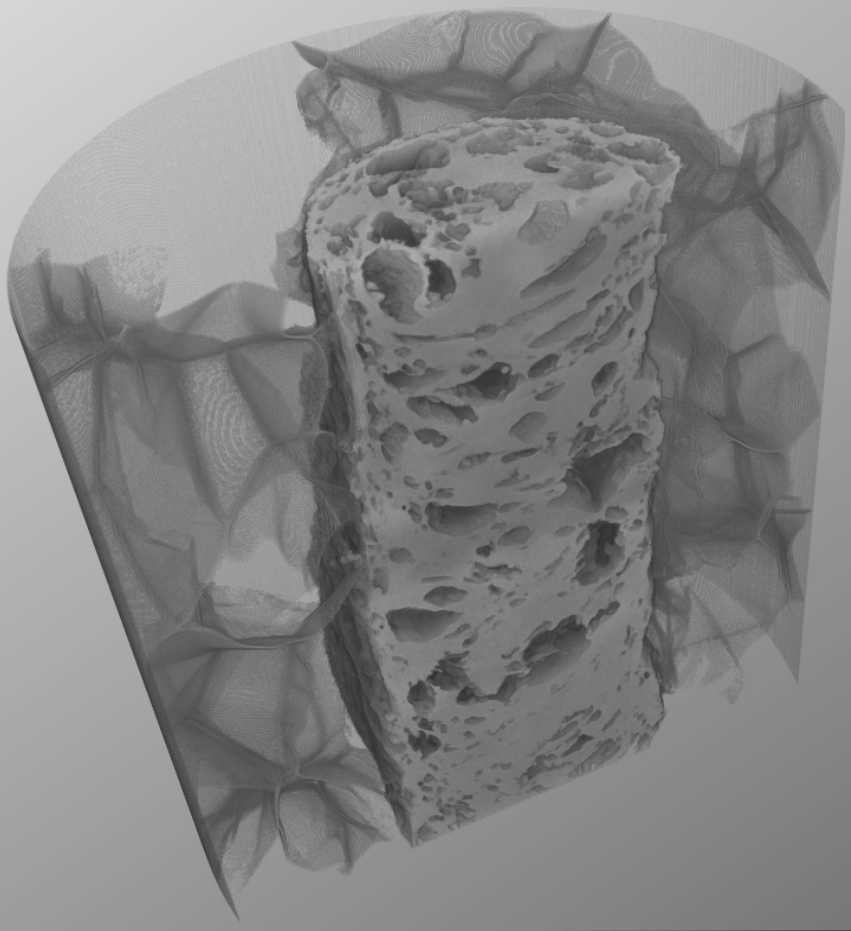

PhD thesis

Kristian Romlund Rix
Niels Bohr Institute
Copenhagen University

January 2019

Niels Bohr Institute

Copenhagen university

Applications of New X-ray Imaging Modalities in Food- and Medical Science

Author
Kristian Romlund Rix

Supervisors
Prof. Robert Feidenhans'l
Prof. Brian Vinter
Assoc. Prof. Martin Bech

This thesis has been submitted to:
The PhD School,
The Faculty of Science,
University of Copenhagen,
Denmark

For the PhD degree

The Niels Bohr Institute,
University of Copenhagen,
Universitetsparken 5,
2100 Copenhagen,
Denmark

January 2019

Front image

An absorption contrast tomographic 3D reconstruction of a peadough snack. Here threshold segmentation is applied to distinguish air from snack. The snack was placed in a tube and embedded in foam for stabilization purposes during its measurement. Segmentation threshold is insufficient as the foam and dough absorption is to similar and hence the foam is not removed. To remove the foam other segmentation tools must be applied.

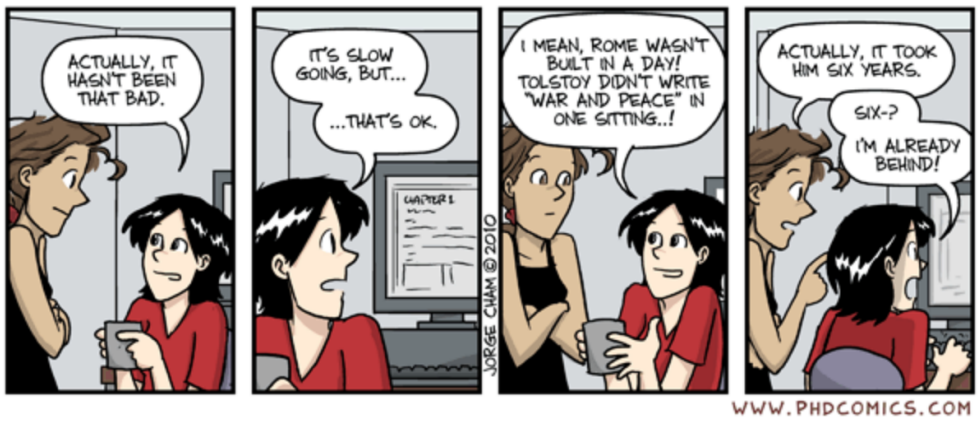
ACTUALLY, IT HASN'T BEEN THAT BAD.
IT'S SLOW GOING, BUT...
...THAT'S OK.
CHAPTER 1
JORGE CHAM © 2010
I MEAN, ROME WASN'T BUILT IN A DAY! TOLSTOY DIDN'T WRITE "WAR AND PEACE" IN ONE SITTING..!
ACTUALLY, IT TOOK HIM SIX YEARS.
SIX-?
I'M ALREADY BEHIND!
WWW.PHDCOMICS.COM

Abstract

The general population will most likely recognize x-ray imaging as the radiographic images taken in hospitals to determine bone fractures. Fewer would know that a CT-scanner uses x-rays to make the tomography images, while only a fraction would associate phase contrast imaging with x-rays or anything meaningful. This is for good reason as only a few decades ago x-ray imaging was mainly used as a hospital diagnostic tool or applied by a few research groups at universities. This is no longer the case and the development within x-ray imaging has been considerable over the last two decades. Advanced micro tomographic scanners are increasingly industrialized which is also the case for Talbot interferometer three image modality systems. Today, this means that the use of x-ray imaging is widely spread within many research areas as well as industrial. The important knowledge that x-ray imaging provides also means that many industries is now paying for beam times at large scale synchrotron facilities.

This thesis starts with a brief introduction to x-ray imaging and the methods considered in this work. Here I will in short terms discuss the nature of x-rays, purely on a phenomenological level and explain were x-rays fit in, in the full electromagnetic spectrum. I will introduced the mechanisms which are exploited in x-ray imaging and from there introduced the techniques used in this work.

This thesis contains three theory chapters. Chapter 2 contain some short introductions to the three main types of x-ray sources. These are the x-ray tube, the synchrotron and the newly developed free electron laser. Chapter 3 contains a thorough explanation of the important radiation matter interaction mechanisms where essential expressions are derived. This chapter also serves as a conceptual comparison between the optical light- and x-ray regimes of the electromagnetic spectrum. As the chapter progresses I will try to highlight the derived concepts which are of interest, from an imaging

point of view, and relate it to a specific technique. Chapter 6 is more general and touches on more topics compared to chapter 3. Due to this, most topics are only superficially discussed and many concepts will be stated with reference instead of a full derivation. Concepts and topics that are used in the publication are the main focus in this chapter. The subjects discussed is x-ray wave propagation, different image formation and -enhancement techniques.

The following four chapters are introductions to the publications of this work. Chapter 5 is a short introduction to article A.1. Here I have used an industrial micro CT-scanner to image and characterize the micro-structure of pea dough. Chapter 6 is the introduction to article A.2, where x-ray phase contrast holographic nanotomography is used to image and segment human peripheral nerves. Additionally, a supplementary work which is not intended for publication elsewhere is also included. This describes the ring artefact removal method which increased the image quality of the peripheral nerve tomograms. Chapter 7 is the introduction to article A.3 which is about our newly developed three modality imaging method that work without movable mechanical parts and have a reduced resolution loss compared to similar methods. Finally, Chapter 8 is an introduction to the secondary article B.1, which is phase corrected tomographic, of botox injected rat muscle fibers, performed at a synchrotron beamline.

Dansk Resumé

Den generelle befolkning vil sandsynligvis genkende røntgenbilleder som de radiografiske røntgen fotografier, der tages på hospitalerne for at finde knoglebrud. Færre vil vide, at en CT-scanner bruger røntgen til at lave tomografibillederne, mens kun en brøkdel vil associere fasekontrastbilleddannelse, med røntgenstråler. Dette er der god grund til. Røntgenbilleddannelsen har historisk set først og fremmest været brugt som et diagnostiseringsværktøj på hospitaler eller anvendt af nogle få forskningsgrupper på universiteterne. Dette er ikke længere tilfældet, udviklingen inden for røntgenbilleder har været intensiv over de sidste to årtier. Avancerede mikro-tomografiske scannere bliver i stigende grad industrialiseret, hvilket også er tilfældet for Talbot interferometer tre billedmodalitetssystemer. I dag betyder det, at brugen af røntgenbilleddannelse er spredt til mange forskningsområder såvel som industrien. Den vigtige viden som røntgenbilleddannelse giver, betyder også at mange brancher nu betaler betydelige beløb for stråletider på storskala synkrotronfaciliteter.

Denne afhandling starter med en kort introduktion til røntgenbilleddannelse samt metoderne brugt i dette arbejde. Her vil jeg kort diskutere røntgenstråler på et fænomenologisk niveau og forklare, hvor røntgenstråler passer ind i det fulde elektromagnetiske spektrum. Jeg vil introducere de mekanismer, der udnyttes i røntgenbilleddannelse og introducere de teknikker, der anvendes i dette arbejde.

Denne afhandling indeholder tre teori kapitler. Kapital 2 indeholde korte introductioner til de tre overordnede typer af røntgenkilder. Disse er; det såkaldte røntgen rør, synchrotoner samt den nyligt udvikelde frie electron laser. Kapitel 3 indeholder en grundig forklaring på de vigtige stråling og stof interaktionsmekanismer, hvor væsentlige formler bliver udledt. Dette kapitel tjener også som en konceptuel sammenligning mellem det optiske lys- og røntgen-regime i det elektromagnetiske spektrum.

Efterhånden som kapitlet skrider frem, vil jeg forsøge at fremhæve de udledte begreber, der er af interesse, fra et billeddannelses synspunkt og relaterer det til en bestemt teknik. Kapitel 6 er mere generel og berører flere emner i forhold til kapitel 3. På grund af dette er de fleste emner kun overfladisk diskuteret, og mange begreber vil blive angivet med reference i stedet for en fuldstændig udledning. Begreber og emner, der bruges i publikationen, er hovedfokus i dette kapitel. Emner som bølge propagering, forskellige billeddannelses og billed forbedrings teknikker vil blive diskuteret.

De efterfølgende fire kapitler er introduktioner til publikationerne af dette værk. Kapitel 5 er en kort introduktion til artikel A.1. Her har jeg brugt en industriel mikro CT scanner til at lave tomografi og karakteriserer mikrostrukturer af ærtedej. Kapitel 6 er introduktionen til artikel A.2, hvor røntgenfasekontrastholografisknanotomografi bruges til at illustrere og segmentere menneskelige perifere nerver. Der er ligeledes en tilføjelse til introduktionen som er supplerende arbejde til artiklen. Dette er ikke tiltænkt offentliggørelse andetsteds og er derfor inkluderet her. Dette beskriver en ring artefact fjernelsesmetode, som øgede billedkvaliteten af de perifere nerve tomogrammer. Kapitel 7 er introduktionen til artikel A.3, der omhandler vores nyudviklede tre billeddannelsesmetode der ikke bruger flytbare mekaniske dele og har et reduceret opløsningtab sammenlignet med lignende metoder. Endelig er Kapitel 8 en introduktion til den sekundære artikel B.1, som er fasekorrigeret tomografi af botox injicerede rottemuskelfibre udført på en synkrotron-strålelinje.

Acknowledgment

First of all, I would like to thank my principle supervisor throughout most of my PhD, Prof. Robert Feidelhans'l, who gave my the great opportunity to become a PhD student under his valuable supervision. I will also like to thank Prof. Brian Vinter for taking over as principal supervisor when Robert was no longer able to continue. Additionally, I will have to thank my co-supervisor Assoc. Prof Martin Bech of Lund University, who made him self available as such, at an extremely critical moment of my project where I really needed guidance to make my project concrete. I have difficulty imagining how I would have been able to finish this project without his guidance.

Secondly, I must give a special thanks to my fellow PhD student Torsten Lauridsen, who had the job of introducing me to x-ray imaging. He has been a great teacher and support during my development. Even after he left the university he was always ready to discuss my issues, read my papers and suggest improvements to both experiments and analysis. For this I am very grateful. In the same turn I will also extend my thanks to my other fellow PhD students Mikkel Schou Nielsen and Erik Schou Dreier with whom I have had a lot of fruitful x-ray imaging conversations and enjoyable moments.

In addition I will also like to thank a number of prominent collaborators these being, Lars Bager Christensen, Martin Rehr, Tao Shen, Vedrana Andersen Dahl, Anders Bjorholm Dahl, Lars Dahlin, Jessica Pingel, Mette Holse and Rikke Miklos.

Writing this thesis I have also been blessed with help from good friends and former fellow students at DTU physics, Tau B. Lehmann, Rasmus Fydendal and Felipe M. G. Poulsen, whom did proof-reading and improvement suggestions for the thesis.

Finally I will have to thank my girlfriend Tine E. G. Pedersen for her endless support

of me. Her effort on the home front especially during the finalization of the thesis have been extraordinary. She have been almost solely responsible for taking care of our almost 2 year old daughter, Edith, while she her self is pregnant and also talking care of her own full time job as nurse. I am extremely grateful for her hard effort and limitless support which have allowed me to finish this thesis.

Contents

1 Introduction

1.1 X-rays are just light

Humans see the world through what is called the optical spectrum. The optical spectrum is the frequency range of electromagnetic radiation that the eye can detect. Conveniently this frequency range is also the most abundant electromagnetic radiation emitted by the sun. The frequency of an electromagnetic wave is equivalent to the photon energy of the particles in the wave. From every day observation it is evident that different photon energies interacts differently with everything around us. This is for instance why things have color. The leaf on a tree is green because it absorbs most photon energies in the optical spectrum except the green energies which are reflected. A rainbow appears because different photon energies have different refraction angles in an air-water interface. The sky is blue as the atmosphere scatters blue energies more than other energies.

Outside the narrow optical spectrum materials still have optical properties. Consequently the well known phenomenons from classical optics also exists in the x-ray regime and this is exploited in various x-ray imaging systems. The boundaries between different regimes of electromagnetic radiation are not well defined but the x-ray spectrum can roughly be defined as photon energies between $100eV$ and $1000keV$. Both extremes overlapping with the ultraviolet- and gamma-regime respectively. To put this in perspective a normal red light photon will have an energy up to $2eV$.

1.1.1 X-ray imaging contrast mechanisms

The arguably most known feature of x-rays is its property to penetrate matter. Ironically it is the absorption properties of different materials that started the development of x-ray imaging. The first x-ray photography was taken by Wilhelm Röntgen in 1895 (Als-Nielsen and McMorrow 2010) and is an so-called absorption- or attenuation image. This is quit misleading as it is the transmitted x-rays which are detected. The observed effect stems from the attenuation of the x-ray in different materials. Absorption x-ray imaging is based on the different attenuation properties of materials. Since 1895 x-ray radiation has been exploited in hospitals to make radiographic imaging. It works as bones that mainly consist of calcium have a higher electron density than the surrounding soft tissue and thus absorbs more x-ray radiation. The absorption ability is still the most exploited contrast mechanism as it is very simple to measure and is thus utilized in both laboratory and synchrotron based setups.

At the end of the previous millennium the exploitation of other contrast mechanisms started. Refraction is a consequence of the real part of the complex refractive index. In imaging techniques, this quantity is measured through the phase shift of a x-ray wave. Therefore this contrast mechanism is called phase contrast. This is a very useful tool when the sample in question do not absorb much or when two different materials absorbs the same amount of radiation but have different refractive abilities. In practice this is useful when considering soft tissue samples. There are several approaches to utilize this contrast mechanism. In this thesis two approaches will be treated. The first one being propagation based phase contrast. Here several projections are made at different distances from the sample. From the phase evolution at the different distances an algorithm is then used to determine the varying refraction from different elements within the sample. This method is utilized by radiation from a synchrotron which will be discussed in section 2.2. The second approach is a product of the grating based imaging setup or three modality imaging systems. The original instrument for such measurements is the Talbot interferometer first demonstrated in x-ray regime by Momose et al. (2003), which have been developed into many different systems and methods. Here a grating is used to map the phase of the beam and by comparing the phase maps with and without the sample one can effectively record the phase shift caused by the sample. Because a reference is used this method is called differential phase contrast.

Finally, with the development of the Talbot interferometer the final contrast mechanism could be exploited in the lab. This is based on scattering of x-rays. The grating based interferometer made it possible to measure the decrease in visibility along with the refraction and absorption of a sample. The decrease in visibility in the interferometer happens due to scattering of x-ray photons in the sample. This is similar to the dark field microscopy technique in classical optics. Due to this similarity this x-

ray imaging modality is called Dark Field imaging and is a measure of the scattering ability of the sample. The dark field imaging modality is sensitive to small particles and fiber structures.

1.2 My contribution to science

I have several times after working days on end on figures from especially tomographic data sets, experienced what best can be categorized as an academic existential crises. Sometimes it felt like I was just sitting and rotating tomograms around without achieving any improvements in its presentation. However, one must also realize that science is as much a craftsmanship as anything else. Especially in the field of applied imaging, were much of the work is as a binding segment between other sciences. My contribution has mostly been interdisciplinary as either a guide for experiments or the one carrying out the experiments for other branches of science where I did not have detailed academic foundation and knowledge. My work has in such situations been focused on data analysis, image generation and reconstruction which provided hypotheses and conclusions for the collaborator. In effect, much of my work have not directly contributed to the imaging community. It does, however, benefit the imaging community, when other sciences realize the possibilities that x-ray imaging, in form of ideas and funding. During my PhD studies I have mainly collaborated with computer-, food- and medical scientists. I provided one paper with direct contribution to the x-ray imaging community. In the following a short description on the techniques which have been applied throughout this thesis is given.

1.2.1 Cone beam tomography to determine microstructure extruded pea dough

In collaboration with researchers at the Department of Food Science at Copenhagen University, Mette Holse, Rikke Miklos and Jacob Frydendahl the characterization of the microstructures of extruded pea dough is investigated. Here an industrial CT-scanner is applied, the specific model being ZEISS XRADIA 410 Micro-CT. The tomographic reconstruction on such systems is a little more complicated compared to that of CT measurements at for instance synchrotron facilities. This is because the distance between the source and the sample is relatively short, meaning that the beam cannot be considered to have a plane wavefront. Instead if the beam is considered to have a cone beam shape an improved reconstruction result can be obtained. This is a well documented technique that have been treated in depth in many other works, for instance by Turbell (2001). However, I will present a short discussion on the matter

in section 4.2.1.

1.2.2 X-ray phase contrast holographic nanotomography to map the 3D architecture of human nerves

During the, "change of scientific environment"[1] a research project to map the three-dimensional architecture of human diabetic peripheral nerves and compare these to a control group is conducted. The samples are collected by Professor and medical doctor Lars Dahlin while Martin Bech is the main responsible for the beam time application and choosing the experiment at ESRF that provided the facilities to conduct x-ray phase contrast holographic nanotomography. X-ray phase contrast holographic tomography is a propagation based phase contrast method that on paper is a straight forward and simple setup as the technique only requires a rotational stage for the sample and a translation stage for the detector (Guigay et al. 2010). If the radiation passing through the sample exhibits a measurable phase displacement, the interference pattern at different distances of the detector will reveal the real part of refractive index distribution in the sample through the reconstruction algorithm. The method however has high requirements for beam coherence as well as high setup stability and stepping precision demands. This means that the method can only be utilized at synchrotron facilities as it is currently impossible to achieve x-rays radiation with well defined monochromatic plane waves using any conventional x-ray source. In section 4.3.2 a short description of the method and the underlying reconstruction algorithm is made.

1.2.3 Lab based three modality x-ray imaging systems

Martin Bech, co-supervisor of this thesis has started a new x-ray laboratory to which a lot of this PhD work has been dedicated. It is the ultimate goal to be able to do three modality tomography at this setup. The status of the setup is represented in the publication in article A.3. It is a further development on well established systems such as Talbot interferometer discussed in section 4.4 and the other well known approach called spatial harmonic analysis based on Fourier analysis (Wen et al. 2010) that requires only one grating compared to the three gratings required in the Talbot system. However, an additional requirement of such a system is a microfocus source. Both systems has their own drawbacks.

The Talbot interferomter systems are notoriously difficult to align and are very sensi-

[1] A mandatory research oriented visit, to a foreign research institution, as part of the danish PhD-program. Normally the visit last between 3 and 6 months.

tive to vibrations as well as thermal drifts and are long term unstable. Here a grating is used to map the phase of the beam and by comparing the phase maps with and without the sample one can effectively record the phase shift caused by the sample. The phase map also contains the visibility information and is thus used to create the dark field image as well. However, this phase map is easily changed or destroyed due to its extreme sensitivity.

Sensitivity is not an issue of spatial harmonic analysis or single exposure method as it is also called. The downside here is a drastic reduction in resolution as only the information around the 0th and first order harmonics of Fourier transformed projection is used. The absorption information is contained around the 0th order harmonic, while phase and visibility information is found in two of the four first order harmonics. In article A.3 it is described how the loss in resolution is reduced compared to the single exposure method. This is done using recording a series of slightly distinctive projections and applying a mathematical algorithm called Blind Super Resolution. With such an approach there are no additional requirements for stability. A short explanation of the Talbot interferometer and the single shot method in seen section 4.4.

1.2.4 Refraction corrected tomography of muscle fibers

An investigation of the influence of botox injected in to the muscles of humans suffering from cerebral palsy is done. This study is conducted at the tomographic absorption imaging beam line TOMCAT at the synchrotron facility SLS (Swiss Light Source). At well defined edges in tomographic projection one will often see an edge enhancement due to high difference between the real part of refractive indexes at sample- edges or interfaces. As the detector is placed fare from the sample, which is often the case at synchrotron facilities, interference causes this effect to increase. In normal radiography this is of little importance and can even highlight the boundaries between different materials in a positive manner. However, in tomography due to the reconstruction a more homogeneous image without sharp edges is preferred. In this specific study a phase correction algorithm developed by Paganin et al. (2002) is applied to avoid reconstruction artifacts and thereby achieving better tomograms with higher resolution. The algorithm of the method is discussed further in section 4.3.1.

1.3 Outline of the thesis

This thesis consists of three background and theory chapters; 2, 3 and 4 and is then followed by 4 publication introductions chapters. In general, the introduction chapters

will be short except for chapter 5 which contains some work which have not been included in the corresponding publication.

1.3.1 Theory - fundamentals of imaging

Chapter 2 of this thesis contains a short introduction and comparison between the three kinds of x-ray sources exploited in imaging systems. These are known as x-ray tubes, synchrotrons and free electron lasers. Recently a former colleague and fellow PhD student T. Lauridsen successfully defended his PhD thesis. The theory section of Lauridsen's thesis is highly focused in the area of wave propagation, such as Fourier optics, transport of intensity equation, magnification, etc. Basically everything that happens between the sample and the detector. However, it is the samples that interact with the radiation and thereby create the wave structure that eventually is measured. Of course Torsten knows this better then anyone but as he did not exploit the opportunity to discuss the matter in detail, the theory of this thesis is focused on this subject. Further motivation to do so is explain in the beginning of chapter 3 and that chapter is the theoretical backbone of this thesis. On the other hand the theory from the wave propagation perspective is limited somewhat, although not fully. This perspective is discussed if necessary alongside the relevant x-ray imaging techniques used in this work. The wave formalism approach can be found in the thesis by Lauridsen (2018). In chapter 6 I will discuss the imaging methods that have been applied in the publication and when necessary include relevant wave theory.

1.3.2 Original work - publication introductions

Chapters 5, 7 and 8 are short introductions to the publications of this thesis. The Chapters will be a brief description on the content, method and conclusion of the papers. Furthermore, I will emphasize what my specific contribution have been to the work.

Chapter 6 will contain the same relevant information as the other introduction chapters, as well as additional background work which was not include in the publication. To avoid the risk of self plagiarism I here inform that most of this additional work have already been used in a course project that I took during my "change of scientific environment" at Lund university in Sweden. I do not believe it to be public available but I can provide a copy if the reader might be interested.

2 X-ray Sources

X-ray sources can be divided into two main categories. The first category is sources that are available in regular lab facilities at the university, at hospitals, and so forth. Sources in this category are also used in commercial products, such as radiographic imaging systems, luggage scanners, industrial and medical CT-scanners and many others. I will refer to this category of sources as lab sources. The second category is large-scale facility x-ray sources. Sources in this category are all based on particle accelerators which are not possible to utilize in normal labs or commercial products, therefore, these are purely used for scientific research. I will refer to this category of sources as synchrotron sources.

2.1 Lab sources

The radiation generated by lab sources is characterized as bremsstrahlung in an x-ray tube. Bremsstrahlung is a German word and is directly translated as brake radiation. As the name implies, the radiation is created as electrons decelerate. The radiation is created by applying a voltage between a cathode and an anode. Electrons then travel at a given kinetic energy defined by the voltage and experience extreme deceleration when they hit the anode. The maximum energy of the emitted photons is given by the full kinetic energy of the electron so that if a voltage 70kV is applied, the maximum photon energy will be 70keV. Additional spectral lines are also observed in the spectrum. These are the characteristic electron transitions of the matter in the

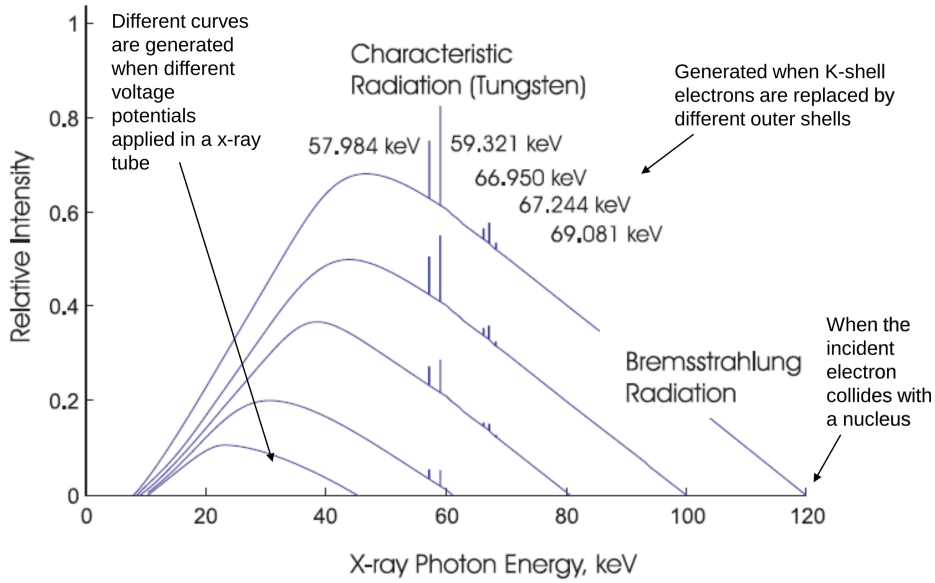

Figure 2.1: Characteristic x-ray tube spectrum with a tungsten anode. *This image is found via google search* (Mamou and Y. Wang 2019).

anode and are a result of ejection of electrons from the atom by collisions with the incoming electron beam.

The limit of the maximum power output is a result of how well the anode is cooled. It is possible to increase this limit by actively cooling the anode with for instance water cooling inside the anode. A different solution is to also disperse the electron beam onto a larger area. This is achieved by a rotating anode solution where the anode is rotated so a much larger area is heated instead of a fixed area.

As discussed in the publication described in chapter 5 and the publication seen in section A.3, an enhancement of the x-ray beam quality is obtainable applying a well defined electromagnetic field which focuses the electron beam to a small area. This means that the x-rays can radiated from a small spot down to a few micro meters (FWHM) (*Excillum source spot size* 2019). This technique greatly reduces blur effects, which is essential in x-ray micro tomography, but also in some three modality imaging techniques, discussed in sections 4.1 and 4.4. This enhancement comes at a price; because the electron beam power is now focused on a much smaller area, there is a much lower intensity limit. In the recent years, inventions such as liquid metal jets by Excillum have been utilized to counter reduced output power (*Excillum MetalJet* 2019).

2.2 Synchrotron sources

2.2.1 Historic development of the synchrotron

Even though this is not a thesis of history, the history of the development of synchrotron radiation needs to be briefly outlined, as this is a classical example of how science in one specific topic unintentionally gives rise to a completely unrelated topic, with extraordinary implications to many other branches of science. It is difficult to imagine what materials science would look like today without synchrotron radiation. Today the application of synchrotron radiation has spread to many other fields, such as medicine, geology, biology, food science, etc. Furthermore, the synchrotron technology is also the basis for the more resent developed Free Electron Laser (Winick 1997).

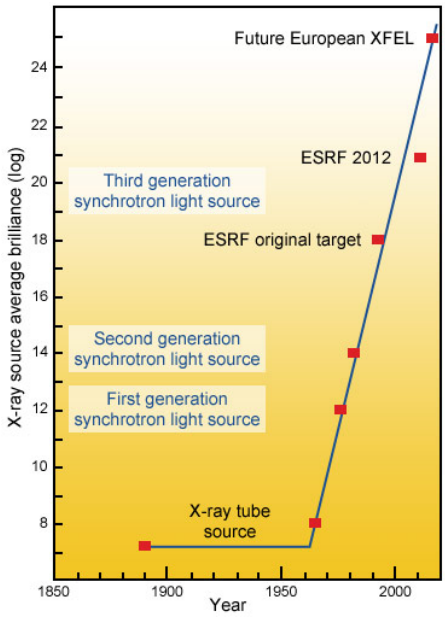

Figure 2.2: Evolution of the x-ray sources over time. *This figure is found via google search* (*Brilliance* 2019)

There is more than one factor that contributes to the beam quality. These factors are combined into one factor for easy comparison which is called the brilliance or sometimes the brightness. The brilliance factor is given by (Als-Nielsen and McMorrow 2010):

$$\text{Brilliance} = \frac{\text{photon rate}}{(\text{beam divergence})^2 \cdot \text{source area} \cdot \text{band width}} \tag{2.1}$$

where the photon rate is the number of photons emitted per second, the beam divergence is measured in $mrad$, the source area is measured in mm^2, and the band width is the relative bandwidth of the monochromator crystal relative to 0.1%. Although some experiments might have requirements determined from other parameters than these, this is the convention used as a measure for beam quality and is referenced as such in the following.

The first emitted synchrotron radiation was discovered by accident in 1945 (Blewett 1945). Since then, the development of the synchrotron continued until the beginning of the 1970's, not as a source of radiation but, for nuclear and high energy particle experiments. For that reason these sources are often recognized in the x-ray community as 0^{th}-generation. Although the brilliance was intense compared to the classical x-ray tube, the cycle-to-cycle nature of this type of synchrotron results in changing spectra and a non-stationary source position (Winick 1997). This problem was solved with the invention of the storage ring that made a stable spectrum and source point, and a long lifetime beam available. At this stage, the brilliance from conventional sources had increased by a factor of 10^5. At this point the synchrotron radiation experiments was still parasitic to the high energy particle experiments, however its potential was almost instantly recognized with the development of the storage ring. In the mid 1970's, the demand for fully synchrotron radiation dedicated rings realized the construction of the 2^{nd} generation synchrotrons. This lead to a further increase of brilliance by a factor of 10^2. At the same time, insertion devices, which are discussed shortly, were also introduced to the storage rings, boosting the brilliance an additional factor of 10^2 using the so called undulator. The brilliance of the beam is dependent on the transverse size and divergence of the electron beam in the storage ring. In the 3^{rd} generation synchrotrons the transverse size and divergence was drastically decreased, which combined with appropriately designed insertion devices further increased the brilliance by a factor of 10^4. The first 3^{rd} generation were ready for operation in the early 1990's. At this point, the brilliance of the synchrotron was 10^{13} higher than the conventional x-ray sources. Finally, what is considered to be the first 4^{th} generation synchrotron started operating in 2016, further increasing the brilliance by a factor of 10. The scaling of the brilliance over time as new sources are developed is seen in figure 2.2.

2.2.2 Generating the x-rays

In synchrotrons, three different devices are used to create x-rays with different characteristics. These are bending magnets, wigglers and undulators. The simplest and oldest one is the bending magnet. The bending magnet was incorporated into the very first synchrotrons as these devices were used to contain the electrons in the synchrotron ring. A series of bending magnets are placed in the ring such that the trajectory of

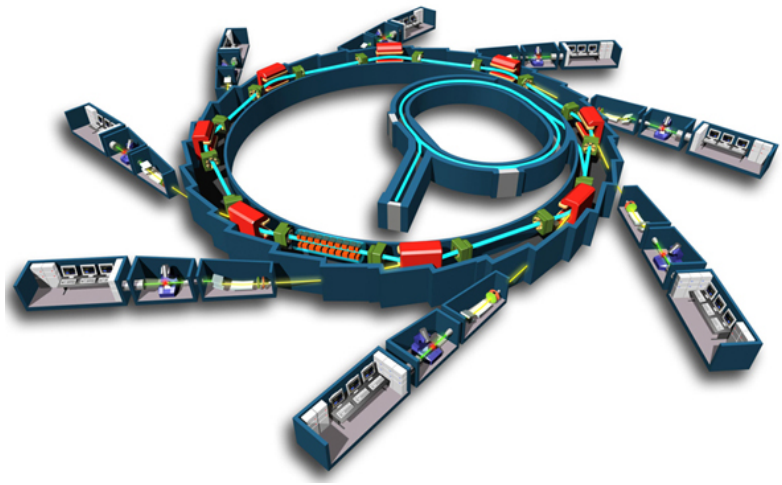

Figure 2.3: Outline on of a synchrotron facility (Soleil). A "short" linear accelerator called the linac accelerates electrons into a smaller ring called the booster ring. Here the electrons are further accelerated to near light speed and then injected to the storage ring. The different devises - bending magnets, wigglers and undulators produces the x-rays in the storage ring. In this illustration only bending magnets is illustrated to produce x-rays, however in theory every straight section of the storage ring could be swapped with an insertion devise. The produced x-rays are then transmitted into the beamline were the experiments are conducted. *This figure is found via google search* (*Soleil* 2019)

.

the electron beam is bent several times until a circular path is obtained and repeated. Because of the bending of the electron trajectory, it is accelerated in a given direction, and a wavefront of radiation with tangential direction to the electron trajectory is emitted. Notice that in the instance this radiation is emitted, the photon energy is much lower than the x-ray energy. However, because the electron speed is relativistic, the electron is only "slightly" delayed compared to the wave front traveling at light speed. At the next instance a new wavefront is emitted compressing the emitted wave. To the stationary observer in the wave path, the wave appears as x-ray waves. This means, that unlike in the x-ray tube where the extreme deceleration directly generates the x-rays, that it here is the Doppler effect that drives the generation of x-rays.

In the late 1970's, the first insertion devices were introduced to the synchrotrons (Winick 1997). These are called wigglers and undulators. These replace one of the straight sections in the ring with two arrays of magnets similar to figure 2.4. The wiggler oscillates the electron beam several times in the same manner as the bending magnet bends the electron trajectory once. Effectively, the radiation from a wiggler can be viewed as the sum of a number of bending magnets. The undulator is different from the wiggler as it consists of many more and smaller magnets. This means that the

oscillations are more frequent with smaller amplitude. Hence the source area becomes much smaller compared to the wiggler, which by definition implies higher brilliance. However it also means that the overall amount of photons produced is much smaller compared to the wiggler. The undulator is designed such that the radiation of a given electron oscillation will be in phase with the next oscillation of that electron. This enhances the output due to constructive interference.

It is more than the source size and total output power that deviate the emitted radiation from the three different devices. The spectra from bending magnets and wigglers are similar. These are quite broad and the major difference is the overall intensity. On the other hand, the spectrum of an undulator is much more narrow, almost laser-like, due to the small amplitude of the electron oscillation. This is very advantageous if monochromaticity is required. In addition, the photon energy is tunable by changing the magnetic field. Moreover, higher order harmonics are observed in the undulator output although these are not discussed further here.

2.3 Free electron laser

Although I never had the pleasure of doing experiments at a free electron laser facility, it still deserves a mentioning here, as it is the newest and most advanced addition to the x-ray source family. The free electron laser works in similar manner as the undulator in a synchrotron, but deviates in two major ways. The first one is the accelerator design, as this is solely a linear accelerator, typically 1-3 km in length. The second is an undulator which succeeds the accelerator. The difference compared to the synchrotron undulator is its length. While the undulator in a synchrotron is no longer than a few meters, the undulator in a free electron laser can be more than 100 meters.

It works when an electron beam is emitted in bunches of electron clouds and accelerated into the undulator. The length of the free electron laser undulator enables the effect known as Self Amplified Spontaneous Emission (SASE) (Milton et al. 2001), which is illustrated in figure 2.4. As the electron bunch travels along the undulator, the electrons are mainly effected by the magnetic fields of the undulator, which builds up radiation. When the radiation gets strong enough, the radiated field starts to affect the electron bunch. The bunch gets separated into smaller bunches modulated by the wavelength of the emitted x-rays. This means that electrons comes more and more in phase with the radiation. Hence it is not only the radiation from one electron that is in phase, the radiation from every single electron is in phase, which drastically increases the brilliance as also observed in figure 2.2. According to the web page of XFEL *XFEL* (2019), which is the most brilliant free electron laser currently in operation, its

average brilliance is 10.000 times that of the most brilliant synchrotrons. If one is considering peak brilliance, the XFEL produces one billion times that of the cutting edge synchrotrons. This is due to the fact that the micro-bunched electrons are extremely closely packed. An additional very useful effect of the micro-bunched electrons is an extremely closely packed train of x-ray pulses, less than 100 femtoseconds, which can be used as the worlds fastest high speed camera.

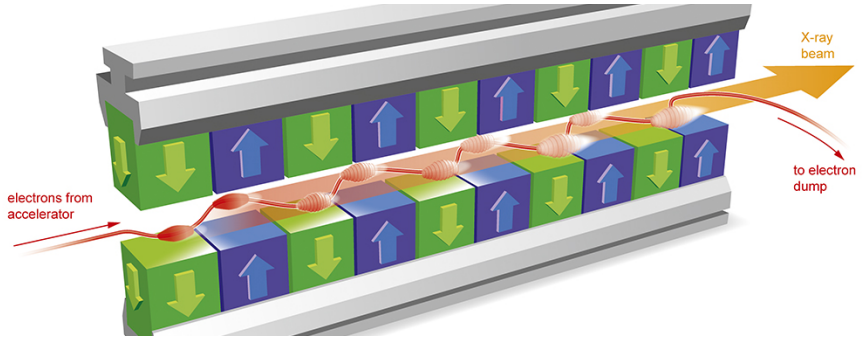

Figure 2.4: The layout and effect of the undulator. At the start of the undulator, the electron bunch is spread out as in the case of a synchrotron, as the radiation intensity builds up, the micro bunches start to form and then self amplify. *This figure is found on the European XFEL web page* (*XFEL* 2019)

.

3 Interaction between x-ray radiation and matter

In this chapter the interaction between electromagnetic radiation and matter is discussed. This subject is discused heavily in the literature and textbooks, yet, the difference in the nature of light and x-rays are almost never considered in the same turn. It is difficult to find good literature, that directly compares the two different regime, discussing the similarities and the differences. Such comparisons are always briefly touched without any illustrative examples or explanations which might make the transition betweeen the sciences troublesome. For instance absorption- and scattering cross-sections can be confusing concepts to one with an optical background as these are rarely used in the "light" context. As the term "cross-section" suggest it is an area, but it is also an abstract concept that can simply be considered the proportionality constant for the attenuation in materials. Hence it is a material parameter which is quite easy to measure but difficult to calculate through the theory. Additionally if the characteristics of the x-ray scattering that is governed by scattering cross-section is considered, its extreme complexity provides an almost endless amount of characterization tools for many kinds of matter. Contrary in the optical regime scattering is often avoided as it has few constructive applications in this regime. In this chapter the differences and similarities of light and x-rays are highlighted and discussed through analogies when possible. The chapter is an attemp to compare and thereby make a transition from light optics science to x-ray science a little easier. To a varying degree the math is kept at a minimum in the main text, where mainly the physical aspect of the concepts are discussed. This chapter is inspired by the books; Elements of Modern X-ray Physics by Als-Nielsen and McMorrow (2010) and Optical Properties of Solids

by Fox (2010) and is supplemented by Introductory quantum optics by Gerry and Knight (2005) and Introduction to Electrodynamics by Griffiths (1999).

For state of the art synchrotron microscopy imaging, the maximum achievable resolution is currently in the 10 nm range as shown by Silva et al. (2017). Investigations on this scale is impossible using conventional light microscopy due to the diffraction limit. However when considering the interaction between light and matter, classical models are still valid in the visible regime. This is not always the case for x-rays. For instance, no classical model is able to explain, the most applied feature in x-ray imaging, which is absorption. Here a quantum mechanical model is required.

On the other hand the elastic scattering variant of x-ray matter interaction is sufficiently described by a classical approach. This is known as Thomson scattering and is discussed in section 3.2. Another effect which is sometimes considered to be scattering is the Compton effect or Compton scattering and is an inelastic scattering effect. Historically the Compton effect was of great importance as it is a single photon that interacts with a single electron. It is described as a collision between a x-ray photon and an electron, free or bound, where transference of energy from the photon to electron momentum happens. The result is a lower photon energy and a different direction than the incoming photon. This discovery was of huge significance as the inelastic behavior could only be explained through the quantum photon. This of course highly supported the, at the time, emerging quantum theory. Personally I like to view the Compton effect as an absorption property as it, unlike the elastic Thomson scattering, can only be described by quantum mechanics, as the case is for x-ray absorption. Furthermore a good x-ray-light analogue is photoluminescence. Here the photon is absorbed before a photon of lower energy is emitted. It is of course impossible to observe the Compton phenomenon directly, but I take the liberty to state the Compton effect as an absorption effect. In imaging the Compton effect is mostly negligible or indistinguishable from conventional absorption as it mainly contributes to the absorption contrast. This effect will not be considered further in this work.

Finally the refraction phenomenon is also present in both the visible and the x-ray regime. In the classical models applied here it is seen that the refraction of visible light is derived along side the absorption. When considering all electrons in a given material to be free a decent approximation of the refractive behavior of x-rays do appear. However a fully valid description is achieved by averaging over the x-ray scattering ability of the matter in question. For this reason it is often stated, on the elementary level, that diffraction and refraction is one and the same. Scattering is often associated with small structures like particles and as such structures becomes bigger and bigger, compared to the wavelength of the radiation, the behavior of the radiation is also described by refraction. However there is no strict definition of this transition and can therefore be defined in the eyes of the beholder. By the end of this chapter it is shown that diffraction and refraction is two sides of the same coin.

3.1 Absorption of electromagnetic radiation in matter

Attenuation of both optical light and x-rays is described by the same law which is known as Beers law. This is given by:

$$I(x) = I_0 \cdot e^{-\mu x} \tag{3.1}$$

Here I is the wave intensity at a given position x in the attenuating material, I_0 is the intensity of the incoming wave and μ is the attenuation constant. It should be noted that μ is dependent on both the material and the frequency in question. This law is valid for both visible light and x-rays, although the underlying mechanisms are quite different.

3.1.1 Classical absorption of electromagnetic radiation

A well known factor which describes some of the optical properties of matter is the complex refractive index. When dealing with visible light this is given as:

$$\tilde{n} = n + i\kappa \tag{3.2}$$

Here the real part n is the refractive index which is implied by for instance Snells law of refraction between two media. The matter of refraction is further discussed in the latter section 3.3. The complex part of the index κ is directly coupled to the absorption coefficient α:

$$\alpha = \frac{4\pi\kappa\nu}{c} \tag{3.3}$$

Here ν is the frequency of the wave and c is the speed of light in vacuum. α is often equated with μ in Beers law. One should however be certain that absorption is the majority contributor to the attenuation for this statement to be valid. Another important phenomenon is reflection. It turns out that reflection between two media is dependent on both the real and complex part of the refractive index. In the most simple case were a wave propagates in vacuum and encounters a medium at normal incidence it can be shown that the reflectivity is given by (Fox 2010):

$$R = \frac{(n-1)^2 + \kappa^2}{(n+1)^2 + \kappa^2} \tag{3.4}$$

In the x-ray regime of the spectrum, a slightly different complex refractive index governs the interaction between electromagnetic waves and matter:

$$\mathsf{n} = 1 - \delta + i\beta \tag{3.5}$$

As in the case of the visible regime the real part δ governs the refraction, but unlike the visible regime were $n \geq 1$, $\delta << 1$. δ describes the difference from unity which is why 1 has been included in the real part of refractive index. The reason and implications of $\delta < 1$ is discussed in detail in section 3.3 as this gives x-rays some interesting properties which is not observed in the visible spectrum, such as total external reflection. Experiments can easily determine factors such as $\tilde{n}$, n, α. However, such experiments do not explain why it is so.

To understands why solids that are transparent to x-rays are not transparent to visible light one needs to consider the wave-particle duality. The Lorentz oscillator model is a very good model which describes absorption lines in materials without free electrons. Even though it is not a general model and uses several assumptions, it still explains why the interaction mechanism of x-rays and light with matter is very different. In the Lorentz oscillator model the atoms or molecules in the medium in question is considered harmonic oscillators with given natural resonant frequencies. As a wave is propagating in the medium these oscillators are driven by the electric field of the wave $\mathcal{E}(t)$.

$$m_0 \frac{d^2y}{dt^2} + m_0\gamma\frac{dy}{dt} + m_0\nu_0^2 y = -e\mathcal{E}(t) \tag{3.6}$$

Here m_0 is the electron mass and as the electron mass is much smaller than the nuclear mass of any atom, it will only be the electrons of the medium that oscillates. γ is the dampening term and ω_0 is the natural resonance frequency of the electrons. e is the elementary charge. This model is illustrated in figure 3.1. By solving the differential equation, eq. 3.6 and applying Maxwells equations, an expression of the frequency dependent complex dielectric constant of a medium can be derived as done in appendix C:

$$\epsilon_r(\nu) = 1 + \chi + \frac{Ne^2}{\epsilon_0 m_0} \cdot \frac{1}{(\nu_0^2 - \nu^2 - i\gamma\nu)} \tag{3.7}$$

Here it is seen that the relative dielectric constant is complex which is why it is also called the complex dielectric constant and can be written as $\tilde{\epsilon}_r(\nu) = \epsilon_1(\nu) + i\epsilon_2(\nu)$, where $\epsilon_1(\nu)$ and $\epsilon_2(\nu)$ is given as:

$$\epsilon_1(\nu) = 1 + \chi + \frac{Ne^2}{\epsilon_0 m_0} \frac{\nu_0^2 - \nu^2}{(\nu_0^2 - \nu^2)^2 + (\gamma\nu)^2} \tag{3.8}$$

$$\epsilon_2(\nu) = \frac{Ne^2}{\epsilon_0 m_0} \frac{\gamma\nu}{(\nu_0^2 - \nu^2)^2 + (\gamma\nu)^2} \tag{3.9}$$

Here χ is the electric susceptibility, ϵ_0 is the electric permittivity of free space and N is the number of dipoles per unit volume. Furthermore a relationship between the dielectric constant of the medium and the refractive index can also be derived from Maxwells equations:

$$n = \frac{1}{\sqrt{2}} \left(\epsilon_1 + \sqrt{\epsilon_1^2 + \epsilon_2^2} \right)^{\frac{1}{2}} \tag{3.10}$$

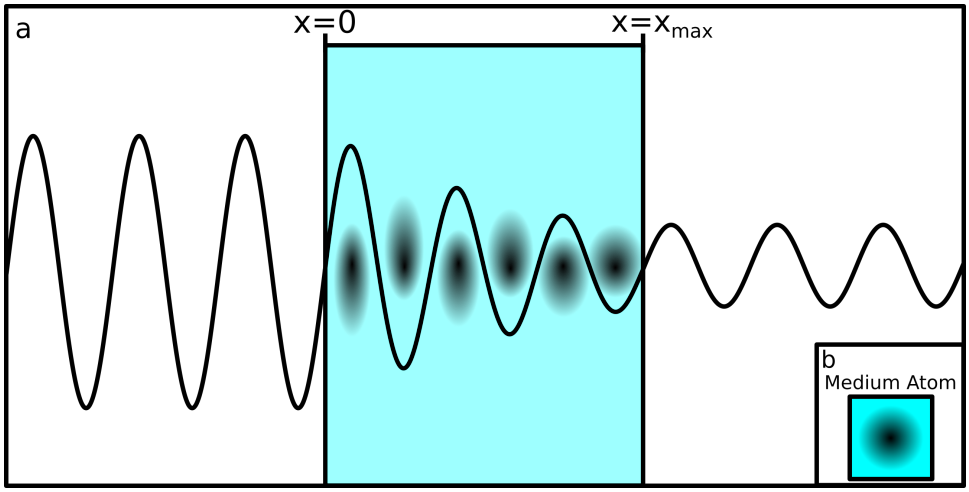

Figure 3.1: Illustration of the attenuation of an electromagnetic wave. It shows the mechanism of a solid absorbing optical light. a) Here a electromagnetic wave is propagating in three regimes. A vacuum regime before and after an absorbing medium. b) Illustration of an atom in rest, where the much darker center represents the nuclei while the lighter surrounding represents an electron cloud. It is seen how the absorbing medium attenuate the wave as it propagates. At the same time the atoms in the medium are polarizes by the electrical field of the wave. Notice that the nuclei is fixed while the translated and distorted electron cloud alone causes the polarization. The polarization also becomes smaller as the strength of the electrical field attenuate.

$$\kappa = \frac{1}{\sqrt{2}} \left(\sqrt{\epsilon_1^2 + \epsilon_2^2} - \epsilon_1 \right)^{\frac{1}{2}} \tag{3.11}$$

A short mathematical derivation of the refractive index of a medium interacting with a monochromatic wave is seen in appendix C.

When considering absorption it is the imaginary parts κ and ϵ_2 which are of interest. These are plotted for the full visible range with a given resonant frequency ν_0 in figure 3.2. From figure 3.2 it is seen that κ and ϵ are closely related and although κ is displaced, γ still determines the height and width of both κ and ϵ_2. As derived in appendix C and claimed in eq. 3.3, κ is directly proportional to the absorption coefficient α, which is why κ is also called the extinction coefficient.

The example calculated in figure 3.2 is naturally a simplified case. There are more resonant frequencies of bound electrons in a solid, which leads to more absorption peaks which still are a simplification of reality. A peak in this model can be equated with an electron transition and is actually observable in experiments. This becomes especially evident in gases as there are no interaction between atoms (Fox 2010). To get the full description of absorption in solids one needs quantum mechanics to calculate

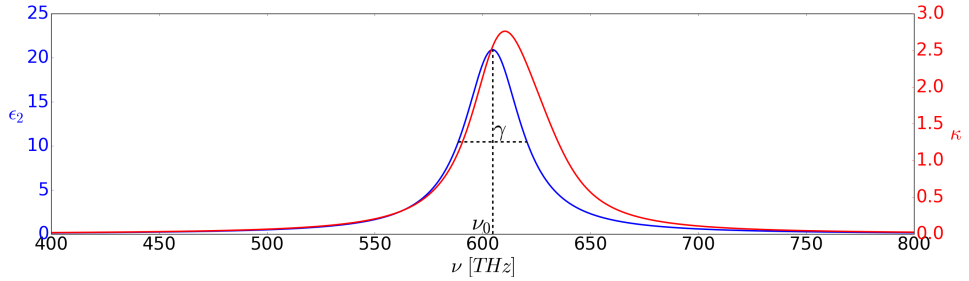

Figure 3.2: Here the imaginary parts of the dielectric constant and refractive index are plotted.It is seen that the extinction coefficient κ is closely related to ϵ_2. Both curves are Lorentzian shaped although κ is slightly shifted from the resonant frequency ν_0. The FWHM is marked by a horizontal line which is equal to the dampening term γ in eq. 3.11 and 3.12. The calculations are performed with $\gamma = 2 \cdot 10^{14} s^{-1}$ and $N = 5 \cdot 10^{17} m^{-3}$

the band structures of a given solid. Band structures induce a continuum of absorption energies. However, the absorption peaks predicted by the Lorentz model can still be observed.

Even though this is a classical approach figure 3.2 actually gives a good explanation of why many materials are transparent to x-rays. The frequency of even the lowest x-ray energies are often well beyond any natural resonance frequencies as $100eV$ is equal to $24180THz$. Obviously a different mechanism leads to the absorption of x-rays. The frequency of the x-rays is so high that all materials appears as an ideal Drude model material. The Drude model normally applies to conductive materials like metals or doped semi conductors. The model basically states that all electrons in the conduction band can be considered to be free. The reason that this applies for most electrons in all materials when considering x-rays is due to the extremely high frequency. The oscillating electron simply does not have the time to "feel" the restoring force caused by the electron displacement from the rest, before the electrical field of the x-ray wave is reversed. This indicates that electrons in any material behave as if they are free when an electrical field from an x-ray wave is applied. In general this assumption holds when the photon energy is much bigger the the electron binding energy. Indeed this is the case for most electrons in any material, but the binding energy of the most tightly bound electrons in heavy elements are comparable to soft x-ray energies, in which case the Lorentz oscillator also applies. This effect is often negligible and for the sake of simplicity all electrons are here assumed to be free.

The combined "perfect Drude material" and "Lorentz oscillator" model is a.k.a. the Drude-Lorentz model. It is actually a simplification of the Lorentz model from eq. 3.6 as the displacement is left out due to negligible restoring force.

$$m_0 \frac{d^2 y}{dt^2} + m_0 \gamma \frac{dy}{dt} = -e\mathcal{E}(t) \tag{3.12}$$

Here the dampening term γ is the average frequency of scattering events of the electrons in the material. Solving the eq. 3.12 is done in the same manner as the solution of eq. 3.6. The complex dielectric constant becomes (Fox 2010):

$$\epsilon_r(\nu) = 1 - \frac{Ne^2}{\epsilon_0 m_0} \frac{1}{4\pi^2\nu^2 + i2\pi\gamma\nu} \tag{3.13}$$

$\Downarrow$

$$\epsilon_1(\nu) = 1 - \frac{\nu_p^2}{4\pi^2\nu^2 + \gamma^2} \tag{3.14}$$

$$\epsilon_2(\nu) = \frac{\nu_p^2\gamma}{\nu\left(6\pi^3\nu^2 + 2\pi\gamma^2\right)} \tag{3.15}$$

Here ν_p is called the plasma frequency an given by:

$$\nu_p = \frac{\omega_p}{2\pi} = \sqrt{\frac{Ne^2}{4\pi^2\epsilon_0 m_0}} \tag{3.16}$$

Normally the term $\sqrt{\frac{Ne^2}{\epsilon_0 m_0}}$ is affiliated with ω_p which is an angular plasma frequency. The 2π term in eq. 3.16 is introduced to keep the frequency convention. In the x-ray regime all materials are considered to be an ideal Drude material, N then becomes the number of electrons per unit volume which is equivalent to the electron density. However, when considering a metal in the ultraviolet or optical region, N is the number of free valence electrons per unite volume. It is seen that the plasma frequency only varies with the electron density.

There is not much interesting to be said about the absorption as the model predicts almost 100 percent reflectivity below the plasma frequency and total transparency above as the complex refractive index becomes very small above the plasma frequency. The Reflectivity and complex refractive index of copper is calculated from eq. 3.4, 3.10, 3.11, 3.14 and 3.15 and seen in figure 3.3. Here $\nu_p = 2610Thz$ and $\gamma = 40.0THz$. In most cases the plasma frequency is located in the ultra violate region well below the x-rays regime that starts at $24180THz$. The most interesting behavior predicted by this model is in the real part of refractive index, which is discussed in section 3.3.2. The combined conclusion of the Lorentz and the Drude-Lorentz model is that everything is totally transparent at x-ray frequency. Obviously that is not the case. It is well known that especially heavy elements such as lead is an extremely good x-ray absorber.

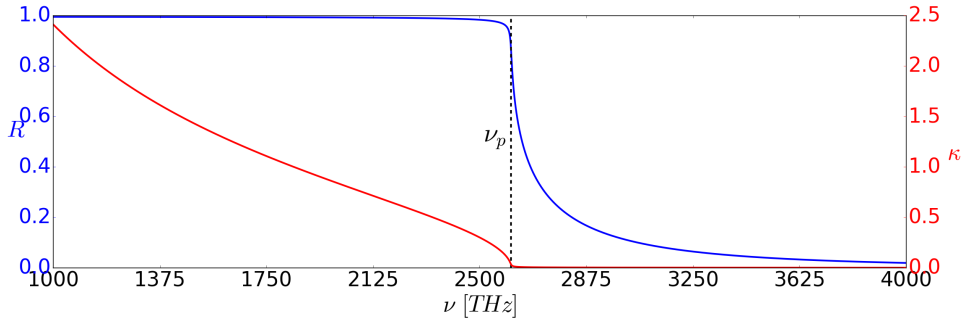

Figure 3.3: The extinction coefficient(κ) and the reflection coefficient(R) plotted as function of the frequency. These are calculated with $\nu_p = 2610Thz$ and $\gamma = 40.0THz$.

3.1.2 Quantum mechanical x-ray absorption

The reason why all the classical approaches fails to explain x-ray absorption is due to the wave-particle duality. Instead of being considered a wave, x-rays must be considered quantum photons. The principle of the absorption mechanism is illustrated in figure 3.4. Figure 3.4 shows that the absorption, is independent on the oscillating electric field, but, instead is determined as probability of the individual photon hitting an individual atom.

Three different mechanisms are associated with absorption of x-rays. In the extreme high energy case the absorption can happen as the so called pair production process. In this process, a high energy photon is absorbed by a nuclei and an electron and its antiparticle the positron is created and ejected from the atom. The photon energy required for this process is in the MeV energy range which arguably is beyond what can be considered x-rays. This energy however is most definitely too high to have any practical use in x-ray imaging. Another "absorption" process is the Compton effect. The Compton effect happens as a x-ray photon collides with an electron orbiting a nuclei. This ionizes the atom as the electron is ejected from the atom. Furthermore a photon of lower energy and different direction of the incident photon is emitted. This is basically inelastic scattering and is therefore also known as Compton scattering, but it is often included as an "real" absorption incidence. Finally the main contributing process is photoelectric effect. An x-ray photon is absorbed after a photon-electron collision. All the energy of the photon is transferred to the electron ionizing the atom of which the electron was a part of. Excess energy from the ionizing process is given to the electron as momentum. Especially at lower photon energies the photoelectric effect becomes so dominating that it can be considered to be the only attenuation contributor.

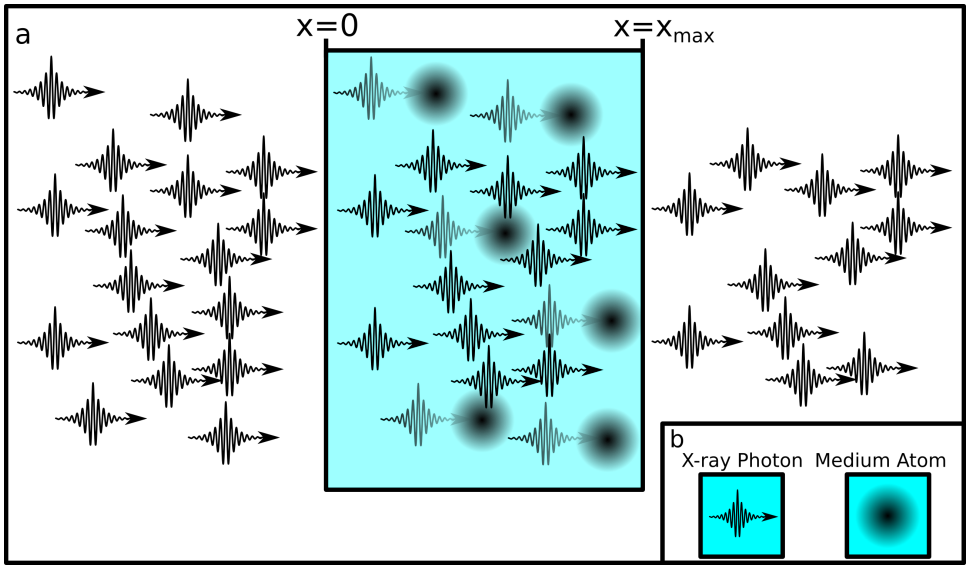

Figure 3.4: Illustration of the attenuation of an electromagnetic wave that shows the mechanism of a medium absorbing x-ray photons. a) Here three snap shots of an ensemble of high energy photons that propagate in three regimes is seen. An air regime before and after an absorbing medium. It is seen how the absorbing medium attenuate the wave as some individual photons gets absorbed by the atoms in the medium. b) Illustration of a single atom and a single photon.

Here the derivation of the theoretical description of x-ray absorption is made. The derivation requires a significant amount of calculation which here is kept to a minimum while a more in-depth calculation is placed in appendix D. As mentioned earlier Beers law given by eq. 3.1, is as valid for x-ray as it is for optical light even though the mechanisms are different. We know the dominant mechanism is photoelectric absorption. The strength of the attenuation coefficient is determined by two factors. Photon energy and electron density of the absorbing medium. For absorption to happen a photon must collide with an electron. The absorption coefficient basically describe the probability for this collision to happen. This means that the attenuation coefficient is proportional to the atomic number density ρ_{atom} and the probability factor called the absorption cross-section σ_a. :

$$\mu = \rho_{atom}\sigma_a = \sigma_a \cdot \left(\frac{\rho_m N_A}{M}\right) \tag{3.17}$$

Here ρ_m is the mass density, N_A is Avogadro's number and M is the molar mass. In the case where a medium consists of more than one kind of atoms μ becomes a sum.

$$\mu = \sum_k \rho_{atom,k}\sigma_{a,k} \tag{3.18}$$

For the case of simplicity only materials consisting of one kind of atoms is considered. The absorption cross-section σ_a is a direct result of first-order perturbation theory. Starting by considering the number of absorption events per second is often denoted W. This must be proportional to the flux Φ_0 of the incoming beam. The proportionality constant is the absorption cross-section σ_a and is a measure of the probability of an absorption event:

$$W = \Phi_0 \sigma_a \Rightarrow \sigma_a = \frac{W}{\Phi_0} \tag{3.19}$$

This defines the absorption cross-section. To describe the transition from the initial state $|i\rangle$ to the final state $\langle f|$, a Hamiltonian describing the interaction must be defined. This is done using Fermi's Golden Rule, which describes the number of transitions per second from one eigenstate to another. W is therefore given by:

$$W = \frac{2\pi}{\hbar}|M_{if}|^2 \rho(\mathcal{E}_f), \quad \textbf{where} \quad M_{if} = \langle f| \mathcal{H}_I |i\rangle \tag{3.20}$$

M_{if} is called the Matrix element and $\rho(\mathcal{E}_f)$ is the density of states in the final state continuum. The calculation of density of state is performed in appendix D:

$$\sigma_a = \frac{V^2}{2\pi^2 \hbar c} \int |M_{if}|^2 \delta(\mathcal{E}_{pe} - (\mathcal{E}_p - \mathcal{E}_b)) q^2 \sin(\theta) dq d\theta d\varphi \tag{3.21}$$

Here q is the length of the wave vector of the photoelectron while θ and φ are the corresponding direction angles. $\mathcal{E}_{pe}$ is the energy of the photoelectron, $\mathcal{E}_b$ is the binding energy of the bound electron and $\mathcal{E}_p$ is the energy of the x-ray photon. Finally the matrix element needs to be calculated. The next step is to define the interaction Hamiltonian. For this, a good starting point is to consider the situation where there is no interaction. In that case the Hamiltonian will be the sum of the Hamiltonian describing the x-ray and the Hamiltonian describing the electron:

$$\mathcal{H}_0 = \mathcal{H}_{x\text{-}photon} + \mathcal{H}_{electron} \tag{3.22}$$

The Hamiltonian is basically the energy of the system and considering a free electron $\mathcal{H}_{electron}$ is therefore given as:

$$\mathcal{H}_{electron} = \frac{\mathbf{p}^2}{2m_e} \tag{3.23}$$

The approach for introducing the interaction Hamiltonian is to consider the free electron in an electromagnetic field. In that case the momentum $\mathbf{p}$ becomes $\mathbf{p} - q\mathbf{pA}$. Here q is the charge of the electron which is equal to $-e$ and $\mathbf{A}$ is the quantified vector potential discussed in appendix D. The full Hamiltonian then becomes:

$$\mathcal{H} = \mathcal{H}_{x\text{-}photon} + \frac{(\mathbf{p} + e\mathbf{pA})^2}{2m_e} \tag{3.24}$$

The electron Hamiltonian can then be split up in a sum of three terms:

$$\mathcal{H} = \mathcal{H}_{x\text{-}photon} + \frac{p^2}{2m_e} + \frac{e\mathbf{A}\cdot\mathbf{p}}{m_e} + \frac{e^2A^2}{2m_e} = \mathcal{H}_{x\text{-}photon} + \mathcal{H}_{electron} + \mathcal{H}_I \tag{3.25}$$

The interaction Hamiltonian is therefore recognized as:

$$\mathcal{H}_I = \frac{e\mathbf{A}\cdot\mathbf{p}}{m_e} + \frac{e^2A^2}{2m_e} \tag{3.26}$$

The first term in the interaction Hamiltonian governs the absorption while the second is the scattering term. In this section the second term has no interest but is discussed in section 3.2. The initial state $|i\rangle$ is defined as a state of one x-ray photon and zero photoelectrons $|i\rangle = |1\rangle_{x-p}|0\rangle_{pe}$. Conversely the final state $|f\rangle$ is defined as a state of zero x-ray photons and one photoelectron $|f\rangle = |0\rangle_{x-p}|1\rangle_{pe}$. With this and only considering the absorption contribution of the interaction Hamiltonian the matrix element defined in eq. 3.20 then becomes:

$$M_{if} = \langle 1|_{pe}\langle 0|_{x-p}\frac{e}{m}\mathbf{p}\cdot\mathbf{A}\,|1\rangle_{x-p}|0\rangle_{pe} \tag{3.27}$$

The the matrix element is treated in appendix D, however it is appropriate to mention that to get an analytical solution the free electron approximation is used. This means that the Coulumb interaction between the photoelectron of the final and the created ion is completely ignored. Under this approximation it is found that the absolute square of the element is:

$$|M_{if}|^2 = \hbar^3\left(\frac{e}{m_eV}\right)^2\left(\frac{1}{2\pi\epsilon_0\nu}\right)\left(q^2\sin^2(\theta)\cos^2(\varphi)\right)\left(\int e^{i(\mathbf{Q})\cdot\mathbf{r}}\psi_{1s}(\mathbf{r})d\mathbf{r}\right)^2 \tag{3.28}$$

Again q is the length of the wave vector of the photoelectron while θ and φ the corresponding direction angles. $\psi_{1s}(\mathbf{r})$ is the wave function of the bound electron and $\mathbf{Q}$ is the so-called wave vector transfer. Substituting this in the absorption cross-section defined in eq. 3.21, one arrives at the full expression:

$$\sigma_a = \left(\frac{\hbar^2e^2}{8\pi^3\epsilon_0cm^2\nu}\right)I_{3D} \tag{3.29}$$

Where I_{3D} is short for the following integral:

$$I_{3D} = \int q^4\sin^2(\theta)\cos^2(\varphi)\left(\int e^{i(\mathbf{Q})\cdot\mathbf{r}}\psi_{1s}(\mathbf{r})d\mathbf{r}\right)^2\delta(\mathcal{E}_f-\mathcal{E}_i)\sin(\theta)dqd\theta d\varphi \tag{3.30}$$

At this point the absorption cross-section is rather complicated, but it can be drastically simplified if the 1s bound state hydrogen is considered, where the atomic number Z can be set to any given value to represent the K electron in a given atom.

$$\sigma_a = 32r_0\frac{c}{\nu}\frac{4}{3}\frac{\tau_0^{3/2}\kappa^5}{\left(\left(2k\sqrt{\tau_0}\right)^2-\left(k^2+\kappa^2+\tau_0\right)^2\right)^2} \tag{3.31}$$

Here, k is the wave number, τ_0 is a parameter that contains the frequency of the x-ray in question and the binding energy of K-electron, κ is the inverse of the K-electron-nuclear effective radius and r_0 is the so-called Thomson scattering length. For a detailed explanation see appendix D.4.
The expression of eq. 3.31 can be further simplified under the limit assumption which states that under the condition that the x-ray photon energy is much bigger than the binding energy of the K-electron and still much smaller than the pair production energy,

$$2\pi\hbar\nu_k \ll 2\pi\nu\hbar \ll 2\pi\nu_c\hbar \tag{3.32}$$

the absorption cross-section can be simplified:

$$\sigma_a = 32r_0\frac{c}{\nu}\frac{4}{3}\left[\frac{(c\kappa)^2}{(\nu\cdot\nu_c)}\right]^{5/2} \tag{3.33}$$

This simplification is also discussed in appendix D.4. For the two representations of the absorption cross-section of eq. 3.31 and 3.33, all parameters are well known to consist of universal constants, or be material parameters. Figure 3.5 shows two different ways

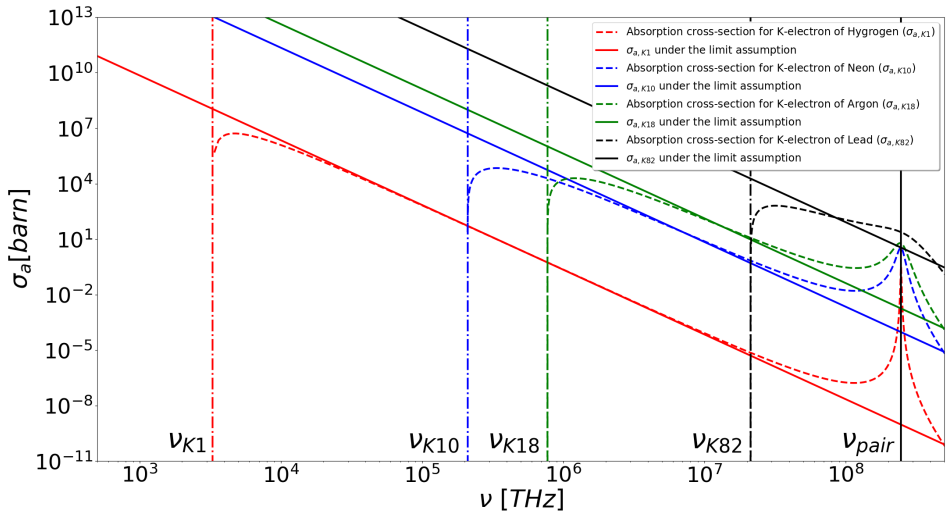

Figure 3.5: Calculation of the absorption cross-section of a K-electrons in different atoms. The dashed lines is absorption cross-section under the free electron approximation. The solid lines represents a further simplification of absorption cross-section when using the limited range assumption of eq. 3.32. The vertical dash dot lines represent the photon frequency equivalent to the binding energy of the K-electrons of the atoms. The vertical black line represents the photon frequency required to achieve pair production

to calculate the absorption cross-section of the K-electron in four different atoms under the free electron approximation, using eq. 3.33 and 3.31. Both axes are logarithmic,

which is necessary to show all aspects at the same time. The dashed lines represent σ_a calculated from eq. 3.31 while the solid lines represent σ_a calculated from 3.33. For illustrative purposes, the solid lines are plotted well beyond the limitation assumption of 3.32. It clearly shows how the approximation is working well as long as the frequency is far beyond the K-electron binding frequency, illustrated by the vertical dash-dotted lines, and far below the pair production frequency illustrated by the vertical solid black line. If the very heavy elements, in this case lead, is considered the assumption does not hold for the K-electrons as the binding energy becomes comparable to the pair production energy. This is clearly observed by $\sigma_{a,K82}$ representations of figure 3.5. Another feature which is observed is that a higher atomic number material in general absorb more, especially for higher frequencies. However below the K-electron binding energy there will be no absorption. This is contradictory to the perception that heavy materials have higher absorption for any frequency. But it should be remembered that this atomic absorption cross-section only accounts for one K-electron. To get the full atomic absorption cross-section one needs to sum over all bound electrons, which substantiates the perception that heavy elements absorb more x-ray radiation in general. The electron binding energy also explains another well known feature of the absorption spectrum of x-rays. This is the so-called absorption edges that arises when the x-ray photon energy surpasses the binding energy. Considering an absorption spectrum for any given material one will observe an exponential decrease in absorption as the photon energy increases until the binding energy of a bound electron is surpassed. Here one will observe a jump in the spectrum. In x-ray science it is often K and L edges that are of significance. Finally it should be mentioned that a clear absorption peak is observed at the pair production energy.

The free electron assumption is actually very crude and makes the model deviate significantly from what is observed in experiment. However, for the purpose of explaining the absorption mechanisms and illustrating not only the absorption cross-section but also explaining absorption edges, this model is surely sufficient.

3.2 Scattering

As mentioned in the beginning of the chapter attenuation in a medium is not only a consequence of absorption but also scattering. This is well illustrated by the beer-analogue to the attenuation law of eq. 3.2. In most cases the main contributor to the attenuation will be absorption which also is the case for liquid part of a drafted beer. However the white foam on top of a draft beer is white due to scattering. In case for the foam the main contributor to the attenuation is scattering. In conventional optics this type of scattering is known as Mie scattering while this effect in x-ray scattering is known as small angle scattering.

As mentioned in the beginning of the chapter a fully valid classical model for scattering do exist. However the quantum mechanical derivation is closely related to the absorption theory discussed in the previous section. Therefore, the quantum mechanical approach is continued. As in the case of absorption we are interested in defining a parameter that predicts how a given material scatters, however the scattering ability of matter is much more complex than the case of absorption. Here the consideration of electron density is far from sufficient to describe the scattering effects from different materials. For instance, the properties of crystalline materials are very different from that of non-crystalline materials. It will be far to extensive to go deeply into all of the subjects considered scattering in material science. However the basics of the Thomson effect will be discussed in depth together with scattering of very simple systems such as atoms and small homogeneous structures. The latter being the only case in this work, where scattering effect is used constructively as most of the time scattering is rightfully neglected or viewed as a source of noise. It is however worth mentioning that the complexity of the scattering mechanisms gives rise to various material characterization methods. One of the widely used approaches is x-ray crystallography. Due to the high complexity of the scattering, the diffraction pattern from conventional crystals can be used to determine parameters such as lattice constants orientation and purity. The same technique can also be applied to complex structures such as proteins. If such are placed in a crystal like lattice, it is possible to deduce the complex structures of these proteins due to complex but well known scattering mechanisms (Als-Nielsen and McMorrow 2010). The scattering mechanism is also used in Coherent Diffraction Imaging techniques such as ptychography, that scans an object which is then reconstructed in real space from a series of diffraction images (Rodenburg et al. 2007).

3.2.1 Thomson scattering

The simplest case of x-ray scattering is scattering from a single electron. The effectiveness of scattering ability of a free electron is called the Thomson scattering cross-section of the free electron. As seen later the scattering event of a photon from a free electron will be in a random direction (if the wave is unpolarized) and independent of the photon energy. Therefore, if a Fermi gas medium of completely uncorrelated electrons is considered, the scattering will also be independent of photon energy and the scattering direction will be random. This is predicted by both classical- and quantum mechanical approaches as seen later in this section. Analogously to the absorption models, figure 3.8 illustrates the quantum mechanical scattering model of a x-ray photon by a Fermi gas medium. From the figure it is evident that if a detector is placed at a large distance from the medium in the path of a incoming wave it will be impossible to determine if the contribution to the attenuation is from absorption or scattering. However, if x-rays are detectable outside the direction of the incoming wave scattering must be a contributor to the attenuation. Considering classical electric dipole radi-

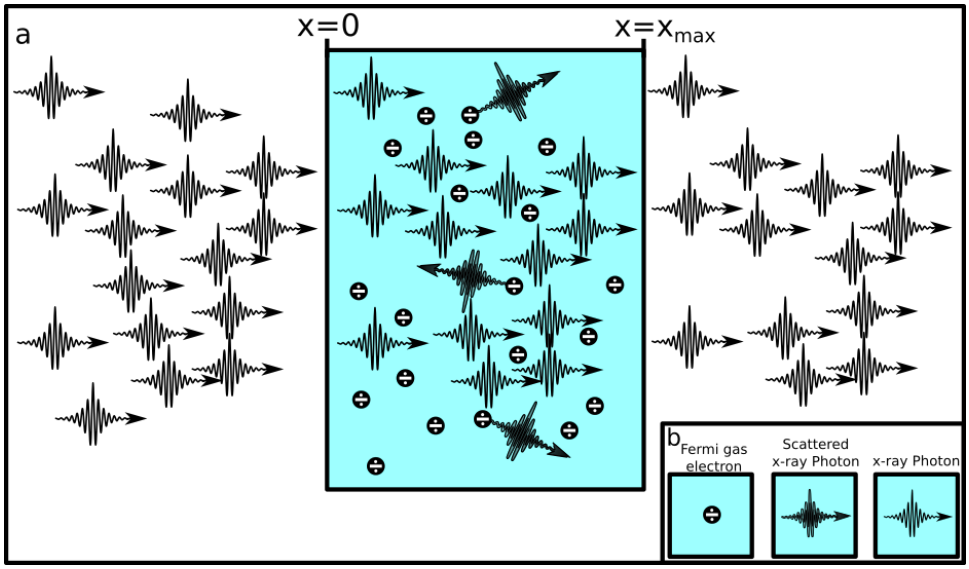

Figure 3.6: Illustration of quantum scattering in a Fermi gas. b) Illustration of an electron, a photon and a scattered photon respectively.

ation as described in appendix B of (Als-Nielsen and McMorrow 2010), where it is shown that under the dipole approximation the Thomson scattering cross-section of a single free electron is given by:

$$\sigma = \left(\frac{8\pi}{3}\right) r_0^2 \tag{3.34}$$

This suggests that the scattering from an electron is independent of energy. This does however not say anything about the direction of the radiated wave. As mentioned this direction is completely random under the assumption that the wave is unpolarized. Within quantum mechanics this becomes different in the simplest system considerable; "one photon and one electron". By nature a photon is linearly polarized due to which some radiation directions becomes less probable than others. This becomes even more significant in complex systems where correlation between more electrons, atom and molecules needs to be considered.

When performing scattering experiments it is often essential to measure a diffraction pattern as this contains a lot of structural information. It is therefore very interesting to determine the scattering direction and diffraction pattern. Hence, when considering scattering, a "differential" scattering cross-section is appropriate to consider. This is defined as:

$$\frac{d\sigma}{d\Omega} = \frac{W_d}{\Phi_0 \Delta\Omega} \tag{3.35}$$

Here Φ_0 is the flux of the incident wave. $\Delta\Omega$ is the solid angle where the scattered x-rays are considered. In scattering experiments $\Delta\Omega$ will be the area of the detector. W_d is the intensity of the scattered x-ray within the area $\Delta\Omega$.
From here on the procedure is very similar to the calculation of the absorption cross-section. The starting point is Fermi's Golden Rule seen in eq. 3.20. Again the density of final states ($\rho(\mathcal{E}_f)$) must be determined (Als-Nielsen and McMorrow 2010):

$$\rho(\mathcal{E}_f) = \left(\frac{V}{(2\pi)^3}\right)\frac{d\mathbf{k}_f}{d\mathcal{E}_f} \tag{3.36}$$

Here $d\mathbf{k}_f$ is the volume element which contains the number of possible states of scattered photons with the wave vector between k_f and $k_f + dk_f$. It should also be noted that because the photon is a boson it does not have a degenerated state. The factor 2 of the photoelectron discussed in the previous section is therefore not extended to this case. The calculation of the the differential scattering cross-section is done in detail in appendix E and is given by:

$$\frac{d\sigma}{d\Omega} = \frac{V^2}{4\pi^2\hbar^4c^4}\int |M_{if}|^2\mathcal{E}_f^2\delta(\mathcal{E}_f - \mathcal{E}_i)d\mathcal{E}_f \tag{3.37}$$

For later convenience the energy variables are shifted to frequency $\mathcal{E}_f = 2\pi\nu'\hbar$:

$$\frac{d\sigma}{d\Omega} = \frac{V^2}{\hbar^2c^4}\int |M_{if}|^2\nu'^2\delta(\nu - \nu')d\nu' \tag{3.38}$$

At this point it simply remains to calculate the matrix element using the appropriate Hamiltonian which is already known as the second term in eq. 3.26. Then the initial and final states needs to be defined. Starting with the initial state it is denoted as:

$$|i\rangle = |p\rangle\,|i_1, o_0\rangle \tag{3.39}$$

Here $|p\rangle$ is the ground state of the scattering electron while i_1 represents one "unscattered" photon and o_0 is zero scattered photons. In the final state this is reversed as the state in this case is described as zero "unscattered" photons and one scattered photon:

$$|f\rangle = |p\rangle\,|i_0, o_1\rangle \tag{3.40}$$

As the scattering is elastic the electron continue to be in the ground state. The matrix element then becomes:

$$M_{if} = \langle f|\,\mathcal{H}_{II}\,|i\rangle = \langle i_0, o_1|\,\langle p|\,\frac{e^2A^2}{2m}\,|p\rangle\,|i_1, o_0\rangle \tag{3.41}$$

As the square of the quantized vector operator is defined in eq. D.15, a cross-term that annihilates the initial photon and creates the scattered one appears. The matrix element can then be described as (Als-Nielsen and McMorrow 2010):

$$M_{if} = \frac{e^2\hbar}{2m\epsilon_0 V}\frac{[\boldsymbol{\varepsilon}_i\cdot\boldsymbol{\varepsilon}_o]}{2\pi\sqrt{(\nu\cdot\nu')}}\,\langle p|\,e^{i2\pi(\nu-\nu')t}e^{i(\mathbf{k}-\mathbf{k}')\cdot\mathbf{r}}\,|p\rangle \tag{3.42}$$

Then by substituting the absolute square of 3.42 in eq. 3.38 one arrives at:

$$\frac{d\sigma}{d\Omega} = \left(\frac{e^2}{4\pi\epsilon_0 mc^2}\right)^2 \left[\boldsymbol{\varepsilon}_i \cdot \boldsymbol{\varepsilon}_o\right]^2 \mid \langle p \mid e^{i(\mathbf{Q}\cdot\mathbf{r})} \mid p \rangle \mid^2 \tag{3.43}$$

The squared factor is recognized as the square of the Thomson scattering length (r_0), $\left[\boldsymbol{\varepsilon}_i \cdot \boldsymbol{\varepsilon}_o\right]^2$ is called the polarization factor, where $\boldsymbol{\varepsilon}_i$ $\boldsymbol{\varepsilon}_o$ is the unit vectors of the incident and radiated photons respectively, and $\mathbf{Q}$ is in the case of elastic scattering called the scattering vector given by the wave vectors of the incident and radiated photons respectively. The last term is the absolute square of the form factor and is denoted $f(\mathbf{Q})$. The different scattering cross-section then becomes:

$$\frac{d\sigma}{d\Omega} = (r_0)^2 \left[\boldsymbol{\varepsilon}_i \cdot \boldsymbol{\varepsilon}_o\right]^2 |f(\mathbf{Q})|^2 \tag{3.44}$$

The form factor describes the shape of the scattering object and can be indirectly measured in scattering experiments and is discussed in 3.11. Here the absolute square of the form factor is one and therefore of no consequence. This is because the electron is so small that it is considered to be structure-less. As seen momentarily, this is a rare case where total agreement between a classical- and quantum mechanical model is found. I the following the classical model is summarized.

3.2.2 Classical scattering

Here the simplest imaginable case is discussed. The scattering object is again an electron, but unlike the quantum mechanical approach one must consider an electromagnetic wave instead of a quantum. The differential scattering cross-section is again defined as:

$$\frac{d\sigma}{d\Omega} = \frac{I_s}{\Phi_0 \Delta\Omega} \tag{3.45}$$

Again Φ_0 is the flux of the incident wave. $\Delta\Omega$ is the solid angle where the scattered x-rays are considered. In scattering experiments $\Delta\Omega$ will define the area of the detector together with the distance to the detector (R) so that the detector area is given as $\Delta\Omega \cdot R^2$. The intensity of the scattered x-ray within the area $\Delta\Omega$ is this time denoted I_s which is a more classical notation. The model is illustrated in figure 3.7 where the electrons interacts with a electromagnetic plane wave, that in turn results in the electromagnetic radiation from the electrons. Due to this the scattering cross-section should therefore be rewritten so that it is given by the Electrical field of the incident wave. This is easily done as both a proportional to there own electrical field squared:

$$\Phi_0 \propto \frac{c}{2\pi\hbar\nu}|E_{in}|^2 \quad \textit{and} \quad I_s \propto \frac{c\Delta\Omega R^2}{2\pi\hbar\nu}|E_s|^2 \tag{3.46}$$

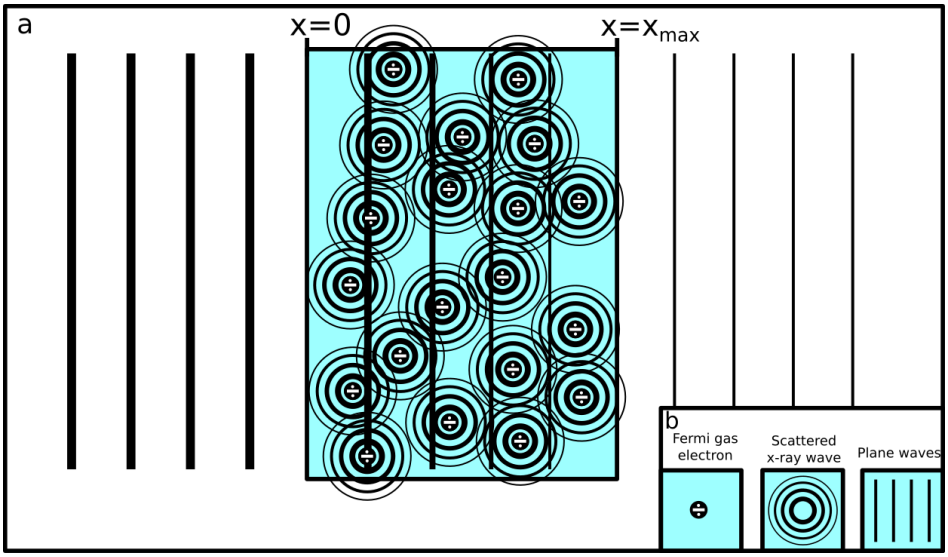

Figure 3.7: I b) Illustration of classical scattering model where the incident electromagnetic radiation is considered to be waves. a) The intensity of incident plane waves are attenuated as the free electrons in the Fermi gas Scatters the waves.

Exploiting these the differential cross-section is rewritten:

$$\frac{d\sigma}{d\Omega} = \frac{|E_s|^2 R^2}{|E_{in}|^2} \tag{3.47}$$

From the classical approach as illustrated in figure 3.7 the electrical field of the incoming waves which makes the electron oscillate. This is very much equivalent to the Drude-Lorentz model from previous sections, where all electrons were considered free because of the extremely high frequency of x-rays. Here we are only considering one free electron, which makes this approach valid for the full spectrum range. As in any classical approach Maxwell's equations must treated. If both the magnetic and the Electrical field should be considered a given point it is often advantageous to consider the vector potential ($\mathbf{A}$). In a given point of interest the electric- and magnetic fields is described by the vector potential as:

$$\mathbf{E} = -\nabla P - \frac{\partial \mathbf{A}}{\partial t} \tag{3.48}$$

$$\mathbf{B} = -\nabla \mathbf{A} \tag{3.49}$$

Here P is the scalar potential. The vector potential of an arbitrary charge distribution is given as (Griffiths 1999):

$$\mathbf{A}(\mathbf{r},t) = \frac{1}{4\pi\epsilon_0 c^2}\int_V \frac{\mathbf{J}(\mathbf{r}', t-|\mathbf{r}-\mathbf{r}'|/c)}{|\mathbf{r}-\mathbf{r}'|}d\mathbf{r}' \tag{3.50}$$

It is however, possible to simplify this expression under the dipole approximation, which states that distance r (the distance to the observer point) from the charge distribution is much larger lager than its distribution in space. Then considering an electron it is very difficult to imagine and situation were that is not the case. A second useful assumption is to assume that the wavelength is much smaller than the r. Again it is difficult to imagine it not being so. Solving the above, the electrical field in the observer point can be found to be given as (Als-Nielsen and McMorrow 2010):

$$E(t) = -\left(\frac{1}{4\pi\epsilon_0 c^2 r}\right)\ddot{p}(t)\cos\psi \tag{3.51}$$

Here $\ddot{p}(t)$ is the double derivative of the dipole moment of the electron when a linear polarization from the incident beam is applied. ψ is the angle that defines the direction to the observer, so that, if the electric dipole is oriented in the z direction, ψ is the angle on to the xy-plan. The spherical coordinates are defined by θ and φ. θ defines the angle on the z axis so that $\psi+\theta = \pi/2$ and φ is the direction in the xy-plane. The linear polarization is assumed for simplicity, as only the magnitude of dipole moment needs to be considered, however as seen later we are still able to determine what happens when the incident beam is unpolarized. The magnitude of dipole moments is by definition $p = qd$, where q is the charge and d is the displacement. It therefore follows that $\ddot{p}(t') = q\ddot{d}(t')$. As d is defined as a length, $\ddot{d}$ must be an acceleration which here is the force applied be the electrical field divided by the mass. The force applied is the magnitude of the incident electrical field on the charge q. The double derivative then becomes:

$$\ddot{p}(t') = q\frac{qE_{in}(t')}{m_e} = \frac{q^2}{m}E_0 e^{-i2\pi\nu(t-r/c)} = \frac{q^2}{m}E_0 e^{-i2\pi\nu(t)}e^{i2\pi\nu(r/c)} \tag{3.52}$$

E_0 is the amplitude of the electrical field and the factor r/c is a result of the time it takes the emitted radiation to travel from the dipole to the observer point ($t' = t-r/c$). The electrical field in the observer point is then found by substituting eq. 3.52 into 3.51.

$$E(t) = -\left(\frac{e^2}{4\pi\epsilon_0 c^2 m_e}\right)\left(\frac{e^{ikr}}{r}\right)E_{in}(t)\cos\psi \tag{3.53}$$

$\Downarrow$

$$\frac{E(t)}{E_{in}(t)} = -r_0\left(\frac{e^{ikr}}{r}\right)\cos\psi \tag{3.54}$$

As in the case of the quantum mechanical absorption and scattering, the Thomson scattering length (r_0) appears, this time through a purely classical approach. The

physical implication of the minus in eq. 3.54 is a π phase shift of the scattered wave compared to the incident wave. The differential cross section is then found by substituting eq. 3.54 into eq. 3.47.

$$\frac{d\sigma}{d\Omega} = r_0^2 \cos^2 \psi \tag{3.55}$$

Here the polarization factor is given by $cos^2\psi$. This is fully equivalent to the result of the quantum mechanical result of eq. 3.44. By this we can conclude that the scattering is direction dependent. In quantum mechanics this means that scattering in some directions are more probable than others and not allowed in direction of the dipole moment. In classical optics this means that the wavefront is stronger in some directions compared to others or even zero in the dipole moment direction, which yields the same result. In figure 3.8.a and .b this is illustrated. The black lines on the x-axis illustrates the wave front and is the maximum value of the magnetic field. That of course means that the oscillation of the electrical field is in the z-direction of figure 3.8.a and ind the y-direction of 3.8.b. The dipole moment of the electron is illustrated by the doubled ended green arrow. It is observed that the incident wave is attenuated after propagating past the electron, illustrated by a thinner wavefront line. The geometric surface represents the polarization factor in a given direction. For illustrative purposes only half of the factor is displayed. In figure 3.8.b it is seen that the factor is largest (1) in the xy-plane and zero on the z axis. In figure 3.8.b this behavior is rotated 90 degrees around the axis so that the polarization factor is largest in xz-plane and zero on y-axis. The scattering is illustrated as the black arrow with perpendicular lines. These lines represent the wave front of one possible scattering direction. It should be noticed that the wave front has a π phase shift compared to the incident wave. If the source is unpolarized the polarization factor will be the average of the two perpendicular cases. The result is an almost perfect peanut shell shape as displayed in figure 3.8.c. This is described by a polarization factor given as $[\boldsymbol{\varepsilon} \cdot \boldsymbol{\varepsilon}']^2 = \left(1 + \cos^2 \psi\right)/2$. Here it is observed that the maximum scattering direction is in the propagation direction of incident wave while the minimum is in the yz-plane (perpendicular to the incident wave direction).

Finally, the total scattering cross-section is discussed. The differential cross-section is known by eq. 3.55. The total scattering cross-section is simply calculated as the integral over the right hand side of eq. 3.55 over all angels for θ and φ:

$$\sigma_{total} = \int_0^{\pi} \int_0^{2\pi} \cos^2(\psi) \sin\theta d\theta d\varphi \tag{3.56}$$

Remembering that $\psi + \theta = \pi/2$ the polarization factor is rewritten:

$$\sigma_{total} = \int_0^{2\pi} \int_0^{\pi} \sin^2(\theta) \sin\theta d\theta d\varphi = r_0^2 \frac{8\pi}{3} = 0.665 \cdot 10^{-28} m^2 = 0.665 \text{ barn} \tag{3.57}$$

The unpolarized case yields the same total scattering cross section. Interestingly this means that the scattering from a free electron is completely independent of frequency. That means that in scattering from free electrons there is no differences between light and x-rays. In reality free uncorrelated electrons are not common and is of little interest for experiments. In the following some simple systems are discussed.

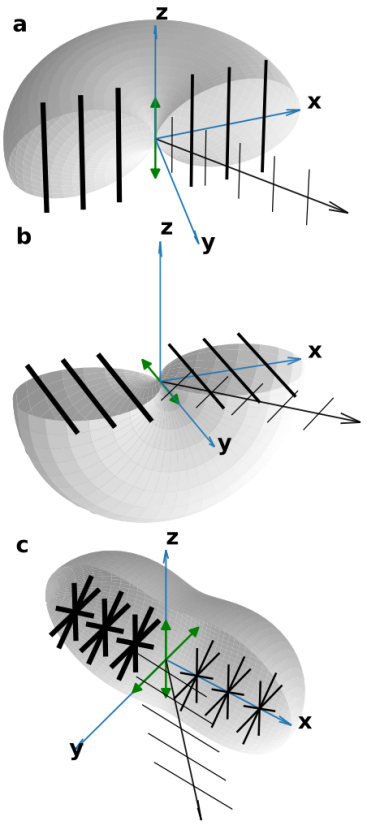

Figure 3.8: Wave amplitudes for different polarizations of the incident waves. a) The wave fronts (lines parallel to z-axis) represents the maximum value of the magnetic field, which means that the electrical fields oscillates in the z-direction. The green double ended arrow illustrates the dipole moment of the driven electron. The wave amplitude geometry illustrates that the maximum scattering happens in the xy-plan. The black arrow illustrates a scattered wave with a phase shift of π. b) equivalent to a), however the polarization of the incident have an oscillating electrical field in the y-direction. c) Illustration of an unpolarized incident wave. Here the wave amplitude is the average of a) and b).

3.2.3 Small Angle X-ray Scattering - Dark Field Constrast

Earlier the so called form factor was introduced (eq. 3.44). In the free electron case this had no implications. This is because the electron is considered to have no structure. In all other cases the form factor will be of great consequence to the scattering as it determines the diffraction pattern of a given charge distribution. The form factor is a function of the scattering vector $\mathbf{Q}$ first introduced in eq. 3.43. $\mathbf{Q}$ is given as $\mathbf{Q} = \mathbf{k} - \mathbf{k}'$, the wave vector of the incident and scattered wave respectively This is also illustrated in figure 3.9. Here it is seen how the incident and scattered wave vectors spans the scattering vector. As only elastic scattering is considered it follows

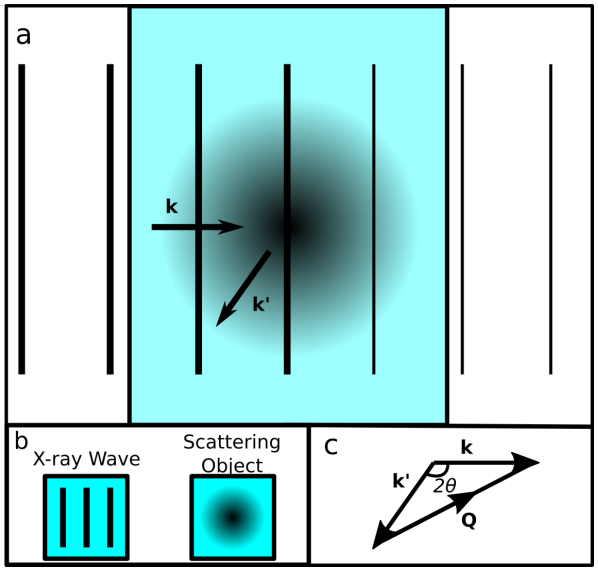

Figure 3.9: Defining $\mathbf{Q}$. a) An incident wave propagates in the direction of the wave vector $\mathbf{k}$ a scattering incident happens in a direction defined by the scattered wave vector $\mathbf{k}'$. b) Illustrates of a wave front and the scattering object. c) The wave vectors $\mathbf{k}$ and $\mathbf{k}'$ is used to illustrate the scattering vector $\mathbf{Q}$.

that $|\mathbf{k}| = |\mathbf{k}'|$. It then follows that the magnitude of $\mathbf{Q}$ is given by:

$$|\mathbf{Q}| = 2k \sin\theta = \frac{4\pi}{\lambda} \sin\theta \tag{3.58}$$

In section E.2 of appendix E, the small angle scattering from simplest imaginable structures (two electron) up to simple molecules are discussed. From a imaging point of view such structures are not feasible to image. However, it is shown in E.2 that the scattering from even the simplest structures is dependent on photon energy. Furthermore the scattering does also have an angular dependence. This is also the case for

larger particles and when these becomes big enough the scattering effect utilizes by particles of such sizes can be image through the dark field imaging technique.

Considering a "larger" spherical structure of single molecules or atoms is one of the few cases which can be solved analytically. The small angle scattering from such a particle is determined by the particle form factor (Als-Nielsen and McMorrow 2010):

$$F_p = \frac{1}{V_p} \int_{V_p} e^{i\mathbf{Q}\cdot\mathbf{r}} dV_p \tag{3.59}$$

The scattering intensity is proportional to the $|F_p|^2$, V_p^2 and ρ_{sl}^2. By integration over the full sphere, $F_p(Q)$ can be described by (Als-Nielsen and McMorrow 2010):

$$F_p(Q) = 3\left[\frac{\sin QR - QR\cos QR}{Q^3R^3}\right] \tag{3.60}$$

Here R is the radius of the particles. In figure 3.10 $|F_p(Q)|^2$ are calculated for different sized particles. Two nano-particles of specific sizes as well as three particles with sizes

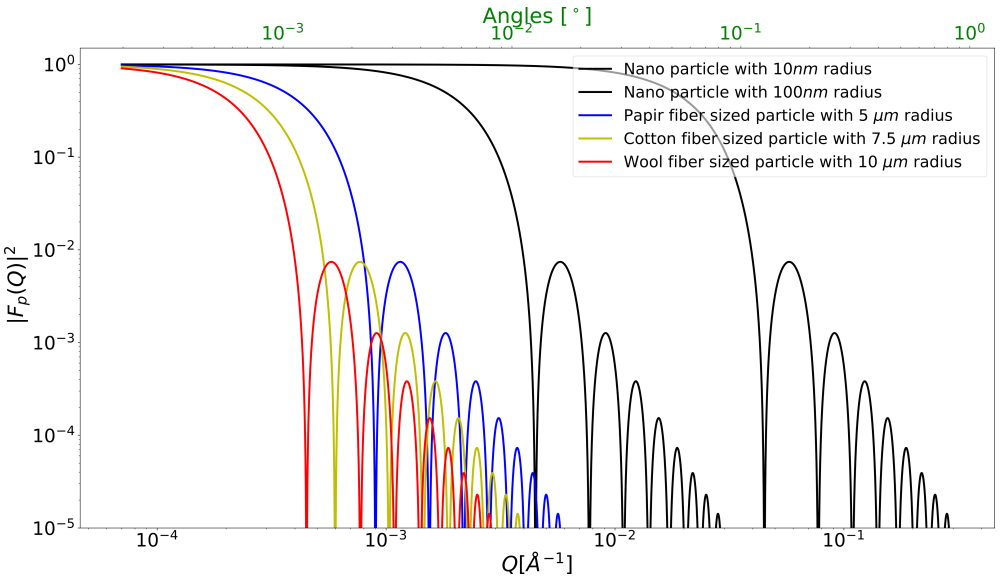

Figure 3.10: Form factor of different sized and spherical shape particles. The form factors are calculation for 20 KeV radiation, which means that Q is a function of the angle θ. The corresponding angles i seen as the top x-axis.

very comparable to real world structures that are able to produce a strong dark field signal. Although these structures are fibers, they will still induces similar scattering angles as these particles, perpendicular to fiber direction. These particle calculations

are very good representations of what scattering angles are expected for these specific materials. It is very evident from figure 3.10 that even for the extremely small nanoparticle the scattering angles are very small. For a particle of $10nm$ radius one must consider a scattering angle of less than a degree to measure anything significant. This clearly illustrates that measuring such scattering is no trivial matter when considering structure sizes given in figure 3.10.

3.2.4 Dark field imaging and x-ray Fog

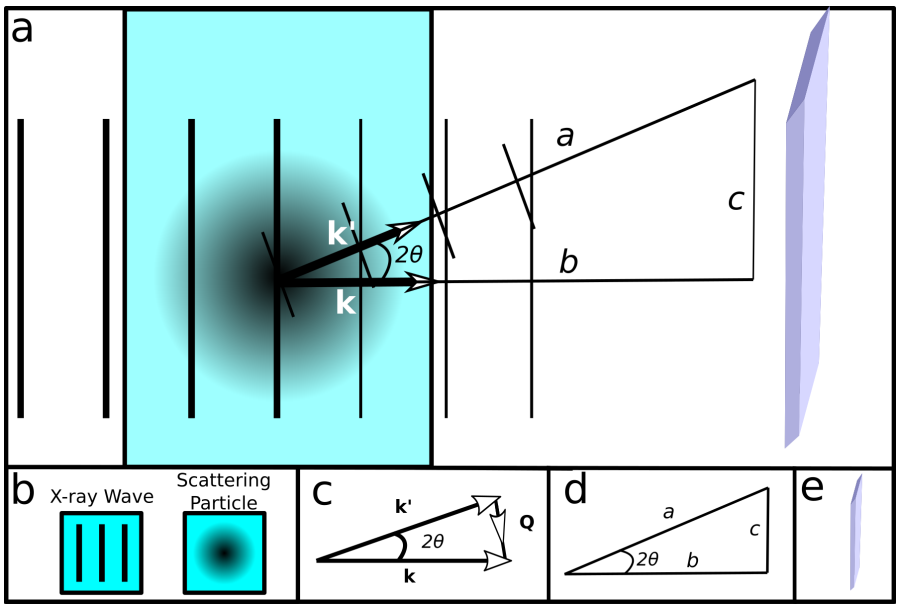

Figure 3.11: Geometric consideration to determine how much a scattering wave is diverged from the the incident wave. a) The scattering of an incident wave measured by an detector pixel at distance b from the scattering object. b) Definition of planar x-ray and the scattering particle. c) Vector consideration of incident wave $\mathbf{k}$, scattered wave $\mathbf{k}'$ and $\mathbf{Q}$. d) Geometry of interest in this setup. e) Detector pixel.

Figure 3.11 illustrates an geometric consideration of an x-ray setup. In figure 3.10 a vertical line marks the angle were a significant amount of scattering is observed for all structures of interest. In interferometer imaging setups a realistic distance between sample and detector could be one meter. From this it is straight-forward to determine how much the scattered wave have diverged from the incident wave by the value of c:

$$c = \tan(2\theta) \cdot b = \tan\left(2 \cdot 7 \cdot 10^{-4}\right) \cdot 1m = 24.4\mu m \tag{3.61}$$

The high end pilatus detector "PILATUS3 R 1M" produces by Dectrice has a pixel size of $(172x172)\mu m$ (*Pilatus* 2019). Such pixel sizes is much bigger than horizontal or vertical divergences the angle scattering that these structures induces. In a regular x-ray imaging system the scattering is therefore not measurable and in conventional radiography or tomography this is neither desirable as larger angle scattering will be a noise contributor. One way such small angle scattering is detected is to have an extremely small source spot size and a phase grating. A second approach is to have two gratings which makes a well defined interference pattern after passing through an absorption grating and phase grating (Talbot interferometer). No matter the approach an interference pattern which is much smaller than the pixel size is obtained and final absorption granting scanned to characterize the interference pattern on sub pixel level. If a small angle scattering object is placed in such an interference pattern it will be disrupted and visibility goes down. By comparing to a reference measurement with full visibility the dark field image is created.

An analogue to the visible regime and everyday observation is the weather phenomenon fog. Fog manifests when very small water particles in the air scatter the visible light and reduces our ability to look fare. It is the exact same principle of dark field imaging. One could say that an object producing a high dark field signal actually produces "x-ray fog" and that is what is measured. If the structures in a sample become too big the angles will become even to small for the interferometer to detect. Again, this also applies to everyday experiences as bigger water particles in the air such as rain drops in a much lesser degree prohibit our ability to see fare as the scattering angle is to small for the eye to notice. Dark field imaging is discussed in more detail in 4.4.

Another way to view the interaction of radiation and the structures, discussed in this section, is as refraction. When radiation is passing through structures greater than the wavelength of the radiation it is just as valid to view the change of direction as a difference in refractive index between the particle/structure in question and its surrounding. Earlier it was suggested that the refraction and diffraction/scatting is two sides of the same coin. Indeed this is the case as seen in following.

3.3 Refraction

The last kind of radiation and matter interaction is refraction. In short refraction is the consequence when phase velocity of electromagnetic waves propagating in matter changes with different refractive indexes.

$$v = \frac{c}{n} \tag{3.62}$$

where n is real part of the complex refractive index.

3.3.1 Refraction of the Lorentzs oscillator

In the visible regime the phase velocity in matter becomes smaller than the speed of light which again means that n is bigger than one. X-ray radiation experiences an real refractive index smaller than one, which means a phase velocity greater than light speed. This is of course not a violation of physics as the phase velocity is allowed to travel faster than light speed. Another interesting consequence of a refractive index smaller than one is the phenomenon know as total external reflection which under normal conditions is not seen in the optical regime. In the following the Lorentz- and Drude-Lorentz models is first continued and then followed by scattering consideration that ended the previous section with large particle scattering. In the classical absorption section, the focus was on the complex part of the refractive index, however the real part of the refractive index is as much a result of the Lorentz oscillator as the complex part and is actually already derived in eq. 3.7, 3.8 and 3.10. As a reminder the real parts of the dielectric constant $\epsilon_1(\nu)$ and the refractive index n are given by:

$$\epsilon_1(\nu) = 1 + \chi + \frac{Ne^2}{\epsilon_0 m_0} \frac{\nu_0^2 - \nu^2}{(\nu_0^2 - \nu^2)^2 + (\gamma\nu)^2} \tag{3.63}$$

$$n = \frac{1}{\sqrt{2}} \left(\epsilon_1 + \sqrt{\epsilon_1^2 + \epsilon_2^2} \right)^{\frac{1}{2}} \tag{3.64}$$

Clearly the refractive index in such materials are very sensitive to photon energies

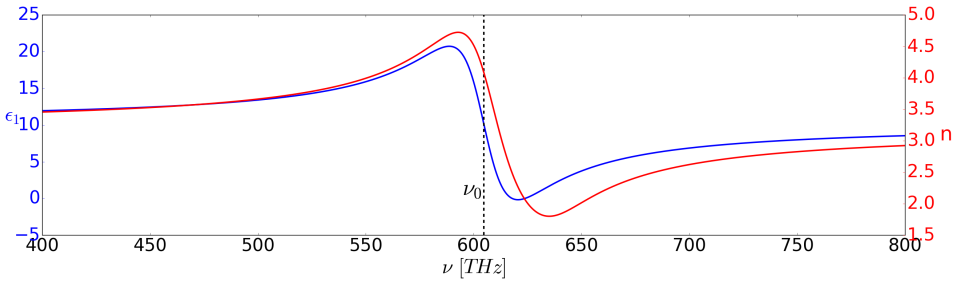

Figure 3.12: The real parts of the dielectric constant and refractive index are plotted here. It is seen that n is closely related to ϵ_1. Both curves have a very characteristic behavior around the resonant frequency ν_0 where both becomes very energy sensitive. The calculations are performed with $\gamma = 2 \cdot 10^{14} s^{-1}$ and $N = 5 \cdot 10^{17} m^{-3}$ and corresponds to the calculation of figure 3.2

around material resonance frequencies. However as already discussed in the Lorentz

oscillator absorption part the model breaks down in the x-ray regime as the electrical field cannot be considered constant in time as the frequency is much bigger than any resonance frequencies.

3.3.2 The real part of Drude-Lorentzs model

To make the Lorentz oscillator model relevant for higher frequencies all electrons were in the absorption section also considered to be free. This is the Drude-Lorentz model which normally is applied to describe the optical properties of metals in the visible- and and ultra violet regime. Even though it did not explain absorption it did a good job explaining the transparency property of x-rays. As seen momentarily the model does a even better job describing the refraction of x-rays.
From eq. 3.13, 3.14 and 3.16 the dielectric properties is well known and are seen here:

$$\epsilon_r(\nu) = 1 - \frac{Ne^2}{\epsilon_0 m_0} \frac{1}{4\pi^2\nu^2 + i2\pi\gamma\nu} \tag{3.65}$$

Here the real part is given as:

$$\epsilon_1(\nu) = 1 - \frac{\nu_p^2}{4\pi^2\nu^2 + \gamma^2} \tag{3.66}$$

The dampening term γ is the average frequency of scattering events of the electrons in the material. ν_p is still the plasma frequency:

$$\nu_p = \frac{\omega_p}{2\pi} = \sqrt{\frac{Ne^2}{4\pi^2\epsilon_0 m_0}} \tag{3.67}$$

The real part of the refractive index can again be calculated as in eq. 3.64. From eq. 3.66 it is evident that the dielectric constant becomes negative below the plasma frequency. In figure 3.13 n and the absolute value of ϵ_1 is plotted. The reason why the absolute value of ϵ_1 is plotted is because the axes are logarithmic. Values below the plasma frequency is therefore negative. Notice that this are not the case for n which is purely positive. This predicts an asymptotic behavior of the refractive index towards one, as the frequency increases. At high frequency it is also possible to simplify the expression for the dielectric constant observed in eq. 3.65, as γ becomes negligible in that regime which in turn means that the complex part of the dielectric constant vanishes:

$$\epsilon_r(\nu) = 1 - \frac{Ne^2}{\epsilon_0 m_0} \frac{1}{4\pi^2\nu^2 + i2\pi\gamma\nu} \approx 1 - \frac{Ne^2}{4\pi^2\epsilon_0 m_0} \frac{1}{\nu^2} \tag{3.68}$$

At this point it is advantageous to express the dielectric constant in terms of the wave number instead of frequency. The wave number is given as $k = 2\pi\nu/c$. eq. 3.68 then

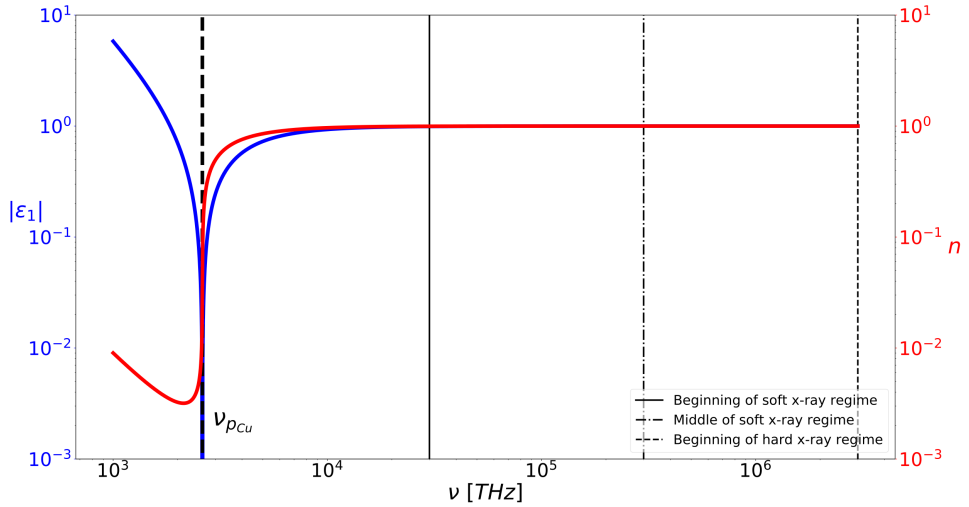

Figure 3.13: The real parts of the dielectric constant and refractive index derived from the Drude-Lorentz model are plotted here. The real dielectric constant(ϵ_1) and the refraction index (n) are plotted as function of the frequency. These are calculated with $\nu_p = 2610Thz$ and $\gamma = 40.0THz$.

become:

$$\epsilon_r(\nu) = 1 - \frac{Ne^2}{4\pi^2\epsilon_0 m_0}\frac{1}{\nu^2} = 1 - \frac{Ne^2}{4\pi^2\epsilon_0 m_0}\frac{4\pi^2}{k^2c^2} = 1 - 4\pi N \cdot \frac{r_0}{k^2} \tag{3.69}$$

n can then be calculated by substituting eq. 3.70 into eq. 3.64:

$$n = \frac{1}{\sqrt{2}}\left(\epsilon_1 + \sqrt{\epsilon_1^2 + \epsilon_2^2}\right)^{\frac{1}{2}} = \frac{1}{\sqrt{2}}\left(1 - 4\pi N \cdot \frac{r_0}{k^2} + 1 - 4\pi N \cdot \frac{r_0}{k^2}\right)^{\frac{1}{2}} \tag{3.70}$$

$\Downarrow$

$$n = \frac{1}{\sqrt{2}}\left(2 - 8\pi N \cdot \frac{r_0}{k^2}\right)^{\frac{1}{2}} = \sqrt{1 - \frac{4\pi N r_0}{k^2}} \tag{3.71}$$

Due to the high values of k in the x-ray regime the approximation $\sqrt{1-x} \approx 1 - x/2$ for small x can be applied:

$$n = \sqrt{1 - \frac{4\pi N r_0}{k^2}} \approx 1 - \frac{2\pi N r_0}{k^2} \tag{3.72}$$

Again the equivalence between refraction and diffraction becomes apparent as the Thomson scattering length appear in the refractive index. As seen in the following this is for a good reason. In the x-ray regime the real part of the refractive index is defined as:

$$n = 1 - \delta = 1 - \frac{2\pi\rho_e r_0}{k^2} \tag{3.73}$$

Here N and ρ_e is both the electron number density. This is a good approximate description of the refractive index especially for higher frequencies. This holds if the scattering amplitude is equal to r_0. From the previous section it is known that the scattering amplitude is not only equivalent to r_0 as it also has some angular dependencies even on the electron level. In the following the form factor is used to give an even more precise description of the δ.

3.3.3 Scattering consideration to refraction

Here two different approaches is used to visualize the refractive behavior of x-rays in materials. Normal refraction described as a change in phase velocity and scattering from the smaller substances composing the material. In figure 3.14.a the first case

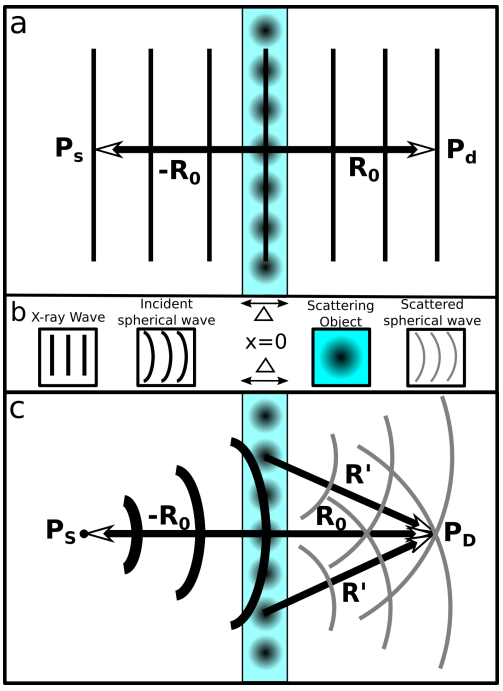

Figure 3.14: The diffraction and the refraction consideration. a) Plane waves travels from left to right and encounters a slab of a refractive index n smaller than one for x-rays. This educes a small phase shift. b) Definitions of the objects in a and c. $x = 0$ is defined as the middle of the slabs. The thickness of the slabs is given by Δ. c) Spherical x-ray waves travels from left to right and is scattered by scattering particles which are encountered in the slab. The wave fronts after the slab is the super position of all the scattered waves.

i observed. A plane wave is propagating from left to right. In the intermediate area between the source point P_S and the detection point P_D, the wave encounters a material slab of thickness Δ with a given refractive index n. If the absorption is neglected and R_0 is perpendicular to the material slab the wave phase of the wave will travel at little faster in the material, hence the wave at the point P_D will have a small phase shift compared to the situation without a slab:

$$E_D^P = E_0^P e^{i(n-1)k\Delta} \tag{3.74}$$

Here E_0^P denotes the electrical field in the observer point without any slab. As it is well known, that (n-1) is very close to zero, the approximation $e^x \approx 1 + x$ can be applied:

$$E_d^P = E_0^P \left(1 + i(n-1)k\Delta\right) \tag{3.75}$$

Then the scattering approach is considered. Here the waves are considered to be spherical and only experience scattering. Then two contributions to the wave at P_D must be investigated. Observing the wave on exact path between P_S and P_D the wave looks plane although it is loosing amplitude as it propagates. The contribution is therefore:

$$E_0^P = \frac{e^{ik2R_0}}{2R_0} \tag{3.76}$$

In all other cases E_D^P is contributed by scattering in the material slab. One case is illustrated in figure 3.14.b. From some geometric considerations and performing the math as seen in appendix F, E_D^P can be shown to be:

$$E_D^P = E_0^P \left(1 - i\frac{2\pi\rho_{at} f_{at} r_0}{k^2} k\Delta\right) = E_0^P \left(1 - i\delta_{at} k\Delta\right) \tag{3.77}$$

By this the scattering length is determined to be:

$$\delta_{at} = \frac{2\pi\rho_{at} f_{at} r_0}{k^2} \tag{3.78}$$

The scattering length of the smaller particles which are distributed within a larger bulk material is shown to define the refractive properties of the bulk material. By this scattering approach it is also possible to introduce the form factor of the scattering particles and thereby improve the result derived from the Drude-Lorentz model.

4 Introduction to x-ray imaging modalities

In this chapter the fundamentals of the imaging techniques used in the publications are discussed. Here, the starting point is the generation x-rays and there several established methods of generating these. It is essential that the right source is chosen for the right experiment, as different type of imaging methods have different requirements for the wave. Such requirements are for instance, beam power, photon energies, spot size, monochromaticity, shape, and coherence of the x-ray beam.

How the contrast mechanism can be exploited is described briefly together with the source requirements. More thorough discussions are made on the specific imaging techniques applied in the publication presented in this thesis.

4.1 Absorption Contrast

Absorption x-ray imaging is often equated with the measure of attenuation in different materials. When considering x-rays, this is indeed the most dominant attenuation effect. This attenuation effect is also very easy to measure as this is basically the x-ray intensity distributions deposited on a detector surface in a given time span. This time span is called the exposure time. Due to its simple measurability, absorption contrast is the oldest and most widely used contrast mechanism in imaging. The intensity can be measured as two different quantities, either as the number of measured photons,

or as the power deposited in a given pixel of the detector. If a monochromatic wave is considered, these measures will be equivalent. It is not straightforward to obtain a monochromatic x-ray lab source although not impossible (Wagner et al. 2008). The monochromaticity also comes at a price, which is lower power of the x-ray beam. In absorption imaging in the lab, this often not a price worth paying, as attenuation of any energy is often relevant. In tomography, beam hardening effects can become an issue, but this is often sufficiently handled with a high pass filter.

In practice, absorption image projections are often made from two radiographic projections. The attenuation projection and a so-called flat field projection, which is just a detector readout without a sample. With these, the transmission, T is calculated as:

$$T = \frac{I_a}{I_f} \tag{4.1}$$

Here I_a is the measured intensity with an absorption sample, and I_f is the intensity measured without the sample, known as the flat-field projection. An example of this is

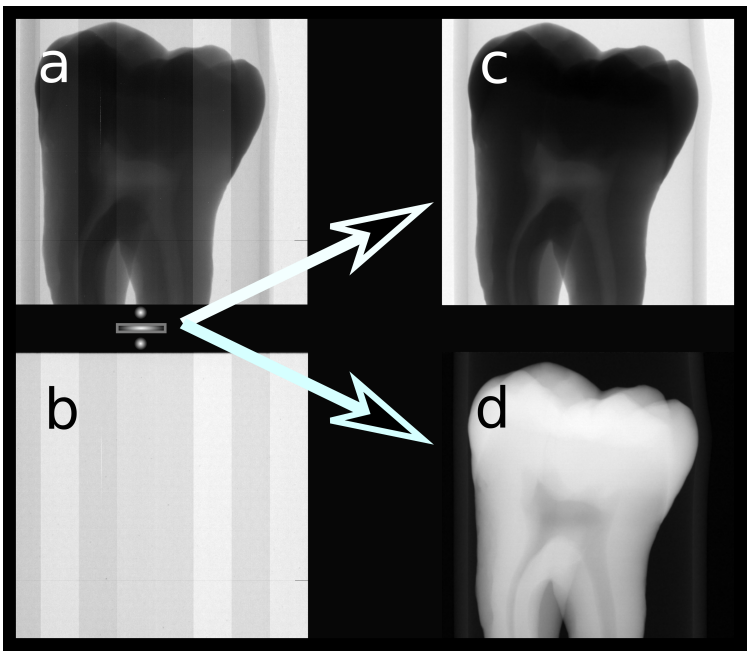

Figure 4.1: Example of simple absorption imaging. a) Attenuation projection of a human tooth. b) Flatfield projection. c) Flatfield corrected absorption image. d) Inverted absorption image.

seen in figure 4.1, where an absorption image of a tooth is made. Panel a shows the I_a projection while panel b shows the flat field projection, I_f. From the two projections,

clear detector features are seen, as the detector is composed of 10 separate panels all with different responses to the x-ray radiation. To get a proper image, I_a should be normalized with I_f. The result is seen in figure 4.1 panel c. Some times, the inverted absorption image is presented, not because it adds information, but because historically x-ray photographs film was made so that high absorbing areas appear lighter. An inverted absorption image of panel c is displayed in panel d.

The transmission is associated with Beer's law seen in eq. 3.1 by integrating over the distance the x-rays has propagated in the absorbing sample:

$$T = \frac{I_a}{I_f} = e^{-\int_0^\rho \mu dx} = e^{-\mu\rho}, \tag{4.2}$$

where ρ is the evident projected thickness of the sample. This is in accordance with Beer's law as I_f is equivalent to I_0 of Beers law. In many cases, a sample will contain material with different absorbing abilities which implies that μ is a function of the x position. A transmission image will not be able to tell whether a sample is highly absorbing or thick compared to other areas of the images. This means that μ in eq. 4.2 is just the average absorption ability of the sample. This is an issue which is overcome in absorption tomography.

4.2 Tomographic imaging

The most recognized tomographic imaging system is probably the medical CT-scanner. Here a line- or 2D-detector is placed on one side of the patient and an x-ray source is placed on the other side. The tomographic images are then made from a series of line or image projections measured as a detector and a source synchronously are conducting a circular movement around the patient. These projections are all equivalent to a projection described by eq. 4.2. In practice this means that a projection series resulting from a full 360° rotation around the patient must be obtained. Medical x-ray scanners are often very impractical, as they have strict requirements due to stability and minimization of vibrations. X-ray sources and detectors are often big and heavy making it difficult to avoid vibrations while rotating the equipment around a sample. Due to this practicality, in all other cases of tomographic imaging it is not the equipment that is moved around the sample, but the sample which is rotated around a rotational axis in its center.

When the accumulation of projections is done, a mathematical algorithm is applied to determine how μ is distributed within the sample. This procedure is called tomographic reconstruction. This means that if a 2D detector is used, one can obtain a 3D representation the ability of the sample to absorb. The mathematical algorithm used

to perform the reconstruction is called the inverse Radon transform. This has been treated elsewhere innumerable times and I will only do a brief summery here.

The basis of the inverse Radon transform is the Fourier slice theorem which is given by (Turbell 2001):

$$F_1 P_\theta \mu(x,y) = S_\theta F_2 \mu(x,y) \tag{4.3}$$

Here F_1 is the 1D Fourier operator, P_θ is the projection operator at a given angle θ and is defined as:

$$p(\theta) = \int \mu(x,y)dy = P_\theta \mu(x,y) \tag{4.4}$$

Here $p(\theta,t)$ is just equivalent to a horizontal line in the absorption image as discussed earlier in this section and is defined as integrating over a 2D distribution function $\mu(x,y)$ projected from the angle θ. F_2 is the 2D Fourier operator and S_θ denotes the slice operator which extracts a line in the 2D Fourier space through origo with the angle θ and is given by:

$$F(0,q_y) = \int p(\theta)e^{-iq_y y}dy = S_\theta F_2 \mu(x,y) \tag{4.5}$$

In words, what the Fourier slice theorem says, is that the 1D Fourier transform of projected distribution is equal to a line through the distribution function in the 2D Fourier space.

Ultimately it is is the 2D distribution $\mu(x,y)$ in real space that is desired to be determined. From eq. 4.3, 4.4 and 4.5 this is determined to be:

$$\mu(x,y) = \int\int F(q_x,q_y)e^{i(xq_x+yq_y)}dq_x dq_y \tag{4.6}$$

In practice this means to calculate $\mu(x,y)$, $F(q_x,q_y)$ must be determined and is done so by conducting a 1D Fourier transform of every projection line and thereby building $F(q_x,q_y)$ one Fourier line at the time as represented in figure 4.2. To get back into real space is then achived by a 2D inverse Fourier transform as implied by eq. 4.6. However as observed in figure 4.2, lower frequencies are overrepresented even with an infinite number of projection angles. By transforming to polar coordinates, and introducing a simple ramp filter which is denoted, g, which can be shown to be the convolution between P_θ and itself in the integration over all angles so that (Turbell 2001):

$$\mu(x,y) = \int_0^{2\pi} (P_\theta * g)(x\cos\theta + y\sin\theta)d\theta \tag{4.7}$$

Where the ramp filter is given by:

$$g(t) = \frac{1}{2}\int_{-\infty}^{\infty} e^{i2\pi p_r t}|p_r|dp_r \tag{4.8}$$

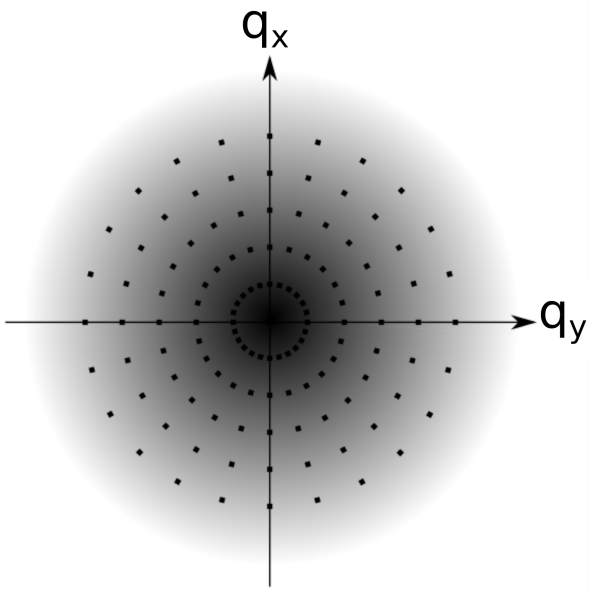

Figure 4.2: Fourier space representation of a sinogram. *This image is made by Lauridsen (2018)*

eq. 4.7 is known as the filtered back projection. Where p is a 2D representation of eq. 4.4 and a function of both θ and t. $g(t)$ is recognized as the inverse Fourier transform of $|p_r|$ meaning that $|p_r|$ is the representation of g in the Fourier space. This becomes very practical as the convolution theorem states that a convolution in real space is equivalent to a multiplication in the Fourier space (Arfken and Weber 2005). This makes the filtering much more computationally practical as only a simple multiplication is necessary compared to the much more time consuming convolution.

Real measurements are finite and discrete. The discrete representation of eq. 4.7 is:

$$\mu_{FBP}(x,y) = \frac{2\pi}{N_\theta} \sum_{n=0}^{N_\theta - 1} \hat{p}[n, k(x,y,\theta)] \tag{4.9}$$

Here $\hat{p}$ is the discrete representation of the convolution between $p(\theta_n, t_n)$ a.k.a the sinogram and $g(k, \Delta x)$ where the latter can be shown to be:

$$g[k] = t\Delta \cdot g(k\Delta t) \begin{cases} \frac{1}{4\Delta t}, & \textbf{for} \quad k = 0 \\ 0, & \textbf{for} \quad k: \text{ even} \\ -\frac{1}{k^2\pi^2\Delta t}, & \textbf{for} \quad k: \text{ ood} \end{cases} \tag{4.10}$$

Here Δt is the pixel size. As mentioned earlier, the filter should be applied in the Fourier space.

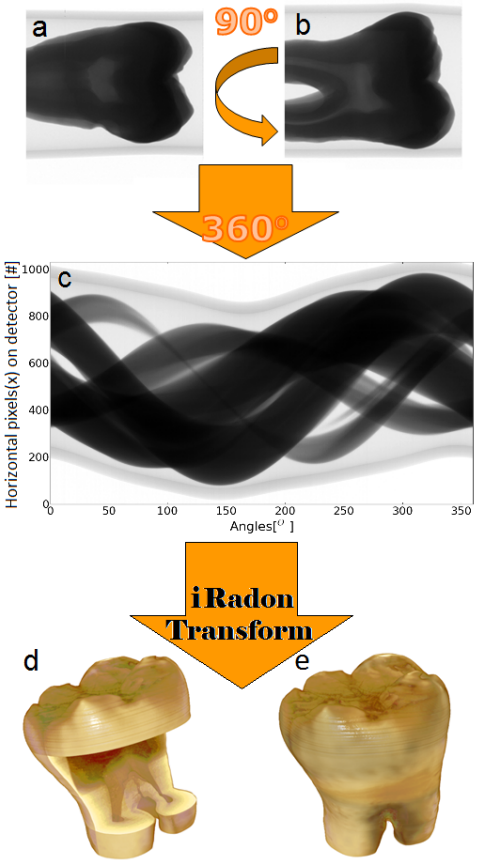

Figure 4.3: a) Absorption measurement of tooth. b) 90 degree rotated projection of tooth measurement. c) An example of a sinogram constructed from one detector line and all angular measurement. d) A full 3D visualisation of the reconstructed tooth tomogram, where a piece is removed by taking out parts of the data. e) 3D visualisation of the reconstructed tooth tomogram. **Self Plagiarism note**: *I made this image using my supervisor Martin Bech's x-ray laboratory at Lund University. This is the first tomogram produced in this lab and I have therefore previously used this as an example in presentations and it was also included in the ring removal project discussed in Chapter 5*

This is advantageous not only for a computational perspective, but also considering how a tomographic measurement is translated into a tomographic slice. In practice, one measures a projection line from every rotational angle and from these projection lines one builds a so-called sinogram. To recall, the sinogram is a discrete 2D representation of eq. 4.6 and was denoted above as $p(\theta_n, t_n)$. Such a sinogram is seen

in figure 4.3.c. The sinogram is the input to the inverse Randon transform described above. The lines are 1D Fourier transformed one at a time, and placed in the Fourier space as seen in figure 4.2. The ramp filter is then multiplied to weigh all frequencies appropriately. The 2D Fourier distribution is transformed back into real space with a 2D inverse Fourier Transform. The procedure is illustrated in figure 4.3. This procedure considers the ideal case of a parallel beam. As figure 4.3 shows, the method can produce good tomographic reconstruction. However, to overcome the effects of fan- or cone beam shapes normally produced by laboratory sources, the sample and detector must be placed sufficiently far from the source. Considering industrial micro tomography scanners, physical sizes are often minimized for practical reasons. Furthermore, when imaging micro-structures the magnification is much more extreme compared to the tooth example. In such cases the beam shapes cannot be neglected.

4.2.1 Cone beam imaging

Chapter 5 is the introduction to a publication where an industrial micro CT-scanner is applied to image the micro structures of protein snacks. In such a case the beam shape cannot be ignored and a cone beam consideration is added to the reconstruction algorithm. This problem is treated heavily in the literature, and there is an exact solution to the problem, as has been described by Defrise and Clack (1994). However, the exact algorithms require that the three-dimensional sinogram data is handled at once, which is computationally heavy. These algorithms are also considered to be rather complicated and have a significant geometric requirements, which is why they are often not used (Turbell 2001).

The arguably most common approach is the FDK-reconstruction, named after the inventors of the method Feldkamp, Davis, and Kress (1984). The method is very simple compared to exact methods and computationally it is not more difficult to handle, as longitudinal detector lines are treated one at the time. This is an approximation that, contrary to the parallel beam case, reconstructs the image somewhat differently from the real object, even with an infinite number of measurements. Only at $z = 0$ the solution is exact, as the ideal fan-beam is described in this special case. However, as long as the cone angle is small, the error is much smaller than what would be obtained with a parallel beam assumption, also at points further along the z-axis (Turbell 2001). The implementation is rather simple as the variation from the regular inverse Radon transform seen in equation 4.7 is a multiplication of a cone-angular factor weighted before filtering on P_θ, and a flux-density factor weighted after filtering (Lauridsen 2018).

$$\mu_{FDK} = \int_0^{2\pi} U^2((\omega P_\theta) * g)(y\cos\theta + x\sin\theta)d\theta \tag{4.11}$$

Both of the factors are geometric considerations that are determined from the beam

shape. Here ω describes how the beam changes along the z-axis and U describes how the wavefront is delayed along the beam direction axis.

4.3 Wave propagation and phase effects

After a wave has interacted with a sample, interference causes the image to distort more and more as the wave propagates. Intuitively one might expect this to be a result of refraction, as this phenomenon changes the phase velocity of the wave. However, as shown below, similar effects are observed from absorbing objects. In this section, the interference pattern induced by sample absorption and refraction is discussed, and it is explained how the effect caused by absorption can be corrected, while the refraction effect is utilized as a contrast mechanism. In the last section of this chapter, diffraction is also utilized as a contrast mechanism.

In imaging setups (and optical setups in general) wave propagation is often described in the so called paraxial regime which is the also the case for the considerations here. In this regime it is assumed that the wave propagation directions are primarily defined along a specific axis. Under this assumption the so called transport of intensity equation (TIE) can be derived (Lauridsen 2018):

$$\nabla_\perp \cdot (I \nabla_\perp \phi) = -k \frac{\partial}{\partial z} I \tag{4.12}$$

The intensity and phase of a propagating wave are denoted by I and ϕ, respectively. $\nabla_\perp$ is the gradient in the plane perpendicular to the propagation direction. This equation describes how the intensity in the perpendicular plane changes as the wave travels. As seen in the following, this is the basis of both phase correction and phase retrieval algorithms.

To get an idea of how a wave evolves after leaving a sample with either absorptive or refractive abilities, or both, one can consider the so-called transmittance function. This function describes a transmitted wave at an infinitesimally small distance from the sample under the thin-film-at-aperture-approximation, which simply states that all the matter in the sample can be projected onto a thin film at the aperture plane (Lauridsen 2018):

$$\Psi_a = e^{ik(iB-D)} \tag{4.13}$$

Here k is the wave number while B and D is related to the refractive index as:

$$B = \int \beta dz \qquad \textbf{and} \qquad D = \int \delta dz \tag{4.14}$$

This is of course a very specific case, but it is a very good illustrator of how a transmitted wave evolves in the Fresnel diffraction regime after leaving the sample. A

well-established approach to propagate a wave in free space is produced by the concept know as Fourier optics which propagates the wave in the Fourier space using a so called propagation factor. It can be shown that the wave in the Fourier space, at a given distance d from the aperture/sample, is described as (Lauridsen 2018):

$$\tilde{\Psi}_d = \tilde{\Psi}_a e^{i2\pi d f_z} \tag{4.15}$$

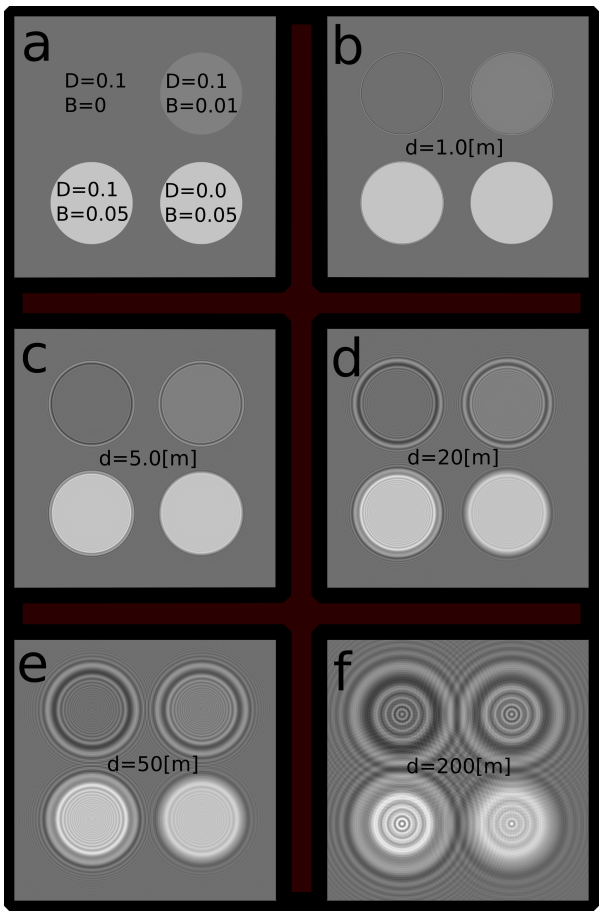

Figure 4.4: Fresnel wave propagation. a) Absolute value representation of constructed transmittance wave function. b-f) Absolute value of the propagated wave at a given distance from a. *This is calculated using a Fresnel propagation python tool, made by Lauridsen (2018)*

The advantage of propagating the wave in the Fourier space is evident from its simplicity. This is much more difficult in real space, as one here will have to deal with the

Laplacian operator in the Helmholtz equation. By using eq. 4.13 as input in eq. 4.15 one can calculate how the wave has evolved at different distances from the sample. An example of this is simulated in figure 4.4. In figure 4.4 it is evident that the propagation changes the wave front even for a purely absorptive element (D=0) although to a lesser extent compared to an element that contains a real part of the refractive index. As seen in the following, this effect can be an issue that needs correction or used to determine the distribution of the real part of the refractive index in a sample.

4.3.1 Phase correction imaging (Paganin)

To achieve better tomographic results it is sometimes advantageous to apply a phase correcting algorithm which I often called the Paganin method after the inventor Paganin et al. (2002). Due to the nature of the tomographic reconstruction, discontinuous features induced by, for instance, faulty detector pixels or measurement errors, leaves a significant artefact in the tomographic reconstruction, this because the propagation of the x-rays also induces discontinuous features through interference. In particular, the interference becomes strong with sudden changes in the refractive index, which is the case around structure edges in the sample, as illustrated in figure 4.4. Edge enhancement can especially become an issue when dealing with micro tomography using a monochromatic wave, because the edge enhancement significantly disrupts the outcome of the tomographic reconstruction. The edge enhancement is often an issue associated with synchrotron radiation for two reasons: (1) it is only at synchrotrons that the wave can truly be considered monochromatic, (2) the sample-detector distances and magnification relationship are so big that edge enhancement effects are amplified. However, when the spectrum from a lab source is dominated by a characteristic emission line, the effect can also be observed. The aim of the Paganin algorithm

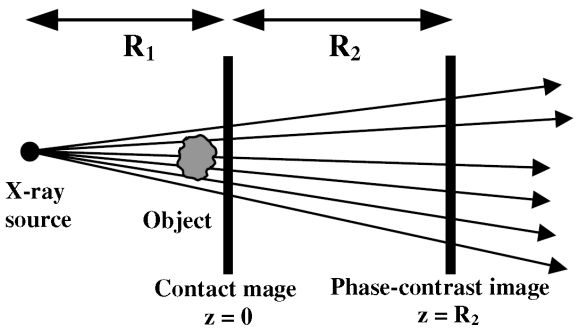

Figure 4.5: Schematic of measurement system and definition of the contact image. Here the image denoted Phase-contrast image is the measured image while the Contact is calculated image. *This image is taken from the original publication by Paganin et al. (2002)*

is to calculate what an image taken at a given distance from the sample would look like if it was taken an infinitesimally small distance from the sample a.k.a as the contact image. The principle is illustrated in figure 4.5.

The starting point og the algorithm is the transport of intensity equation:

$$\nabla_\perp \cdot (I(\mathbf{r}_\perp, z)\nabla_\perp \varphi(\mathbf{r}_\perp, z)) = -\frac{2\pi}{\lambda}\frac{\partial}{\partial z} I(\mathbf{r}_\perp, z) \tag{4.16}$$

This equation describes how the intensity evolves as a monochromatic paraxial electromagnetic wave propagates. The wave is described by I and φ, the intensity and phase respectively. $\nabla_\perp$ is the gradient in the $\mathbf{r}_\perp$ plane. To proceed, a couple of assumptions are made: (1) the source point is infinitely far away, (2) the material composing the object is homogeneous. In that case the contact image is perfectly described by Beer's law:

$$I(\mathbf{r}_\perp, z = 0) = -I_0 e^{-T(\mathbf{r}_\perp)\mu} \tag{4.17}$$

μ is the linear attenuation coefficient, $T(\mathbf{r}_\perp)$ is the projected thickness. An additional assumption is that the object is sufficiently thin, so that the phase will be proportional to the object thickness. Employing this assumption, the following holds true:

$$\varphi(\mathbf{r}_\perp, z = 0) = -\frac{2\pi}{\lambda}\delta T(\mathbf{r}_\perp), \tag{4.18}$$

where δ is the real part of the refractive index. Substituting eq. 4.17 and 4.18 into 4.16, eq. 4.16 can be rewritten to (Paganin et al. 2002):

$$-\frac{\delta}{\mu} I_0 \nabla_\perp^2 e^{-\mu T(\mathbf{r}_\perp)} = \frac{\partial}{\partial z} I(\mathbf{r}_\perp, z = 0) \tag{4.19}$$

An expression for $T(\mathbf{r}_\perp)$ can be shown to be (Paganin et al. 2002):

$$T(\mathbf{r}_\perp) = -\frac{1}{\mu} ln\left(F^{-1}\left[\frac{F(I(\mathbf{r}_\perp, z = R_2)/I_0)}{R_2\delta|\mathbf{k}_\perp|^2 + \mu}\right]\right) \tag{4.20}$$

Equation 4.20 can be utilized to compute the contact image. Equation 4.20 can simply be interpreted as a low-pass filter operating on $\frac{I(\mathbf{r}_\perp, z=R_2)}{I_0}$. Nevertheless, it is still very applicable in many cases. An example of this is seen in figure 4.6, where clear edges and streak artefacts are reduced significantly. The paganin method is often called a phase contrast method. I would argue that a more correct name would be a phase correction method, as the aim of the filter is to remove, or at least reduce, the phase effects. In the following, a real phase contrast method is considered.

4.3.2 Propagation based phase contrast tomography

The emergence of the first x-ray propagation base micro imaging method coincided with the introduction of the first third generation synchrotrons at which point the

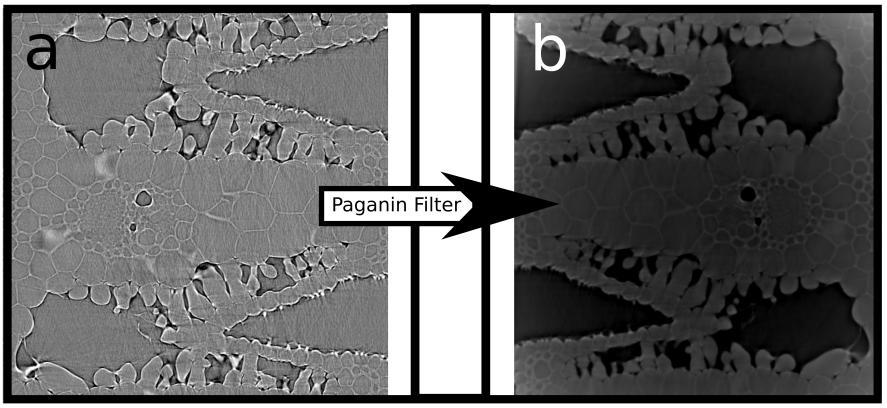

Figure 4.6: Tomographic reconstruction of a spartina cordgrass straw. a) Original reconstruction. b) Paganin filtered reconstruction.

electron beams became sufficiently coherent to measure the phase evolution. One of the first to describe this was Snigirev et al. (1995). Since then a lot of algorithms have been developed to improve the approach and combine it with tomographic imaging. One of the most commonly used approaches is described by Guigay et al. (2010). This approach removed some of the limitations from the previous approaches, such as the short detector-sample distance in the transport of intensity equation (TIE) approach (Cloetens et al. 1999) (which is introduced in eq. 4.16), and the contrast transfer function (CTF) approach, which requires weak absorption (Langer, Cloetens, and Peyrin 2010). The method is however still limited to slowly varying refractive index decrement (δ), very good coherence and single chromaticity.

The practical approach of obtaining data is seen in figure 4.7. Here the tomographic recording is made as the sample is rotated during the measurements. The detector is then moved a given distance and the procedure is repeated at a specified number of distances. The object considered has a 3D distributed complex refractive index given by:

$$n(x, y, z) = 1 - \delta_r(x, y, z) + i\beta(x, y, z) \tag{4.21}$$

In the Fresnel regime the transmitted wave after leaving the object is given as (Guigay et al. 2010):

$$T(\mathbf{x}) = a(\mathbf{x})e^{i\varphi(\mathbf{x})} = e^{-B(\mathbf{X})+i\varphi(\mathbf{x})} \tag{4.22}$$

Here $\mathbf{x}$ is the spatial coordinates in the transverse plane and $a\mathbf{x}$ is the absorption. $\varphi\mathbf{x}$ is the phaseshift induced by the object and thereby contains the information of δ_r and

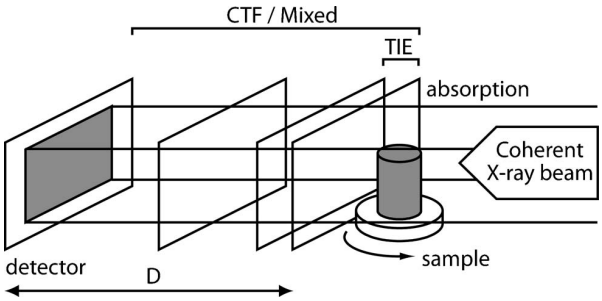

Figure 4.7: Schematic of measurement system for phase retrieval in both the CTF and TIE regime. *This illustration is taken from the original method publication by Guigay et al. (2010)*

$B\mathbf{x}$ containing the information of β and is given as:

$$\varphi(\mathbf{x}) = \frac{2\pi}{\lambda}\int(1-\delta_r(x,y,z))dz$$
$$B(\mathbf{x}) = \frac{2\pi}{\lambda}\int\beta(x,y,z)dz \tag{4.23}$$

The Fourier transform of the intensity in the Fresnel regime can be described as (Guigay et al. 2010):

$$\tilde{I}_D(\mathbf{f}) = \int T\left(\mathbf{x}-\frac{\lambda D\mathbf{f}}{2}\right)T^*\left(\mathbf{x}+\frac{\lambda D\mathbf{f}}{2}\right)e^{-i2\pi\mathbf{x}\cdot\mathbf{f}}d\mathbf{x} \tag{4.24}$$

Only by assuming a slowly varying phase object, the above eq. 4.24 can be rewritten to be:

$$F\left(I_0\varphi^{(n+1)}\right)(\mathbf{f}) = \frac{\sum_D A_D(\mathbf{f})\left(\tilde{I}_D(\mathbf{f})-\tilde{I}_D^{\varphi=0}(\mathbf{f})-\Delta_D(\mathbf{f})\right)}{A_D^2(\mathbf{f})} \tag{4.25}$$

Here the term $\Delta_D(\mathbf{f})$ can be considered to be a perturbation, which means that the equation can be iteratively improved. Here $\tilde{I}_D^{\varphi=0}(\mathbf{f}$ is the Fourier transform of the intensity of a distance D without a phase contribution. It is possible to calculate $\tilde{I}_D^{\varphi=0}(\mathbf{f})$, however $\tilde{I}_0(\mathbf{f})$ is often a sufficient approximation. Furthermore $A_D(\mathbf{f}) = 2\sin\pi\lambda D|\mathbf{f}|^2$ and $\Delta_D(\mathbf{f}) = cos(\pi\lambda D|\mathbf{f}|^2)(\lambda D/2\pi)F\left(\varphi^{(n)}\nabla I_0\right)(\mathbf{f})$, where $\varphi^{(n)}(\mathbf{f})$ denotes the phase at the n^{th} iteration. The iteration procedure is started by the case where $\varphi^{(0)} = 0$. 3-5 iteration are recommended.

4.3.3 Holographic nanotomography

When the features of the object of interest are very small it is often necessary to turn to microscopy, as the limitation of resolution is otherwise defined by pixel size on the

detector. In conventional absorption tomography this is straight forward to implement as the magnification is given by:

$$M = \frac{z_s + z_d}{z_s} \tag{4.26}$$

Here z_s is the distance between the focal point defined by preceding optics and sample and z_d is the distance between the sample and the detector. This is for instance applied in Chapter 5.

In the case of holographic nanotomography this is a little more complicated, but still very similar. The technique is described in detail by Mokso et al. (2007), and this is the technique applied in Chapter 6. The method builds on phase retrieval/holotomography method discussed in the in section 4.3.2. The setup is illustrated in figur 4.8. Here KB-optics is used to focus a parallel undulator beam. The approach is here to generate the

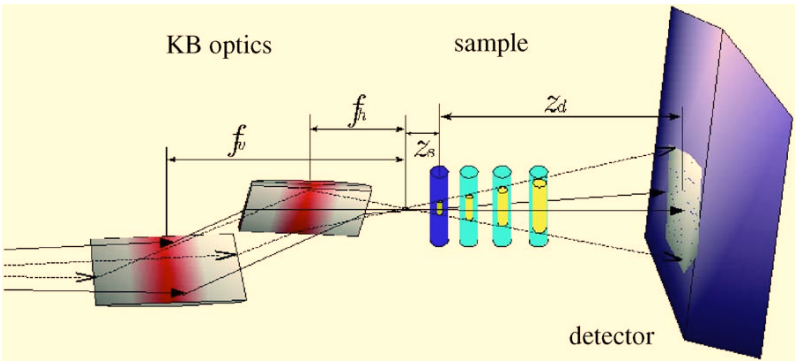

Figure 4.8: Illustration of how the KB-optics is introduced to the phase retrieval system to achieve sample magnification. *This illustration is taken from the original method publication by Mokso et al. (2007)*

same magnification on the detector and still let the phase evolve different distances as described in section 4.3.2. The trick is here a setup where it is possible to manipulate both z_s and z_d and thereby achieve the same magnification for different values of z_d. This leads to a number of projections with same magnification but different phase evolutions. These can then be used as arguments in the phase retrieval algorithm.

4.4 Three modality imaging

Three modality imaging is a common term of imaging involving a grating or reference pattern to measure differential absorption, phase or small angle scattering contrast of

x-rays. First, the original instrument, the Talbot Interferometer, is described in order to introduce the general principle. Subsequently, some techniques evolved from the talbot interferometer is superficially described.

4.4.1 Talbot Interferometer

The Talbot Interferometer can be constructed using two or three gratings, which both have pros and cons. The three grating version is the most commonly used in laboratory setups and a schematic of this version is shown in figure 4.9. This was developed to counter the blurring effect induced by the relatively large spot size (some mm sized FWHM) of regular lab sources. In figure 4.9 an additional grating (G0) is used to

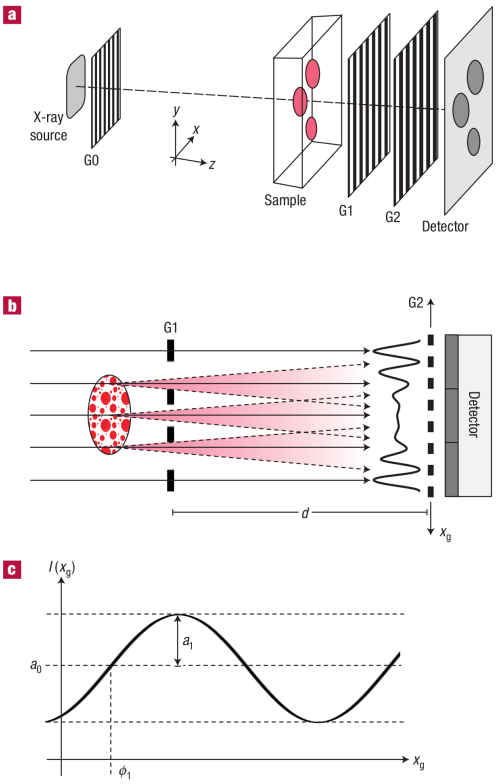

Figure 4.9: Illustration of how the KB-optics is introduced to the phase retrieval system to achieve sample magnification. *This illustration is taken from Pfeiffer et al. (2008)*

create a long row of very narrow line sources. The downside of this system is that an

additional grating will have to be aligned, which in practice is a very real issue, as Talbot systems can be very difficult to align and are very sensitive to short and long term drifts. It is possible to utilize a system in the lab without a G0 grating, however that requires a micro focus source which is significantly more expensive than a regular source and has a much smaller output power. The two lab sources are discussed further in section 2.1. No matter which source is applied, the further configuration of the systems is the same. At a distance from the source/G0, a so called phase grating is placed. This grating creates the Talbot interference pattern, which at specific distances of z repeats a periodic intensity pattern along the x-axis, as defined in figure 4.9.a and 4.9.b. This repeatable distance is given as (Weitkamp et al. 2005):

$$d_m = \left(m - \frac{1}{2}\right)\frac{g_1^2}{4\lambda}, \qquad where \qquad m = 1, 2, 3, ... \tag{4.27}$$

Finally, an absorption grating is placed in an appropriate Talbot distance. Here it should be noted that the G2 grating period in figure 4.9.b is significantly smaller than the detector pixel size. If sections 3.11 and 3.2.4 are recalled, scattering angles as well as refraction angles produced by relevant samples are so small that most intensity shifts on the detector happen within a given pixel, hence no scattering or refraction can be measured. However the G2 grating allows us to measure these quantities on a sub pixel level. If no sample is placed in the system and the G2 grating is prepared with appropriately small steps in the x direction, the intensity in every pixel will exhibit a sinusoidal behavior. A single detector pixel measure is shown in figure 4.9.c. The parameters describing the sinusoidal function is given by a_0, ϕ_1 and a_1. Here a_0 is the average intensity measured while ϕ_1 is the phase of the function and a_1 is the corresponding amplitude. These values determine the reference of that specific pixel. In the most ideal case, all pixels would display the exact same sinusoidal behavior without a sample in the system. However, due to small grating misalignment as well as beam shape effects, these parameters will vary over the full 2D pixel array of the detector. This means that values for a_0, ϕ_1 and a_1 must be collected for every detector pixel.

If a sample is placed in the system, the sinusoidal function in a given pixel will change according to the optical properties of the sample. For instance, if the sample area in the path between source and pixel is transmitted through an absorbing element, the values of a_0 and a_1 will be smaller by the same ratio compared to the reference. If the sample element in question has purely refractive abilities, the value of ϕ_1 will change, while a_0 and a_1 will be the same as the reference measurement. Finally, if the sample element has scattering ability, only the values of a_1 changes. In most cases a sample will induce more than one effect, fortunately, these effects are often distinguishable. When the sinusoidal parameters are determined with and without the sample, three images can be calculated. The absorption-, phase-, and diffraction contrast are defined

as (Bech 2009):

$$A_0 \equiv \frac{a_0^s}{a_0^r} \qquad \Phi_1 \equiv \phi_1^s - \phi_1^r \qquad V \equiv \frac{V^s}{V^r} = \frac{a_0^r}{a_0^s}\frac{a_1^s}{a_1^r} \tag{4.28}$$

Here A_0 is the adsorption contrast value of a given pixel, Φ_1 is the phase contrast value of that pixel and V is the SAXS contrast value a.k.a. the dark field signal. V_s and V_r is the called the visibility with and without a sample in the system. These are by definition given as $V_s = a_1^s/a_0^s$ and $V_r = a_1^r/a_0^r$. Figure 4.10 shows three different measurements of wooden swab. Here panels a-c of figure 4.10 shows the absorption, dark field and phase images respectively. It is seen in the absorption that the wooden part of the swab contributes to absorption while the cotton tip does not. The cotton tip, however, becomes very visible in the darkfield image. The sample does not expose any phase contrast, but if one looks closely at the swab in the phase contrast image noise can be identified. The reason why this is so, is due to a very high scattering ability of wood and especially cotton. The noise signal makes sense, as it is impossible to determine a phase of a sinusoidal function with no amplitude. The panels d-f of figure 4.10 shows an identical measurement where the swab is rotated 90 degrees. Here panel d shows the same as panel a, while panel e only shows the cotton tip. Looking closely at the cotton tip in panel e, it is seen that the center is almost transparent as there is no wood in the sample. This is because the fiber structure in wood has a directional orientation while the fiber structure in the cotton tip is completely random. As the gratings used in this setup are 1D, the spatial coherence is only sufficiently high in one direction to measure scattering. This is also observed in panel f, as noise created by the tip is smaller, because the wood does not contribute to the decrease in visibility. Finally, a measurement of the swab submerged in water is displayed in the images of panels g-i of figure 4.10. As seen in panel g, the swab becomes completely invisible. This is because the absorption signal of the wood is literally drowned by the much stronger absorption signal of the water. Panel h, however, clearly shows a strong dark field signal from the wooden part of the swab. On the other hand, the previously strong dark field signal of the cotton tip has vanished. This is probably due to index matching, as the cotton is soaked in water. In panel i, the phase noise has reappeared as which is expected.

4.4.2 Developments from the Talbot Interferometer

Although the Talbot interferometer is the first and most widely used three modal imaging system, many new systems building on the Talbot interferometer have appeared during the last decade. Here the most relevant are discussed briefly, as these are used as the basis of the technique introduced in Chapter 7.

The method described in Chapter 7 is a combination of three well documented pro-

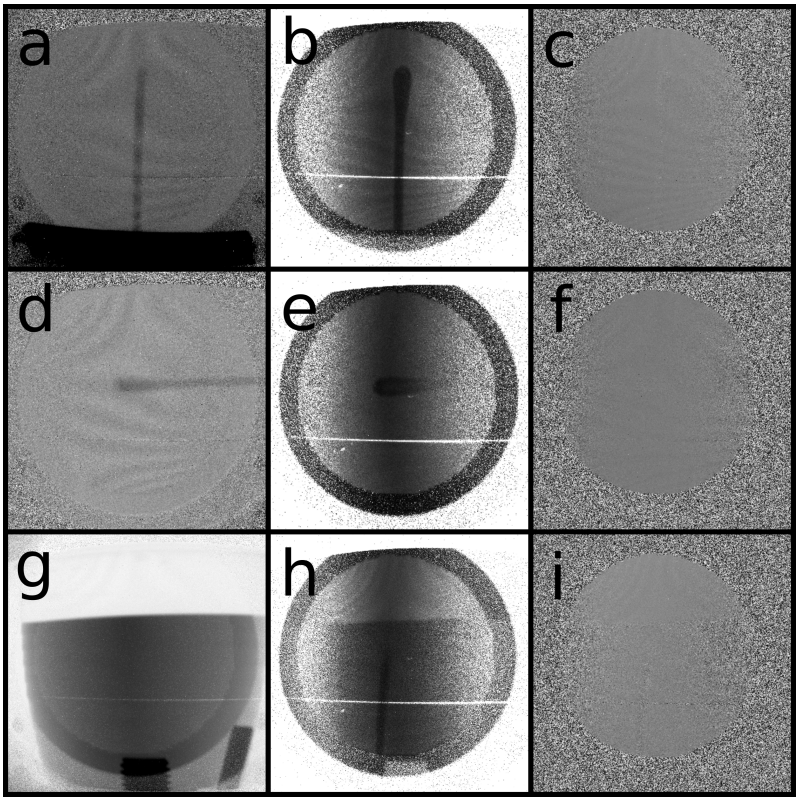

Figure 4.10: Three measurements of a wooden swab where each measurement produces a three modal images series. a,d and g) The absorption image modality. b,e and h) The differential phase contrast image modality. c,f and i) The dark field image modality. a-c) The swap is vertically oriented in the Talbot system. d-f) The swap is horizontally oriented in the Talbot system. g-i) The swap is vertically oriented in the Talbot system, but submerge in water.

cedures called Spatial Harmonic Analysis a.k.a. the single shot imaging (Wen et al. 2010), a 2D motionless stepping approach similar to that of Harmon et al. (2014) and image enhancement by the so-called Blind Super Resolution (BSR) by Šroubek, Flusser, and Cristóbal (2007).

The single shot imaging method achieves phase contrast and darkfield imaging by applying a 2D transmission grating and a micro focus source to minimize blurring. The x-ray refraction and diffraction in a sample is measured as variations in the 2D fringes pattern created by the grating. The three contrast parameters are found in the Fourier space where the information of the refraction and diffraction is located the 1^{st} -order harmonics while the absorption information is contained within the 0^{th} -order harmonic. The reconstruction from these quantities are called the Spatial

Harmonic Analysis. This method is thoroughly explained in the publication introduced in Chapter 7.

Motionless electromagnetic phase stepping described by Harmon et al. (2014) is basically a regular Talbot interferometer system. Recalling the above, a regular Talbot interferometer works by mechanically stepping a grating in the transverse direction and achieving two phase maps with and with out a sample. In the motionless electromagnetic phase stepping approach, two electromagnetic coils are used to step the source point in the transverse direction, effectively creating the same image modalities as mechanical stepping.

An additional method evolved from the Talbot interferometer, which has become available in the recent years, is the so called Speckle Scanning Technique (Zhou et al. 2015). Here a simple film with a random speckle pattern, is stepped in the same manner as the Talbot interferometer with and without sample. By comparing the scans, the phase and the darkfield image can be reconstructed. This method is both applicable with synchrotron and lab sources (H. Wang, Kashyap, and Sawhney 2016).

5 Introduction to publication A.1

Microstructure, texture and secondary protein structure of extruded high protein snacks studied by FT-IR spectroscopy and X-ray tomography

In this work we want to study the effect of extrusion processing on protein digestibility as well as the quality of yellow peas and potato starch snacks using different extrusion recipes. The varying recipe conditions are protein contents which are 7- and 15 percent, moisture content at 23- and 40 percent and finally the temperature during the extrusion 130- and 150 degrees C°. Another objective is to study the 3D micro structural information gained through x-ray micro tomography and the molecular information of the secondary protein structure, which is a measure of the protein digestibility, obtained through spectroscopy to determine if there is any correlation. After the extrusion the effects of the different recipes are studied. Here the most important parameters are texture, expansion as well as the mentioned secondary protein structure and micro structure. The latter being my focus area. Here 3D microstructure tomograms of the samples are obtained by X-ray microtomograhpy. The technique applied is the standard filtered back projection for cone-beam algorithm discussed in section 4.2.1. The number of voxels is approximately $1000x1000x1000$ pr. tomogram and the voxel size is 6.05 μm. The x-rays emitted are created using a voltage of $40KV$ and a $200\mu A$ current.

Extrusion processing is altering the secondary protein structure as measured by FT-IR indicating an improved digestibility of the pea raw material. Measurements with X-ray tomography shows that an increase in the protein content does not result in significantly changes in the snack structure, when the water content is kept at 23% The results show that extruded snacks may be a convenient way to improve the digestibility of plant proteins from legumes without compromising product structure.

5.1 My contribution

I was the main responsible for performing the experiment and collecting the data afterwards. I did the segmentation of all measurement as well as presenting the tomograms af 3D structural images. I also developed the analytical algorithm which extracted the relevant structural data. Finally I was responsible for writing the sections describing the x-ray micro tomography technique as well as describing the segmentation and analysis procedures.

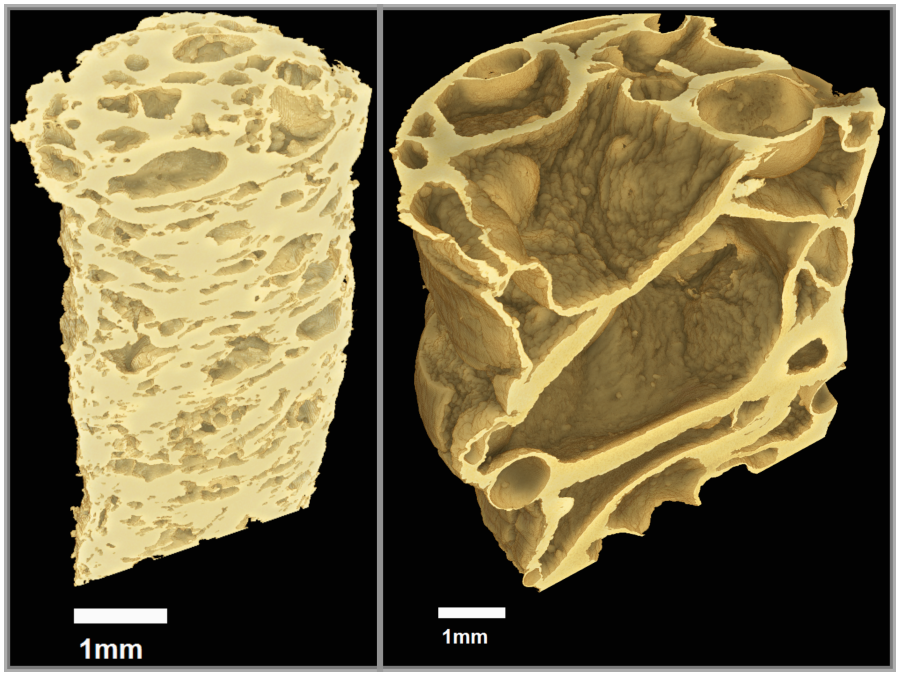

Figure 5.1: Exampels of extrusion using two different recipes. Left) P7-W23-T150. Rigth) P7-W40-T150

6 Introduction to publication A.2

Three-dimensional architecture of human diabetic peripheral nerves revealed by X-ray phase contrast holographic nanotomography

In the beginning of my PhD I was part of a team conducting experiments at the Paul Scherrer Institut using the Swiss Light Source. These results are presented in article 4. One of the team members whom I met for the first time was Associate Professor Martin Bech from Lund University. Not too long after the experiments we decided that I should do my "change of scientific environment" in his group at Lund University. Right away I became part of a project to map the three-dimensional architecture of human diabetic peripheral nerves and compare these to a control group. The state of the project was at this point advanced. Professor and medical doctor Lars Dahlin had over a period of more than 20 years collected nerve samples from wrists and ankles of control groups, diabetic patients with type 1 and type 2 diabetes and patients with predisposition to evolve type 2 diabetes, some of whom later developed the disease. My supervisor Martin Bech was the main responsible for the x-ray related in the experiments such as determining what experiment would be appropriate to apply for at ESRF. The experiment technique chosen was x-ray phase contrast holographic nanotomography, which is introduced in Chapter section 4.3.2.

Shortly after the experiments were conducted I became part of the project. Right

away I was thrown into the data analysis. Quickly it was decided that we wanted to pursue two high impact factor publications. The first one being proof of concept which is the article introduced here. Actually the aim of the paper was to prove two concepts. First to show that it was possible to apply the imaging technique and obtain decent tomographic reconstruction with sufficient contrast and resolution. Secondly and equally important it should be shown that it was possible to do good segmentation which would lead the way for a second publication. Both goals we were satisfied to have achieved. The second paper was intended as quantitative analysis paper where segmentation and analytical tools would be applied to investigate if there would be a statistical difference between patients and control groups. The main responsibility for developing and implementing these tools was Anders Dahl and Vedrana Dahl and their group at DTU compute.

We truly believed that by proving this concept there would be a basis for a high impact factor publication. However after a few rejection, where it at one point was in review for more than a 100 days, it was decided that the two publication should be combined. This is currently an ongoing process which is why the original paper is only presented here.

6.1 My contribution

My contribution have mainly been to present the measurements in the best possible way and high light the important features recognized by the medical doctors. I have also contributed to the x-ray experiment and segmentation related discussions, as well as formulated the figure descriptions. In this paper only a single tomogram is considered. However the experiment at ESRF produced 15 different tomograms from different samples. These were of varying quality and some of them would be very dfficult to apply a proper segmentation to, mainly due to ring artefacts. For that reason I used a significant amount of work to develop my own ring removal algorithm. To avoid the risk of self plagiarism, I here inform that most of this additional work have already been presented in a course project that I took during my "change of scientific environment" at Lund University in Sweden. To my knowledge this was not public available or its contribution to this work was not mentioned elsewhere, therefore it makes good sense that the most important results are presented here as well.

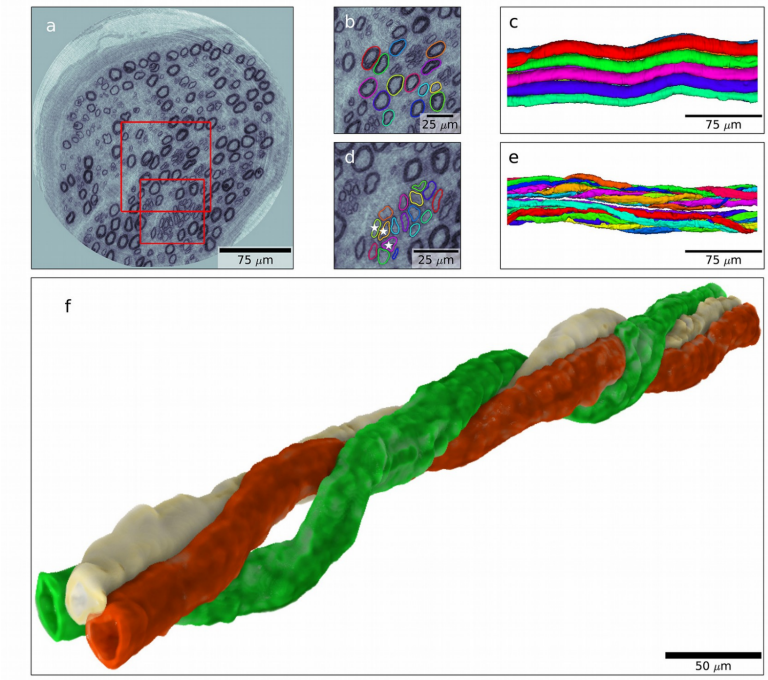

Figure 6.1: Examples of our ability to segment the tomogram. a) Tomographic slice through the data volume of the subject with type 1 diabetes. b) Enlarged area marked by a large red square in (a). Colored rings mark the segmented nerves calculated by our semi-automated algorithm. c) 3D rendering of the segmented nerves marked in (b). d) Enlargement of area marked by small red square in (a). Clusters of regenerated nerves are segmented by our semi-automated algorithm. e) 3D rendering of the segmented nerves clusters segmented in (d). f) 3D volume rendering of the three nerves marked by stars in (d).

6.2 Contaminated tomographic slice

Here a tomogram from the collection of low quality is used as an example, figure 6.2 shows a slice of the worst ring artefact contaminated tomogram. It is evident that the most prominent feature disrupting the image of the tomogram slice is the ring artefacts. To make any meaningful segmentation it is necessary to remove these rings. In absorption tomography ring artefacts are often results of one or more malfunctioning pixels in the applied detector or is a consequence of the reconstruction algorithm. Here a method to remove ring artefacts from the entire collection of data is applied. Because the tomogram, of which the slice seen in figure 6.2 is part of, is a particularly bad infected tomogram, that slice will be used as an example to show the effect of the ring removal approach. However the algorithm is applied to most tomograms in the entire collection.

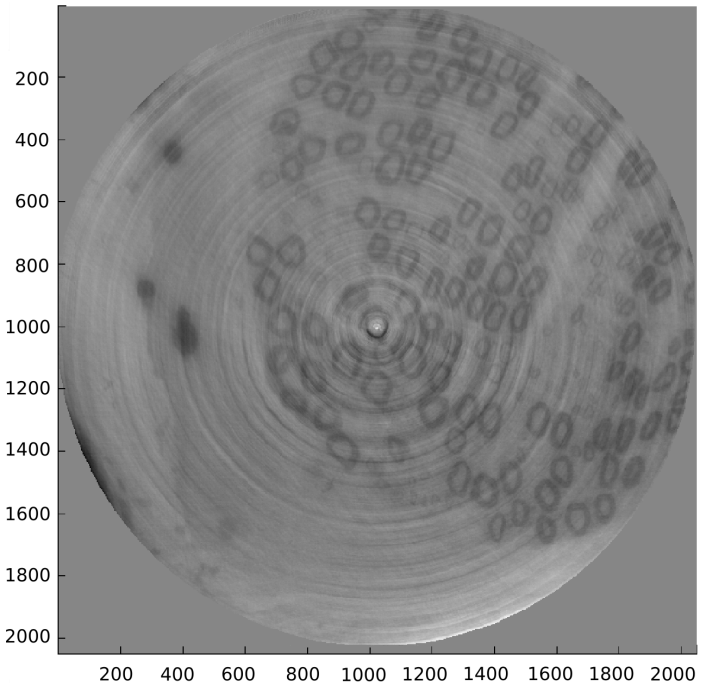

Figure 6.2: Heavily ring artefact contaminated tomographic slice.

6.3 Parallelization of calculations

When dealing with ring artefacts it is advantageous, as seen in a moment, to consider the sinogram. Normally the participant, of an absorption tomographic beam time experiment at synchrotron facilities, receives both the reconstructed images as well as the corresponding sinograms. However as this experiment is an x-ray phase contrast holographic tomography experiment, sinograms in that classical absorption form do not exist. For that reason a radon transform is performed on every tomographic slice to obtain all the corresponding sinograms. The radon transformation can be a computational heavy operation. In this case it is exceptional heavy. There is two computational challenges removing the ring artefacts. First, the computational time is an issue, this problem is discusses later in this section. Second, the data format of the tomograms is 32-bit floating points and the dimensions was $2048x2048x2048$. This means that the size of a single tomogram is 32GB and when the tomogram data is processed it is necessary to keep the original data and the processed data in the memory at the same time at some points. This effectively doubles the memory requirements. Even today it is not normal to have 64GB of ram available. One solution is to do a

lot of read and write from a hard drive. This however is a very slow procedure and as shown later the computation time is all ready very long. Specially designed imaging computers often have the memory capacity necessary to handle such data. This is why such a computer is applied for these calculations.

6.3.1 Calculation times

The reason why a parallelization is necessary is easily calculated. The calculation time of the Radon transform varies a bit if the computer is processing other things also. However the computer used here applies between 8-9 minutes to perform a radon transform of a $2048x2048$ elements array (tomogram slice). 15 full tomograms must be radon transformed, each of these tomogram have 2048 slices. That means that a "conventional" calculation time will be:

$$t_{calculation} = 60\frac{s}{min} \cdot (8 \quad to \quad 9)min \cdot 15 \cdot 2048 = 14745600s \quad to \quad 16588800s \tag{6.1}$$

$$\Downarrow$$

$$t_{calculation} = \frac{14745600s}{60 \cdot 60 \cdot 24\frac{s}{day}} \quad to \quad \frac{16588800s}{60 \cdot 60 \cdot 24\frac{s}{day}} = (171 \quad to \quad 192)days \tag{6.2}$$

In other words these calculations will take around half a year to finish using the conventional approach. Notice that this is only for creating the sinograms, which then is processed and then again used to reconstruct the tomogram. That will at least double the calculation time, so that this time is more than a year. However this calculation time is fairly easy scaled down by a factor equal to the number of CPU cores available in the computer, by using the package "multiprocessing" in python. This package makes it relatively easy to just split up the tomogram and let each available CPU-core process a part of the tomogram independently of each other. This reduces the calculation time proportional to number of cores available. In this case by a factor of 8.

6.3.2 Implementing multiprocessing

The algorithm to perform the radon transformation using the multiprocessing package is described in Algorithm tabel 1.
By design the memory in one process cannot surpass 4GB. This will happen if a full tomogram is separated into only 8 pieces as the number of CPU cores otherwise dictates. Therefore the procedure is to process a quarter of a tomogram at a time,

Algorithm 1 Multiprocessing algorithm

```
Determine all tomogram paths
Createcircular mask
for Every tomogram do
    Separation of the tomogram in four chuncks of equal size
    for Every chunk do
        Element multiplication of circular mask slice wise on the tomogram chunk
        Separate chunk in evenly sized parts (num of parts = num of CPU-cores)
        Create queue and define processes (num of processes = num of CPU-cores)
        for Every part do
            Slice wise radon transform to calculate the corresponding sinograms
            Place sinograms in 3D array
            Send 3D sinogram array to queue
        end for
        Build sinogram chunk from sinograms returned from each process
        Write sinogram chunk on hard drive
    end for
    Load all 4 sinogram chunks from hard drive
    Place all 4 sinogram chunks in a single 3D array
    Save full sinogram set on hard drive and
    Delete the 4 sinogram chunks from harddrive
end for
```

then temporally save the fraction to the hard drive and hereafter reload all 4 chunks of sinograms when all are calculated. After that the 4 chunks are collected in one array which is saved on the hard drive as a raw-file. As the sinograms are created the the filtering process can begin.

6.4 Signal processing in 1D

When filtering any kind of signals it is often advantageous to handle the the data in the frequency domain. The idea is to clean up a noisy or contaminated signal by removing certain frequencies without disrupting the original signal. The simplest form of filters that work in the frequency domain are low-, high- and band-pass filters. Here a simple example of the procedure applying a band-pass filter is constructed.

A signal, which is the sum of two 2 sin functions, is used as example. This function is seen in figure 6.3.a. This signal is then contaminated with 4 other sin functions of different frequencies. Further more random noise is introduced to the signal. The contaminated signal is seen in figure 6.3.b. The objective is now to clean up the signal from containments and noise.

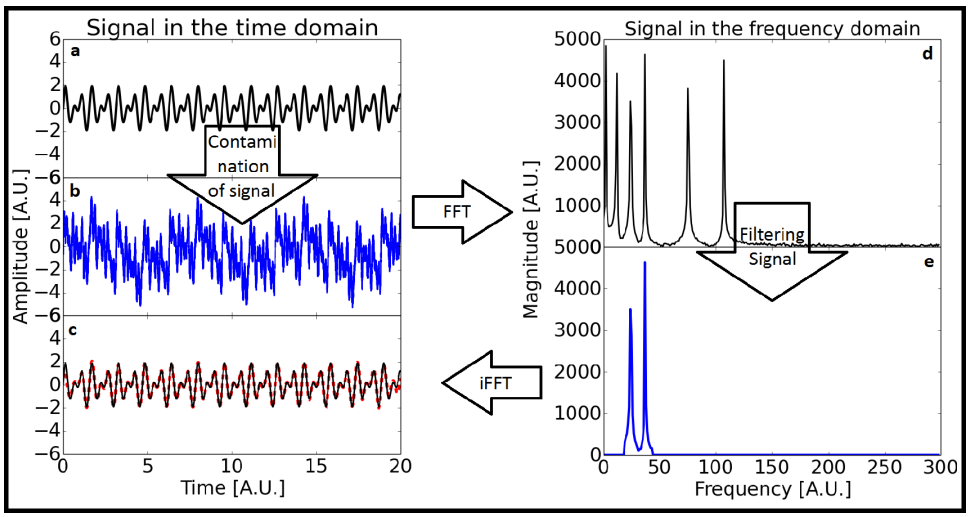

Figure 6.3: Applying a simple filter in the frequency domain. a) Original signal. b) Contaminated signal. c) Filtered signal (red dash line) and original signal. d) Contaminated signal in the frequency domain. e) Filtered signal in the frequency domain

To get back and forth between the frequency domain and the time/space domain, the Fourier transformation is applied. In figure 6.3.d. the absolute value of the Fourier

transformation of the signal is plotted. This is done by using a RFFT function provided by the NumPy package in Python. RFFT is used because it makes it easier to get an overview of the frequencies in the data. It is seen that the symmetric part, which is normally expected, is missing when using the RFFT. The reason why the absolute value is plotted is to give a better overview of the different frequency contributions. From figure 6.3.d. it is seen as expected that 6 frequencies are identified. Further more the noise contribution is easiest seen as higher frequencies. It should also be noticed that there is no zero order contribution as the mean value of the signal is close to zero. A simple band pass filter is applied to the signal in the frequency domain. The filter is just an array of zeros, ones and zeros again of the same length as the signal. The ones of the array are chosen such that, when the filter is multiplied with the signal, only the frequency band of interest is different from zero. The filtered signal which is seen in figure 6.3.e. is returned to the time domain by the inverse Fourier transformation. This is done using the iRFFT function provide by the NumPy package in python. The result of this is seen in figure 6.3.c. The filtered signal is plotted as the red dashed line on top of the original signal, which is plotted as the black solid line.

This is of course a simplified case, however it still illustrates how a filter is applied in the frequency domain. Here the data in question is images, but the exact same approach can be applied. In this case the data structure is 2D and the dimension is space instead of time. Here the image will be the Fourier transformation into the reciprocal space also called the Fourier space, were the image is filtered and transformed back to real space. The next section is about how a filter is applied in the Fourier space and thereby removing the ring artifacts in real space.

6.5 Removal of ring artefacts

In this section a tomogram slice and its corresponding sinogram is treated. The tomogram is processed by the algorithm discussed in the previous section. Here it is shown how the calculated sinogram can be used to enhance the image quality of the original tomogram by applying a specially designed filter.

6.5.1 The Sinogram

The sinogram chosen to demonstrate the procedure is calculated from a slice of the tomogram containing the worst ring artefacts in the entire tomogram collection. Figure 6.2 shows the original tomogram slice, while figure 6.4.a shows the corresponding sinogram.

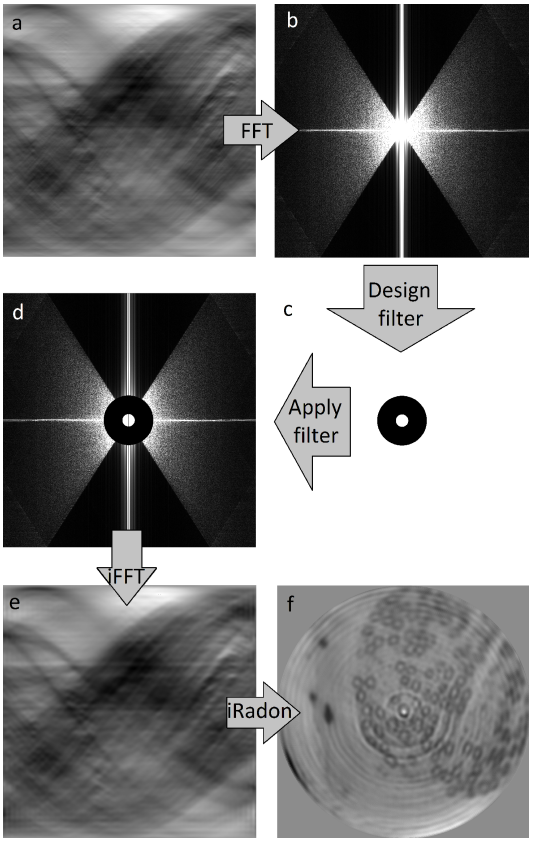

Figure 6.4: a) Picture of contaminated sinogram containing unwanted vertical lines. b) Picture of the absolute values of the sinogram in the Fourier space. c) Picture of the applied band pass filter where white equals 1 and black equals 0. d) Fourier Space picture multiplied by filter. e) Filtered sinogram. f) Reconstructed tomogram slice.

The rings in figure 6.2 are very pronounced and it is very evident that it can induce problems for automated analysis algorithms. Considering the sinogram, very distinct features are also observed as clear horizontal lines. It is these lines which cause the rings to appear in the tomogram. As mentioned earlier this feature is normally caused by faulty pixels with abnormal pixel response functions in the 2D detector, such as dead, white or noisy pixels. Considering how the sinogram is constructed from projections as described in section 4.2, it makes perfect sense that defective pixels cause ring artefacts in tomogram slices and straight lines in the sinogram. These lines will normally be very thin and a standard low pass filter might have been sufficient to remove the lines without loosing essential information. However as these tomograms are made using a propagation based phase contrast technique, these rings are quite different

from ”normal” high frequency rings. In this case the lines vary a lot in thickness and transitions between circles and background is not always prominent. This means that many of these line effects are part of the low frequency regime. Furthermore as the source of rings is not known it is also difficult to be sure that the lines are stationary, meaning they might exhibit a small slope instead of being horizontal in the sinogram. Additionally some of the lines might not pass all the way through the sinogram.

In figure 6.4.b a picture of the absolute values of the Fourier transformed sinogram is shown. As in the case of the 1D example in the previous section, the Fourier transformed sinogram also has both negative and complex values. This representation gives a good overview on the location of the frequencies. In the following a special filter, used to remove the lines and thereby the rings in the tomogram, is designed.

6.5.2 Design of filter used in the Fourier space

As discussed earlier one approach might have been to apply a low pass filter. However as indicated this procedure is not expected to work as the rings do not seem to be ”high frequency” rings. It is relevant to ask if a high pass filter is an appropriate approach. In this case too many ”wanted” features might be lost by applying a high frequency filter. Finally there is the possibility of a band filter. This also requires that all of the ”ring frequencies” do not vary too much, though fewer frequencies will be removed from the sinogram compared to the other filters. In figure 6.4 an attempt of applying a band pass filter is seen. This is 2D equivalence to the 1D case displayed in figure 6.3. As seen in figure 6.4.e and .f, this results in the removal of some lines in the sinogram and therefore also some rings in tomogram slice. However a lot of rings are not removed. Furthermore a lot of the ”wanted” features is lost or blurred, making the quality of the tomogram even worse than the starting point.

A different approach to designing a filter is to look at what the different coordinates in the Fourier space represents in real space. Every point in the Fourier space represent a propagating wave in a specific direction with a specific frequency. If it is possible to identify the points in the Fourier space that represents propagating waves in one specific direction of interest, this could be used to design a filter. Considering figure 6.4.a or 6.5.a it is known, that the horizontal line features is the ones that should be removed. If every horizontal line is considered to be a vertical propagating wave, the points in the Fourier space describing these lines must be on the x-axis of the sinogram. This means that in the ideal case all points on the x-axis could be set equal to zero and therefore remove the horizontal lines. This only works if the horizontal lines have no slope at all. As discussed in the previous subsection it is difficult to determine whether the lines are stationary or not. To make sure that lines with small slopes are also removed, the filter seen in figure 6.5.c is designed. By making a band,

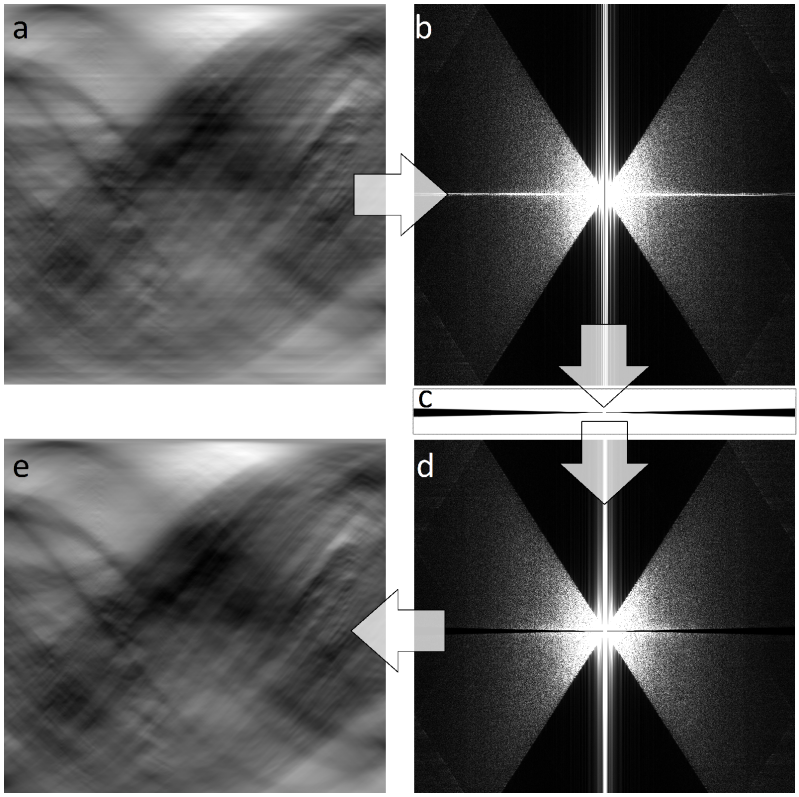

Figure 6.5: Sinogram filtering. a) Picture of contaminated sinogram containing unwanted vertical lines. b) Picture of the absolute values of the sinogram in the fourier space. c) Middle part of filter in gray scale. white equals 1 and black equals 0. d) Fourier Space picture multiplied by filter. e) Filtered sinogram

which opens with a small angle, the slightly tilted lines (mostly in the high frequency regime) should also be removed from the sinogram. Figure 6.5.c only shows the part of the filter around the x-axis. The filter is in gray scale where white equals 1 and black equals 0. The rest of the filter is equal to 1 so that dimensions of image and filter are the same (2048x2048). Furthermore a small circle of ones is placed in center of the filter, so that the 0th-order from the Fourier transformation is not lost using the filter. This serves to keep the scale on the image the same as the original image. Figure 6.5.d shows how the picture looks in the Fourier space after applying the filter. The last step is then to do the inverse Fourier transformation. The result is seen in figure 6.5.e. As seen in the figure the vertical lines are removed from the sinogram picture.

6.5.3 Reconstruction of filtered sinogram

The final step is to do the inverse radon transformation as described in section 3. The result is seen in figure 6.6.b where figure 6.6.a shows the original tomogram slice. It is evident that most of the rings are removed from the tomogram slice. The image quality has therefore been enhanced, but the method has only been proven sufficient if the segmentation is good enough.

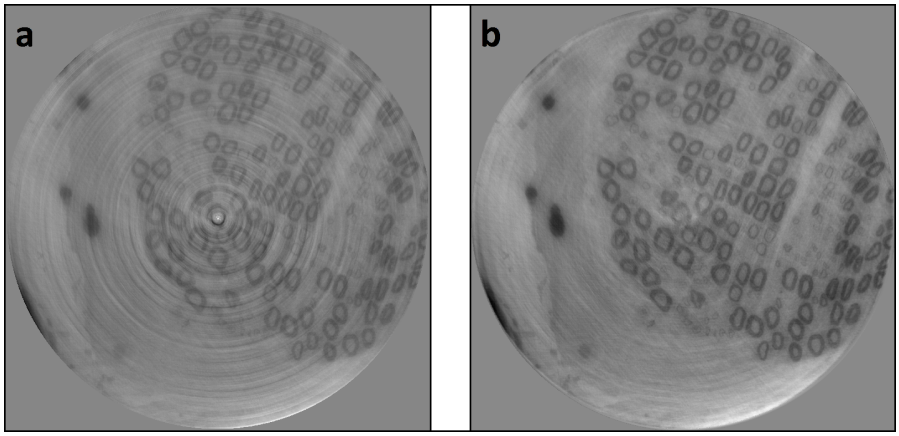

Figure 6.6: Comparison between original and processed tomographic slice. a) Original slice. b) Processed slice

7 Introduction to Article 3

Super resolution x-ray phase-contrast and dark-field imaging with a single 2D grating and electronic source stepping

When preforming grating based three imaging modality measurements one must often compromise on either high stability requirements or large reduction in resolution. In this publication we eliminate the requirement for any mechanical movable parts as well as stability concerns which are required by the talbot interferometer. At the same time we reduce some of the resolution lose normally seen when applying spatial harmonic analysis, which is a method not requiring any mechanical movable parts. We utilize the Super Resolution algorithm using a micro focus x-ray source with a none mechanical movable source spot. By slightly and randomly translating the source spot in two direction a series of slightly different absorption- differential phase contrast- and dark field images are obtained using applying spatial harmonic analysis. The so-called Blind Super Resolution algorithm is then applied on each modality series to enhance the resolution of the images. A clear enhancement of all three image modality is clearly observed. Some example are given in figure 7.1.

7.1 My contribution

This publication was another product of my "change of scientific environment". Together with my supervisor Martin Bech I was responsible for putting together the setup in his new x-ray lab. I made the scripts to perform the measurement which included a randomness. I performed the measurements and applied the BSR algorithm to the measurements. I utilized a software package introduced to me and installed by co-author Tao Shen whom also helped setting up the BSR experiments. Finally I was the main author of the paper and wrote the first draft.

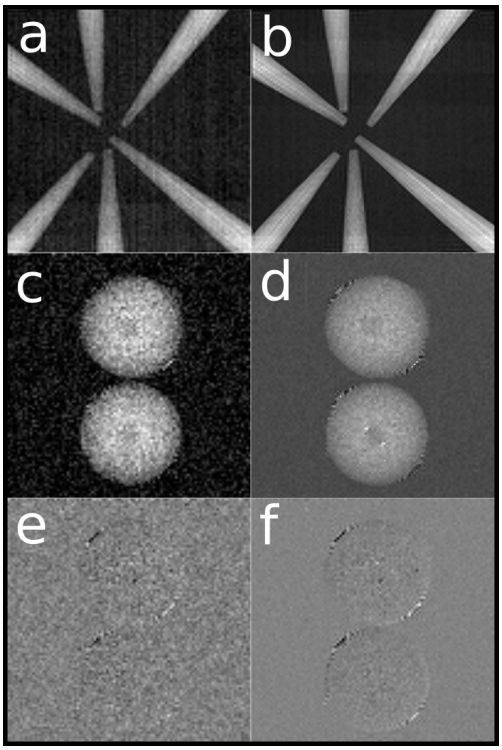

Figure 7.1: Comparison between regular spatial harmonic analysis and BSR enhanced spatial harmonic analysis. a) Absorption contrast b) BSR enhanced absorption contrast image. c) Dark field image. d) BSR enhanced dark field image. e) Differential phase contrast. F BSR enhanced differential phase contrast.

8 Introduction to secondary publication

Injection of high dose botulinum-toxin A leads to impaired skeletal muscle function and damage of the fibrilar and non-fibrilar structures

Botulinum-toxin A (BoNT/A) is highly toxic, however it is used for medical treatments. Other than its cosmetic application, this toxin offers pain relief to patients suffering from sometimes very impairing, and otherwise untreatable, conditions, such as cerebral palsy. The aim of the study is to studie how a high dose intramuscular BoNT/A injections (6 UI = 60 pg) effects the muscle tissue in rats. Within 3 weeks after injection the gait pattern of the rats become severely disabled. The goal of the synchrotron measurements is to investigate if this could be observed on a micro structural level. These measurements are performed on the TOMCAT (TOmographic Microscopy and Coherent rAdiology experimenTs) beam line at SLS. The mesurements are refraction corrected absorption tomography a.k.a. the paganin method discussed in section 4.5.

The images provide strong evidence for micro-structural changes of tissue. Both the fibrillar and the non-fibrillar tissues are affected. The volume fraction of fibrillary tissue is significantly reduced, while non-fibrillar tissue increase. Furthermore the linear structure of the muscle tissue is also reduced. This is illustrated in figure 8.1

8.1 My contribution

This publication is the one were I contributed the least which is why I have denoted it as secondary. I participated in the measurement at SLS in Switzerland and as the most Junior member of the team I can truly say that I pulled the most night Shifts. I only contributed to paper on a discussion level, but was not otherwise involved in the data analysis. Though the publication only present measurements from rats most of the samples measured at the beam time were from human. Here I also contributed with a personal muscle fiber sample.

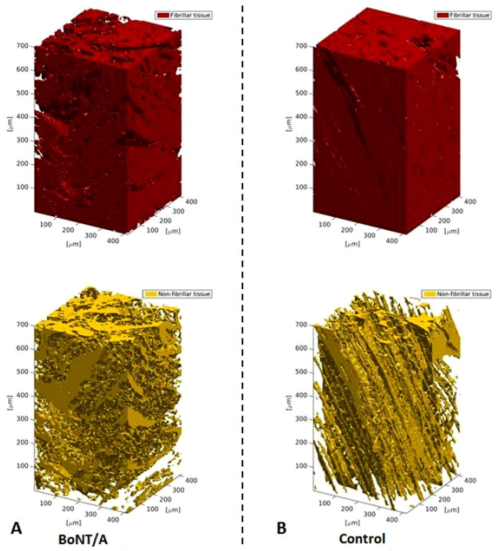

Figure 8.1: 3D visualizations of tomograms from the Synchrotron radiation x-ray tomographic microscopy measurements. Shown are the fibrillar (red) and non-fibrillar tissue (yellow) of the muscle in BoNT/A injected (A) and control leg (B) of one of the rats (3 weeks post injection of 6UI BoNT/A (3 x 20 pg BoNT (2UI)/a $\sim$ 60 pg BoNT/A in total). The SRXTM data indicate that BoNT/A injection causes damage to the muscle tissue structure and organization. [This figure was made by Mikkel Schou Nielsen]

9 Conclusion

In many cases the x-ray imaging part of scientific studies is mainly applied in other scientific fields to test hypotheses and draw conclusions. This is also one of the themes of the papers included in this thesis. This conclusion is made from the imaging and data acquisition point of view contrary to the publication conclusions where the majority is focused towards what is revealed by the method. In this thesis the theoretical background for the methods used in the publication have been discussed in the chapters 2, 3 and 6. With this knowledge the main publications are introduced in separate chapters 5, 6 and 7. The conclusion is managed in the same way as it is separated by publication, however, with an imaging and data analysis focus which is the subject of this work.

9.1 Microstructure, texture and secondary protein structure of extruded high protein snacks studied by FT-IR spectroscopy and X-ray tomography

In article A.1, x-ray micro tomography was applied to study the micro-structural information of high protein pea dough snacks. These tomograms were imaged using a 2D threshold segmentation procedure available in the so called Drishti imaging software. The data analysis required a proper segmentation. Here, a relatively simple semi-automated segmentation algorithm was devised. From the segmented

tomograms, quantitative parametric data is extracted by an additional automated algorithm. These being quantities such as object volume, percentage of object volume, object surface to volume ratio, directional average structure thickness, average air particle size etc. This algorithm is developed to produce a reliable and consistent way to calculate important parameters of the micro structures in the snack, but it will also be applicable to other similar structures where similar parameters must be determined.

Outlook

The purpose of the analytical algorithm was to make it simple and reliable such that it could be applied to similar structures. Looking forward, the aim is to test the algorithm on similar structures, and if it proves itself reliable, to propose it as a standard to extract relevant parameters of micro-structures of extruded foods. This is very relevant as there is, at the time of writing, no universal standard to determine these parameters.

9.2 Three-dimensional architecture of human diabetic peripheral nerves revealed by X-ray phase contrast holographic nanotomography

Article A.2 is a proof of concept study with two goals: (1) to determine whether it is possible to image human peripheral nerves by applying phase contrast holographic nanotomography, (2) to do a proper segmentation, where the segmentation of the 3D nerve structures is of such a quality that a reliable quantitative analysis can be made. Both goals are successfully achieved. Additionally, a preliminary outcome this work was to develop a filtering algorithm to enhance the image quality of the full tomographic data set. This was successfully achieved and is described in the introduction to this publication in Chapter 6.

Outlook

This paper was attempted to be published in a number of high impact factor journals, but it was rejected although it was in review for more than a hundred days at some point. However, to strengthen the paper the scope of it will be widened to also include a statistical analysis of different patient groups, including a comparison of these. At the time of writing this thesis, the rework of the paper is ongoing.

9.3 Super resolution x-ray phase-contrast and dark-field imaging with a single 2D grating and electronic source stepping

In article A.3 it is shown that it is possible to overcome some of the resolution loss from the single shot imaging method with no demand for system stability, which is a well known issue of the Talbot interferometer. This was done by applying a random electronic source stepping approach and collect an image series during the stepping. The image series is then used by the blind super resolution algorithm to increase the resolution of all three image modalities. This method is much more reliable compared to the Talbot approach as it is insensitive to any kind of short or long term instabilities or thermal drift. This is because the technique requires a geometrical change from image to image, which can be random. The results presented in article A.3. are a strong indication of a very reliable and applicable technique.

Outlook

It should be possible to construct a system which achieves higher resolution. The decrease in resolution, dictated by the setup design, could be reduced in an alternate setup where the distance between the grating and the detector is smaller. However, this would increase the signal to noise ratio which is already critical in this system. Furthermore, it is possible that the image reconstruction would benefit from a better aimed blind super resolution algorithm, which should be investigated going forward. In theory it should be possible to achieve sub-pixel resolution if such enhancements are made.

Bibliography

Als-Nielsen, Jens and Des McMorrow (2010). *Elements of Mordern X-ray Physics*. WILEY (cit. on pp. 2, 9, 15, 28–30, 33, 37, 190, 198).

Arfken, George B. and Hans J. Weber (2005). *Mathematical Methods for Physicists - Sixth Edition*. Elsevier Academic Press (cit. on p. 49).

Bech, Martin (2009). "X-ray imaging with a grating interferometer". PhD thesis. University of Copenhagen (cit. on p. 61).

Blewett, J. P. (Sept. 13, 1945). "Radiation Losses in the Induction Electron Accelerator". In: *Physical Review* (cit. on p. 10).

Brilliance (2019). Spanish National Research Council. URL: http://www.xtal.iqfr.csic.es/Cristalografia/parte_02-en.html (visited on 01/06/2019) (cit. on p. 9).

Cloetens, P. et al. (Sept. 8, 1999). "Holotomography: Quantitative phase tomography with micrometer resolution using hard synchrotron radiation x rays". In: *Applied Physics Letters* (cit. on p. 56).

Defrise, M. and R. Clack (Mar. 1, 1994). "A Cone-Beam Reconstruction Algorithm Using Shift-Variant Filtering and Cone-Beam Backprojection". In: *IEEE Transactions on Medical Imaging* (cit. on p. 51).

Excillum MetalJet (2019). Excillum. URL: https://www.excillum.com/products/metaljet-sources/ (visited on 01/06/2019) (cit. on p. 8).

Excillum source spot size (2019). Excillum. URL: https://www.excillum.com/products/metaljet-sources/metaljet-d2-160-kv/ (visited on 01/06/2019) (cit. on p. 8).

Feldkamp, L. A., L. C. Davis, and J. W. Kress (Feb. 28, 1984). "Practical cone-beam algorithm". In: *Journal of the Optical Society of America A* (cit. on p. 51).

Fox, Mark (2010). *Optical Properties of Solids*. OXFORD (cit. on pp. 16, 17, 19, 21).

Gerry, Christopher C. and Peter L. Knight (2005). *Introductory Quantum Optics*. CAMBRIDGE (cit. on p. 16).

Griffiths, David J. (1999). *Introduction to Electrodynamics*. PRENTICE HALL (cit. on pp. 16, 33).

Guigay, J. P. et al. (Aug. 16, 2010). "Mixed transfer function and transport of intensity approach for phase retrieval in the Fresnel region". In: *IEEE Transactions on Image Processing* (cit. on pp. 4, 56, 57).

Harmon, Katherine J et al. (June 27, 2014). "Motionless electromagnetic phase stepping versus mechanical phase stepping in x-ray phase-contrast imaging with a compact source". In: *Physics in Medicine and Biology* (cit. on pp. 62, 63).

Langer, M., P. Cloetens, and F. Peyrin (Aug. 16, 2010). "Regularization of Phase Retrieval With Phase-Attenuation Duality Prior for 3-D Holotomography". In: *IEEE Transactions on Image Processing* (cit. on p. 56).

Lauridsen, Torsten (2018). "New Methods in X-ray Imaging". PhD thesis. University of Copenhagen (cit. on pp. 6, 49, 51–53).

Mamou, Jonathan and Yao Wang (2019). *Physics of Radiography*. New York University. URL: http://eeweb.poly.edu/~yao/EL5823/Lect2_PhysicsRadiography_ch4_JM.pdf (visited on 01/06/2019) (cit. on p. 8).

Milton, S. V. et al. (June 15, 2001). "Exponential Gain and Saturation of a Self-Amplified Spontaneous Emission Free-Electron Laser". In: *Science* (cit. on p. 12).

Mokso, R. et al. (Apr. 5, 2007). "Nanoscale zoom tomography with hard x rays using Kirkpatrick-Baez optics". In: *Applied Physics Letters* (cit. on p. 58).

Momose, Atsushi et al. (July 1, 2003). "Demonstration of X-Ray Talbot Interferometry". In: *Japanese Journal of Applied Physics* (cit. on p. 2).

Paganin, D. et al. (Apr. 1, 2002). "Simultaneous phase and amplitude extraction from a single defocused image of a homogeneous object". In: *Journal of Microscopy* (cit. on pp. 5, 54, 55).

Pfeiffer, F. et al. (Jan. 13, 2008). "Hard-X-ray dark-field imaging using a grating interferometer". In: *Nature Materials* (cit. on p. 59).

Pilatus (2019). Dectrice. URL: https://www.dectris.com/products/pilatus3/pilatus3-r-for-laboratory/details/pilatus3-r-1m (visited on 01/07/2019) (cit. on p. 39).

Rodenburg, J. M. et al. (Jan. 18, 2007). "Hard-X-Ray Lensless Imaging of Extended Objects". In: *Physical Review Letters* (cit. on p. 28).

Silva, J. C. da et al. (Apr. 24, 2017). "Efficient concentration of high-energy x-rays for diffraction-limited imaging resolution". In: *Optica* (cit. on p. 16).

Snigirev, A. et al. (Sept. 1, 1995). "On the possibilities of x-ray phase contrast microimaging by coherent high-energy synchrotron radiation". In: *Review of Scientific Instruments* (cit. on p. 56).

Soleil (2019). Soleil Synchrotron. URL: http://www.cepia.inra.fr/Outils-et-Ressources/Synchrotron-SOLEIL (visited on 01/06/2019) (cit. on p. 11).

Šroubek, Filip, Jan Flusser, and Gabriel Cristóbal (Dec. 10, 2007). "Super-Resolution and Blind Deconvolution For Rational Factors With an Application to Color Images". In: *The Computer Journal* (cit. on p. 62).

Turbell, Henrik (2001). "Cone-Beam Reconstruction Using Filtered Backprojection". PhD thesis. Linköpings universitet (cit. on pp. 3, 48, 51).

Wagner, A.R. et al. (Feb. 15, 2008). "Monochromatic X-ray sources based on a mechanism of real and virtual photon diffraction in crystals". In: *Nuclear Instruments and Methods in Physics Research B* (cit. on p. 46).

Wang, H., Y. Kashyap, and K. Sawhney (Feb. 16, 2016). "From synchrotron radiation to lab source: advanced speckle-based X-ray imaging using abrasive paper". In: *Scientific Reports* (cit. on p. 63).

Weitkamp, T. et al. (Aug. 1, 2005). "X-ray phase imaging with a grating interferometer". In: *Optics Express* (cit. on p. 60).

Wen, Harold H. et al. (June 3, 2010). "Single-shot x-ray differential phase-contrast and diffraction imaging using two-dimensional transmission gratings". In: *Optics Letters* (cit. on pp. 4, 62).

Winick, H. (May 1, 1997). *Fourth generation light sources*, 37–41 vol.1 (cit. on pp. 9–11).

XFEL (2019). European XFEL. URL: https://www.xfel.eu/facility/overview/facts_amp_figures/index_eng.html/index_eng.html (visited on 01/06/2019) (cit. on p. 12).

XFEL (2019). European XFEL. URL: https://www.xfel.eu/facility/overview/how_it_works/index_eng.html (visited on 01/06/2019) (cit. on p. 13).

Zhou, Tunhe et al. (June 15, 2015). "Speckle-based x-ray phase-contrast imaging with a laboratory source and the scanning technique". In: *Optics Letters* (cit. on p. 63).

A Appendix A - Main Publications

A.1 Article 1 - Microstructure, texture and secondary protein structure of extruded high protein snacks studied by FT-IR spectroscopy and X-ray tomography

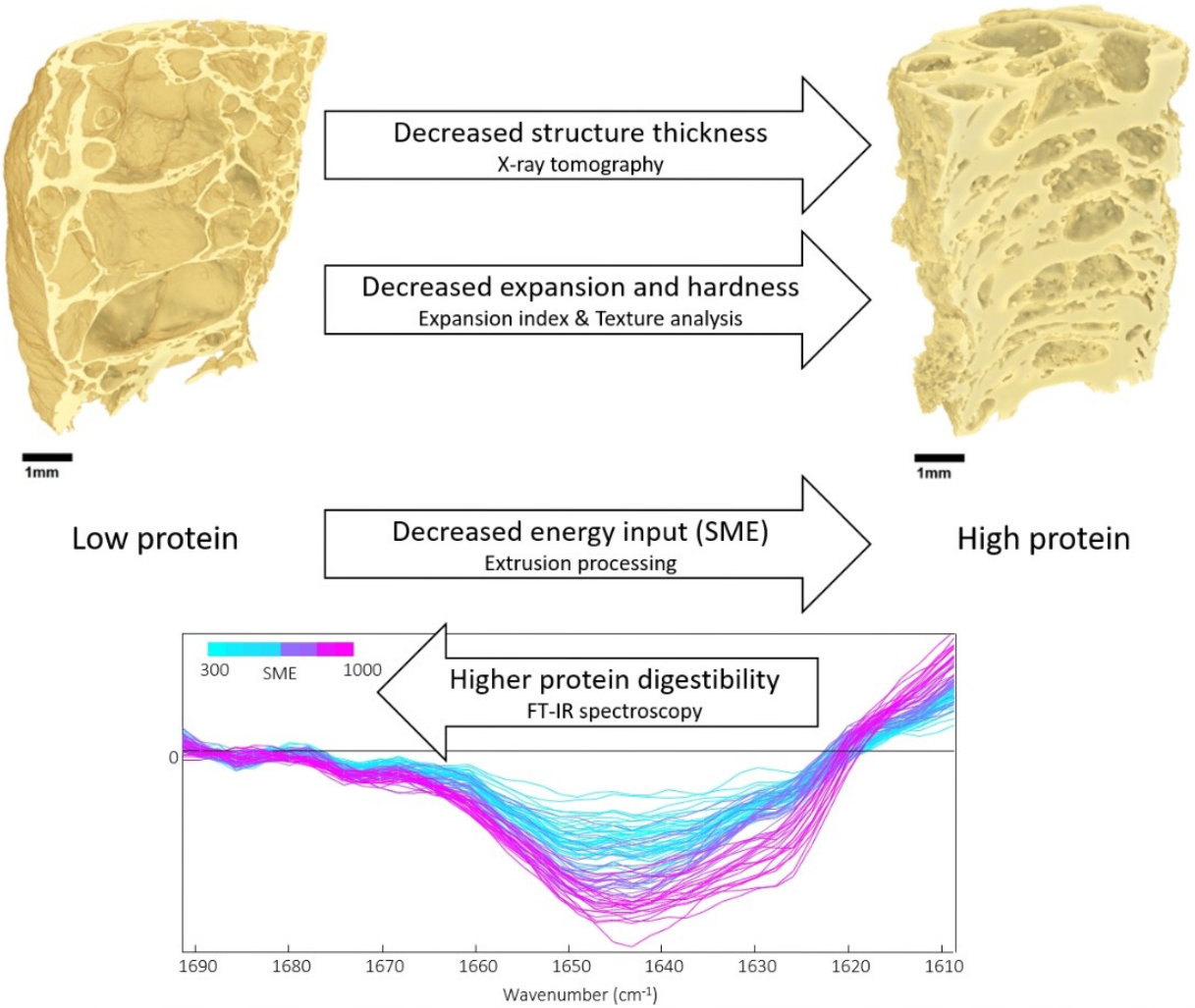
Decreased structure thickness
X-ray tomography
Decreased expansion and hardness
Expansion index & Texture analysis
1mm
1mm
Low protein
Decreased energy input (SME)
Extrusion processing
High protein
300
SME
1000
Higher protein digestibility
FT-IR spectroscopy
0
1690
1680
1670
1660
1650
1640
1630
1620
1610
Wavenumber (cm-1)

Microstructure, texture and secondary protein structure of extruded high protein snacks studied by FT-IR spectroscopy and X-ray tomography

Mette Holse[ac], Jacob Frydendahl[a], Krisitian Romlund Rix[b], Rikke Miklos[ad*]

[a] Department of Food Science, Faculty of Science, University of Copenhagen, Rolighedsvej 26, DK-1958 Frederiksberg C, Denmark, [b]Niels Bohr Institute, Faculty of Science, University of Copenhagen, Blegdamsvej 17, DK-2100 Copenhagen, Denmark

*Corresponding author: Tel.: +45 72202274; E-mail: rimi@dti.dk

Abstract

The effect of extrusion processing on protein digestibility and the product structure of snacks prepared from yellow peas and potato starch was investigated. The impact of protein content (7-15%), moisture content (23-40%) and extrusion temperature (130-150 °C) on the microstructure, texture, expansion and secondary protein structure of extruded pea snacks was studied by X-ray tomography, texture analysis and FT-IR spectroscopy. The results showed that extrusion processing altered the secondary protein structure of the pea proteins indicating an improved digestibility. This effect was negatively correlated to the protein content. While a higher protein content restricted the expansion of the extrudate.

Key words: Extrusion; X-ray tomography; FT-IR; Plant protein, 3D visualization; Snacks; Microstructure

1. Introduction

The snack market is forecasted to keep growing rapidly the coming years, as snacks are an increasingly important part of the consumers' diet due to convenience (Brennan, Derbyshire, Tiwari, & Brennan, 2013; Patil, Brennan, Mason, & Brennan, 2016). Meanwhile, global problems with obesity and non-communicable diseases are an ever-growing threat. Today, snack products are usually based on refined cereal flours (e.g. corn, rice or wheat), and thus of relatively poor nutritional quality; high in calories and low in protein and dietary fibres. Being the building blocks of life, proteins are essential for the well-being of the human body. Hence, a snack product rich in protein and fibre and low in salt, saturated fats and easily digested carbohydrates could contribute to the solution and hereby have an enormous market potential.

With increasing populations worldwide, it is necessary to explore the use of plant proteins to cover future protein needs in a sustainable way. Legumes in general are important food crops due to their nutritional attributes such as high protein and essential amino acid content. They are also a good source of dietary fibre, minerals and vitamins while they usually contain small amounts of oil. Yet the number of extruded legume-based snacks in the market is still quite limited. This is probably due to several constraints, such as consumers' perception of legumes. Another issue is that puffed protein-based snacks have difficulties gaining the same texture as the starch-based snacks. Changes in the protein structure occur during extrusion processing and protein-protein interactions will take place along with interactions between proteins and other components, however, there is not a consistent model explaining the phenomena of the three-dimensional network which is formed during the process (Alonso, Orue, Zabalza, Grant, & Marzo, 2000; Day & Swanson, 2013). Moreover, the textural and physical properties of the extrudate depends on the physical profile of the feed material from particle size to moisture content, the extruder profile from screw speed to die shape as well as temperature, pressure and shear leading to specific mechanical energy delivered to the extrudate.

When using legumes as the protein base of a product, it is important to consider the nutritional protein quality, which depends on factors such as the amino acid composition, digestibility, presence of anti-nutritional factors and the effect of processing of the food. The structural composition of the proteins has an influence on the digestibility. A direct correlation between digestibility and β-sheet content has been found (Carbonaro et. al. 2012). The lower digestibility of proteins containing high amounts of β-sheets may be explained by the hydrophobic nature of these structures. This will promote protein-protein interactions and aggregate formation which will reduce the susceptible sites for proteases.

Protein digestibility may be improved through extrusion processing, since proteins are denatured during this high temperature, short time, high pressure process. Extrusion also inactivates many native enzymes and anti-nutritional factors without modifying the protein content (Abd El-Hady & Habiba, 2003; Alonso, Aguirre, & Marzo, 2000; Czarnecka, Czarnecki, Nowak, & Roszyk, 1998).

Spectroscopic sensors are fast, non-invasive and provide multifactorial information. For instance, amid bands found in FT-IR spectra have shown to contain information about the secondary protein structure and hereby the protein digestibility. By calculating the second derivative of the amide I band, information about the proportion of α-helix, β-sheets, β-turns and random coil conformations can be obtained (Carbonaro, Maselli, & Nucara, 2012; Guzman-Ortiz et al., 2015; Holse, Larsen, Hansen, & Engelsen, 2011).

X-ray computed tomography (CT) has shown to be a valuable method in non-destructive three-dimensional imaging of microstructure of food. X-ray μCT has been used in studies of a wide range of commodities including e.g. meat, fruits, cereals, coffee beans, dairy products, contributing to a better understanding of the physical structure of the samples (Schoeman, Williams, du Plessis & Manley, 2016). Further, the non-destructive characteristics of the method add to the unique properties in order to visualize and quantify structural changes during processing of food as bubble growth and foam setting during bread making (Babin, DellaValle, Chiron, Cloetens, Hoszowskad, Pernot, Réguerrec,

Salvoa, & Dendievela, 2006) or microstructural evolution of ice cream (Pinzer, Medebach, Limbach, Dubois, Stampanoni & Schneebeli, 2012).

The objective of this work was to study the impact of the protein content and the processing conditions (added moisture and temperature) on the relationship between the 3D structural information gained from X-ray tomography and the molecular information of the secondary protein structure obtained through spectroscopy to investigate the effect of extrusion processing on protein digestibility and the product quality.

2. Materials and Methods

2.1Experimental design

The impact of protein content, moisture content and extrusion temperature on the microstructure, texture, expansion and secondary protein structure of extruded pea snacks were studied by production of eight snack varieties. The study was designed as a two-level full factorial design with three-factors as given in Table 1**Table 1**. The sample names are composed of protein content in % (P_x), water content in % (W_y) and temperature in °C (T_z). The samples that were post treated by microwaving are denoted with an M. The levels of the process parameters were based on pre-trials. Moisture contents lower than 23% and temperature higher than 150°C lead to product burning.

Table 1: Effects of extrusion conditions on process and product responses. Results are given as mean values: SME (mean values of two extrusion batches), EI and Hardness (mean values of 20 replicates, 10 from each extrusion batch).

Sample	Post treatment	Extrusion conditions			Product responses		Process response
		Protein content (g/100g DM)	Moisture content (%)	Temperature (°C)	Expansion index	Hardness/ Max. force (N)	SME (Wh/kg)
P_{15}-W_{23}-T_{130}	None	15	23	130	1,28	31,7	910
P_{15}-W_{23}-T_{150}	None	15	23	150	1,11	20,7	708
P_{15}-W_{40}-T_{130}	None	15	40	130	1,02	4,9	449
P_{15}-W_{40}-T_{150}	None	15	40	150	1,44	5,4	399
P_{7}-W_{23}-T_{130}	None	7	23	130	1,64	46,7	1037
P_{7}-W_{23}-T_{150}	None	7	23	150	2,22	50,9	910
P_{7}-W_{40}-T_{130}	None	7	40	130	2,10	18,3	448
P_{7}-W_{40}-T_{150}	None	7	40	150	1,63	12,5	417
P_{15}-W_{23}-T_{130}M	Microwave	15	23	130	2,03	23,5	910
P_{15}-W_{23}-T_{150}M	Microwave	15	23	150	1,43	22,2	708
P_{15}-W_{40}-T_{130}M	Microwave	15	40	130	1,32	20,6	449
P_{15}-W_{40}-T_{150}M	Microwave	15	40	150	1,23	31,0	399
P_{7}-W_{23}-T_{130}M	Microwave	7	23	130	2,42	40,7	1037
P_{7}-W_{23}-T_{150}M	Microwave	7	23	150	2,47	50,9	910
P_{7}-W_{40}-T_{130}M	Microwave	7	40	130	2,50	58,0	448
P_{7}-W_{40}-T_{150}M	Microwave	7	40	150	1,92	50,6	417

2.2Raw materials

Commercial pre-boiled pea granulate (Møllerens Gule Ærter, Valsemøllen A/S, Denmark) and potato flour (Dansk Kartoffelmel, Nordic Food Partners A/S, Denmark) were obtained from a local supermarket. The proximate composition of pea granulate was 59,2% dm carbohydrates, 13,0% dm fibres, 26,0% dm protein and 1,8% dm lipid, while potato flour was 99,6% dm carbohydrate, 0.2% dm protein and 0.1% dm lipid. The pea granulate was milled in a coffee mill (OBH Nordica 2393, Vallensbæk strand, Denmark) and mixed with potato flour to a final particle size ≤ 500 µm.

2.3Extrusion

The extrusion process was performed on a laboratory scale co-rotating and intermeshing twin screw extruder (Process 11, Thermo Fisher Scientific, Karlsruhe, Germany). The barrel diameter and its length to diameter were 11 mm and 40:1, respectively. The extruder barrel was fitted with a circular 2 mm die nozzle. The extruder was run by a 1.5 kW motor with fixed screw speed of 500 rpm and a

feed rate at 0.5 kg/min. The raw material was metered into the extruder by a gravimetric twin-screw feeder (MT-S, MiniTwin, Brabender Technologie, Duisburg, Germany). Water was pumped into the extruder by a peristaltic pump (Fillmaster Type 421, Delta Scientific Medical, Store Heddinge, Denmark). The extruder had 7 heating zones. The temperature in the experimental design refers to the end temperature of two different temperature profiles; a) zone 1-7: 60-60-80-80-120-130-130 °C and b) zone 1-7: 70-80-80-90-150-150-150 °C.

2.3.1 Sample collection and determination of process responses

Data from the extrusion process (torque, power, the temperature of zone 7, 8 and the die as well as the melt temperature, actual feed rate, screw speed and die pressure) was collected every 5 seconds by a data logging software (V3.2, Thermo Fisher Scientific).

Samples were collected 3 minutes after the feed rate, water flow, temperature and screw speed had reached a steady-state. The samples were cooled to room temperature, packed in polyethylene bags and stored at 5 °C until further treatment and analysis.

The specific mechanical energy (SME) is a measure of the energy put into producing one kilo of extrudate and was calculated (Equation 1) from the rated screw speed (1000 rpm), actual screw speed, % motor torque, motor power rating (1.5 kW), and mass flow rate and expressed as Wh/kg (Meng, Threinen, Hansen, & Driedger, 2010).

$$SME = \frac{actual\ screw\ speed\ (rpm)}{rated\ screw\ speed\ (rpm)} * \frac{\%\ motor\ torque}{100} * \frac{motor\ power\ rating\ (kW)}{feed\ rate\ \left(\frac{kg}{h}\right)} \quad (1)$$

2.3.2 Post extrusion treatment

The extrudates were microwaved to fully expand and to lower the moisture content. Samples were microwaved (Microwave R-25AT 2100W, Sharp, Osaka, Japan) in bulk of app. 20 g. A sequence of

microwave steps was applied; 20 s at 2100 W, 30 s at 630 W and finally 30 s at 420 W. Samples were cooled to room temperature and packed in polyethylene bags and stored at room temperature until further analysis.

2.4Characterisation of extrudates

2.4.1 Expansion index

The expansion index (EI) was expressed as the ratio of the diameter of the extrudate to the diameter of the die (Kumar et. al. 2015). The cross-sectional diameter of the extrudates was determined by use of a digital Vernier caliper. The EI was determined 10 times for each extrusion sample before and after microwave treatment.

2.4.2 Texture Analysis

The breaking strength of the extrudates before and after post treatment was determined using a TA.XT*plus* Texture Analyser (Stable Micro System, Surrey, UK) equipped with a 30 kg load cell and a Warner-Bratzler shear blade (V-shaped, 2mm). The shear force was measured at a constant cross head speed of 1.5 mm/s and a trigger force of 10 g. A force-time curve was recorded and the hardness determined as the peak breaking force (N). Data was analysed by use of the software Texture Exponent 32 (ver.6.1.9.0 Surrey, UK). Ten extrudates were tested for each processing condition.

2.4.3 X-ray microtomography

3D microstructure images of the extrudates were obtained by X-ray microtomograhpy (μCT). X-ray measurements were performed on a ZEISS XRadia 410 Micro-CT. The applied technique is the standard filtered back projection for cone-beam algorithm described by (Feldkamp *et al*., 1984). Here a series of projection images were made as the sample was rotated 360 degrees in short steps. From which the 3D tomogram was reconstructed. The number of pixels was approximately

1000x1000x1000 pr. tomogram and the voxel size is 6.05 µm. The x-rays emitted were created using a voltage of 40 KV and a 200 µA current.

2.4.4 Secondary protein structure

The absorbance measurements were performed on an Arid-Zone MB100 FT-IR instrument (ABB Bomen, Quebec, Canada) with an Attenuated Total Reflectance (ATR) device with a triple-bounce diamond crystal. IR spectra were recorded in the range from 1800-1500 cm^{-1} with a spectral resolution of 4 cm^{-1}. Before analysis, the samples (both with and without microwave treatment) were dried at 50 °C for 12 hours to remove water, which could otherwise interfere with the amide I band (Dong, Huang, & Caughey, 1990). The samples were ground in a mortar to a small particle size (≤250 µm) and placed on the crystal surface and squeezed against the crystal with a concave needle compressor. Each spectrum represents the average of 64 scans ratioed against the background (64 scans measured on the surrounding air). Each sample was measured 10 times.

2.5Data analysis

2.5.1 3D Image processing and micro-structural parameters

To quantify the image data the tomograms were segmented. First an appropriate threshold value for each tomogram was determined and afterwards applied to the full volume. The threshold value was determined from the histogram of a tomogram slice by identifying the peak intensity value (I_{peak}) of air- and dough-peak respectively. The threshold value (T_{seg}) for the segmentation was determined by Equation 2:

$$T_{seg} = \frac{I_{peak,dough} - I_{peak,air}}{2} + I_{peak,air} \quad (2)$$

Ideally, by discarding all voxels below T_{seg} as having zero value, the pixels remaining must represent dough voxels. As the samples were embedded in foam for stabilization during the measurements, the threshold segmentation was not sufficient. To remove the foam structure some manual correction of

the threshold value together with standard morphological operations was used. These operations were: “largest connected elements”, ”erotion” and ”dilation” applied in 3D. If the ”erotion” and ”dilation” are combined the operation was known as morphological opening and closing depending when they were applied. It was necessary to distinguish the air ”inside” the sample from the air outside the sample. This was done by applying a 2D hole filling algorithm on all planes i.e. all x-y, x-z and y-z plane of the segmented tomogram. This procedure was repeated until convergence was achieved. Typically, 3-5 iterations were applied. If a given not-dough voxel was hole-filled in any of the three plane orientations, it was classified as ”internal” air and assigned the value 1 (dough was set to 2). The entire segmentation- and air classification process is illustrated in Figure 1. The entire algorithm is summarized in Appendix.

From the segmented and classified tomograms, the following microstructural parameters were calculated:

1) The object volume (OV) which is described by the voxels of value 2.
2) Percentage of object volume (POV).
3) Object to surface volume (OSVR).
4) Average structure thickness (AST) in the three axial directions, used as a measure of the anisotropy.
5) The average air particle size (APS) inside the volume of interest.

These parameters can be extracted from the two volumes of interest. The OV was calculated as the voxel size and number of voxel with the value two is well known

$$OV = N_{voxel=2} \cdot V_{voxel} \quad (3)$$

Equally simple the percentage POV was calculated as:

$$POV = \frac{N_{voxel=2}}{N_{voxel=2} + N_{voxel=1}} \cdot 100\% \quad (4)$$

To extract the OSVR, the surface area must be determined. To do this an additional algorithm was made. Here the voxels of value two in the classified tomograms were considered, so all values smaller than two is set to zero, while values equal to two was set to one. This is also equivalent to the segmented tomogram seen in Figure 1 panel C before the hole filling procedure. Six copies of the tomogram were made and in each copy the full structure was shifted one pixel on the x, y and z axis in both positive and negative direction of each axis. By subtracting one of the six translated copies from the original structure, the edges corresponding to the translation axis and direction remained one. The rest was 0 except next to the opposite edge, here the value was minus one. It might be suggested that the minus one values described the position of opposite edge. Though, it described the pixel next to the edge. Due to this, the translation was done twice in positive and negative direction of each axis. This is illustrated in Figure 1. In panel J+I the edges found by lateral translation in positive and negative direction are displayed. The positive translation determines left side edges while the negative translation resulted in right side edges. Panel L displays both left and right edges. This was made by pixel-wise adding the edge images. To make the image of panel L, all values larger than zero were set equal to one. The same procedure was expanded to the Up/Down (y-axis) and in/out (z-axis) of plane axis (panel M and N). In panel O of Figure 1, two perpendicular edge planes are displayed together with a slice from the raw tomographic reconstruction to illustrate the edge data. The algorithm is summarized in Appendix. The full surface area was then determined. Every voxel of value one in the 6 edge volume contributes $36.65\mu m^2$, which is the pixel area (pA), to the surface area (note that some voxels might contribute more than once). The OSVR can then be calculated as:

$$OSVR = \frac{N_{-x} + N_{-y} + N_{-z}}{OV} \cdot 2p_A \quad (5)$$

Structure thicknesses is often determined by skeletonization algorithms. In this study a new and more simple method to describe structural anisotropy and directional thicknesses at the same time were developed using the previously acquired data. This measure is the average structure thickness in the

three different directions using the number of edge pixels in a given axis and direction, the pixel size (pS) and the structure volume pixels (white pixels). Hence the average thickness on the x-axis becomes:

$$T_x = \frac{p_s \cdot N_{white}}{N_{-x}} = \frac{p_s \cdot N_{white}}{N_{+x}} \quad (6)$$

This was evidently applicable in y and x axis also. Finally, the average particle size (APS) was determined. The approach was done using functions available in python through the packages known as ”scipy” and ”numpy”. The starting point of determining the APS is visualized in Figure 1 panel F. The full 3D structure was considered, where all values equal to two was set to zero. Applying the function called ” label” in the ”scipy” package all voxels in a connected structure in the 3D volume was given a specific integer value, while voxels of other structures are assigned different integer values. The function ”bincount” from the ”nympy” package was then applied to count the number of voxels with a given integer. In this way the volume of all ”inside” air cavities of the structure was determined. APS is then easily calculated without knowing the volume of individual particles only the number of particles is of interest:

$$APS = \frac{N_{gray}}{N_{struct}} \quad (7)$$

It turned out by applying the bincount function that a significant amount of the structures detected were less than 10 connected voxels. It is our educated observation that such small air particles are not a real feature, but rather small imperfections in the segmentation algorithm. Therefore, to get a more realistic and useful number for the APS, the calculation was:

$$APS = \frac{N_{gray}}{N_{struct} - N_{struct10}} \quad (8)$$

$N_{stuct10}$ is the number of labelled structures containing less than 10 voxels.

Another parameter that was extracted from the explained approach, is the largest connected air structure, which is equivalent to the biggest particle size and calculated as the air percentage of biggest particles (APBP) compared to all internal air

2.5.2 Secondary protein structure from FT-IR spectra

Characterization of the protein secondary structure was done by exploring the amide I band in the region from 1600-1700 cm^{-1}. Data was MSC treated and the second derivative was calculated (Savitzky-Golay, 2^{nd} order polynomial, window size of 9, derivative calculated: 2). Data handling was done using LatentiX (v.2.12, Latent5 Aps, Copenhagen, Denmark).

2.5.3 Statistics

Three-way ANOVA with two levels of each factor (moisture content, protein content and temperature profile) was carried out for each response variable (EI, hardness and SME) using MatLab (2016b, MathWorks, US).

2.5.4 Multivariate analysis

Principal component analysis (PCA) was used as a descriptive method during data exploration. PCA allows the main variability aspects of the dataset to be visualised. The main goals of this procedure are to find relationships between the different parameters (objects and variables) and to detect possible clusters within objects and/or variables. PCA was performed using LatentiX (v.2.12, Latent5 Aps, Copenhagen, Denmark).

3. Results and discussion

3.1Expansion index and texture of extruded pea snacks

The expansion index and hardness, measured by texture analysis, is used to express the product characteristics after extrusion as well as after additional microwave treatment. Furthermore, the

process response SME is used as an indirect quality parameter. SME is a measure of the mechanical energy delivered to the product, which is known to affect the melting temperature and macromolecular degradation and thus the expansion and cellular and textural characteristics of extrudates (de Mesa et al., 2009). Three-way ANOVA was done to examine whether there was a statistically significant interaction between the three independent variables (protein content, moisture content and temperature) on the dependent variables EI, hardness and SME. The same analysis was done for both extrudates and post microwave treated extrudates. The results of the physical characterizations of the extrudates are given in Table 1 along with the experimental design and the SME while results from the three-way ANOVA are given separately in Table 2.

Table 2: Results from three-way ANOVA. Only significant p-values are given.

	No post treatment			**Microwave**		
	EI	**Hardness**	**SME**	**EI**	**Hardness**	**SME**
Protein content	***	***	***	***	***	***
Moisture content		***	***	***		***
Temperature		*	***	***		***
Protein content * Moisture content		***	***	*		***
Protein content * Temperature profile			*			*
Moisture content * Temperature profile	*		***			***
Protein content * Moisture content * Temperature profile	***	***		***	*	

* Significant at P < 0.05, ** Significant at P < 0.01, *** Significant at P < 0.001.

For both extrudates and post microwave expanded extrudates, there was a significant three-way interaction for EI at a significance level of $p < 0.001$ and a three-way interaction for hardness at a significance level of $p < 0.05$. Hence, the examined parameters all influence the expansion of the extrudates significantly. A higher protein content results in lower expansion and a weaker texture, which is a well-known phenomenon, since the degree to which extrudates expand depends highly on the degree of starch gelatinization. Hence, substituting starch with protein will – in most cases – decrease the expansion (Kokini, Karwe, Jaluria, & Wang, 1992). Moreover, proteins have an influence on the expansion through their effect on the water distribution in the matrix, and on the melt

viscosity due to their macromolecular structure and conformation (Moraru & Kokini, 2003). The sites for cross-linking among proteins and starches increase with an increase in protein concentration, also affecting the textural quality of the extrudates (Aboagye & Stanley, 1987; Onwulata, Smith, Konstance, & Holsinger, 2001). However, proteins are complex and their type and concentration will determine their effect on the end-product due to unfolding, realignment, hydrolysis and denaturisation. The molecular changes taking place are not known in detail for all types of protein. Disulphide bonds, hydrophobic and electrostatic interactions are hypothesized as the predominant texturization mechanisms during extrusion of soy and whey proteins. Electrostatic forces supplemented by inductive forces, hydrogen bond stabilization and hydrophobic affinities are relevant to the texture obtained following extrusion (Day & Swanson, 2013).

The results confirm what is known from literature, that expansion is inversely related to moisture content (Day & Swanson, 2013), while there is not a clear pattern for the effect of temperature, which is probably due to the relatively small difference in die temperature settings (130 °C vs. 150 °C). The textural attributes extracted from the shear force measurements confirm that extrudates with lower moisture content are significantly harder to break while an increase in temperature results in less hard extrudates. The microwave treatment resulted in an increased expansion. Factors that lead to lowering of the mass viscosity as e.g. the interactions between moisture and temperature or the interactions between protein content and moisture resulted as expected in a reduced transfer of SME to the product.

3.2Qualitative and quantitative analysis of the 3D structure

The effects of composition and processing conditions on the 3D structure of the extruded pea snacks was studied by X-ray tomography. Figure 2 shows the 3D visualization of the reconstructed

tomograms of the raw and microwave treated extrudates, while the results of the quantitative analysis of the 3D structure is presented in Table 3.

Table 3. Quantitative analysis of X-ray tomograms. Object volume (OV), Percentage of object volume (POV), Object to surface volume (OSVR), Average structure thickness (AST) in the three axial directions, used as a measure of the anisotropy, The average air particle size (APS) inside the volume of interest. Air percentage of biggest particles (APBP) compared to all internal air.

Sample	OV (um^3)	POV (%)	OSVR (1/um)	AST x (um)	AST y (um)	AST z (um)	APS (um^3)	APBP (%)
P_{15}-W_{40}-T_{130}	$4{,}22 * 10^{10}$	85,57	$6{,}47 * 10^{-3}$	395,0	402,2	393,1	$8{,}86*10^{5}$	42,6
P_{15}-W_{40}-T_{150}	$3{,}98 * 10^{10}$	81,90	$7{,}94 * 10^{-3}$	307,3	303,6	317,9	$1{,}16*10^{6}$	86,9
P_{7}-W_{40}-T_{130}	$1{,}08 * 10^{10}$	86,82	$1{,}66 * 10^{-3}$	1534,1	1456,0	1752,9	$3{,}50*10^{6}$	51,5
P_{7}-W_{40}-T_{150}	$4{,}45 * 10^{10}$	86,15	$5{,}33 * 10^{-3}$	470,8	521,5	465,8	$1{,}85*10^{6}$	63,6
P_{15}-W_{23}-T_{130}_M	$7{,}45 * 10^{10}$	30,02	$5{,}97 * 10^{-3}$	144,7	145,7	163,1	$1{,}05*10^{7}$	95,2
P_{15}-W_{23}-T_{150}_M	$7{,}45 * 10^{10}$	27,70	$6{,}20 * 10^{-3}$	126,3	128,5	150,0	$1{,}84*10^{7}$	96,2
P_{15}-W_{40}-T_{130}_M	$3{,}29 * 10^{10}$	70,11	$10{,}17 * 10^{-3}$	208,5	203,7	208,5	$1{,}16*10^{6}$	86,6
P_{15}-W_{40}-T_{150}-M	$5{,}66 * 10^{10}$	61,19	$7{,}34 * 10^{-3}$	252,0	254,1	244,5	$3{,}74*10^{6}$	75,1
P_{7}-W_{23}-T_{130}_M	$1{,}23 * 10^{11}$	38,02	$3{,}81 * 10^{-3}$	302,1	303,8	293,1	$1{,}94*10^{7}$	66,8
P_{7}-W_{23}-T_{150}_M	$1{,}35 * 10^{11}$	37,85	$5{,}06 * 10^{-3}$	224,3	220,0	228,6	$2{,}48*10^{7}$	55,9
P_{7}-W_{40}-T_{130}_M	$1{,}67 * 10^{11}$	23,63	$4{,}32 * 10^{-3}$	160,8	165,5	166,4	$2{,}27*10^{7}$	73,1
P_{7}-W_{40}-T_{150}_M	$8{,}42 * 10^{10}$	34,34	$7{,}76 * 10^{-3}$	134,3	130,8	133,4	$1{,}29*10^{7}$	97,7

In Figure 2, the light (yellow) areas represents the cell walls consisting of the extruded pea-starch matrix. The dark areas are air bubbles formed during expansion of the extrudate. Visually it is obvious that, when comparing the extrudates with or without additional treatment with microwaves, the extrusion process alone did not result in a fully expanded product. Generally, extrudates that have not been treated with microwaves (first line in Figure 2) have a compact structure with few and small entrapped air bubbles. Further expansion caused by microwaves lead to a more heterogenous structure with a wide range of cell sizes. It would be obvious to assume that further expansion of the samples would be initiated from the already entrapped air in the extrudate. Though, the visualization of the microwave expanded samples show that the sample $P_{7}W_{40}T_{130}$ has the most compact structure with only a few air bubbles prior to treatment with microwaves, whereas it shows the largest expansion

when microwaved, this is also confirmed by the EI measurements and the calculated POV. Though the combination of high water content and high protein content is reducing the expansion as reflected as a higher POV compared to the corresponding sample with lower water content. While the effect of the temperature generally has seemed not to have a significant influence on the texture and the EI, the calculated AST is generally higher for samples processed to 130 °C compared to 150 °C. The results thereby indicate, that the quantitative analysis of the X-ray tomograms reveals structural differences between samples, that were not possible to detect with conventional physical characterizations methods as EI and texture measurements. Another advantage of the non-destructive characteristics of X-ray tomography is the ability to get an impression of the distribution of the air bubbles along the extrudates e.g. formation of spherical air bubbles versus formation of channels in the length direction of the extrudates. The calculated APBP reveals, that all the internal air is to a large extent interconnected and not trapped in individual cells.

3.3Relation between texture and structure

Comparison of the texture measurements with the microstructure clearly indicates that characterisation of extruded snacks with physical measurements alone may lead to inadequate conclusions as two samples with the same level of measured hardness i.e. $P_{7}W_{40}T_{130}$_M (18,3) and $P_{15}W_{40}T_{130}$_M (22,2) are differing significantly in structure as visualized in Figure 2 and is also reflected in different levels of POV and structure thickness (AST). These characteristics will most likely affect the sensorial properties of the snacks.

3.4Impact of processing on secondary protein structure studied by FT-IR

To gain information on the secondary structure of the proteins in the extruded snacks FT-IR measurements were carried out. The spectral region containing the Amid I band arises mainly from stretching vibrations of C=O in the polypeptide backbone. The vibration energies of the carboxyl

group depend on the different conformations of the protein, such as β-sheet and α-helix structures, β- and α-turns, and inter- or intra-molecular aggregates (Kong & Yu, 2007). Calculating the second derivatives of the spectra (Rinnan, Berg, & Engelsen, 2009) makes it possible to assign the spectral components of the amide I band.

The FT-IR spectra of the extrudates are given in Figure 3 along with score and loading plots from a PCA. It is evident that the raw materials (milled pea granulate and potato flour – Figure 3a) have a higher degree of ordered secondary protein structure than the extruded samples (Figure 3b). That is, the raw samples appear to have mainly α-helixes and β-sheets, and to a much lesser extent β-turns, while the protein structure of the extruded samples seem to be dominated by random coil conformations, which are usually associated with the IR band between 1640 and 1648 cm^{-1} (Krimm & Bandekar, 1986). Figure 3c+d highlight how an increase in the mechanical energy input from the extrusion process results in a less ordered protein structure.

A higher degree of β-sheets in the protein corresponds to a lower digestibility due to the hydrophobic nature of the β-sheets. Hence, the extrudates with a higher protein content and water content, and hereby a lower SME, results in snacks with a lower protein digestibility.

This confirms what is already known from other studies that have looked at processing of plant proteins. In a work by Guzmán-Ortiz et. al. (2015) a decrease of β-sheets was found as a result of extrusion of a soybean/corn mixture. The same was the case when autoclaving different legumes. A reduction close to 50% in β-sheets was found resulting in a higher digestibility of these plant proteins. However, the formation of very stable aggregates was also detected (Carbonaro et al., 2012). In a study by Patil *et al.* (2016) where legume flour was added to wheat based snacks in order to improve the nutritional quality, the extrusion process increased the *in vitro* protein digestibility of the products.

From Table 1 it is seen, that an increase in the protein content lead to a decrease in the SME. This indicates that even though a higher protein content in the first place appears to be beneficial from a nutritional point of view, the actual digestibility of the protein may be negatively influenced when the content is increased.

4. Conclusions

Extrusion processing is altering the secondary protein structure of pea protein as measured by FT-IR indicating an improved digestibility of the pea raw material. The effect on digestibility was directly correlated to the amount of mechanical energy (SME) transferred to the product during the extrusion process. When the protein content was increased from 7% to 15% the SME decreased. Further, the expansion of the snacks was decreased. Nevertheless, X-ray tomography revealed that the structure thickness at the same time decreased indicating that an acceptable compromise between protein content and micro structure may be reached. In general, the results showed that extruded snacks may be a convenient way to improve the digestibility of plant proteins from legumes without compromising on the product structure.

Acknowledgements

The Imaging Portal, Technical University of Denmark is acknowledged for the use of their X-ray scanner facility. R.M. and K.R.R. acknowledge financial support through the NEXIM research project funded by the Danish Council for Strategic Research (contract no. 11-116226) within the Program Commission on Health, Food and Welfare.

References

Abd El-Hady, E. A., & Habiba, R. A. (2003). Effect of soaking and extrusion conditions on antinutrients and protein digestibility of legume seeds. *LWT - Food Science and Technology, 36*(3), 285-293. doi:http://dx.doi.org/10.1016/S0023-6438(02)00217-7

Aboagye, Y., & Stanley, D. W. (1987). Thermoplastic Extrusion of Peanut Flour by Twin-Screw Extruder. *Canadian Institute of Food Science and Technology Journal-Journal De L Institut Canadien De Science Et Technologie Alimentaires, 20*(3), 148-153.

Alonso, R., Aguirre, A., & Marzo, F. (2000). Effects of extrusion and traditional processing methods on antinutrients and in vitro digestibility of protein and starch in faba and kidney beans. *Food Chemistry, 68*(2), 159-165. doi:Doi 10.1016/S0308-8146(99)00169-7

Alonso, R., Orue, E., Zabalza, M. J., Grant, G., & Marzo, F. (2000). Effect of extrusion cooking on structure and functional properties of pea and kidney bean proteins. *Journal of the Science of Food and Agriculture, 80*(3), 397-403. doi:Doi 10.1002/1097-0010(200002)80:3<397::Aid-Jsfa542>3.0.Co;2-3

Babin, P., DellaValle, G., Chiron, H., Cloetens, P., Hoszowskad, J., Pernot,P., Réguerrec, A.L., Salvoa, L. & Dendievela, R. (2006). Fast X-ray tomography analysis of bubble growth and foam setting during breadmaking, *Journal of Cereal Science*, 43(3), 393-397, Doi: https://doi.org/10.1016/j.jcs.2005.12.002

Brennan, M. A., Derbyshire, E., Tiwari, B. K., & Brennan, C. S. (2013). Ready-to-eat snack products: the role of extrusion technology in developing consumer acceptable and nutritious snacks. *International Journal of Food Science and Technology, 48*(5), 893-902. doi:10.1111/ijfs.12055

Carbonaro, M., Maselli, P., & Nucara, A. (2012). Relationship between digestibility and secondary structure of raw and thermally treated legume proteins: a Fourier transform infrared (FT-IR) spectroscopic study. *Amino Acids, 43*(2), 911-921. doi:DOI 10.1007/s00726-011-1151-4

Czarnecka, M., Czarnecki, Z., Nowak, J., & Roszyk, H. (1998). Effect of lactic fermentation and extrusion of bean and pea seeds on nutritional and functional properties. *Nahrung-Food, 42*(1), 7-11. doi:Doi 10.1002/(Sici)1521-3803(199802)42:01<7::Aid-Food7>3.3.Co;2-9

Day, L., & Swanson, B. G. (2013). Functionality of Protein-Fortified Extrudates. *Comprehensive Reviews in Food Science and Food Safety, 12*(5), 546-564. doi:10.1111/1541-4337.12023

de Mesa, N. J. E., Alavi, S., Singh, N., Shi, Y.-C., Dogan, H., & Sang, Y. (2009). Soy protein-fortified expanded extrudates: Baseline study using normal corn starch. *Journal of Food Engineering, 90*(2), 262-270. doi:http://dx.doi.org/10.1016/j.jfoodeng.2008.06.032

Dong, A., Huang, P., & Caughey, W. S. (1990). Protein Secondary Structures in Water from 2nd-Derivative Amide-I Infrared-Spectra. *Biochemistry, 29*(13), 3303-3308. doi:DOI 10.1021/bi00465a022

Feldkamp, L.A., Davis, L.C. & Kress, J.W. (1984). Practical cone-beam algorithm. *Journal of Optical Society of America*, 1(6), 612-619.

Guzman-Ortiz, F. A., Hernandez-Sanchez, H., Yee-Madeira, H., San Martin-Martinez, E., Robles-Ramirez, M. D., Rojas-Lopez, M., . . . Mora-Escobedo, R. (2015). Physico-chemical, nutritional and infrared spectroscopy evaluation of an optimized soybean/corn flour extrudate. *Journal of Food Science and Technology-Mysore, 52*(7), 4066-4077. doi:10.1007/s13197-014-1485-5

Guzmán-Ortiz, F. A., Hernández-Sánchez, H., Yee-Madeira, H., San Martín-Martínez, E., Robles-Ramírez, M. d. C., Rojas-López, M., . . . Mora-Escobedo, R. (2015). Physico-chemical, nutritional and infrared

spectroscopy evaluation of an optimized soybean/corn flour extrudate. *Journal of Food Science and Technology, 52*(7), 4066-4077. doi:10.1007/s13197-014-1485-5

Holse, M., Larsen, F. H., Hansen, A., & Engelsen, S. B. (2011). Characterization of marama bean (Tylosema esculentum) by comparative spectroscopy: NMR, FT-Raman, FT-IR and NIR. *Food Research International, 44*(1), 373-384. doi:DOI 10.1016/j.foodres.2010.10.003

Kokini, J. L., Karwe, M., Jaluria, Y., & Wang, S. (1992). Fundamentals of Single and Twin-Screw Food Extrusion. *Abstracts of Papers of the American Chemical Society, 204*, 149-Agfd.

Kong, J., & Yu, S. (2007). Fourier transform infrared spectroscopic analysis of protein secondary structures. *Acta Biochimica Et Biophysica Sinica, 39*(8), 549-559.

Krimm, S., & Bandekar, J. (1986). Vibrational Spectroscopy and Conformation of Peptides, Polypeptides, and Proteins. *Advances in Protein Chemistry, 38*, 181-364. doi:Doi 10.1016/S0065-3233(08)60528-8

Meng, X., Threinen, D., Hansen, M., & Driedger, D. (2010). Effects of extrusion conditions on system parameters and physical properties of a chickpea flour-based snack. *Food Research International, 43*(2), 650-658.

Moraru, C. I., & Kokini, J. L. (2003). Nucleation and Expansion During Extrusion and Microwave Heating of Cereal Foods. *Comprehensive Reviews in Food Science and Food Safety, 2*(4), 147-165. doi:10.1111/j.1541-4337.2003.tb00020.x

Onwulata, C. I., Smith, P. W., Konstance, R. P., & Holsinger, V. H. (2001). Incorporation of whey products in extruded corn, potato or rice snacks☆. *Food Research International, 34*(8), 679-687. doi:https://doi.org/10.1016/S0963-9969(01)00088-6

Patil, S., Brennan, M., Mason, S., & Brennan, C. (2016). The Effects of Fortification of Legumes and Extrusion on the Protein Digestibility of Wheat Based Snack. *Foods, 5*(2), 26.

Pinzer, B.R., Medebach, A., Limbach, H. J., Dubois, C., Stampanoni, M. & Schneebeli, M. (2012). 3D-characterization of three-phase systems using X-ray tomography: tracking the microstructural evolution in ice cream, *Soft Matter*, 8, 4584-4594, doi: 10.1039/C2SM00034B

Rinnan, Å., Berg, F. v. d., & Engelsen, S. B. (2009). Review of the most common pre-processing techniques for near-infrared spectra. *TrAC Trends in Analytical Chemistry, 28*(10), 1201-1222. doi:http://dx.doi.org/10.1016/j.trac.2009.07.007

Schoeman, L., Williams, P. du Plessis, A. & Manley, M. (2016) X-ray micro-computed tomography (μCT) for non-destructive characterisation of food. *Trends in Food Science and Technology*, 47, 10-24. doi: http://dx.doi.org/10.1016/j.tifs.2015.10.016

Appendix

Algorithms used for segmentation and analysis of X-ray data.

Algorithm 1 Segmentation and volume of interest classification

procedure SEGMENTATION(Tomogram Folder)
  for each Tomogram file in Tomogram Folder **do**
    Threshold segmentation
    Standard morphological operations
    Return Segmented Tomogram
    procedure CLASSEFICATION(Segmented Tomogram)
      Filled = Copy(Segmented Tomogram)
      for Number of Iterations **do**
        3 copies of Filled → $Filled_{x,\ y\ and\ z}$
        for each copy of Filled **do**
          for each plan perpendicular to the axis(x,y,z) **do**
            plan wise 2D hole filling of $Filled_{x,\ y\ and\ z}$
          end for
        end for
        Filled = Sum($Filled_x$, $Filled_y$, $Filled_z$)
        Set all values of Filled larger than zero to one
      end for
      Classified Tomogram = Segmented Tomogram + Filled
      Return Classified Tomogram
    end procedure
    Save Classified Tomogram to Tomogram Folder
  end for
end procedure

Algorithm 2 Direction oriented Surface Detection

procedure SURFACE DETECTION(Tomogram Folder)
  for each Classified Tomogram file in Tomogram Folder **do**
    volume = Classified Tomogram
    in volume set all value equal to one to zero
    in volume set all value equal to two to one
    Define six translation direction:
    Translation[[1,0,0], [-1,0,0], [0,1,0], [0,-1,0], [0,0,1], [0,0,-1]]
    for each element in Translation **do**
      $direction_{edges}$ = Copy(volume)
      Shift $direction_{edges}$ one pixel defined by element
      $direction_{edges}$ = volume-$direction_{edges}$
      set all values smaller than zero to zero
    end for
    All_{edges} = sum($+x_{edges}$, $-x_{edges}$, $+y_{edges}$, $-y_{edges}$, $+z_{edges}$, $-z_{edges}$)
  end for
  Return $+x_{edges}$, $-x_{edges}$, $+y_{edges}$, $-y_{edges}$, $+z_{edges}$, $-z_{edges}$, All_{edges}
end procedure

Figure captions for the manuscript Microstructure, texture and secondary protein structure of extruded high protein snacks studied by FT-IR spectroscopy and X-ray tomography

Figure 1: Illustration of the segmentaion, 2D hole filling procedure and of the edge detection procedure.

A) Raw data of tomographic slice. B) Slice after 3D threshold segmentation. C) Slice after applying standard morphological operations; ”largest connected elements”, ”erotion” and ”dilation”. D) The 2D hole filling procedure applied in 3D volume and in three axial directions. The blue dashed squire is the zoomed area of panel G. E) Second iteration of the 2D hole filling procedure which is continued from the 3D volume presented in panel D. The blue dashed squire is the zoomed area of panel H. F) Third iteration and convergences point of the 2D hole filling procedure, which is continued from the 3D volume represented in panel E. The blue dashed squire is the zoomed area of penal I. G) Zoomed area of D displaying an imperfect hole filling. H) High zoom of E. In the center area of H, a small area shows a small imperfection in the hole filling. I) High zoom of F. The small imperfection displayed in panel H is here corrected. J) Left side edge detection which is equivalent to slice 30 of the volume +xedges described in the algorithm of table 2. K) Right side edge detection which is equivalent to slice 30 of the volume −xedges described in the algorithm of Table 2. L) Left and Right side edge detection, which is equivalent to slice 30 of the summed volumes +xedges and −xedges. All values larger then one is set to one in this illustration. M) Up and Down edge detection, which is equivalent to slice 30 of the summed volumes +yedges and −yedges. All values larger than one is set to one in this illustration. N) In- and Out of plane edge detection, which is equivalent to slice 30 of the summed volumes +zedges and −zedges. O) A raw tomographic slice image with two perpendicular planes of all edge volumes summed. In the illustration of alledges, all values larger than zero is set equal to one.

Figure 2 3D visualisation of tomograms of raw and microwave treated extrudates. P (protein content), W (water content), T (process temperature in the extruder die).

Figure 3 A) FT-IR spectra (4000-750cm^{-1}) of raw materials: milled pea granulate and potato flour. The Amid I band (1600-1700cm^{-1}) is indicated and enlarged in the bottom of the figure as the second derivative of the FT-IR spectrum. B) Second derivative of the Amid I band from an FT-IR spectra of extruded pea snacks. The samples are coloured according to SME. C) Score plot from PCA coloured according to SME. D) Corresponding loading plot.

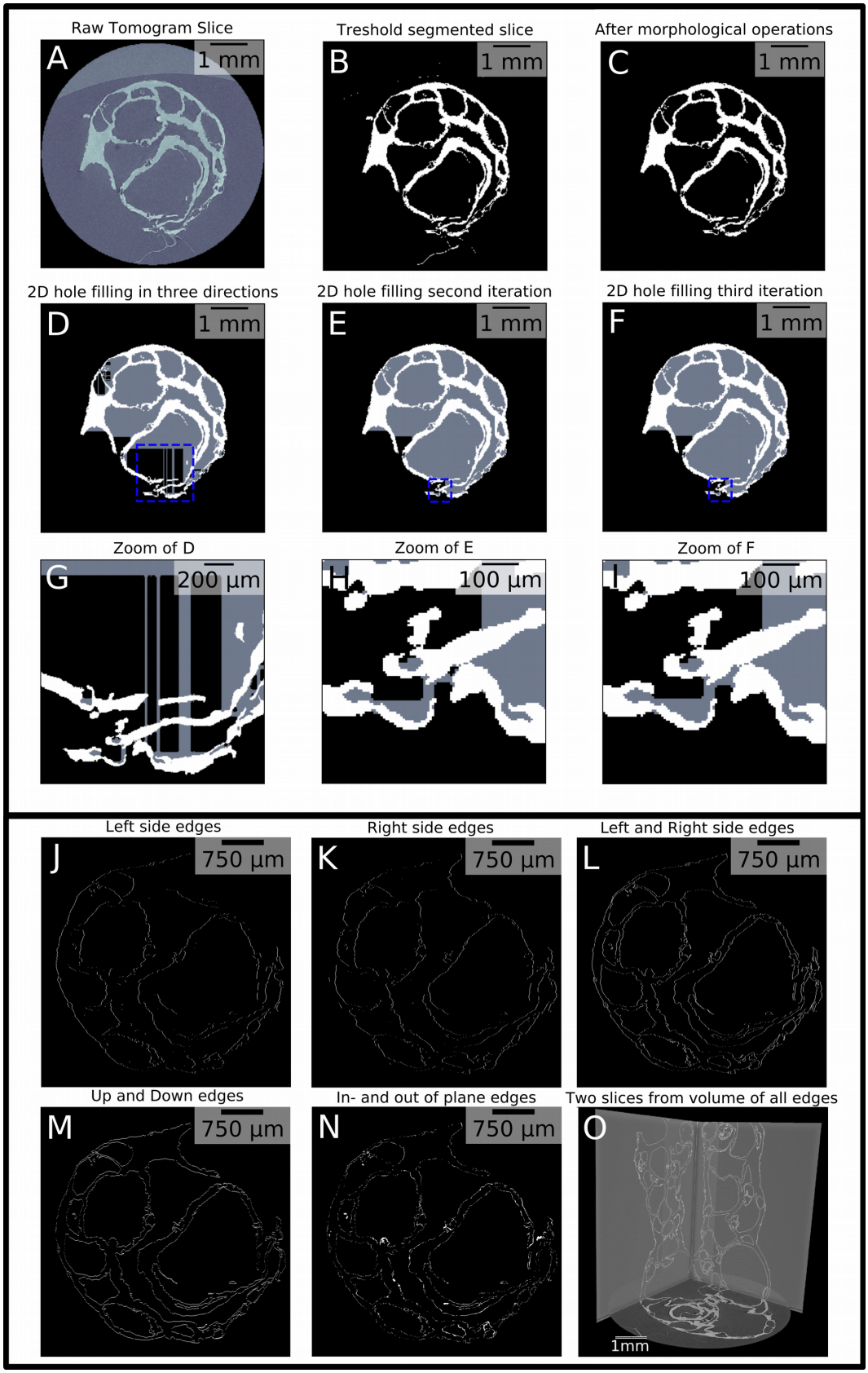
Raw Tomogram Slice
A
1 mm
Treshold segmented slice
B
1 mm
After morphological operations
C
1 mm
2D hole filling in three directions
D
1 mm
2D hole filling second iteration
E
1 mm
2D hole filling third iteration
F
1 mm
Zoom of D
G
200 µm
Zoom of E
H
100 µm
Zoom of F
I
100 µm
Left side edges
J
750 µm
Right side edges
K
750 µm
Left and Right side edges
L
750 µm
Up and Down edges
M
750 µm
In- and out of plane edges
N
750 µm
Two slices from volume of all edges
O
1mm

Raw extrudates

P7-W40-T150

P15-W40-T150

P7-W40-T130

P15-W40-T130

Microwaved extrudates

P7-W40-T130

P7-W40-T150

P7-W23-T130

P7-W23-T150

P15-W40-T130

P15-W40-T150

P15-W23-T130

P15-W23-T150

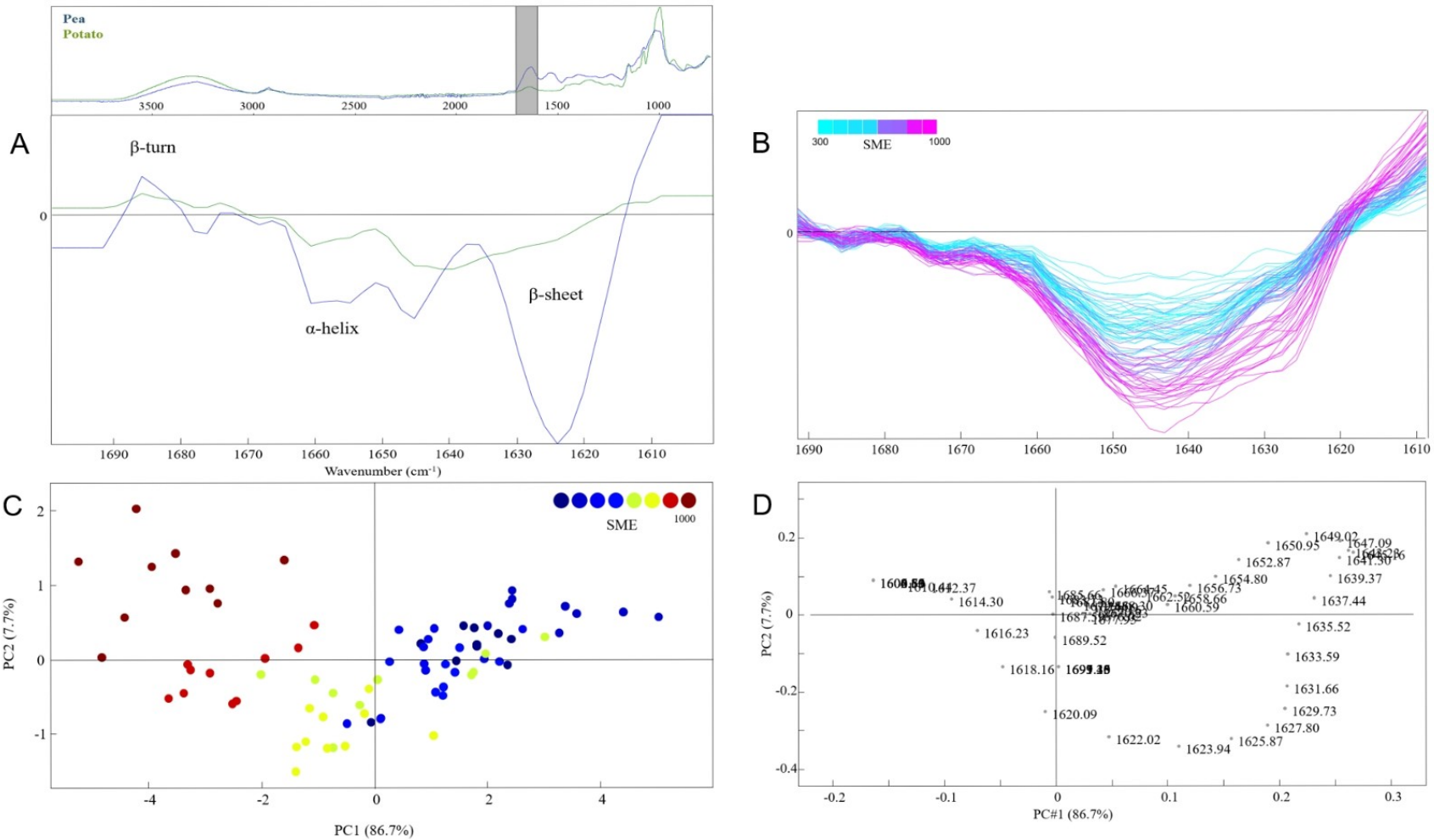
A
Pea
Potato
3500
3000
2500
2000
1500
1000
β-turn
0
β-sheet
α-helix
1690
1680
1670
1660
1650
1640
1630
1620
1610
Wavenumber (cm-1)
B
300
SME
1000
0
1690
1680
1670
1660
1650
1640
1630
1620
1610
C
SME
1000
2
1
0
-1
PC2 (7.7%)
-4
-2
0
2
4
PC1 (86.7%)
D
0.2
0
-0.2
-0.4
PC2 (7.7%)
1649.02
1650.95
1647.09
1652.87
1639.37
1654.80
1656.73
1637.44
1614.30
1660.59
1635.52
1616.23
1689.52
1633.59
1618.16
1631.66
1620.09
1629.73
1627.80
1622.02
1625.87
1623.94
-0.2
-0.1
0
0.1
0.2
0.3
PC#1 (86.7%)

A.2 Article 2 - Three-dimensional architecture of human diabetic peripheral nerves revealed by X-ray phase contrast holographic nanotomography

Three-dimensional architecture of human diabetic peripheral nerves revealed by X-ray phase contrast holographic nanotomography

Lars B Dahlin[1,2†], Kristian R Rix[3†], Vedrana A Dahl[4], Anders B Dahl[4], Janus N Jensen[4], Peter Cloetens[5], Alexandra Pacureanu[5], Simin Mohseni[6], Niels OB Thomsen[2] and Martin Bech[7*]
†=shared first authorship, *=corresponding author

From the [1]Department of Translational Medicine – Hand Surgery, Lund University, Sweden; [2] Department of Hand Surgery, Skåne University Hospital, Malmö, Sweden; [3]Niels Bohr Institute, Copenhagen University, Copenhagen, Denmark; [4]Department of Applied Mathematics and Computer Science, Technical University of Denmark, Lyngby, Denmark; [5]European Synchrotron Radiation Facility, Grenoble, France; [6]Department of Clinical and Experimental Medicine, Linköping University, Linköping, Sweden; [7]Department of Medical Radiation Physics, Clinical Sciences Lund, Lund University, Lund, Sweden;

Corresponding author: martin.bech@med.lu.se

Abstract

The current knowledge of the peripheral nerve structure is based on two-dimensional microscopy techniques offering only a limited understanding of its architecture. The ability to explore in three-dimensions (3D) nerve tissue at sub-cellular scale is instrumental for unraveling the pathophysiology of diseases, such as diabetic neuropathy. Here we demonstrate that X-ray phase contrast holographic nanotomography enables 3D imaging of nerves at high resolution, while covering a relatively large tissue volume. We reveal various subcomponents of human peripheral nerves in biopsies from patients with type 1 and 2 diabetes and in a healthy subject. Together with well organized, parallel myelinated nerve fibers we show regenerative clusters with twisted nerve fibers, a sprouted axon from a node of Ranvier and other specific details. Many of these architectural elements are not described in the literature. Moreover, the technique enables identifying particular effects of diabetes type 1 and 2 on the nerve tissue morphology. These findings provide a basis for deeper understating of diabetic neuropathy and for identifying therapeutic targets.

The delicate structure of peripheral nerves is usually visualized by conventional light and electron microscopy allowing a two-dimensional image of thin tissue slices [1,2]. To further understand dysfunction of the peripheral nervous system due to trauma or disease, a more detailed analysis is required to visualize the cellular network and subcomponents of the nerve trunk. As such, quantitative 3D structural data and images obtained by light or electron microscopical technique followed by alignment procedures, are more relevant, but the procedure is difficult and time-consuming [3]. X-ray phase contrast holographic nanotomography, with a resolution in-between that of light and electron microscope, has recently been used to visualize myelinated nerve fibers and various subcomponents in sciatic nerves of healthy mice [4] with isotropic voxel sizes below 100 nm. Furthermore, other advanced X-ray microscopical techniques have also been used to study teased myelinated nerve fibers from wild type mice and also to map out the element distribution in the myelin sheath (i.e. P, S, Cl, Na, K, Fe, Mn and Cu) [5]. However, such data is mainly restricted to a single isolated neuron. Human peripheral nerves have not previously been visualized by X-ray phase contrast holographic nanotomography, neither from healthy subjects nor from patients with diabetes.

By using X-ray phase contrast holographic nanotomography, we aimed at making a detailed map of the myelinated nerve fibers, including the nodes of Ranvier, and the intricate three-dimensional (3D) anatomical structures in healthy and diabetic human nerves from the upper extremity.

Results

Comparison of microscope images

Histological technique with light and electron microscopy is the standard imaging technique for neuropathology, where thin sections are cut from the sample and studied in a microscope. In this study, we have used X-ray phase contrast holographic nanotomography to study the 3D micro morphology of human peripheral nerves from patients with type 1 and type 2 diabetes as well as from a healthy subject. For details, see Online Methods.

Figure 1 displays a comparison between images obtained with conventional histology with a light microscope (Panels 1a and 1b) and X-ray phase contrast holographic nanotomography (Panels 1c and 1d). Panel 1c displays a single slice of the tomographic X-ray data for direct comparison with the microscopic image in panel 1a, where a thin slice of tissue has been imaged with visible light (i.e. light microscopy). Panels 1b and 1d are magnifications of Panels 1a and 1c, respectively. While the quality of images obtained by light microscope is better than that of X-ray phase contrast holographic nanotomography, these images are limited to two dimensions. The volumetric information obtained from X-ray phase contrast holographic nanotomography allows for slicing the same sample in arbitrary direction (as illustrated in Panel 1e) and creation of 3D renderings (as illustrated in Panel 1f). In addition, browsing through the stack of slices allows for much better identification of morphological features [see Supplementary Figures 1 (S1) and 2 (S2) online]. A node of Ranvier with the adjacent paranode is displayed in three perpendicular virtual

sections in Supplementary Figure 1 (S1). Schmidt-Lantermans incisure is envisioned in a similar manner in Supplementary Figure 2 (S2) online.

Characterization of structures in patients with diabetes and in a healthy subject

Figure 2 displays representative pictures from the X-ray phase contrast holographic nanotomography volumes acquired of samples from patients with diabetes type 1 (Panel 2a and 2b), diabetes type 2 (Panel 2c) and from a healthy subject (Panel 2d).

Peripheral nerve from patient with type 1 diabetes

The specimen of the posterior interosseous nerve from the patient with long-term type 1 diabetes showed a low density of large myelinated nerve fibers (Panels 2a and 2b) relative to the healthy subject (Panel 2d) in agreement with previous work [6]. Smaller myelinated nerve fibers, mainly interpreted as regenerative clusters, were detected in-between the larger myelinated nerve fibers (Panels 2a and 2b). A blood vessel, with less contrast, but with a red blood corpuscle visible, was visualized in the cross section (indicated by a star in Panel 2a). Nodes of Ranvier and Schmidt-Lanterman incisures were also noted [see Supplementary Figures 1 (S1) and 2 (S2), respectively].

Peripheral nerve from patient with type 2 diabetes

The posterior interosseous nerve specimen of the female patient with type 2 diabetes with a shorter duration of diabetes showed a similar density of large myelinated nerve

fibers (Panel 2c) as in the healthy subject (Panel 2d). A smaller number of small myelinated nerve fibers, interpreted as regenerative nerve fibers, was observed in-between the larger myelinated nerve fibers (not shown).

Peripheral nerve from a healthy subject

The specimen of the posterior interosseous nerve from the healthy subject showed a regular and dense distribution of large myelinated nerve fibers (Panel 2d), where the axons and the osmium stained myelin sheaths could clearly be visualized. Medium-sized and small myelinated nerve fibers were also observed in-between the larger myelinated nerve fibers. The structures mentioned above were clearly seen in the 3D volume.

Extraction of morphological data

The semi-automatic segmentation algorithm described in the methods section was applied to the volumetric X-ray phase contrast holographic nanotomography data. Figure 3 displays an example of such segmentation and data extraction on a sample from the patient with type 1 diabetes. Panel 3a displays a single slice of data, where a subset of the larger myelinated nerve fibers has been selected for segmentation. The segmentation algorithm is then applied to the volume, and the resulting segmented fibers can be analyzed and visualized (Panels 3b and 3c). The small myelinated fibers, identified as regenerative clusters and visualized in Panels 3d and 3e, reveal an intertwining of the axons [further visualized in panel 3f and in the Supplementary movie (S3) online], which is completely different from the appearance of normal myelinated nerve fibers with the waveform in the same fascicle. Note that in panel 3e,

two different regenerative clusters are segmented, separated by a thin layer of connective tissue. Thus, there was no intertwining between these two clusters as can be clearly seen in Supplementary movie S3 online.

Regeneration event

In the specimen from the patient with type 1 diabetes, a microanatomical structure, interpreted as a regenerative event, was found (Figure 4). A normal myelinated nerve fiber was found together with a node of Ranvier, but a bulb of myelin with a ”dead end” was observed attached to one of the paranodes (Panel 4a). We interpret the structure to be a degenerated myelinated nerve fiber, with the myelin bulb still attached, from which a new axon has sprouted and become myelinated. Cross sections from the tomography are shown in Figure 4 panels (b-g). In slice 210 (panel 4b), a normal axon is found (arrowhead). A new regenerating axon with myelin is formed in slice 280 (panel 4c; arrow). The regenerating axon (arrow) is leaving the original axon (arrowhead) in slice 320 (panel 4d) and mature in slice 385 (panel 4e; arrow). In slice 450 (panel 4f), the new regenerating axon with myelin (arrow) is visible next to the degenerated axon (arrowhead), which is still seen in slice 490 (panel 4g; arrowhead). A video of all the slices in the volume presented in figure 4 is available as supplementary information online (Supplementary fig S4).

In Supplementary Figure 5 (S5) an electron microscopical image is added to show two different Schwann cells with a similar feature as presented in Panel 4g (slice 490).

Discussion

The present study has demonstrated the potential of X-ray holographic nanotomography to visualize the cellular and subcellular structures of human peripheral nerves. Quantitative three-dimensional (3D) structural data, which can be related to conventional two-dimensional images, is important to further understand the pathophysiology and the detailed cellular networks of peripheral nerves in diabetic neuropathy. By the use of osmium tetroxide staining, it is possible to distinguish between the axon and the surrounding myelin sheath as well as to identify substructures of the nerve fibers, such as the nodes of Ranvier, with their paranodes and paranodal remodelling [7], and Schmidt-Lanterman incisures [4], with the goal to evaluate structural alterations in diabetic neuropathy. In view of the potential use of different imaging techniques, such as synchrotron based X-ray microscopy [4,5,8] and other microscopy techniques [9], we were able to show detailed structures of a peripheral nerve, using biopsies from the posterior interosseous nerve in the upper extremity in a healthy human subject and in patients with type 1 and 2 diabetes [10,11]. Structural alterations in the sural nerve in type 1 and 2 diabetes, characterized by demyelination, degeneration and regeneration events of myelinated nerve fiber with changes in fiber density [12] and with remyelination remodeling found at the paranodal region [7], have previously been studied by conventional light and electron microscopical techniques, which only allows limited dimensional analyses [10,13-15]. We showed degeneration in the patient with type 1 diabetes, which is in agreement with an earlier study on the same nerve biopsies [6]. As in previously published work by Bartels et al [4] from mouse sciatic nerve, the 3D details of human myelinated nerve fibers, such as nodes of Ranvier, including the paranode, and Schmidt-Lanterman

incisures, were observed in the present study. Due to the contrast discrepancies between the osmium stained myelinated nerve fibers and the intraneural blood vessels [13,16], it was not possible to perform a 3D structure of the intraneural microvasculature with the segmentation technique. However, we could visualize one of the blood vessels, including blood corpuscles, with thickened basement membrane in the specimen from the patient with type 1 diabetes. To further characterize intraneural microvasculature in the future, specimens without osmium staining are needed.

Interestingly, we were able to show the detailed 3D structure of the regenerative clusters with intertwining of the nerve fibers; i.e. ”misdirected” outgrowing nerve fibers, in the patient with type 1 diabetes in contrast to the normal appearance of the myelinated wave-formed nerve fibers in the fascicle found in the healthy subject. Intertwining can only be observed with 3D imaging techniques, and has to our knowledge never earlier been described, where it even in the specimen was possible to define two adjacent clusters with thin connective tissue in-between. Such a detailed 3D visualization of pathological alterations at the cellular level in diabetic neuropathy is not possible with conventional imaging techniques.

A remarkable novel finding was the observation in the patient with type 1 diabetes, where a myelinated nerve fiber with its paranodes and node of Ranvier, and with an attached myelin bulb, representing remodeling, was found. We interpret this finding as a degenerating myelinated nerve fiber, with a remaining part observed as a bulb, and a new outgrowing, and remyelinated, axon originated from the nearby paranode. This structure has never been described in 3D or interpreted correctly with conventional light or electron microscopical techniques as shown in Supplementary

Figure 5 (S5); thus, demonstrating the potential of the present technique. Furthermore, with the segmentation at hand, a number of quantitative parameters can be extracted for statistical analysis. Even the thickness of the myelin sheath can be extracted (see Panel 1f).

Conclusions

This is the first study to use X-ray phase contrast holographic nanotomography to visualize human myelinated nerve fibers and their subcomponents in 3D. We are able to present novel findings on differences between a healthy subject and patients with type 1 and 2 diabetes, in which the 3D structure of regenerative clusters with twisted nerve fibers and a novel detailed 3D view of a sprouted axon were visualized. We believe that X-ray phase contrast holographic nanotomography in the future can provide new insights into the pathophysiology of not only diabetic neuropathy, but also of other pathological conditions.

Methods

Patients and nerve biopsies

From a previous study, on nerve biopsies from the posterior interosseous nerve [10,11], we randomly selected, a healthy subject and patients with type 1 and 2 diabetes. According to our previously described technique [11], a biopsy of the posterior interosseous nerve was harvested from the dorsal side of the distal forearm at the same time as the patient underwent carpal tunnel release [10,11]. The patients solely had carpal tunnel syndrome with compression of the median nerve, and no history of trauma to the posterior interosseous nerve. The nerve biopsies were immersion fixed

as described earlier [14] and post-fixed in osmium for visualization of the myelinated nerve fibers as well as embedded in Epon [14]. From the previous study cohort, one sample from each patient category was selected; i.e. a male healthy subject (age span 55-60 years; present HbA1c 4.7 %; 28.0 mol/mmol; nerve conduction study on the lower extremity showing no polyneuropathy), a female patient with type 1 diabetes (age span 50-55 years; duration of diabetes >40 years; present HbA1c 6.9%; 50.0 mol/mmol; nerve conduction study on the lower extremity showing polyneuropathy) and a female patient with type 2 diabetes (age span 60-65 years; duration of diabetes >10 years; present HbA1c 9.0%; 75.0 mol/mmol; nerve conduction study on the lower extremity showing no polyneuropathy).

X-ray phase contrast holographic nanotomography

Epon embedded nerve samples were imaged at the nano-imaging beamline ID16A-NI at the European Synchrotron Radiation Facility (ESRF). An X-ray beam of 17 keV photon energy was focused with an elliptic Kirkpatrick-Baez optics system as described by da Silva et al [17] and Mokso et al [18]. Four tomographic scans at different sample-to-focus distances have been acquired for each sample. For each rotational angle, the four recorded projections were combined to obtain a phase map which was then used for tomographic reconstruction [19]. The effective pixel size was 130 nm, resulting in a reconstructed volume of 2048*2048*2048 voxels of isotropic voxels, covering a 266*266*266 μm^3 field of view.

Segmentation

For quantitative analysis and visualization, the axons illustrated in Figures 1f and 3 were segmented by fitting surfaces to the CT data using a semi-automated approach. In the obtained volumetric data, the nerve fibers are aligned with the z direction, and myelin sheaths appear circular in the x-y slices through the volume. This allowed us to perform a slice-wise segmentation of an individual fiber by aligning a closed curve with the periphery of the nerve. For this, the circle is initialized around the nerve, and is automatically moved to the boundary of the myelin, utilizing the fact that myelin appears dark compared to the background. For segmenting a whole fiber, the curves are automatically propagated trough the volume, such that the surface moves only slightly between the slices, and is in every slice attracted to the boundary of the myelin layer. The approach is similar to the method from Dahl et al [20]. Trough inspection, we ensured that nerves are precisely segmented. We performed a few manual corrections when needed.

Acknowledgements

The project was supported by grants from Lund University, Region Skåne, Funds from Skåne University Hospital, Sydvästra Skånes Diabetesförening, the Swedish Diabetes Foundation, the Crafoord Foundation and the Swedish Research Council (Medicine and Natural science). Especially thanks to Professors Pekka Suorti and Bill Tomlinson for advice during the initial phase of the study and to Veronique Mayeux at ESRF for administrative support. MB acknowledge the Swedish research council for Project Research Grant for Junior Researcher #E0605401. This project was supported by the MAX4ESSFUN subproject of EU interreg project “ESS & MAX IV: Cross

Border Science and Society". The authors acknowledge ESRF for providing beamtime for the proposal MD898.

Author contributions

Collection and preparation of nerve biopsies: NOBT, SM and LBD. Design and concept of study: LBD and MB. Data acquisition and reconstruction: LBD, PC, AP and MB. Data analysis: KRR, VAD, ABD and JNJ. Writing manuscript: LBD, KRR, VAD, SM and MB. All authors have read and corrected the final version of the manuscript.

Ethics

The nerve biopsy procedure was approved by the Ethical Review Board at Lund University as part of a larger research project. Informed consent was obtained from all participants. All observations were performed on coded samples.

Competing financial interests

The authors have nothing to disclose.

References

1 Blaurock, A. E. Myelin x-ray patterns reconciled. *Biophys. J.* **16**, 491-501 (1976).

2 Waxman, S. G., Kocsis, J. D. & Stys, P. K. *The Axon. Structure, function and pathophysiology.*, (Oxford University Press Inc, 1995).

3 Berthold, C. H. & Rydmark, M. Electron microscopic serial section analysis of nodes of Ranvier in lumbosacral spinal roots of the cat: ultrastructural organization of nodal compartments in fibres of different sizes. *J. Neurocytol.* **12**, 475-505 (1983).

4 Bartels, M., Krenkel, M., Cloetens, P., Mobius, W. & Salditt, T. Myelinated mouse nerves studied by X-ray phase contrast zoom tomography. *J. Struct. Biol.* **192**, 561-568 (2015).

5 Ducic, T. *et al.* Structure and composition of myelinated axons: a multimodal synchrotron spectro-microscopy study. *J. Struct. Biol.* **173**, 202-212 (2011).

6 Osman, A. A., Dahlin, L. B., Thomsen, N. O. & Mohseni, S. Autophagy in the posterior interosseous nerve of patients with type 1 and type 2 diabetes mellitus: an ultrastructural study. *Diabetologia* **58**, 625-632 (2015).

7 Thomas, P. K. *et al.* Paranodal structure in diabetic sensory polyneuropathy. *Acta Neuropathol* **92**, 614-620 (1996).

8 Fratini, M. *et al.* Simultaneous submicrometric 3D imaging of the micro-vascular network and the neuronal system in a mouse spinal cord. *Sci Rep* **5**, 8514 (2015).

9 Scopel, J. F. *et al.* Are human peripheral nerves sensitive to X-ray imaging? *PLoS One* **10**, e0116831 (2015).

10 Thomsen, N. O., Mojaddidi, M., Malik, R. A. & Dahlin, L. B. Reduced myelinated nerve fibre and endoneurial capillary densities in the forearm of diabetic and non-diabetic patients with carpal tunnel syndrome. *Acta Neuropathol* **118**, 785-791 (2009).

11 Thomsen, N. O., Mojaddidi, M., Malik, R. A. & Dahlin, L. B. Biopsy of the posterior interosseous nerve: a low morbidity method for assessment of peripheral nerve disorders. *Diabet. Med.* **26**, 100-104 (2009).

12 Hur, J., Sullivan, K. A., Callaghan, B. C., Pop-Busui, R. & Feldman, E. L. Identification of factors associated with sural nerve regeneration and degeneration in diabetic neuropathy. *Diabetes Care* **36**, 4043-4049 (2013).

13 Llewelyn, J. G., D.R., T. & Thomas, P. K. in *Peripheral neuropathy* (eds P.J. Dyck & Thomas P.K.) 1951-1991 (Elesevier Saunders, 2005).

14 Malik, R. A. *et al.* Sural nerve fibre pathology in diabetic patients with mild neuropathy: relationship to pain, quantitative sensory testing and peripheral nerve electrophysiology. *Acta Neuropathol. (Berl).* **101**, 367-374 (2001).

15 Mohseni, S. Neurologic damage in hypoglycemia. *Handb Clin Neurol* **126**, 513-532 (2014).

16 Thrainsdottir, S. *et al.* Endoneurial capillary abnormalities presage deterioration of glucose tolerance and accompany peripheral neuropathy in man. *Diabetes* **52**, 2615-2622 (2003).

17 da Silva, J. C. *et al.* Efficient concentration of high-energy x-rays for diffraction-limited imaging resolution. *Optica* **4**, 492-495 (2017).

18 Mokso, R., Cloetens, P., Maire, E., Ludwig, W. & Buffiére, J. Y. Nanoscale zoom tomography with hard x rays using Kirkpatrick-Baez optics. *Appl Phys Lett* **90**, 144104 (2007).

19 Cloetens, P. *et al.* Holotomography: Quantitative phase tomography with micrometer resolution using hard synchrotron radiation x rays. *Applied physics letters* **75**, 2912-2914 (1999).

20 Dahl, V. A. *et al.* Automatic measurement of orbital volume in unilateral coronal synostosis. *Biomedical Imaging (ISBI), 2016 IEEE 13th International Symposium*, 889-893 (2016).

Figures

Figure 1

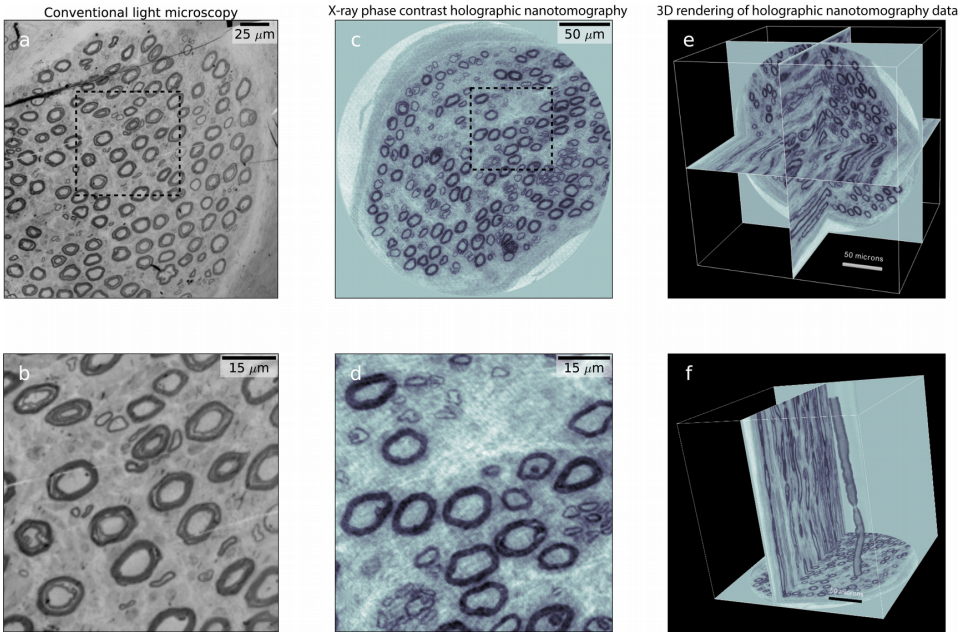

Figure 1. Comparison between conventional light microscopy and X-ray phase contrast holographic nanotomography. a) Light microscopy image of a physical slice of a nerve sample. b) Enlargement of the sample area marked in (a). c) Digital slice from a 3D volume imaged by X-ray phase contrast holographic nanotomography. d) Enlargement of area marked in (c). e) Visualization of three perpendicular planes of the X-ray data volume. f) Visualization of two perpendicular planes and a 3D rendering of a single axon with a node of Ranvier visible.

Figure 2

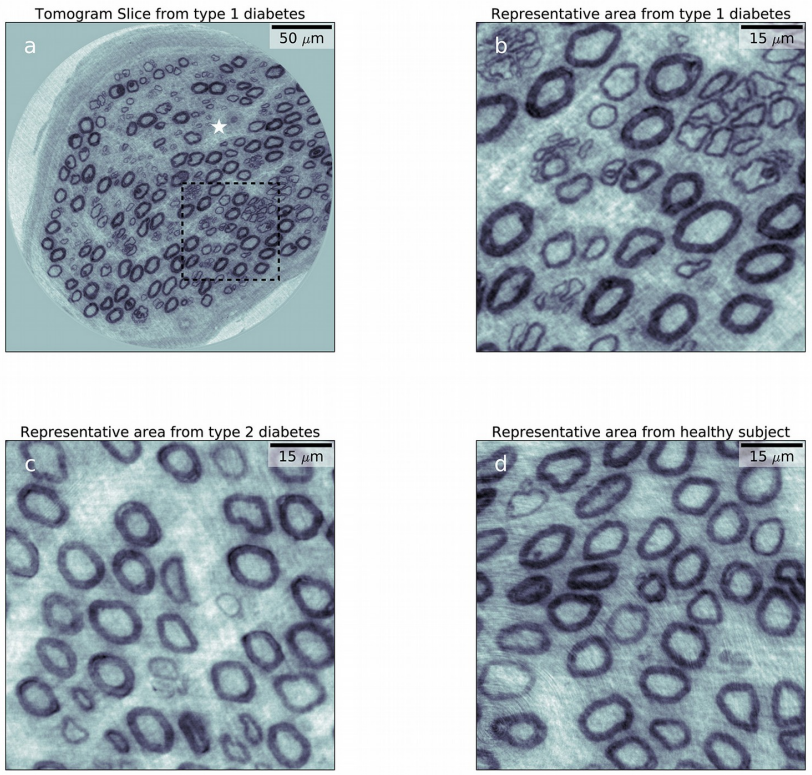

Figure 2. Representative sample areas from subject with type 1 diabetes, with type 2 diabetes and a healthy subject. a) Full view of digital slice from subject with type 1 diabetes. The star marks a blood vessel containing a red blood cell. b) Enlargement of the selected representative area marked in (a). c) Representative area of subject with type 2 diabetes. d) Representative area of healthy subject.

Figure 3

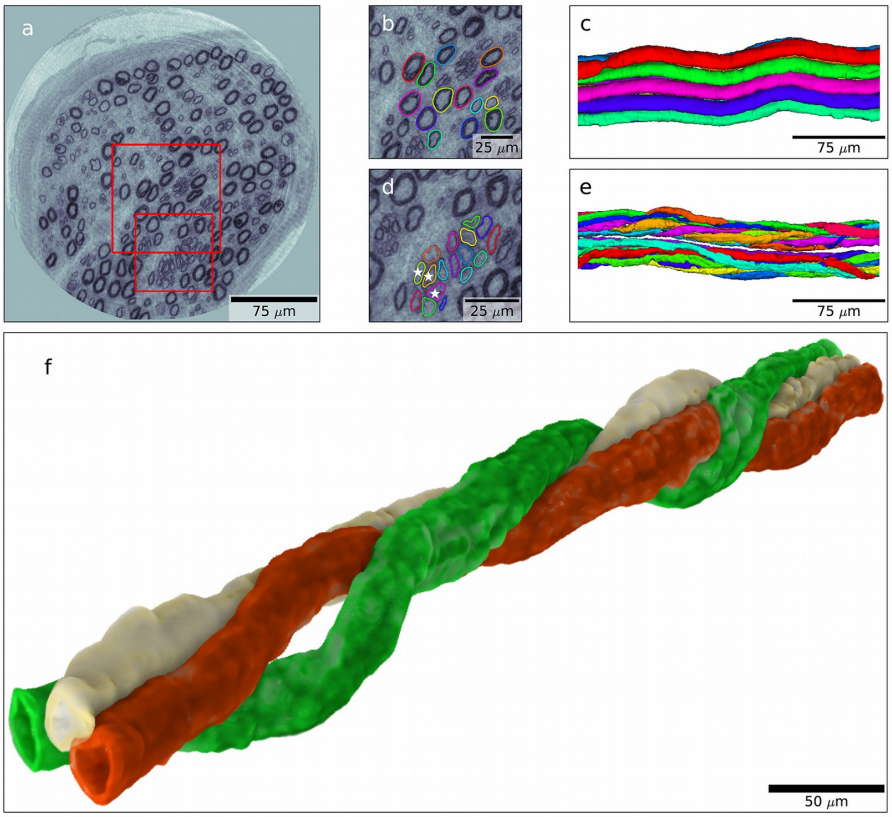

Figure 3. Examples of semi-automatic segmentation. a) Tomographic slice through the data volume of the subject with type 1 diabetes. b) Enlarged area marked by a large red square in (a). Colored rings mark the segmented nerves calculated by our semi-automated algorithm. c) 3D rendering of the segmented nerves marked in (b). d) Enlargement of area marked by small red square in (a). Clusters of regenerated axons are segmented by our semi-automated algorithm. e) 3D rendering of the segmented nerves clusters segmented in (d). f) 3D volume rendering of the three axons marked by stars in (d). Note how one axons twists around the other two.

Figure 4

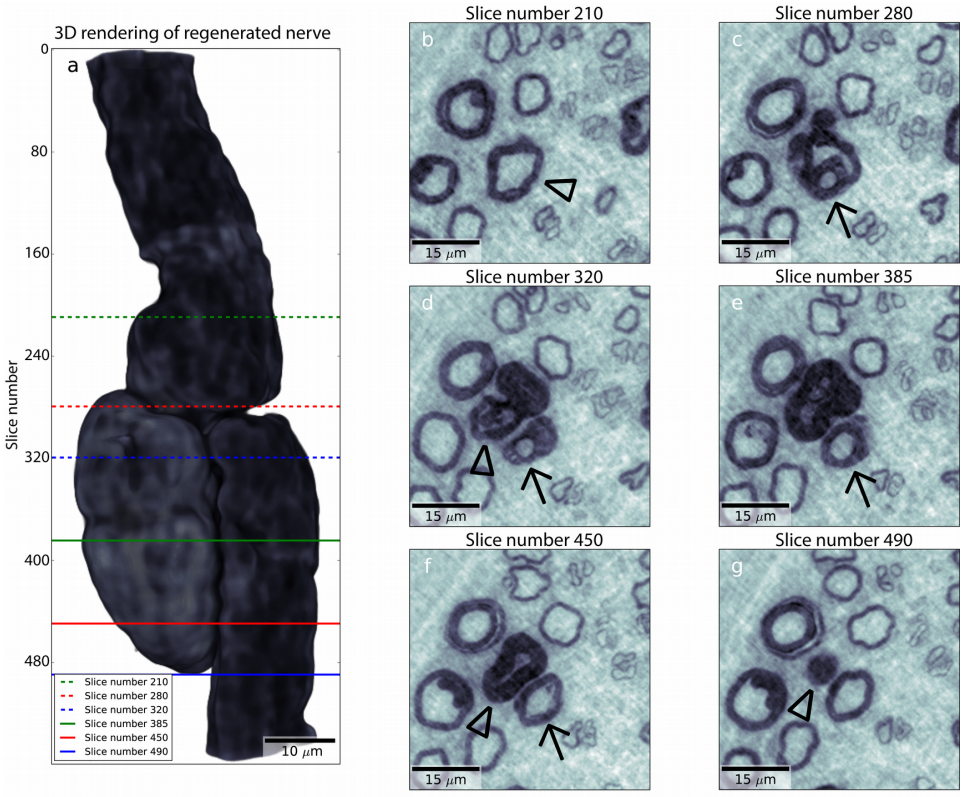

Figure 4. Visualization of regenerative event. a) 3D rendering showing only the abnormal axon. The regeneration event is visualized in panels (b) – (g), indicated by lines in panel (a). Arrow: regenerating axon. Arrowhead: original axon.

Supplementary material to article 2 - Three-dimensional architecture of human diabetic peripheral nerves revealed by X-ray phase contrast holographic nanotomography

Supplementary information

Three-dimensional architecture of human diabetic peripheral nerves revealed by X-ray phase contrast holographic nanotomography

Lars B Dahlin[1,2†], Kristian R Rix[3†], Vedrana A Dahl[4], Anders B Dahl[4], Janus N Jensen[4], Peter Cloetens[5], Alexandra Pacureanu[5], Simin Mohseni[6], Niels OB Thomsen[2] and Martin Bech[7*]
†=shared first authorship, *=corresponding author

From the [1]Department of Translational Medicine – Hand Surgery, Lund University, Sweden; [2] Department of Hand Surgery, Skåne University Hospital, Malmö, Sweden; [3]Niels Bohr Institute, Copenhagen University, Copenhagen, Denmark; [4]Department of Applied Mathematics and Computer Science, Technical University of Denmark, Lyngby, Denmark; [5]European Synchrotron Radiation Facility, Grenoble, France; [6]Department of Clinical and Experimental Medicine, Linköping University, Linköping, Sweden; [7]Department of Medical Radiation Physics, Clinical Sciences Lund, Lund University, Lund, Sweden;

Corresponding author: martin.bech@med.lu.se

Supplementary information

Supplementary figure 1.

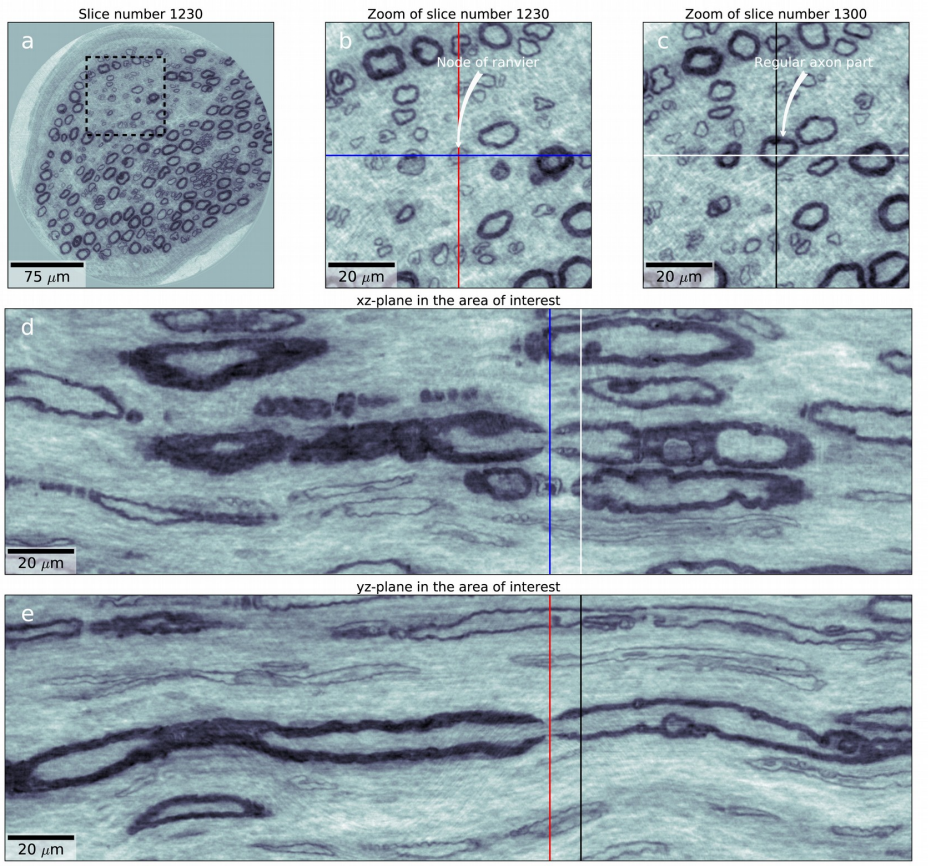

Supplementary figure 1. Illustration of a node of Ranvier. a) Digital slice from data volume containing a node of Ranvier. b) Enlargement of the area marked in (a) with the node of Ranvier marked by an arrow. c) Slice parallel to that displayed in (b), but separated by 9.1µm. d) The xz-plane perpendicular to the slices in panels (b) and (c). Two colored lines show where the planes intersect. e) The yz-plane perpendicular to the slices in panels (b), (c) and (d). Two colored lines show where the plane intersect the slices in panels (b) and (c).

Supplementary figure 2.

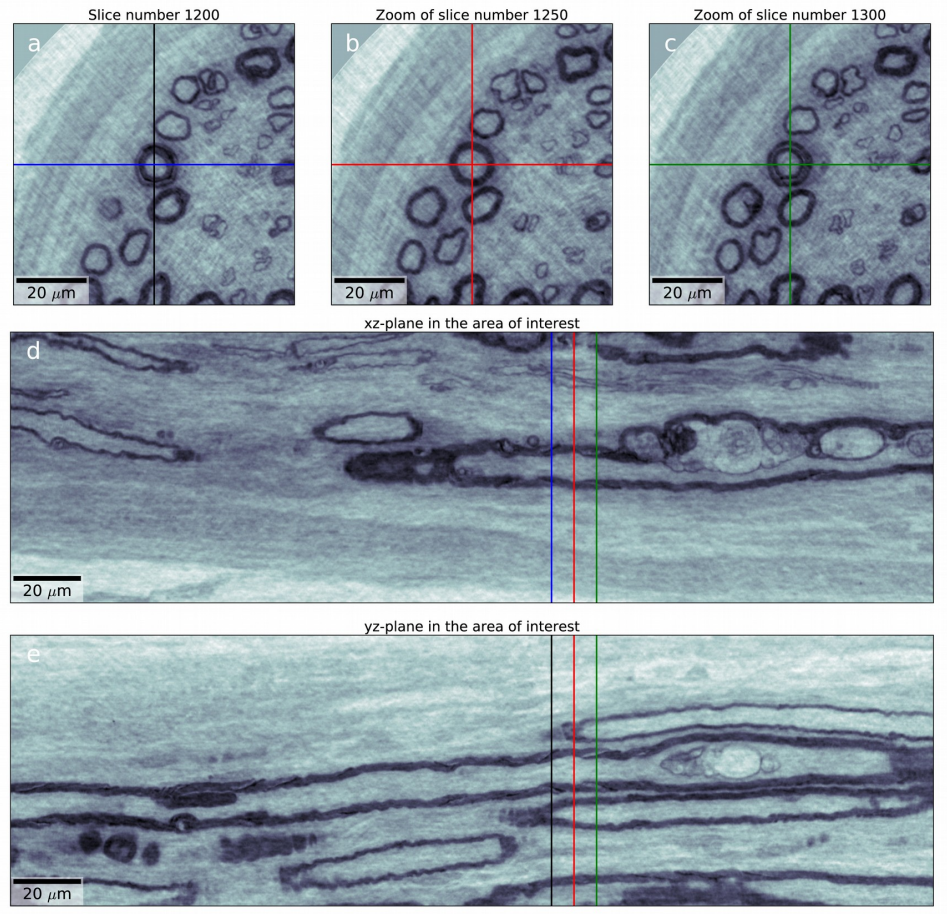

Supplementary figure 2. Illustration of a Schmidt-Lantermans incisure. a) Digital slice 1200 from data volume containing Schmidt-Lantermans incisure. The nerve fiber containing the Schmidt-Lantermans incisure is marked by the intersection of two colored lines. b) and c) Slices parallel to (a) separated by 6.5µm. d) The xz-plane perpendicular on the slices in panels (a), (b) and (c). Three colored lines show where the plane intersects the slices in panels (a), (b) and (c). e) The yz-plane perpendicular to the slices in panels (a), (b), (c) and (d).

Supplementary figure 3. Video

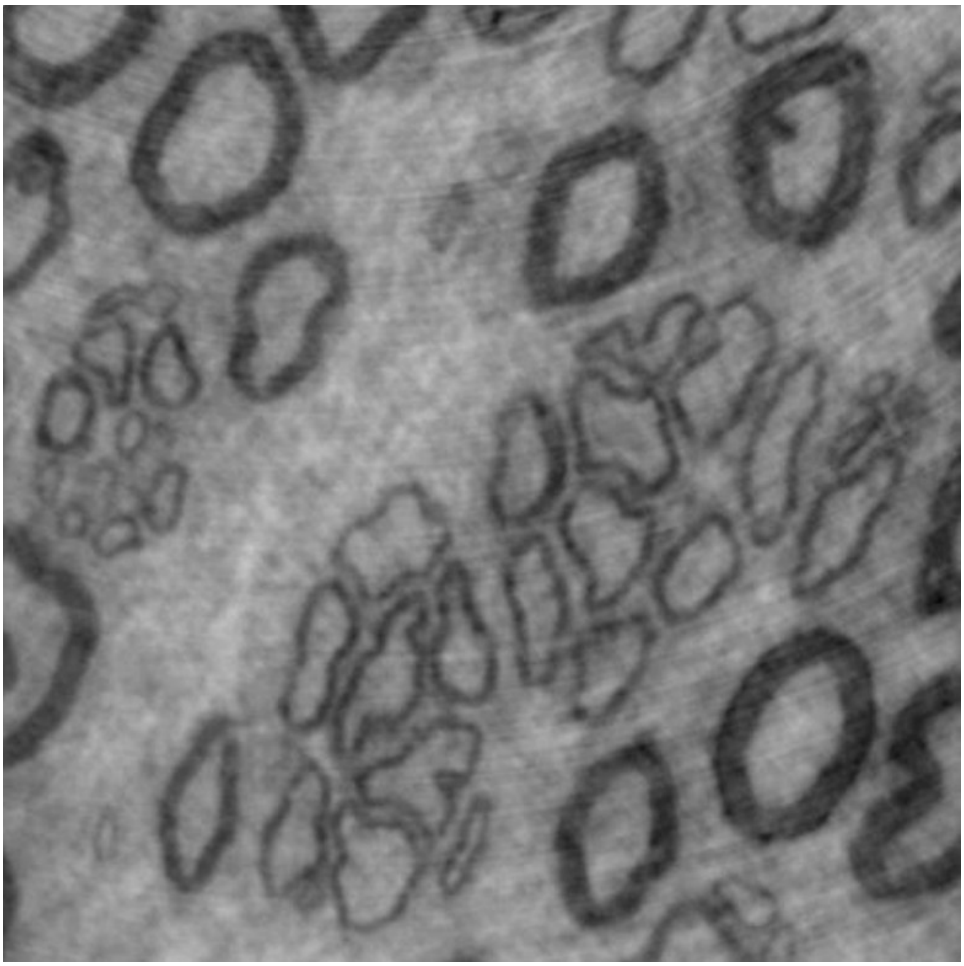

Supplementary figure 3. Video illustrating the intertwining axons in the regenerating clusters. Voxel size 130 nm x 130 nm x 130 nm.

Supplementary figure 4. Video

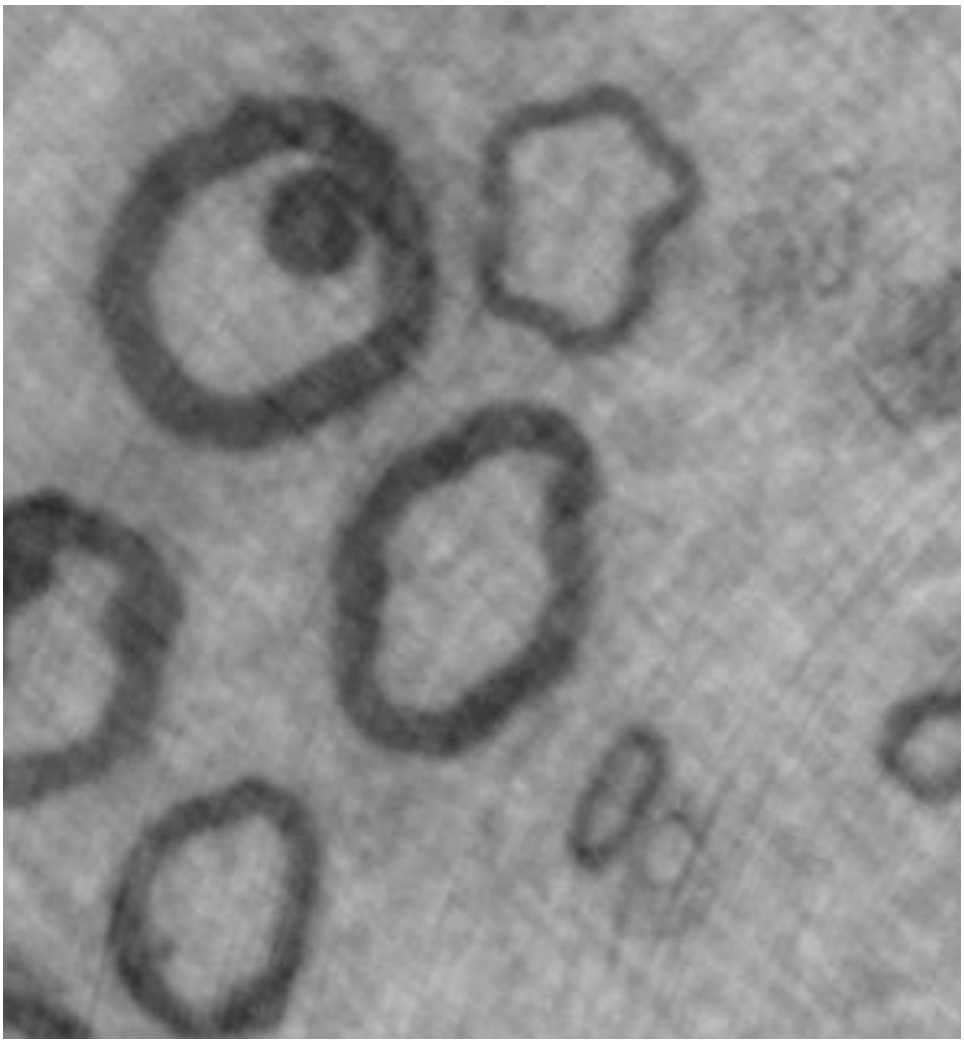

Supplementary figure 4. Video illustrating the regeneration event described in figure 4.

The most interesting biological events appear at the following times:

At time 0-10 second (at the central part of the picture) there is a normal myelinated axon.

At second 11; two axons are separated from each other by myelin.

At second 13; a small axon is identified to the lower right with some myelin around, and a big axon to the left of it. Here a small myelinated axon is “born”.

At second 13.5; a node in the small axon appears.

At second 13.5-15; the small axon is getting more myelin.

At second 17, a normal myelinated axon of the small one,

At the end of second 23, the small axon is now a very nicely myelinated, and the larger axon starts to degenerate.

At second 24; only some myelin is left of the larger axon.

At second 26; the larger axon and its myelin is gone, and does not appear in the rest of the movie.

Supplementary figure 5.

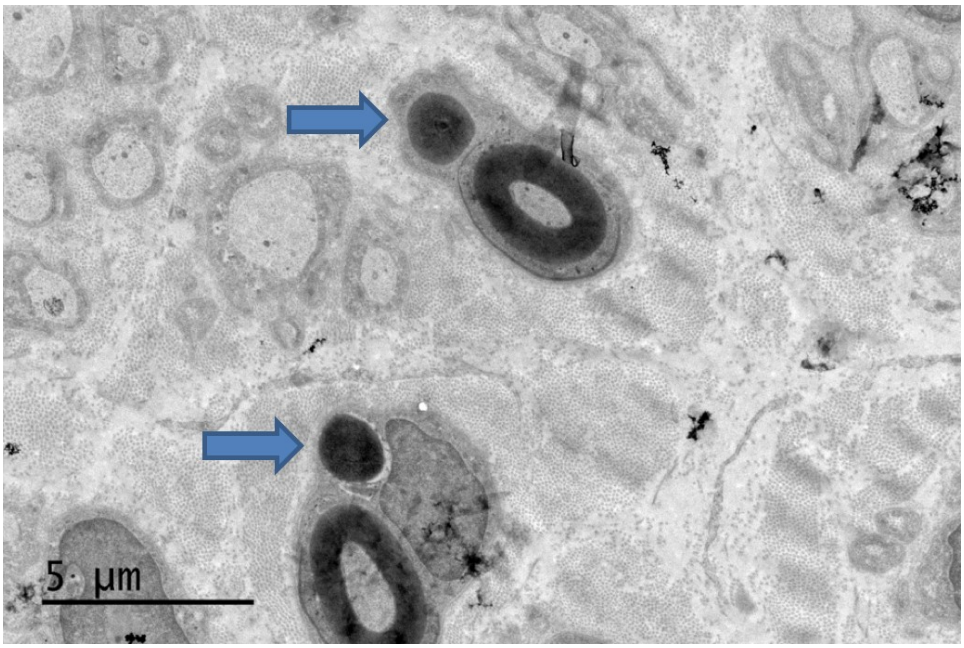

Supplementary figure 5. Electron microscopy image showing two normal myelinated axons, each with a Schwann cell. The Schwann cells also include myelin structures (arrows) that are unrelated to the axons. This is similar to that observed in Figure 4g (slice 490) and in the Supplementary video 4 at seconds 24 - 26, where the degenerated myelinated axon is sealed.

A.3 Article 3 - Super resolution x-ray phase-contrast and dark-field imaging with a single 2D grating and electronic source stepping

Super resolution x-ray phase-contrast and dark-field imaging with a single 2D grating and electronic source stepping

Kristian R. Rix[1], Tao Shen[2] and Martin Bech[3]

[1]University of Copenhagen, Niels Bohr Institute, X-ray and Neutron Science, Universitetsparken 5, 2100 København Ø, DK
[2]Karlsruher Institut für Technologie (KIT) Karlsruhe, Baden-Württemberg, D
[3]Lund University, Medical Radiation Physics, Barngatan 4, Skånes Universitetssjukhus, Lund, S

E-mail: krix@nbi.ku.dk, gustav.tao@gmail.com and martin.bech@med.lu.se

March 2018

Abstract. Here we report a method for increased resolution of single exposure three modality x-ray images using Super Resolution. The three x-ray image modalities are Absorption-, Differential Phase Contrast- and Dark Field-images. To use the Super Resolution algorithm a none mechanical movable micro focus x-ray source is applied. A series of almost identical x-ray projection images is obtained while the micro focus point source is translated a small random amount, in two directions. The three different image modalities are obtained using the so-called spatial harmonic analysis based on Fourier Analysis. The Blind Super Resolution algorithm is then applied to the three different series separately resulting in a higher resolution for each modality.

1. Introduction

The development of x-ray imaging setups has accelerated over the last decade. The improvements in x-ray microscopy and Talbot grating interferometers (Momose et al. 2003), (David, Nöhammer, and Solak 2002) - with hardware such as micro- and nano-focus x-ray tubes have been a catalyst for this. Also different imaging modalities like Differential Phase Contrast (DPC) achieved with the coded-aperture technique explained by Olivo and Speller (2007) and Dark-Field (DF) modality first realized with the Talbot interferometer by Pfeiffer et al. (2008) has become increasingly available in the laboratory.

In most imaging applications the image quality is evaluated by resolution and contrast as the most important factors to consider. This is why enhancement of image resolution and contrast is an ongoing process by optimizing and developing appropriate hardware. Using the Talbot interferometer as a base, new enhancements have recently been achieved, for example a motionless electromagnetic phase stepping approach was

demonstrated by Harmon et al. (2014). Other closely related methods such as the Speckle-Based approach described by Zanette et al. (2014) and the single shot method developed by Wen et al. (2010) can be categorized as non-scanning techniques. Here we present a resolution enhancement method for the three image modalities achievable through image analysis and algorithms.

2. Methods and setup

Our method is a combination of three well documented procedures, these being Spatial Harmonic Analysis (SHA) also recognized as a Single shot imaging (Wen et al. 2010), a 2D motionless stepping approach similar to that of Harmon et al. (2014) and image enhancement by the so-called Blind Super Resolution (BSR) algorithm (Šroubek, Flusser, and Cristóbal 2007).

The SHA method achieves DPC- and DF imaging by a 2D transmission grating and a micro focus source to minimize blurring. The x-ray refraction and diffraction in a sample is measured as variations in the 2D fringes pattern created by the grating. This is realized in the Fourier space where the information of the refraction and diffraction is found in the 1^{st}-order harmonics from which the DPC- and DF images is reconstructed. This reconstruction is the Spatial Harmonic Analysis.

Motionless electromagnetic phase stepping described by Harmon et al. (2014) is a variation of the Talbot-Lau interferometer. In regular Talbot-Lau interferometry three gratings create a fringe pattern on the detector. By stepping one of the gratings and acquiring three or more images, the DPC- and DF images can be reconstructed. In the motionless electromagnetic phase stepping approach the mechanical stepping of the grating is replaced by electromagnetic coils used to step the source point in 1D, effectively creating the same image modalities as mechanical stepping. Here we apply a similar source, however with a 2D stepping feature.

The Super Resolution algorithm is a mathematical method which uses a series of slightly different images of lower resolution to create one of higher resolution. This is achieved through sub-pixel translation and mapping of the lower resolution images onto a high resolution array and then interpolate the missing values. However this method is only practical if you know the exact relative translation of the low resolution images. To account for that, a correlation function is applied allowing the change in the image to be random. Hence the name *Blind Super Resolution*.

This combined method is realized by a custom made Excillum micro focus source, where the point source is movable due to a variable and finely tunable magnetic field which is applied to the electron beam in the x-ray tube. The source spot size is $5\mu m$ FWHM. Furthermore three additional components are used in this setup. All are illustrated in figure 1a. Here a 2D grating with a checkerboard pattern of $36\mu m$ period is used as a coded aperture. Then the sample of interest is illuminated and imaged by the detector: A Hamamatsu CMOS flat panel sensor C7921SK-25 of $50\mu m$ pixel size. From a single projection image the three contrast modalities can be retrieved through SHA method.

2.1. Single shot x-ray phase-contrast imaging

The spatial harmonic analysis is also recognized as a Single shot imaging method, as the method produces three images of different contrast modalities with a single exposure of the object of interest. However this is on the expense of resolution compared to scanning methods, e.g. Pfeiffer et al. (2008) or the newer Speckle scanning method by Zhou et al. (2015). The single shot method works using a numerical Fourier transform on the recorded projection. Illustrations of such a transformation is seen in figure 1c. The 0^{th}-order harmonic contains the absorption information. The absorption image is retrieved by extracting a square with the 0^{th}-order harmonic in its center. The square size MxM is defined by the number of pixels the grating period extends over in the image. In our setup the full grating period spans 10 pixels and is denoted (P_{pixels}). The projection image is 1000x1000 pixels where N is 1000. The MxM square size is determined by; $M = N/P_{pixels} = 100$. This is the maximum size of the square as this is considered to be the limit where there is no overlap between 0^{th}- and 1^{st}-order harmonic information as illustrated in figure 1c. Therefore the square size defines the size of the absorption image as the absorption image is created from absolute value of the inverse Fourier Transform of the 0^{th}-order harmonic. This is normalized with a reference image calculated in the same manner to retrieve the absorption image:

$$\textbf{Absorption-image} = \frac{\mathcal{F}^{-1}[S_{(0,0),s}]}{\mathcal{F}^{-1}[S_{(0,0),r}])} \tag{1}$$

Here $[S_{(0,0),s}]$ and $[S_{(0,0),r}]$ is the extrated 0^{th}-order harmonics of the measurements with sample and reference respectively. The reference correction is the same approach as used in Talbot interferometer setup (Pfeiffer et al. 2008). The division operation is done pixel wise. Evidently the resolution of the absorption image is significantly reduced compared to the original projection as the dimensions are given as MxM pixels.

The 1^{st} order harmonics contain the phase-information in perpendicular directions. Due to the characteristics of the grating which is a checkerboard pattern, the discrete peaks in the 1^{st}-order spatial frequency domain is in the $(-1, 1)$ and $(1, 1)$ position as illustrated in figure 1c. This means that the phase contrast is sensitive in one of the two diagonals of a DPC-image depending on which of the 1^{st}-order harmonics ($(-1, 1)$ and $(1, 1)$) are considered. Due to the symmetry of the Fourier transformation, the information in $(-1, 1)$ is identical to $(1, -1)$ and $(1, 1)$ is equivalent to $(-1, -1)$. By defining a square of size MxM around one of the 1^{st}-order harmonic, the maximum information is achieved without overlapping with the 0^{th}-order harmonic information as seen in figure 1c. The DPC-image is then retrieved by an inverse Fourier transformation of the 1^{st}-order harmonic, followed by pixel wise extraction of the angle of each complex value. The same procedure is used on the reference and then subtracted to obtain the differential phase as follows:

$$\textbf{DPC-image} = angle(\mathcal{F}^{-1}[S_{(-1,1),s}]) - angle(\mathcal{F}^{-1}[S_{(-1,1),r}]) \tag{2}$$

Here $[S_{(-1,1),S}]$ and $[S_{(-1,1),r}]$ is the information containing the 1^{st}-order harmonic with sample and reference measurement respectively. The angle operation is done pixel wise.

The DF-image is made from both the 0^{th}- and 1^{st}-order harmonic. The image is calculated as stated by the Talbot approach (Pfeiffer et al. 2008) follows:

$$\textbf{DF-image} = \frac{\mathcal{F}^{-1}[S_{(-1,1),r}] \cdot \mathcal{F}^{-1}[S_{(0,0),r}]}{\mathcal{F}^{-1}[S_{(-1,1),s}] \cdot \mathcal{F}^{-1}[S_{(0,0),s}])} \tag{3}$$

The multiplication and division operations are done pixel wise. Illustrations of absorption, phase contrast- and dark field images are given in 1d.

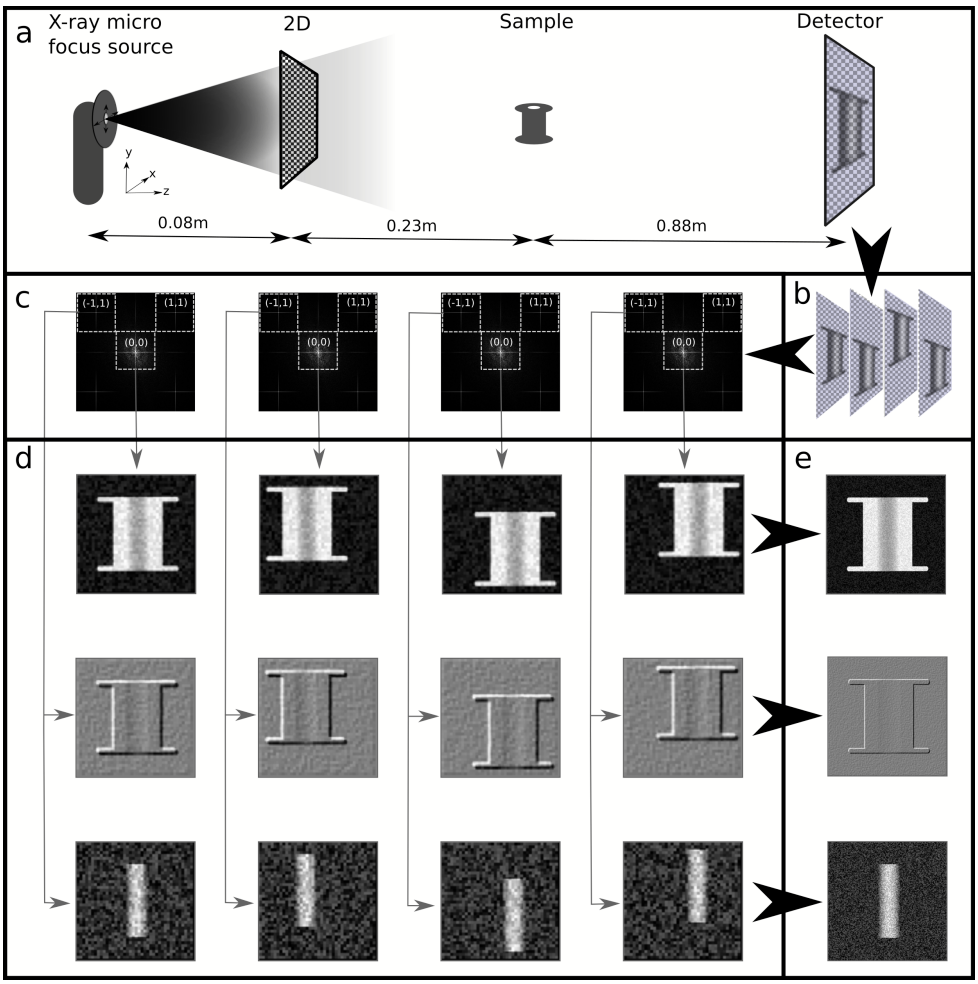

Figure 1. Illustration of how blind super resolution is adapted for x-ray imaging using spatial harmonic analysis. a) The experimental setup which consists of a custom made Excillium A2 source. This is a micro focus source were the position of the point source is movable without using mechanical parts. b) Fourier space illustration of four projections, seen in (c). c) Illustration of four projections, where the point source is in different positions. d) Illustration of the absorption, phase contrast and dark field images extracted from (b). e) Illustration of combining the low resolution examples using the blind super resolution algorithm for all three modalities.

2.2. Blind super resolution

To reduce the loss in resolution by the single shot method, the blind super resolution (BSR) method was implemented. The BSR method is described in detail in Šroubek, Flusser, and Cristóbal (2007) and is developed for increasing the resolution in normal digital photographs.

The setup to create such images is illustrated in fig 1a. The arrows on the source indicates that the point source is movable. With the Excillum source it is possible to slightly deflect the electron beam by tuning the electro-magnetic coils acting on the electron beam. The applied field can be manipulated such that the beam is deflected in the two perpendicular directions to the beam. Consequently this means that the point source is moved a small amount in a given direction defined by the size and direction of the magnetic deflection field. It is possible to control the electron beam very precisely and hence to predict how much a given sample will move on the detector. However, a random movement is sufficient as the BSR method includes an image correlation function to adjust for any translation. Here size and direction (in 2D) of the generated magnetic field is changed randomly for every exposure, as illustrated in figure 1b. In practice we make sure that the sample only translate within tree pixels in any directions. Here a matlab tool† is used to apply the BSR-algorithm. Illustrations from measurement over analysis to final result of the method are made as a flowchart in figure 1(a-e).

3. Results

Here two different samples are used to demonstrate the method. Both samples are displayed in figure 2. Six wooden sticks and two polymer spheres are positioned in figure 2 as they were mounted in the setup for easy comparison. In the setup the wood stick sample is mounted so that two sticks are oriented vertically while the others are roughly at 45 degree angle to the vertical direction. Considering the sample of "wood sticks" the imaging result is seen in figure 3. In panel 3f an absorption image obtained from the single short method is seen. Evidently the resolution here is low as expected from the single shot method. Using the BSR algorithm the resolution is increased as seen in panel 3g. This is highlighted in the zoom panels 3h and 3i. The increase in resolution is made from 17 images, which is the minimum of required images to achieve the theoretical increase of resolution by a factor of 4†. The theoretical increase in resolution is given by:

$$R = \lceil \sqrt{n_{im}} \rceil - 1 \tag{4}$$

Here $\lceil \ \rceil$ is the "ceil function" and n_{im} is the number of images. ‡ The SR-factor is the desired increase in resolution, which is equivalent to R in eq. 4. The PSF size is an estimate of the blur in the images.

†Matlab Tool for Blind Super resolution version 1.0 by Filip Šroubek September 27, 2006

‡Good results have been achieved using a superresolution(SR)-factor of four, PSF size of [3,3] and only two iterations. All other parameters of the algorithm are set to their default values.

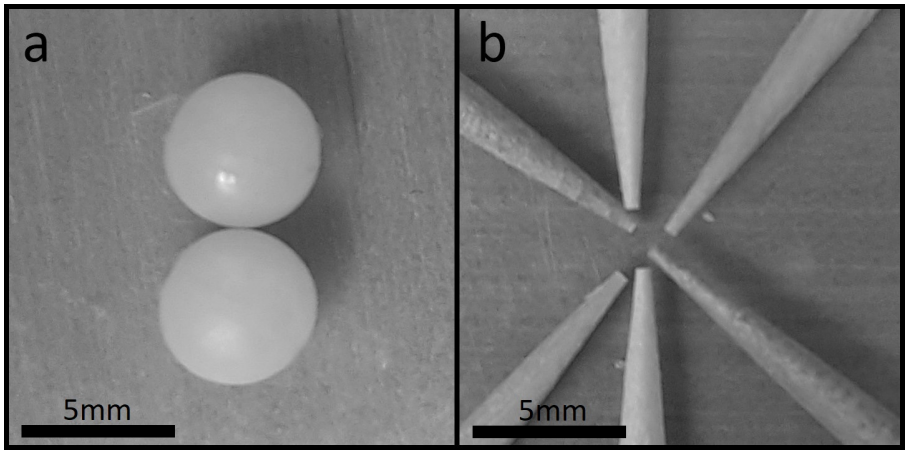

Figure 2. Photograph of six wooden sticks and two polymer spheres used as samples.

The DF-image modality retrieved from the single shot image method is seen in figure 3a. This method is more sensitive in the direction affiliated with the orientation chosen in the Fourier space. Here a much more pronounced and distinctive signal is seen in the diagonal direction chosen. In the vertical and opposing diagonal direction a less significant but still clear signal is observed. Panels 3b and 3c shows the BSR-enhancement in the two perpendicular directions (1,1) and (-1,1). A clear enhancement of resolution is here observed from the digital zoom in panels 3d and 3e. Finally, the DPC-image modality retrieved from the single shot image method is displayed i panel 3j. Similar to the DF-image the DPC-image has a distinctive signal in the direction corresponding to the chosen Fourier direction. Here only the wood sticks in the chosen diagonal direction can be seen. However with the BSR enhancement displayed in panels 3k and 3l the vertical wood sticks also become visible due to the resolution improvement. Again the increase of resolution by the BSR algorithm is highlighted by a digital zoom in panels 3m and 3n.

The x-ray images of the polymer spheres are displayed in figure 4. The majority of the features observed for the wooden sticks are also observed for the polymer spheres. However the distinct features of the direction defined in the Fourier space is less pronounced in both the DF- and DPC-modality as only a small part of the sphere is oriented at 45 degrees. One very significant result of the polymer sphere measurement is the BSR enhancement of the DPC-modality. In the original single shot DPC-image, displayed in panel 4j, it is very difficult to determine the shape of sample. With the BSR enhancement the sphere shape is evident. It is however difficult to determine if this is a result of better signal to noise ratio or a result of the BSR enhancement achieving sub-pixel features.

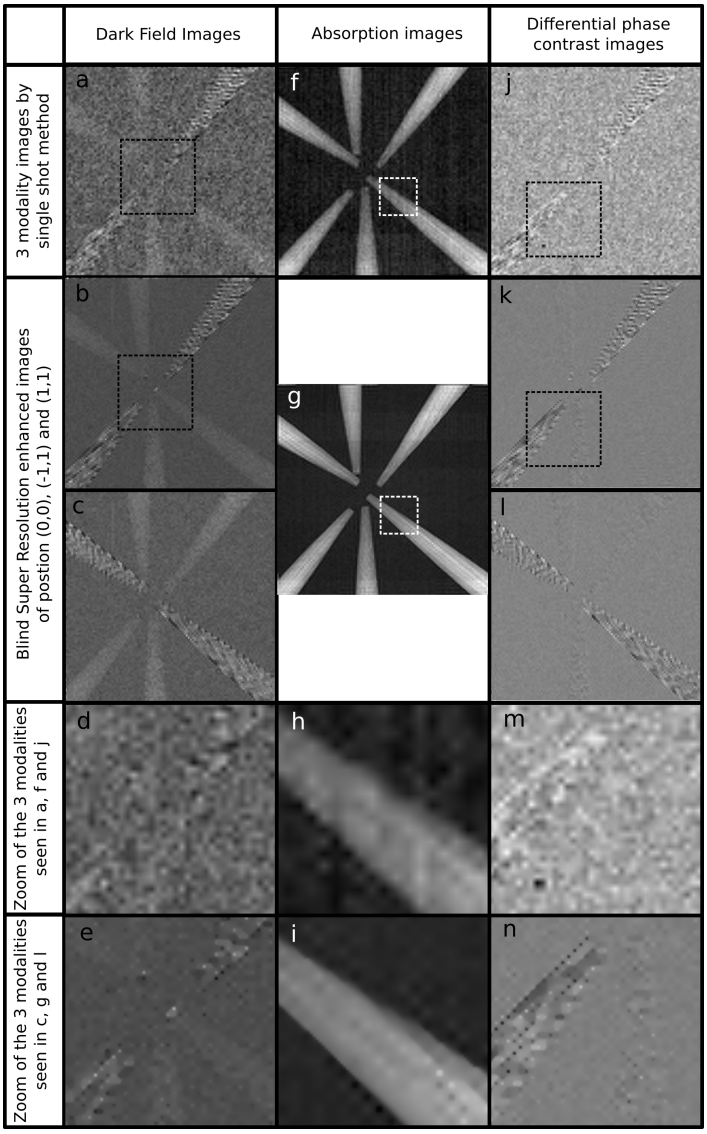

Figure 3. Combining single shot imaging and Blind Super Resolution to image wooden sticks. a) DF-image in the (-1,1) direction obtained from the single shot method. b) BSR enhanced DF-image in the (-1,1) direction c) BSR enhanced DF-image in the (1,1) direction. d) Digital zoom of a (marked by dashed square). e) Digital zoom of b. f) Absorption image obtained from the single shot method. g) BSR enhanced absorption image. h) Digital zoom of f. i) Digital zoom of g. j) DPC-image in the (-1,1) direction obtained from the single shot method. k) DPC-image in the (-1,1) direction. l) BSR enhanced DPC-image in the (1,1) direction. m) Digital zoom of j. n) Digital zoom of k.

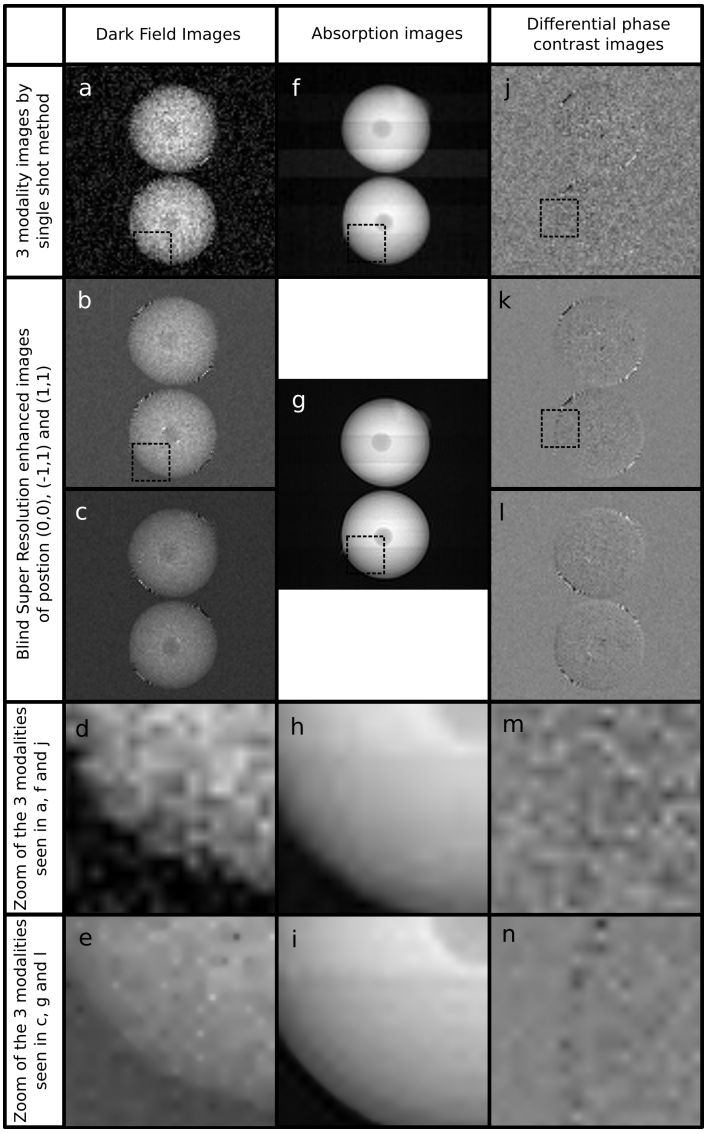

Figure 4. Combining single shot imaging and Blind Super Resolution to image two polymer spheres. a) DF-image in the (-1,1) direction obtained from the single shot method. b) BSR enhanced DF-image in the (-1,1) direction c) BSR enhanced DF-image in the (1,1) direction. d) Digital zoom of a (marked by dashed square). e) Digital zoom of b. f) Absorption image obtained from the single shot method. g) BSR enhanced absorption image. h) Digital zoom of f. i) Digital zoom of g. j) DPC-image in the (-1,1) direction obtained from the single shot method. k) DPC-image in the (-1,1) direction. l) BSR enhanced DPC-image in the (1,1) direction. m) Digital zoom of j. n) Digital zoom of k.

4. Discussion and conclusion

It is possible to generate high resolution DPC and DF images with very precise stepping setups, such as the Talbot-Lau interferometer. However due to the relative alignment between the gratings in these systems, the sensitivity from vibrations and different kinds of drift is substantial. For the single shot method mechanical drift is not an issues as no mechanical stepping is required and only one grating is necessary. The drawback of the single shot method is that the method drastically reduces resolution compared to the stepping setups.

In this paper we have demonstrated that it is possible to overcome some of resolution loss from the single shot imaging method with no increased demand for stability. This can be done using a BSR-algorithm. The decrease in resolution by factor of 10 could be changed in an alternate setup, where the distance between grating and detector would be smaller. This will make the resolution decrease from the single shot method smaller and also enhance the signal to noise ratio. Including such improvements will further reduce the loss in resolution of the single shot method. A higher geometric magnification will however decrease the sample field-of-view.

The method presented here is extremely reliable as it is insensitive to both short or long term instabilities and thermal drift. This is because this approach is based on geometrical change from image to image. In the present work, these changes have been implemented randomly with the only restriction being a maximum extend of induced beam shift. This restriction of the maximum beam shift could be removed, but is included here to reduce the computational time of the BSR-algorithm.

Even though enhancement of the setup and also development of better aimed algorithms could improve the method, these results demonstrate a very applicable and reliable technique.

References

David, C., B. Nöhammer, and H. H. Solak (2002). "Differential x-ray phase contrast imaging using a shearing interferometer". In: *Applied Physics Letters* (cit. on p. 1).

Harmon, Katherine J et al. (2014). "Motionless electromagnetic phase stepping versus mechanical phase stepping in x-ray phase-contrast imaging with a compact source". In: *Physics in Medicine and Biology* (cit. on p. 2).

Momose, Atsushi et al. (2003). "Demonstration of X-Ray Talbot Interferometryn". In: *Japanese Journal of Applied Physics* (cit. on p. 1).

Olivo, A and R Speller (2007). "Modelling of a novel x-ray phase contrast imaging technique based on coded apertures". In: *Physics in Medicine and Biology* (cit. on p. 1).

Pfeiffer, F. et al. (2008). "Hard-X-ray dark-field imaging using agrating interferometer". In: *Nature Materials* (cit. on pp. 1, 3, 4).

B Appendix B - Secondary Publication

B.1 Article 4 - Injection of high dose botulinum-toxin A leads to impaired skeletal muscle function and damage of the fibrilar and non-fibrilar structures

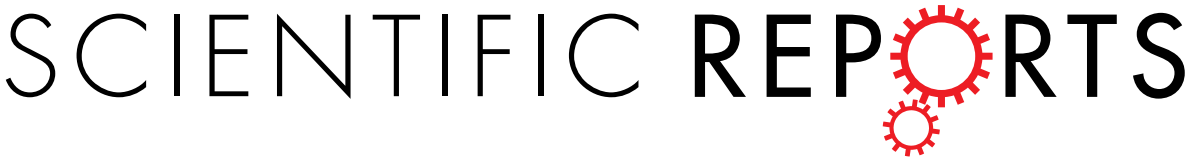

OPEN

Injection of high dose botulinum-toxin A leads to impaired skeletal muscle function and damage of the fibrilar and non-fibrilar structures

Received: 18 April 2017
Accepted: 20 October 2017
Published online: 07 November 2017

Jessica Pingel[1], Mikkel Schou Nielsen[2], Torsten Lauridsen[2], Kristian Rix[2], Martin Bech[3], Tine Alkjaer[1], Ida Torp Andersen[1], Jens Bo Nielsen[1] & R. Feidenhansl[2,4]

Botulinum-toxin A (BoNT/A) is used for a wide range of conditions. Intramuscular administration of BoNT/A inhibits the release of acetylcholine at the neuromuscular junction from presynaptic motor neurons causing muscle-paralysis. The aim of the present study was to investigate the effect of high dose intramuscular BoNT/A injections (6 UI = 60 pg) on muscle tissue. The gait pattern of the rats was significantly affected 3 weeks after BoNT/A injection. The ankle joint rotated externally, the rats became flat footed, and the stride length decreased after BoNT/A injection. Additionally, there was clear evidence of microstructural changes on the tissue level by as evidenced by 3D imaging of the muscles by Synchrotron Radiation X-ray Tomographic Microscopy (SRXTM). Both the fibrillar and the non-fibrillar tissues were affected. The volume fraction of fibrillary tissue was reduced significantly and the non-fibrillar tissue increased. This was accompanied by a loss of the linear structure of the muscle tissue. Furthermore, gene expression analysis showed a significant upregulation of COL1A1, MMP-2, TGF-b1, IL-6, MHCIIA and MHCIIx in the BoNT/A injected leg, while MHVIIB was significantly downregulated. In conclusion: The present study reveals that high dose intramuscular BoNT/A injections cause microstructural damage of the muscle tissue, which contributes to impaired gait.

Botulinum toxin (BoNT/A) is among the most potent toxins to humans that are known[1,2]. One gram of crystalline preparation of BoNT/A can potentially kill 1.000.000 people. In several incidents its use as a biological weapon has been attempted[3]. Nevertheless, BoNT/A is the first biological toxin that has been licensed for treatment of human disease after the pioneering work of the ophthalmologist Alan Scott who used BoNT/A for the treatment of strabismus[4]. Today, the list of diseases that are treated by using BoNT/A is long and includes cervical dystonia[5], blepharospasm[6], urinary incontinence[7], anal fissure[8] and numerous movement disorders[9], including cerebral palsy[10], migrane[11], depression[12], mandibular recontouring[13] and, fascial wrinkles[14]. Furthermore, BoNT/A continues to be the most common minimally invasive procedure performed by plastic surgeons and has during the past decade grown into a billion dollar industry[15].

BoNT/A injection is also commonly used against the development of contractures in patients with central motor lesions. However, only a few studies have investigated the effect of BoNT/A injections on the muscle at tissue level. Skeletal muscle consists of the contractile proteins myosin and actin, which are incorporated into thick and thin filaments, respectively. Together they form arrays in longitudinally repeated banding patterns termed sarcomeres. Sarcomeres in series form myofibrils, and many parallel myofibrils exist in each fiber. A muscle contraction occurs when an action potential reaches the presynaptic terminal of a motor neuron. This activates voltage-dependent calcium channels and allows calcium ions to enter the neuron. Calcium ions bind to proteins (synaptotagmin) on synaptic vesicles, triggering vesicle fusion with the cell membrane and subsequent neurotransmitter release from the motor neuron into the synaptic cleft. The motor neurons then release acetylcholine (ACh), which diffuses across the synaptic cleft and binds to nicotinic acetylcholine receptors (nAChRs) on the cell membrane of the muscle fiber, also known as the sarcolemma. The binding of ACh to the receptor

[1]Center for Neuroscience, University of Copenhagen, Copenhagen, Denmark. [2]Niels Bohr Institute, University of Copenhagen, Copenhagen, Denmark. [3]Medical Radiation Physics, Clinical Sciences, Lund University, Lund, Sweden. [4]Present address: European XFEL, Hamburg, Germany. Correspondence and requests for materials should be addressed to J.P. (email: jpingel@sund.ku.dk)

depolarizes the muscle fiber, and triggers a series of molecular events that includes the binding of calcium to the muscle-regulatory proteins, and causes the interaction between myosin and actin filaments, and subsequently the formation of cross-bridges causing muscle contraction.

Botulinum toxin works by blocking the release of acetylcholine from presynaptic motor neurons, and this chemical denervation causes a cascade of downstream events in the muscle thus causing muscle paralysis[16]. BoNT/A asserts its effect by proteolysis of the SNARE protein synaptosyme-associated protein of 25 kDa (SNAP25) in the synapses of the motor neurons[17]. SNAP25 is a cytoplasmic protein, which is crucial in the fusion between the membranes of the vesicles containing ACh and the cell membrane at the axon terminal. When BoNT/A is injected into muscle tissue, the proteolysis of SNAP25 prevents the exocytosis of ACh, and effectively leads to muscle paralysis[2,18,19].

Muscle atrophy has been noted as a common side effect as a result of denervation[20,21]. Furthermore, considerable fiber atrophy has been observed after BoNT/A (5–10 UI) injections into the longissimus dorsi muscle of rabbits[22]. One rat study investigated changes in different muscle proteins after BoNT/A injections (dosage of 5 units/kg body weight) and observed that the expression of various proteins changed after injection when compared to saline injections[23]. In fact, thirty-eight proteins were associated with alterations of energy metabolism, contractile function of the muscle, transcription and translation, cell proliferation and cellular stress response[23]. In addition, intramuscular BoNT/A injections (Each dose was 6 U/kg, in a 100 µL volume) have been shown to induce significant changes of fiber type composition with a shift from faster to slower isoforms[24]. Nonetheless, it is still unclear whether or not the fibrillar structure of the muscle fibers is damaged as a result of BoNT/A injections. To resolve this issue a 3D visualizations of the tissue is required. Standard lab-based X-ray tomography does not have the sufficient X-ray brilliance to resolve the details of tissue at microstructural level within a reasonable time frame. However, Synchrotron Radiation X-ray Tomographic Microscopy (SRXTM) dramatically improves the sensitivity within biomedical applications[25,26]. The tunable-energy monochromatic beam allows us to achieve high sensitivity to small variations in mass densities. This makes SRXTM well-suited for imaging biological tissue in contrast to conventional X-ray CT[25]. Within medical science, the modality has been successfully applied to study the microstructure of a range of tissues such as the 3D brain anatomy in murine model[27], the microvascular network and thrombi in hepatocellular carcinoma[28] and hyaline cartilage in human knees[29]. Hence, the SRXTM is ideal for the purpose to monitor tissue changes in muscles after high dose BoNT/A injections. In this study, x-ray attenuation and phase contrast was taken into consideration by implementation of the Paganin approach[30]. The aim of the present study was to explore the effects of high dose intramuscular BoNT/A injections on healthy muscle tissue using SRXTM. This was done to confirm whether or not the muscle tissue maintained its integrity and microstructure following BoNT/A injections. In Fig. 1 an example of a 3D reconstruction of the fibrillar and the non-fibrallar tissue is shown for a BoNT/A injected muscle and the corresponding control. The scale is 400 µm × 400 µm × 700 µm. It is clearly seen that the BoNT/A injection causes significant changes in the microstructure of the tissue. Most obvious is that the ratio between fibrillary and non-fibrillar tissue changes and that the linear structure of the muscle tissue is lost. In order to quantify these changes we calculate the volume fraction of the fibrillary tissue and the isotropy index as defined below. As secondary study aims we also investigated the effects of high dose BoNT/A injections on both the gait pattern and the gene expression profile in healthy rats.

Results

Volume fraction. The muscle tissue organization was severely affected by the BoNT/A injections 3 weeks after injection (Figs 1 and 2) of 20 pg BoNT/A per muscle head (60 pg in total). The amount of the fibrillar tissue significantly decreased ($p = 0.02$), while the non-fibrillar tissue was significantly increased ($p = 0.02$).

Muscle atrophy. Three weeks after BoNT/A injection the wet weight of the triceps surae was decreased significantly ($p = 0.00005$) by 45% (BoNT/A injected leg (BoNT/A): 0.78 ± 0.03 g and Contralateral saline injected leg (Con): 1.43 ± 0.07 g) in the BoNT/A injected leg. A 2D image of the muscle crossections displays the atrophy observed in the BoNT/A leg (Fig. 3).

Anisotropy. The isotropy index from the star length distribution (SLD) analysis significantly increased ($p = 0.002$) after the BoNT/A injections (3 weeks post injection), which indicates a loss of linear structure of the muscle tissue. This was further supported by visualization of the 3D orientation of the muscle tissue using rose diagrams (Fig. 4). The diagram displays the strength of directions of the non-fibrillar tissue in the volume of interest (VOI). For linearly structured tissues, the diagram will take the shape of a strongly elongated ellipsoid whereas isotropic tissues with uniformly distributed directions will take the shape of a sphere. As seen from Fig. 4, the BoNT/A injection has resulted in a loss of directionality of the non-fibrillar tissue.

Gait pattern analysis. The gait pattern of the rats was significantly affected. There was a significant main effect of both time ($p < 0.0001$) and leg ($p = 0.0008$) on the stride length but not of the interaction. Across time, the stride length was significantly reduced for the BoNT/A leg compared to the non BoNT/A leg ($p = 0.0006$). Across legs, the second pre-test stride length value was significantly higher than any post-test values ($p < 0.0006$ for all comparisons). No significant differences were observed between the post-tests. There was a significant main effect of time, leg and the time-leg interaction on the foot length ($p < 0.0001$ in all cases) indicating that the rats became flat footed after BoNT/A injections. The post hoc test revealed that for the BoNT/A leg the foot length was significantly increased in all post-test observations when compared to the pre-test observation ($p < 0.0001$ in all cases). For the non BoNT/A leg, the foot length was significantly shorter at the pre-test compared to the first three post-tests ($p = 0.004$, $p = 0.012$ and $p = 0.028$, respectively). However, the last post-test foot length did not differ significantly from the pre-test. The foot length of the BoNT/A leg was significantly greater at all post-tests compared to the non BoNT/A leg ($p < 0.0001$ in all cases). The foot angle was measured as indicated in Fig. 5.

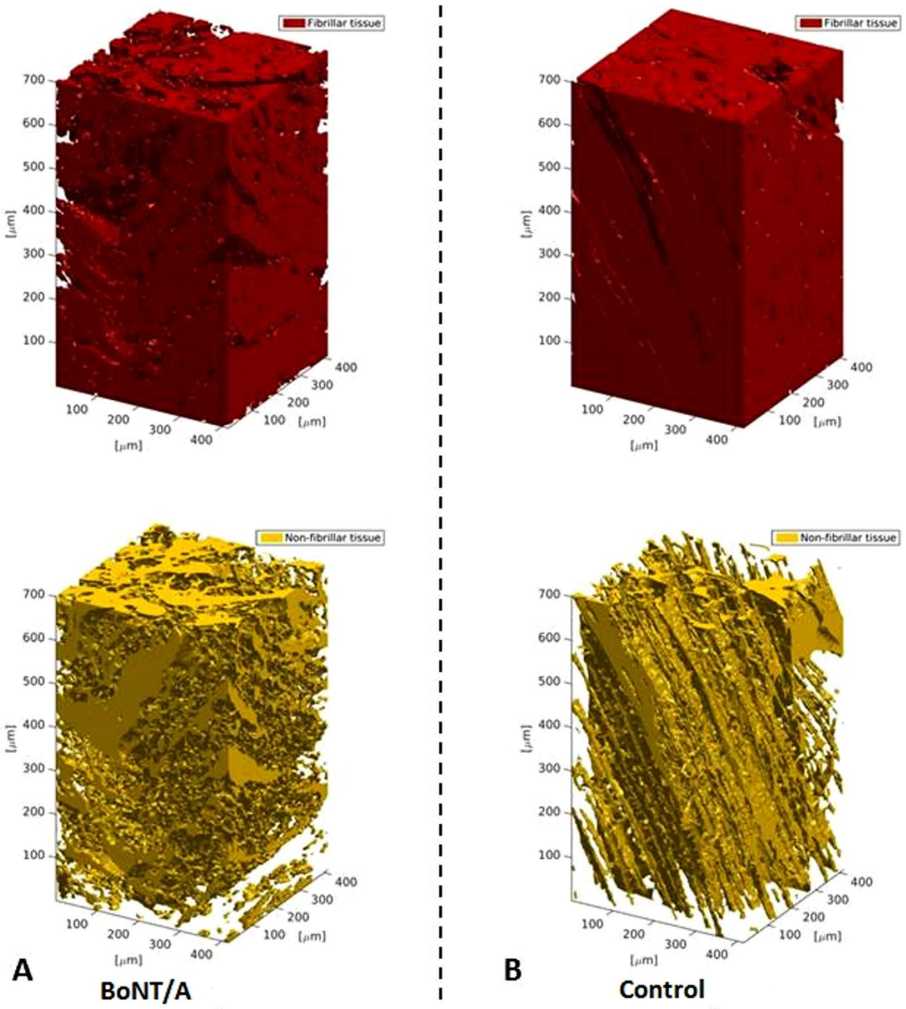

Figure 1. 3D visualizations of tomograms from the SRXTM measurements. Shown are the fibrillar (red) and non-fibrillar tissue (yellow) of the muscle in BoNT/A injected (**A**) and control leg (**B**) of one of the rats (3 weeks post injection of 6UI BoNT/A (3×20 pg BoNT (2UI)/a $\sim$ 60 pg BoNT/A in total). The SRXTM data indicate that BoNT/A injection causes damage to the muscle tissue structure and organization.

A positive foot angle indicates external rotation, and a negative foot angle indicates an internal rotation of the foot. There was a significant main effect of time, leg and the time-leg interaction on the foot angle ($p < 0.0001$ in all cases). The post hoc test revealed that for the BoNT/A leg all post-test observations were significantly larger than the pre-test observation ($p < 0.002$ in all cases). For the non BoNT/A leg, the foot angle did not significantly change from the pre-test to the post-tests. The foot angle of the BoNT/A leg was significantly greater at all post-tests compared to the non BoNT/A leg (Fig. 6).

Clinical score assessment. The clinical score dropped significantly already 24 h post injection ($p = 0.0001$) and reached the lowest level on day 3 post injection ($p = 0.00001$). The rats never recovered during the protocol and the clinical score was still decreased three weeks post injection. There was a significant main effect of time on the clinical score ($p < 0.0001$). The post hoc test revealed that all post-test observations were significantly lower compared to the pre-test observation ($p < 0.0001$ in all cases) (Fig. 6).

Gene expression. The gene expression of seventeen gene targets were analyzed in $n = 8$ rats (Fig. 7). Specific gene targets were selected covering the areas of muscle structure, muscle metabolism, Extracellular matrix components, connective tissue breakdown and muscle fiber types. There was a significant main effect of both BoNT/A treatment ($p < 0.001$) and gene ($p < 0.001$) on the gene expressions and a significant interaction ($p < 0.001$). Post

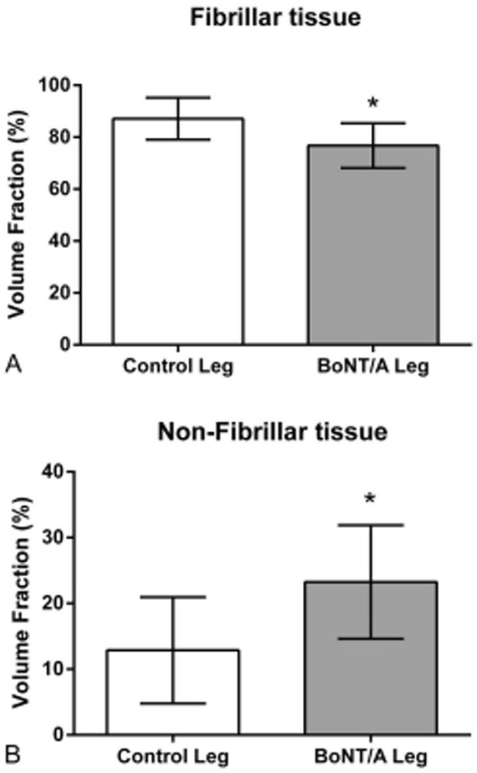

Figure 2. Volume fraction in percent of the fibrillar (**A**) and non-fibrillar tissue (**B**) of the muscle. All data are shown as Mean ± SEM. *Indicates a significant difference between BoNT/A and Con leg. Dose of injection 6UI BoNT/A (3 × 20 pg BoNT (2UI)/a ~60 pg BoNT/A in total). The level of significance was $p < 0.05$.

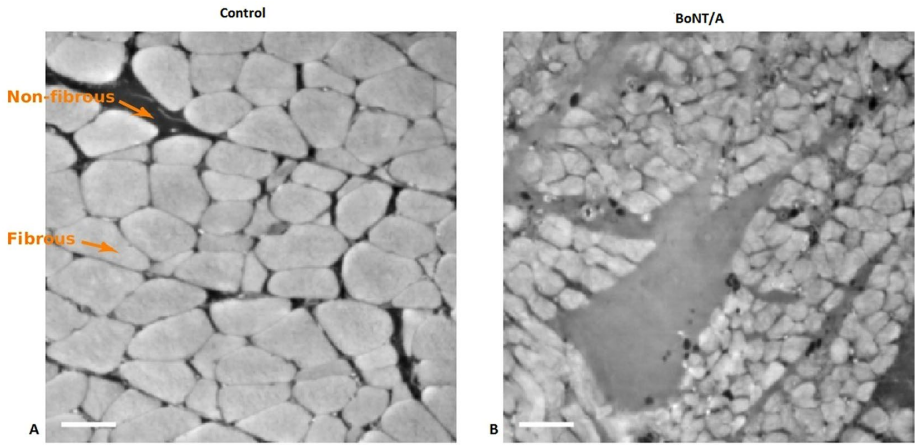

Figure 3. 2D images of muscle cross sections. Left image control leg, right image BoNT/A injected muscle (3 weeks post injection). The BoNT/A injected muscle contains smaller muscle fibers than the control muscle, indicating muscle atrophy. Arrows are indicating fibrous and non-fibrous tissue. Dose of injection 6UI BoNT/A (3 × 20 pg BoNT (2UI)/a ~60 pg BoNT/A in total). The scale bar equals 50 µm.

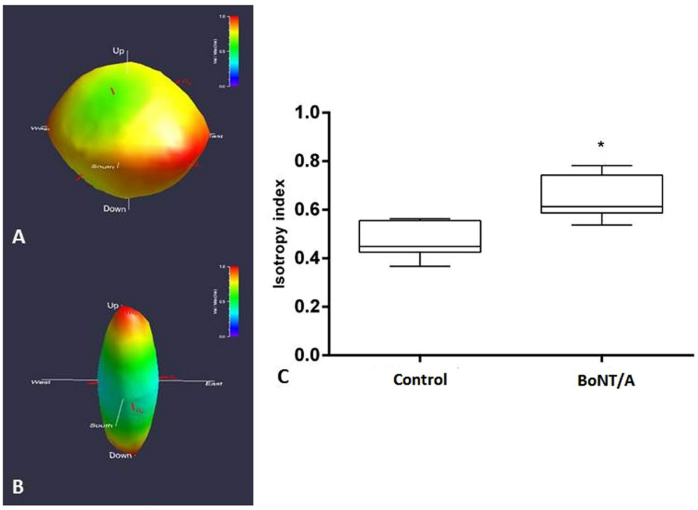

Figure 4. Star length distribution (SLD) rose diagrams depicting non-fibrillar tissue orientation in BoNT/A (**A**) and control (**B**) muscle from one of the rats (3 weeks post injection). Dose of injection 6UI BoNT/A (3 × 20 pg BoNT (2UI)/a ~60 pg BoNT/A in total). Distance from origin and colour (violet = minimum, red = maximum) indicate relative component value. Red axes show principal component directions and relative magnitudes. The boxplot (right **C**) shows the isotropy index of n = 6 rats shown as Mean ± SEM. *Indicates a significant difference between BoNT/A and Con leg, showing an significantly increased anisotropy index after the BoNT/A injections, which indicates a loss of linear structure of the muscle tissue. The level of significance was $p < 0.05$.

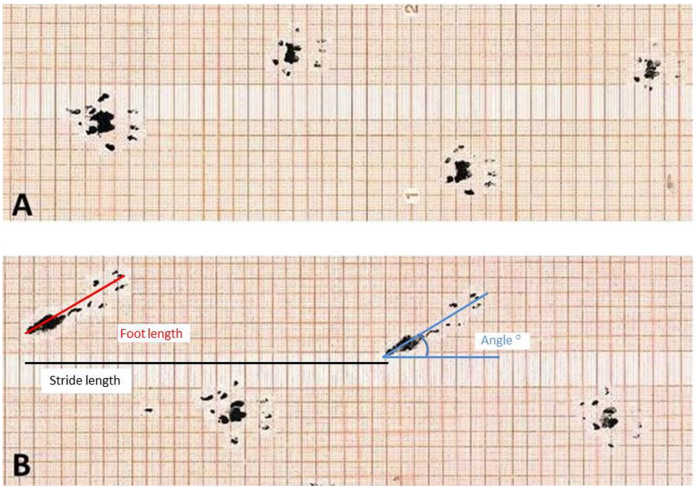

Figure 5. Foot step analysis. The hind paws were dipped in ink and the rats ran over graph paper at (**A**) baseline (2 days pre injection), and (**B**) post (21 days) after BoNT/A injection into the left triceps surae. Dose of injection 6UI BoNT/A (3 × 20 pg BoNT (2UI)/a ~60 pg BoNT/A in total). The strife length, foot angle and the foot length were analyzed. All parameters were significantly affected in the BoNT/A leg when compared to baseline and the control leg ($p < 0.05$).

hoc tests revealed a significant upregulation of gene expression in: collagen type 1 (*COL1A1*), interleukin 6 (*IL-6*), transforming growth factor beta 1 (*TGF-β1*), matrix metallopeptidase 2 (*MMP-2*), myosin heavy chain IIA (*MHCIIA*) and myosin heavy chain IIX (*MHCIIX*). Myosin heavy chain IIb (*MHCIIB*) was significantly down-regulated in the BoNT/A leg compared with the control leg.

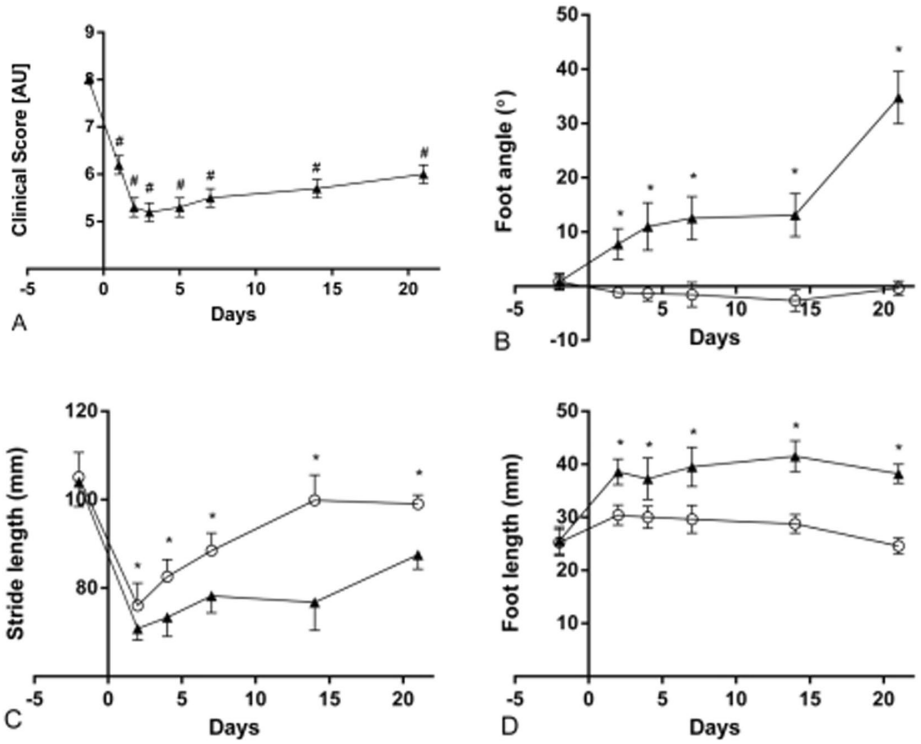

Figure 6. The stride length, foot angle and foot length was analyzed as indicated on Fig. 5. The clinical score (**A**) shows all animals in arbitrary units AU. The foot angle (**B**) is shown in degrees (°). The stride length (**C**) is shown in mm. And the foot length is shown in mm. In both B,C and D the black triangles represent the BoNT/A injected leg, and the open circles represent the contralateral Con injected leg. Dose of injection 6UI BoNT/A (3 × 20 pg BoNT (2UI)/a ∼60 pg BoNT/A in total). All data are shown as Mean ± SEM. *Indicates a significant difference between BoNT/A and Con leg, #indicates a significant difference from baseline. The level of significance was $p < 0.05$.

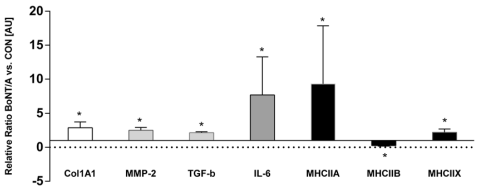

Figure 7. The relative changes of gene expression after botulinum toxin injection. The control leg equals 1 and all expressions are shown relative to the expression of the control leg. All data are shown as Geo Mean ± SEM. *Indicates a significant difference between BoNT/A and Con leg. Dose of injection 6UI BoNT/A (3 × 20 pg BoNT (2UI)/a ∼60 pg BoNT/A in total). The level of significance was $p < 0.05$.

Body weight. The development of the body weight differed significantly between the BoNT/A injected animals and the Control group ($p < 0.0001$) (Fig. 8). In addition both groups changed significantly over time (after 1 week) ($p < 0.0001$).

Discussion

The main finding of the present study is that the microstructure of the skeletal muscle showed signs of muscle damage following high dose BoNT/A injections (3 × 20 pg BoNT (2UI)/a ∼60 pg BoNT/A in total (6UI)), both at the fibrillar- and non fibrillar level of the tissue. The 3D tomographs showed that the tissue lost its linear structure, and that the structural composition was clearly affected. The anisotropy analysis of the tomograms gives further

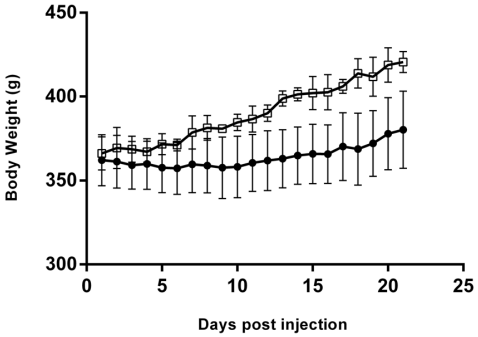

Figure 8. The development of the body weight of the rats after botulinum toxin injection. The open squares represent control rats (n = 2), and the black dots represent BoNT/A rats (n = 6). All data are shown as Mean ± SEM. *Indicates a significant difference between BoNT/A and Con leg. The level of significance was $p < 0.05$.

support to these indications. The isotropy index increased after high dose BoNT/A injection, which indicates that the muscle tissue was more randomly oriented following high dose BoNT/A injections.

Botox is used in several different disciplines with many different purposes. In addition, it is becoming more and more common for healthy individuals to receive BoNT/A injections, not to cure a disease, but in order to improve the appearance. BoNT/A is among others used to sculpt different muscles of the body, including the masseter muscles for mandibular recontouring (used for when individuals complaint of a "squared" lower face[31] or the medial and lateral gastrochnemius for calf recontouring (for when individuals complaint of prominent calf muscles)[31]. However, recent studies have expressed some concerns regarding the use of BoNT/A[32–34].

The chemical denervation induced by BoNT/A injection prevents muscle contraction and causes a cascade of downstream events in the muscle e.g. inflammation, satellite cell activation, oxidative stress, atrophy and metal ion imbalance[35,36]. Whether BoNT/A also has a direct effect on the muscle tissue is unclear. However, it has been shown that repeated BoNT/A injections (once a day for 28 days at doses of 1, 3, and 9 ng kg-1 day-1) result in pronounced muscle atrophy[37] and muscle weakness. In the present study we observed a loss of 45% muscle wet weight after three weeks, and we have previously shown that muscle force drops significantly after BoNT/A injection using the same dose as in the present study[33]. In fact several studies report muscle weakness as the most common treatment-related adverse event[31]. Furthermore it has been shown that side effects are temporary and often related to usage of high doses[38]. Even though the use of BoNT/A has been reported to be safe and many patients are treated without complications, some studies report unwanted side effects[39,40]. One study by Blaszczyk *et al.* examined unwanted side effects (adverse events AEs) after BoNT/A injections in 79 cerebral palsy patients[41]. Altogether 95 AE's were reported in 45 patients. Nineteen patients reported muscle weakness, and four patients did report severe adverse events including speech disorders, swallowing difficulties and respiratory troubles. These findings indicate that side effects after BoNT/A injection are quite common[41]. Cerebral palsy patients are often treated with BoNT/A in order to improve gait function, and several studies have shown that this treatment is safe and without side effects[10,42]. However, we suggest that the success of the treatment should be evaluated with care. We propose that even though patients do not report any unwanted side effects, this does not mean that the BoNT/A treatment was successful in these patients per se. In the present study we observed that BoNT/A injections had a significant effect on the gait pattern of the present rats. The rats developed a flatfoot on the BoNT/A injected leg (Fig. 5). Furthermore the clinical score dropped already after 24 hours and did not return to baseline within three weeks (Fig. 6). The same observation has been made previously by Ozawa *et al.*[43] after BoNT/A injection (dose 5 units/mL). In addition, the BoNT/A injection caused an external rotation of the foot possibly to regain balance (Fig. 6). Furthermore, it appears that more and more people question whether the few positive effects achieved by BoNT/A injection are actually overcome by the negative effects it has on the muscles[32,33,44].

The affected gait after 24 hours is a result of the reduced presynaptic acetylcholine release that follows Botulinum toxin injection. BoNT/A cleaves a SNARE protein SNAP25, which is required for exocytosis and as a result several downstream events are affected including muscle atrophy. The muscle atrophy induces weakness, and the weakness affects the gait pattern. Thus while the gait pattern and clinical score at the early time points reflect the neural effects of BoNT/A, atrophy and muscle weakness is likely to contribute to the impairment of gait function at the later time points (3 weeks post injection).

Eamus *et al.* (1999) have shown that a single injection of BoNT/A into the calf increased the length of gastrocnemius during gait[45]. Furthermore, gait analysis of ninety-seven CP patients revealed that muscle strength was highly related to muscle function and explained more of the gait variance than spasticity[46]. Based on the present findings we suggest that the desired outcome of BoNT/A treatment in cerebral palsy patients should be reconsidered, and future studies should focus on finding a better treatment instead of improving a drug that does not entail the desired effects.

Furthermore, whether muscle contouring of the calf muscles influences the gait pattern in humans has not yet been investigated, but based on the present findings we suggest that it might be an important point to focus on in future investigations as well.

The damage that occurs in the muscle after high dose BoNT/A injection requires a comprehensive remodeling process. This is reflected in gene expressions of the present study (Fig. 7). Both the collagen synthesis and collagen breakdown is upregulated after BoNT/A injection. This finding is in agreement with previous observations showing increased collagen synthesis at gene expression level three weeks after muscle injury in rats[47]. On the other hand, immobilization causes a decrease of collagen expression[48]. Thus, the increased collagen synthesis might indicate an accelerated tissue remodeling after muscle damage rather than being a result of the denervation due to BoNT/A injection (Fig. 7). The anisotropy findings of the present study indicate a loss of tissue orientation, which further indicates that the microstructure of the muscle is undergoing an extensive remodeling process. Furthermore, the inflammation marker IL-6 was upregulated in the present study. IL-6 is a pleiotropic cytokine involved in tissue regeneration and remodeling, indicating an inflammatory response after BoNT/A injection in the muscle[49]. A significantly up-regulation of IL-6 following muscle injury, coinciding with the active period of muscle regeneration has been observed previously in mice[48]. The present upregulation of IL-6 in the BoNT/A injected muscle underlines that the high dose BoNT/A injection caused muscle damage. Furthermore, one study observed a significant increase of satellite cells after intramuscular botox injections in rabbits[50]. In resting muscle satellite cells remain quiescent, while muscle injury and trauma invokes activation of satellite cells[51,52]. Numerous studies have shown that skeletal muscle satellite cells are essential for muscle fiber repair and regeneration[53–55]. Muscle wasting occurs in a variety of conditions, including muscular dystrophies, cancer cachexia and sarcopenia[56]. In the present study the intramuscular BoNT/A injection caused a decrease of muscle mass of (45%). In addition, muscle atrophy can affect specific fiber types, involving predominantly slow type 1 or fast type 2 muscle fibers (slow-to-fast or fast-to-slow fiber type shift)[57]. Age related muscle wasting (sarcopenia) induces a fast-to-slow fibertype shift[58,59]. Spinal cord injury patients on the other hand experience a type 1 fiber atrophy with a slow-to-fast fiber type shift due to disuse[60]. In the present study a significant upregulation of myosin heavy chain IIA and myosin heavy chain IIx expression was demonstrated, while MHCI was unchanged and MHCIIb was downregulated (Fig. 7). These results indicate that BoNT/A injections cause a slow-to-fast fibertype shift due to upregulation of fast fiber type expression rather than due to atrophy of type 1 fibers. This might be a compensatory process in order to compensate for a significant loss of muscle force and mass after BoNT/A injections which has been observed previously after a single injection of 100 μL of BoNT/A of 6.0 units/kg[61]. However, the present findings are in contrast to previous findings showing that BoNT/A injection in the gastrocnemius muscle of rats caused a fast-to-slow fibertype shift when rats received either 3,6,12 or 18 UI of BoNT/A[18]. These contradictory findings may be explained by the difference in how long after the BoNT/A injection the tissue was analyzed. The present findings reflect the early regeneration phase (3 weeks after injury), while the study by Dodd *et al.* demonstrates the long term effect of the damage after BoNT/A injection[18]. Furthermore, the present study investigated mRNA levels only. To clarify whether BoNT/A injections cause a fibertype shift both short- and longterm should rather be investigated using proper fibertyping methods, than mRNA expression only. In addition Fig. 3 shows qualitative transectional images of the microstructure of the muscle, and makes the effect of BoNT/A visible by eye showing that the muscle fibers in the BoNT/A injected leg are smaller and appear with blurred edges, indicating muscle atrophy of all present muscle fibers. By using Synchrotron Radiation X-ray Tomographic Microscopy (SRXTM) the present study revealed that the microstructure of skeletal muscle tissue was significantly damaged three weeks after a single injection of BoNT/A in rats. However, whether repeated injections would lead to even further damage needs further investigations.

Whether repeated injections of BoNT/A might have unwanted and irreversible effects is still unclear for several different treatments. There are to date unfortunately only few studies that have examined the effects on the muscle tissue after repeated injections. However, Minamoto *et al.* investigated the effect of repeated BoNT/A injections into the tibialis anterior muscle in rats and observed that a single injection of BoNT/A caused a 50% decrease of muscle torque, while a second injection of botox decreased the muscle torque to 95% when compared to the pre injection level[61]. The authors concluded that a second BoNT/A injection caused a profound and persistent loss in muscle function and altered muscle structure[61]. Unwanted side effects have also been reported in cosmetic medicine where cumulative and repeated injections into the masseter muscle for lower face contouring can cause different adverse effects including difficulty chewing, speech disturbances and muscle fatigue[31].

In addition, the loss of bodyweight after BoNT/A injections might also be characterized as an unwanted side effect. In the present study, when the body weight of the rats that were injected with BoNT/A was compared with the bodyweight of healthy untreated control rats, it was observed that the body weight was significantly lower in the BoNT/A rats one week after the botox injection until the end of the protocol (Fig. 8). This indicates that a high dose of BoNT/A affects the bodyweight development of the rats, which might reflect an inhibited growth of the rats. Whether this is only experienced after injection of a high dose BoNT/A is unknown, but it is possible that a high dose of BoNT/A injection causes systemic effects which are reflected by the body weight of the rats. However, there is increasing evidence that BoNT/A inhibits growth both in rats and in humans[32,62,63]. Gough *et al.* has previously claimed that BoNT/A injections inhibit muscle growth[64]. In addition, it has been shown that the skeletal muscle tissue in rabbits did not fully recover six month post injection (3.5 UI/kg)[65]. When translating this finding into human years this would mean that the skeletal muscle tissue has not fully recovered 16 years after injection. However, there is no infallible mathematical formula to calculate the human age of a rabbit because its growth and physiological changes during it's life are very different from the development seen in humans. And the existing age equivalence charts are usually based on observations of ages of rabbits from veterinarians. Nevertheless, the finding that high dose BoNT/A injections affect both bodyweight development, microstructure of the muscle and has an influence on the gait pattern of rats, raises a series of questions towards the rational of BoNT/A as a treatment against muscle contractures.

One major limitation of the present study is that the synchroton data are only analysed at one single time-point (3 weeks post BoNT/A injection). This limits the ability to draw any major conclusions regarding the use of BoNT/A, since we cannot rule out that all the effects we observe here are fully reversible. Thus, long-term observations at several time-points are necessary in order to elucidate the recovery of the muscle tissue following BoNT/A injections. Furthermore, this study only reflects effects on the muscle tissue after one single injection. Future studies should investigate whether additional injections cause additive damage to the microstructure and the tissue. Another important issue in the present study is the fact that the injection volume is quite high (100 μl) compared to other studies were only 20 μl injection volume has been used[66]. The high injection volume has certainly produced some edema within the muscle tissue. However, the contralateral leg was injected with 100 μl saline saline as well and showed no signs of muscle damage 3 weeks after injection. However, it should be remembered that a high injection volume might increase the risk of systemic effects due to unintended spread of BoNT/A. One previous study has shown that high dose injections of botulinum toxin caused sporadic SNAP25 expression in distal muscles of rats indicating systemic spread but without evidence of transcytosis (dose: 20 μl of BoNT/A (3, 10, 30 U/kg)[67]. Unfortunately we were not able to investigate whether there was any systemic spread of BoNT/A in the present rats. However, it is possible that the high dose of BoNT/A injection and the high injection volume used in the present study might have caused systemic effects. These might be reflected by the reduced increase of body weight in the rats. On the other hand, the reduced increase of body weight in the BoNT/A injected rats may also be explained by reduced mobility of the rat due to the impaired muscle function caused by the local effect of the injection, but we cannot exclude that it may also be related to a systemic effect of the injection, although there were no visible signs of this.

The rats of present study did not lose much bodyweight; they rather showed a reduction of growth, unlike the animals used in the pilot study (Supplementary Material Figure 1). This difference in weight loss might be due to differences in age and baseline bodyweight. Unlike the rats that were used in the pilot study (Supplementary Material Figure 1) the rats from the present protocol were still growing, and this process might have counteracted the weight loss that was induced by the high dose BoNT/A injections.

Conclusion

The present study leads to serious concerns regarding BoNT/A treatment because of the significant effect it has on the micro structure of the muscle tissue and tissue organization. Furthermore the results of the present study highlight that it is possible that intramuscular high dose BoNT/A injections might cause unwanted side effects such as muscle atrophy, and fatigue which causes an extensive remodeling process in the muscle tissue. The present findings indicate that high dose BoNT/A injections causes damage of the microstructure of the muscle tissue. Furthermore the present study shows that the physical capabilities are significantly reduced and the gait is significantly compromised 3 weeks after a high dose BoNT/A injection into the calf.

Materials and Methods

Animals. All experiments were conducted in accordance with the guidelines of EU Directive 2010/63/EU and were approved by the Danish Animal Experiments Inspectorate. 23 samples in the form of male Sprague Dawley rats (weight: 360 g) were used for the present experiment (n = 4 pilot gait analysis and clinical score (Baseline + 21 days post injection); n = 8 gait analysis and clinical score (21 days), n = 8 gene expression analysis and volume fraction (21 days post injection), n = 1 sham injection (Saline) gene expression normalization, and n = 2 control rats for body weight assessment. The rats were caged two by two (2 rats in each cage) in a 12/12 light dark cycle with access to water and food ad libitum. All recommended procedures for safe and proper handling, storage and preparation for experimental use, and disposal of Botulinum Toxin were complied. (https://www.cdc.gov/biosafety/publications/bmbl5/bmbl5_sect_viii_g.pdf). The entire medial gastrocnemius (including the injection site) of the muscle was dissected and harvested 21 days after BoNT/A injection and was used for gene expression analyses and volume fraction measurements. The tissue was harvested while the animals were anesthetized by 2% isoflurane. After the harvest the animals were euthanized using pentobarbital injections into the heart while the animals still were under anesthesia (2% isoflurane).

Gait pattern analysis. The paws of both hind limbs of the rats were dipped in ink on a stamp pad. Then they were put down on a piece of graph paper and run through a plastic tunnel into a dark box. This procedure was then repeated three times. All paper strips were digitalized and analyzed using ImageJ (http://imagej.net/Welcome University of Wisconsin-Madison). The measurements of stride length, foot angle and foot length was done as indicated in Fig. 5.

Tissue preparation. The rats were anesthetized by 2% isoflurane. The medial gastrocnemius was removed and dissected into smaller pieces with a scalpel (Swann-Morton, Mediq danmark A/S). The wet weight of the triceps surae was measured immediately after removal. One piece of the medial gastrocnemius was snap frozen in liquid nitrogen and stored at −80 °C for further PCR analysis. Another piece was fixed in Bouin's fluid for 24 h and kept at 4 °C in 1.5 ml Eppendorf tubes. The tissue were then transferred into fresh tubes with 96% ETOH and remained at 4 °C until subsequently analysis.

The Clinical score assessment and gait analysis were conducted in four rats in a pilot study where baseline measurements and 21 days post measurements were obtained (Fig. 6). Subsequently eight rats were followed closely for 21 days and the clinical score and gait analysis was assessed every second day to monitor the acute effects over time after BoNT/A injection (Fig. 6).

Injections. In order to test the dosage and injection volume a pilot study was conducted to test the optimal dosage (The optimal dose was defined as the smallest dose that would cause the desired effect of muscle atrophy, without causing any distress for the animals) (Results shown in Supplementary Material Figure 1). All animals

Gene	Sense	Anti sense	P-values
RPLP0	AGGGTCCTGGCTTTGTCTGTGG	AGCTGCAGGAGCAGCAGTGG	<0.001*
GAPDH	CCATTCTTCCACCTTTGATGCT	TGTTGCTGTAGCCATATTCATTGT	<0.001*
Col1A1	ATCAGCCCAAACCCCAAGGAGA	CGCAGGAAGGTCAGCTGGATAG	0.006*
Col3A1	TGATGGGATCCAATGAGGGAGA	GAGTCTCATGGCCTTGCGTGTTT	0.059
DCN	CACTCCAGGAGCTTCGACTCCAC	AGTGGGTTGCCGCCCAGTTC	0.131
FMOD	CCGTCAACACCAACCTGGAGAA	CGTGCAGAAACTGCTGATGGAGA	0.262
FN1	GGGCTTTGGCAGTGGTCATTT	CTCATCCGCTGGCCATTTTCTC	0.055
GLUT4	CTTCATCGTTGGCATGGGTTTC	CAAATGTCCGGCCTCTGGTTTC	0.594
Itga7	GCTGAGAAGAGAAACGTGAC	GTAGAGTGGGCAGCTGAATA	0.135
Prelp	CACCTGTACCTCAACAACAATA	GAAGTCATGGAAGGCCACTA	0.142
IL6	GACAAAGCCAGAGTCATTCAGAGCA	GAGCATTGGAAGTTGGGGTAGGA	<0.001*
MMP2	CTGGGTTTACCCCCTGATGTCC	AACCGGGGTCCATTTTCTTCTTT	0.017*
TGFb1	CCCCTGGAAAGGGCTCAACAC	TCCAACCCAGGTCCTTCCTAAAGTC	0.046*
MHCIb	ATTGCCGAGTCCCAGGTCAACA	GCTCCAGGTCTCAGGGCTTCAC	0.161
MHCIIA	GAAGAGCCGCGAGGTTCACAC	GGGACATGACCAAAGGCTTCACA	<0.001*
MHCIIB	GCCGAGTCCCAGGTCAACAAG	TGTGATTTCTTCTGTCACCTTTCAAC	<0.001*
MHCIIX	GCCGAGTCCCAGGTCAACAA	CTCATCTCTTTGGTCACTTTCCTGCT	0.042*

Table 1. PCR primers.

were anesthetized with 2% isoflurane. Both hind limbs were shaved, and the skin was disinfected. Then a high dose of BoNT/A was injected (1 BoNT/A Unit = 10 picogram). The present high dose injection was 6 UI in total (6 UI = 60 pg in total) and (2 UI = 20 pg per 100 µl saline was injected per muscle head (Botulinum-toxin A (BoNT/A® Allergan INC. Irvine CA)) of was injected into the triceps surae (medial gastrocnemius, the lateral gastrocnemius and soleus) muscle using a 0.5 ml syringe (Omnican® 20 BRAUN, Germany), and 100 µl saline was injected per muscle head in the contralateral control leg. Each rat thereby received a total of 300 µl and 6UI of BoNT/A. Until termination of the experiment the welfare of the rats were routinely checked (e.g. for signs of dehydrations or distress). The rats were weighed every day following the injection in order to monitor weight loss. When any weight loss occurred the rats got 5 ml subcutaneous saline injections twice a day until the body weight was regained. The rats used in Clinical locomotion score assessment: The clinical evaluation system by (Malmsten 1983) was used to estimate the time course of improvement of motor performance in the hind limbs following BoNT/A injections[68]. The animals were tested at the following timepoints: 2 days pre injection and 2 days, 4 days, 7 days, 14 days and 21 days post injection. This is a system which scores the movement ability on a scale from 1 to 8 (1: no active movements of the limb, 2: few involuntary movements when handling the animal, 3: few uncontrolled gait movements with long breaks, 4: leg is used for locomotion without control, 5: leg is used for locomotion with little control, 6: leg is used for locomotion with increasing control, 7: Abnormal movements are only seen during close observation, 8: normal gait). The animals are observed while they walk voluntarily around in their cages for aprox 3 minutes, and the same observer rates the clinical score from 1 to 8.

RNA extraction and real time-PCR analysis. Total RNA isolation: Total RNA was extracted from frozen muscle samples from n = 8 BoNT/A rats by using 1 ml of TRI Reagent (Molecular Research Centre, Cincinnati, OH) 5 steel beads (2.3 mm) and 1 silica bead (1.0 mm Silicon Carbide Beads (454 grams) BioSpec Products Inc.). Extracted RNA was precipitated from the aqueous phase with isopropanol and was washed with ethanol (75%), dried and suspended in 10 µl of nuclease-free water. The RNA concentration was determined using a RiboGreen RNA Quantitation kit 200–2000 Assays, Molecular Probes USA. RNA quality was determined on the basis of a RNA 6000 nano Chip assay kit, Agilent Technologies, Germany. The RNA samples were stored frozen at −20 °C until subsequent use in real-time RT-PCR procedures. To test the quality of the extracted RNA an electrophoresis in an agarose gel was made. The RNA quality was suggested to be satisfactory for further analysis.

cDNA synthesis. 150 ng RNA was reverse transcribed for each muscle sample in a total volume of 20 µl by using the Qiagen Omniscript RT Kit at 37 °C for 1 hour followed by 70 °C for 15 minutes. The resulting cDNA was diluted twenty times in dilution buffer (10 mM Tris EDTA buffer: Sigma Germany) + Salmon Testes DNA (1ng/µl; Sigma Germany), and samples were stored at −20 °C until used in the PCR reactions for specific mRNA analysis.

Polymerase Chain Reaction. The Real-time PCR-method using Glyceraldehyde 3-phosphate dehydrogenase (GAPDH) and 60S acidic ribosomal protein P0 (RPLP0) as reference genes to study specific mRNA's of interest was applied. However, since both reference genes were significantly affected of the BoNT/A injections, all data were normalized to the median values of the control samples of all animals. The primers were purchased from MWG Biotech. For each target cDNA the PCR reactions were carried out under identical conditions by using 5 µl diluted cDNA in a total volume of 25 µl QuantiTect SYBR Green PCR Mix (Qiagen) and 100 nM of each primer (Table 1). The amplification was monitored in real-time using a MX3005 P real-time PCR machine (Stratagene, CA). The threshold cycle (C_t) values were related to a standard curve made with cloned PCR products

to determine the relative difference between the unknown samples, accounting for the PCR efficiency. The specificity of the PCR reaction was confirmed by melting curve analysis after amplification. The real-time PCR conditions were as follows: to denaturate the DNA strands the reaction mix was heated above the melting temperature of DNA (95 °C) for 10 minutes, followed by 50 cycles each of 15 seconds at 95 °C, followed by the annealing step where optimal primer hybridization conditions were obtained by lowering the temperature to 58 °C for 30 seconds, and the extension step, where the reaction mix was heated to 63 °C for 90 seconds.

Synchrotron radiation x-ray tomographic microscopy (SRXTM). The SRXTM measurements were carried out at the TOMCAT (TOmographic Microscopy and Coherent rAdiology experimenTs) beamline at the Swiss Light Source[69]. The X-ray source is a superbending magnet radiation source located 25 m from the sample. A double crystal multilayer monochromator was placed 7 m downstream of the source to extract monochromatic X-ray photons at 25 keV. The detector system consisted of a 100 μm thick, Ce-doped LuAG (Lutetium Aluminum Garnet) scintillator which converted the transmitted X-rays into visible light, a high numerical-aperture microscope which gave a 20 fold magnification, and a pco.edge5.5 16-bit CMOS (Complementary metal–oxide–semiconductor) based camera to record the images. The resulting field-of-view (FoV) was 0.832 mm × 0.702 mm (width × height), and the effective pixel size was 325 nm. Muscle biopsies were placed in a 96% ETOH buffer in a small 0.2 ml Eppendorf tube and soldered to a holder with beeswax. The sample was placed 63 mm in front of the scintillator. Since the sample was larger than the FoV, local tomographic measurements were conducted by collecting 1501 projections of 600 ms exposure time over a 180 degree rotation. Flat-beam images (i.e., images taken with no sample) and dark images (i.e., images taken with no beam) were obtained in order to correct the projections. The total measuring time for all 21 samples took about 24 hours including sample mounting.

The 63 mm distance between sample and detector, combined with an effective pixel size of 325 nm, lead to refraction-induced intensity effects in the images. In order to account for this, refraction corrections were performed in using a local implementation at TOMCAT of a single image first order refraction correction algorithm. The algorithm used the Paganin approach with the assumption that the object consisted of a homogeneous soft tissue material and that the propagation distance was sufficiently short for the transport-of-intensity-equation to apply[30]. For tomographic reconstruction, a filtered back-projection based algorithm was applied.

Image analysis. The background of the slices in the reconstructed tomogram suffered from a low-frequency bias-field. A correction was applied by first subtracting a constant plane and then subtracting a linear radial profile. The two correction functions were found by applying a least-squares fit to the mean of the tomogram stack slices.

For segmentation into a non-fibrillar and fibrillar phase, an alpha-level Markov random field (MRF) segmentation was applied to the tomograms as described by Pedersen *et al.*[70]. First, the data was modeled as a mixture of distribution functions by assigning a probability distribution to each phase. After assigning probability distributions, the spatial information of the data was incorporated into the segmentation process by modeling the data as an isotropic MRF[71]. The MRF smoothing parameter was set to 0.5. To find the optimal segmentation solution the multi-labeling problem was solved using graph cuts with alpha expansions as described in Boykov *et al.*[72].

BoNT/A is expected to alter the microstructural tissue of the muscle and changes the fibrillary organization. This is evident from Fig. 1, where typical images are shown. Clearly, the ratio between the non-fibrillar and fibrillary structure is change significantly which indicates muscle atrophy and tissue damage. Furthermore, the anisotropy in the tissue structure is altered (3 weeks post BoNT/A injection, when compared to the contralateral control leg). In order to quantify these changes we have evaluated the tomograms.

Volume fraction (percent object volume). The tomograms visualize the muscle tissue around the injection site. From the segmented tomograms (3 weeks post BoNT/A injection, when compared to the contralateral control leg), volume fractions for the identified non-fibrillar and fibrillar phases were calculated as the percent object volume (POV) values. Image analysis as well as visualization of the tomograms was performed using custom made software implemented in MATLAB (Mathworks, Inc., Natick, MA).

Anisotropy. The anisotropy analysis was performed 3 weeks post BoNT/A injection, and compared to the contralateral control leg, with a star length distribution (SLD) analysis using the Quant3D software as described elsewhere[73,74]. A volume of interest (VOI) from the non-fibrillar segmentation was used as an input to the SLD in Quant3D. For the orientation parameters, a uniform setting with 513 orientations, random rotations, and dense vectors were applied using 10,000 random points for calculating the SLD. The SLD analysis produces a number of anisotropic descriptors as described in[68]. As a measure of the orientation of the non-fibrillar tissue, the isotropy index was used. A value of one reflects a completely isotropic structure whilst zero reflects an anisotropic one. An assumption for the anisotropy analysis is that all the connected non-fibrillar tissue has been identified in the segmentation of the tomograms. Since the segmentation can have difficulties for samples with a very low non-fibrillar volume fraction, a lower threshold of 5% has been set. Two samples with a volume fraction below this threshold were excluded.

Data availability. Due to the enormous amount of data, the datasets generated during and/or analysed during the current study are available from the corresponding author on reasonable request.

Statistics. All data are presented as Mean ± SEM. Level of significance was set at 5% ($p < 0.05$).

Clinical score. Changes in the clinical score from the second pre-test to the seventh post-test were investigated using an ANCOVA for repeated measures with time as an independent factor and the first pre-test value as a covariate. In case of significant main effect, a post hoc test was applied with Tukey correction for multiple comparisons. Gait analysis: Changes from the second pre-test to the fourth post-test in gait function measures (stride

length, foot angle and foot length) were investigated using an ANCOVA for repeated measures with time and leg (BoNT/A leg and non BoNT/A leg) as independent factors and an interaction of time and leg. The first pre-test value was set as a covariate. In case of a significant main effect, a post hoc test was applied with Tukey correction for multiple comparisons. Volume fraction and anisotropy: Volume fraction and anisotropy was analyzed using a paired Students T-Test. Gene expression: Changes in gene expression between the BoNT/A leg and the control leg were investigated using a 2-Way ANOVA analysis with gene targets and leg (BoNT/A leg and control leg) as independent factors and an interaction of gene targets and leg. In case of a significant main effect, a post hoc test was applied with Tukey correction for multiple comparisons. All p-values from the post hoc tests are shown in Table 1. Changes in the development of body weight were investigated using a 2-Way ANOVA analysis with treatment and time as independent factors and an interaction of treatment and time. All PCR data are presented as the geo mean ± backtransformed SEM. Statistics software: Statistical calculations for gait analysis and the clinical score were performed in SAS Enterprise Guide (SAS Institute Inc. NC, USA 2015, version 7.11). The statistical calculations for changes in gene expressions and volume fraction were performed in Sigma Plot (Systat Software Inc. USA, version 12.5). Figures 1, 4 and 6 were generated in graphpad Prism 6.04 (GraphPad Software, Inc. CA, USA).

References

1. Swaminathan, S. & Eswaramoorthy, S. Structural analysis of the catalytic and binding sites of Clostridium botulinum neurotoxin B. *Nature structural biology* **7**, 693–699 (2000).
2. Lalli, G., Bohnert, S., Deinhardt, K., Verastegui, C. & Schiavo, G. The journey of tetanus and botulinum neurotoxins in neurons. *Trends in microbiology* **11**, 431–437 (2003).
3. Arnon, S. S. *et al*. Botulinum toxin as a biological weapon: medical and public health management. *JAMA* **285**, 1059–1070 (2001).
4. Scott, A. B. Botulinum toxin injection of eye muscles to correct strabismus. *Transactions of the American Ophthalmological Society* **79**, 734–770 (1981).
5. Camargo, C. H., Cattai, L. & Teive, H. A. Pain Relief in Cervical Dystonia with Botulinum Toxin Treatment. *Toxins* **7**, 2321–2335, https://doi.org/10.3390/toxins7062321 (2015).
6. Dashtipour, K., Chen, J. J., Frei, K., Nahab, F. & Tagliati, M. Systematic Literature Review of AbobotulinumtoxinA in Clinical Trials for Blepharospasm and Hemifacial Spasm. *Tremor and other hyperkinetic movements (New York, N.Y.)* **5**, 338, https://doi.org/10.7916/d8cj8cvr (2015).
7. Hsieh, P. F., Chiu, H. C., Chen, K. C., Chang, C. H. & Chou, E. C. Botulinum toxin A for the Treatment of Overactive Bladder. *Toxins* **8**, https://doi.org/10.3390/toxins8030059 (2016).
8. Dat, A. *et al*. Botulinum toxin therapy for chronic anal fissures: where are we at currently? *ANZ journal of surgery*. https://doi.org/10.1111/ans.13329 (2015).
9. Simpson, D. M. *et al*. Assessment: Botulinum neurotoxin for the treatment of movement disorders (an evidence-based review): report of the Therapeutics and Technology Assessment Subcommittee of the American Academy of Neurology. *Neurology* **70**, 1699–1706, https://doi.org/10.1212/01.wnl.0000311389.26145.95 (2008).
10. Balaban, B., Tok, F., Tan, A. K. & Matthews, D. J. Botulinum toxin a treatment in children with cerebral palsy: its effects on walking and energy expenditure. *American journal of physical medicine & rehabilitation/Association of Academic Physiatrists* **91**, 53–64, https://doi.org/10.1097/PHM.0b013e31823caae1 (2012).
11. Schaefer, S. M., Gottschalk, C. H. & Jabbari, B. Treatment of Chronic Migraine with Focus on Botulinum Neurotoxins. *Toxins* **7**, 2615–2628, https://doi.org/10.3390/toxins7072615 (2015).
12. Magid, M. *et al*. Treatment of major depressive disorder using botulinum toxin A: a 24-week randomized, double-blind, placebo-controlled study. *The Journal of clinical psychiatry* **75**, 837–844, https://doi.org/10.4088/JCP.13m08845 (2014).
13. Carruthers, J. & Carruthers, A. Botulinum toxin in facial rejuvenation: an update. *Dermatologic clinics* **27**, 417–425, v, https://doi.org/10.1016/j.det.2009.08.001 (2009).
14. El-Domyati, M. *et al*. The use of Botulinum toxin-a injection for facial wrinkles: a histological and immunohistochemical evaluation. *Journal of cosmetic dermatology* **14**, 140–144, https://doi.org/10.1111/jocd.12144 (2015).
15. Cosmetic Surgery National Data Bank Statistics. *Aesthetic surgery journal* **36** Suppl 1, 1–29, https://doi.org/10.1093/asj/36.Supplement_1.1 (2016).
16. Nigam, P. K. & Nigam, A. Botulinum toxin. *Indian journal of dermatology* **55**, 8–14, https://doi.org/10.4103/0019-5154.60343 (2010).
17. Blasi, J. *et al*. Botulinum neurotoxin A selectively cleaves the synaptic protein SNAP-25. *Nature* **365**, 160–163, https://doi.org/10.1038/365160a0 (1993).
18. Dodd, S. L., Selsby, J., Payne, A., Judge, A. & Dott, C. Botulinum neurotoxin type A causes shifts in myosin heavy chain composition in muscle. *Toxicon: official journal of the International Society on Toxinology* **46**, 196–203, https://doi.org/10.1016/j.toxicon.2005.03.022 (2005).
19. Dressler, D., Saberi, F. A. & Barbosa, E. R. Botulinum toxin: mechanisms of action. *Arquivos de neuro-psiquiatria* **63**, 180–185, doi:/S0004-282x2005000100035 (2005).
20. Hastings-Ison, T. & Graham, H. K. Atrophy and hypertrophy following injections of botulinum toxin in children with cerebral palsy. *Developmental medicine and child neurology* **55**, 778–779, https://doi.org/10.1111/dmcn.12231 (2013).
21. Williams, S. A., Reid, S., Elliott, C., Shipman, P. & Valentine, J. Muscle volume alterations in spastic muscles immediately following botulinum toxin type-A treatment in children with cerebral palsy. *Developmental medicine and child neurology* **55**, 813–820, https://doi.org/10.1111/dmcn.12200 (2013).
22. Borodic, G. E., Ferrante, R., Pearce, L. B. & Smith, K. Histologic assessment of dose-related diffusion and muscle fiber response after therapeutic botulinum A toxin injections. *Movement disorders: official journal of the Movement Disorder Society* **9**, 31–39, https://doi.org/10.1002/mds.870090106 (1994).
23. Han, N. *et al*. Proteomic changes in rat gastrocnemius muscle after botulinum toxin a injection. *Annals of rehabilitation medicine* **37**, 157–166, https://doi.org/10.5535/arm.2013.37.2.157 (2013).
24. Thacker, B. E. *et al*. Passive mechanical properties and related proteins change with botulinum neurotoxin A injection of normal skeletal muscle. *Journal of orthopaedic research: official publication of the Orthopaedic Research Society* **30**, 497–502, https://doi.org/10.1002/jor.21533 (2012).
25. Bravin, A., Coan, P. & Suortti, P. X-ray phase-contrast imaging: from pre-clinical applications towards clinics. *Physics in medicine and biology* **58**, R1–35, https://doi.org/10.1088/0031-9155/58/1/r1 (2013).
26. Zhou, S. A. & Brahme, A. Development of phase-contrast X-ray imaging techniques and potential medical applications. *Physica medica: PM: an international journal devoted to the applications of physics to medicine and biology: official journal of the Italian Association of Biomedical Physics (AIFB)* **24**, 129–148, https://doi.org/10.1016/j.ejmp.2008.05.006 (2008).

27. Marinescu, M. *et al*. Synchrotron radiation X-ray phase micro-computed tomography as a new method to detect iron oxide nanoparticles in the brain. *Molecular imaging and biology: MIB: the official publication of the Academy of Molecular Imaging* **15**, 552–559, https://doi.org/10.1007/s11307-013-0639-6 (2013).
28. Jian, J. *et al*. Visualization of microvasculature and thrombi by X-ray phase-contrast computed tomography in hepatocellular carcinoma. *Journal of synchrotron radiation* **23**, 600–605, https://doi.org/10.1107/s1600577516001016 (2016).
29. Grandl, S. *et al*. Evaluation of phase-contrast CT of breast tissue at conventional X-ray sources - presentation of selected findings. *Zeitschrift fur medizinische Physik* **23**, 212–221, https://doi.org/10.1016/j.zemedi.2013.02.005 (2013).
30. Paganin, D., Mayo, S. C., Gureyev, T. E., Miller, P. R. & Wilkins, S. W. Simultaneous phase and amplitude extraction from a single defocused image of a homogeneous object. *Journal of microscopy* **206**, 33–40 (2002).
31. Durand, P. D. *et al*. Botulinum Toxin and Muscle Atrophy: A Wanted or Unwanted Effect. *Aesthetic surgery journal* **36**, 482–487, https://doi.org/10.1093/asj/sjv208 (2016).
32. Gough, M. Does botulinum toxin prevent or promote deformity in children with cerebral palsy? *Developmental medicine and child neurology* **51**, 89–90, https://doi.org/10.1111/j.1469-8749.2008.03247.x (2009).
33. Pingel, J., Wienecke, J., Lorentzen, J. & Nielsen, J. B. Botulinum toxin injection causes hyperreflexia and increased muscle stiffness of the triceps surae muscle in the rat. *Journal of neurophysiology*, jn 00452 02016, https://doi.org/10.1152/jn.00452.2016 (2016).
34. Barber, L. *et al*. The effects of botulinum toxin injection frequency on calf muscle growth in young children with spastic cerebral palsy: a 12-month prospective study. *Journal of children's orthopaedics* **7**, 425–433, https://doi.org/10.1007/s11832-013-0503-x (2013).
35. Mukund, K. *et al*. Systems analysis of transcriptional data provides insights into muscle's biological response to botulinum toxin. *Muscle & nerve* **50**, 744–758, https://doi.org/10.1002/mus.24211 (2014).
36. Tagerud, S., Libelius, R. & Thesleff, S. Effects of botulinum toxin induced muscle paralysis on endocytosis and lysosomal enzyme activities in mouse skeletal muscle. *Pflugers Archiv: European journal of physiology* **407**, 275–278 (1986).
37. Choi, W. H. *et al*. Skeletal muscle atrophy induced by intramuscular repeated dose of botulinum toxin type A in rats. *Drug and chemical toxicology* **30**, 217–227, https://doi.org/10.1080/01480540701375091 (2007).
38. O'Flaherty, S. J., Janakan, V., Morrow, A. M., Scheinberg, A. M. & Waugh, M. C. Adverse events and health status following botulinum toxin type A injections in children with cerebral palsy. *Developmental medicine and child neurology* **53**, 125–130, https://doi.org/10.1111/j.1469-8749.2010.03814.x (2011).
39. Carraro, E., Trevisi, E. & Martinuzzi, A. Safety profile of incobotulinum toxin A [Xeomin((R))] in gastrocnemious muscles injections in children with cerebral palsy: Randomized double-blind clinical trial. *European journal of paediatric neurology: EJPN: official journal of the European Paediatric Neurology Society* **20**, 532–537, https://doi.org/10.1016/j.ejpn.2016.04.008 (2016).
40. Papavasiliou, A. S. *et al*. Safety of botulinum toxin A in children and adolescents with cerebral palsy in a pragmatic setting. *Toxins* **5**, 524–536, https://doi.org/10.3390/toxins5030524 (2013).
41. Blaszczyk, I., Foumani, N. P., Ljungberg, C. & Wiberg, M. Questionnaire about the adverse events and side effects following botulinum toxin A treatment in patients with cerebral palsy. *Toxins* **7**, 4645–4654, https://doi.org/10.3390/toxins7114645 (2015).
42. Cosgrove, A. P., Corry, I. S. & Graham, H. K. Botulinum toxin in the management of the lower limb in cerebral palsy. *Developmental medicine and child neurology* **36**, 386–396 (1994).
43. Ozawa, J. *et al*. Interaction between gastrocnemius muscle weakness and moderate exercise deteriorates joint integrity in rat knee. *Scandinavian journal of medicine & science in sports* **25**, e11–19, https://doi.org/10.1111/sms.12195 (2015).
44. Schroeder, A. S., Koerte, I., Berweck, S., Ertl-Wagner, B. & Heinen, F. How doctors think–and treat with botulinum toxin. *Developmental medicine and child neurology* **52**, 875–876, https://doi.org/10.1111/j.1469-8749.2010.03692.x (2010).
45. Eames, N. W. *et al*. The effect of botulinum toxin A on gastrocnemius length: magnitude and duration of response. *Developmental medicine and child neurology* **41**, 226–232 (1999).
46. Ross, S. A. & Engsberg, J. R. Relationships between spasticity, strength, gait, and the GMFM-66 in persons with spastic diplegia cerebral palsy. *Archives of physical medicine and rehabilitation* **88**, 1114–1120, https://doi.org/10.1016/j.apmr.2007.06.011 (2007).
47. Hurme, T., Kalimo, H., Sandberg, M., Lehto, M. & Vuorio, E. Localization of type I and III collagen and fibronectin production in injured gastrocnemius muscle. *Laboratory investigation; a journal of technical methods and pathology* **64**, 76–84 (1991).
48. Ahtikoski, A. M., Koskinen, S. O., Virtanen, P., Kovanen, V. & Takala, T. E. Regulation of synthesis of fibrillar collagens in rat skeletal muscle during immobilization in shortened and lengthened positions. *Acta physiologica Scandinavica* **172**, 131–140, https://doi.org/10.1046/j.1365-201X.2001.00848.x (2001).
49. Pedersen, B. K. IL-6 signalling in exercise and disease. *Biochemical Society transactions* **35**, 1295–1297, https://doi.org/10.1042/bst0351295 (2007).
50. Ugalde, I., Christiansen, S. P. & McLoon, L. K. Botulinum toxin treatment of extraocular muscles in rabbits results in increased myofiber remodeling. *Investigative ophthalmology & visual science* **46**, 4114–4120, https://doi.org/10.1167/iovs.05-0549 (2005).
51. Snijders, T. *et al*. Satellite cells in human skeletal muscle plasticity. *Frontiers in physiology* **6**, https://doi.org/10.3389/fphys.2015.00283 (2015).
52. Yablonka-Reuveni, Z. The Skeletal Muscle Satellite Cell: Still Young and Fascinating at 50. *Journal of Histochemistry and Cytochemistry* **59**, 1041–1059, https://doi.org/10.1369/0022155411426780 (2011).
53. Lepper, C., Partridge, T. A. & Fan, C. M. An absolute requirement for Pax7-positive satellite cells in acute injury-induced skeletal muscle regeneration. *Development (Cambridge, England)* **138**, 3639–3646, https://doi.org/10.1242/dev.067595 (2011).
54. McCarthy, J. J. *et al*. Effective fiber hypertrophy in satellite cell-depleted skeletal muscle. *Development (Cambridge, England)* **138**, 3657–3666, https://doi.org/10.1242/dev.068858 (2011).
55. Murphy, M. M., Lawson, J. A., Mathew, S. J., Hutcheson, D. A. & Kardon, G. Satellite cells, connective tissue fibroblasts and their interactions are crucial for muscle regeneration. *Development (Cambridge, England)* **138**, 3625–3637, https://doi.org/10.1242/dev.064162 (2011).
56. Cohen, S., Nathan, J. A. & Goldberg, A. L. Muscle wasting in disease: molecular mechanisms and promising therapies. *Nature reviews. Drug discovery* **14**, 58–74, https://doi.org/10.1038/nrd4467 (2015).
57. Ciciliot, S., Rossi, A. C., Dyar, K. A., Blaauw, B. & Schiaffino, S. Muscle type and fiber type specificity in muscle wasting. *The international journal of biochemistry & cell biology* **45**, 2191–2199, https://doi.org/10.1016/j.biocel.2013.05.016 (2013).
58. Gannon, J., Doran, P., Kirwan, A. & Ohlendieck, K. Drastic increase of myosin light chain MLC-2 in senescent skeletal muscle indicates fast-to-slow fibre transition in sarcopenia of old age. *European journal of cell biology* **88**, 685–700, https://doi.org/10.1016/j.ejcb.2009.06.004 (2009).
59. Verdijk, L. B. *et al*. Reduced satellite cell numbers with spinal cord injury and aging in humans. *Medicine and science in sports and exercise* **44**, 2322–2330, https://doi.org/10.1249/MSS.0b013e3182667c2e (2012).
60. Burnham, R. *et al*. Skeletal muscle fibre type transformation following spinal cord injury. *Spinal cord* **35**, 86–91 (1997).
61. Minamoto, V. B., Suzuki, K. P., Bremner, S. N., Lieber, R. L. & Ward, S. R. Dramatic changes in muscle contractile and structural properties after 2 botulinum toxin injections. *Muscle & nerve* **52**, 649–657, https://doi.org/10.1002/mus.24576 (2015).
62. Gough, M., Fairhurst, C. & Shortland, A. P. Botulinum toxin and cerebral palsy: time for reflection? *Developmental medicine and child neurology* **47**, 709–712, https://doi.org/10.1017/s0012162205001453 (2005).
63. Chen, C. M., Stott, N. S. & Smith, H. K. Effects of botulinum toxin A injection and exercise on the growth of juvenile rat gastrocnemius muscle. *Journal of applied physiology (Bethesda, Md.: 1985)* **93**, 1437–1447, https://doi.org/10.1152/japplphysiol.00189.2002 (2002).

64. Gough, M. & Shortland, A. P. Could muscle deformity in children with spastic cerebral palsy be related to an impairment of muscle growth and altered adaptation? *Developmental medicine and child neurology* **54**, 495–499, https://doi.org/10.1111/j.1469-8749.2012.04229.x (2012).
65. Fortuna, R., Vaz, M. A., Sawatsky, A., Hart, D. A. & Herzog, W. A clinically relevant BONT/A -A injection protocol leads to persistent weakness, contractile material loss, and an altered mRNA expression phenotype in rabbit quadriceps muscles. *Journal of biomechanics* **48**, 1700–1706, https://doi.org/10.1016/j.jbiomech.2015.05.018 (2015).
66. Broide, R. S. *et al*. The rat Digit Abduction Score (DAS) assay: a physiological model for assessing botulinum neurotoxin-induced skeletal muscle paralysis. *Toxicon: official journal of the International Society on Toxinology* **71**, 18–24, https://doi.org/10.1016/j.toxicon.2013.05.004 (2013).
67. Cai, B. B., Francis, J., Brin, M. F. & Broide, R. S. Botulinum neurotoxin type A-cleaved SNAP25 is confined to primary motor neurons and localized on the plasma membrane following intramuscular toxin injection. *Neuroscience* **352**, 155–169, https://doi.org/10.1016/j.neuroscience.2017.03.049 (2017).
68. Malmsten, J. Time course of segmental reflex changes after chronic spinal cord hemisection in the rat. *Acta physiologica Scandinavica* **119**, 435–443, https://doi.org/10.1111/j.1748-1716.1983.tb07359.x (1983).
69. Stampanoni, M. *et al*. Tomographic Hard X-ray Phase Contrast Micro- and Nano-imaging at TOMCAT. *AIP Conference Proceedings* **1266**, 13–17, https://doi.org/10.1063/1.3478189 (2010).
70. Pedersen, E. B. L. *et al*. Improving organic tandem solar cells based on water-processed nanoparticles by quantitative 3D nanoimaging. *Nanoscale* **7**, 13765–13774, https://doi.org/10.1039/C5NR02824H (2015).
71. Li, A. Z. *Markov Random Field Modeling in Image Analysis*. 3rd Edition edn (Springer, 2009).
72. Boykov, Y., Veksler, O. & Zabih, R. Fast Approximate Energy Minimization via Graph Cuts. *IEEE Trans. Pattern Anal. Mach. Intell.* **23**, 1222–1239, https://doi.org/10.1109/34.969114 (2001).
73. Ketcham, R. A. & Ryan, T. M. Quantification and visualization of anisotropy in trabecular bone. *Journal of microscopy* **213**, 158–171 (2004).
74. Ryan, T. M. & Ketcham, R. A. The three-dimensional structure of trabecular bone in the femoral head of strepsirrhine primates. *Journal of human evolution* **43**, 1–26 (2002).

Acknowledgements

We thank Dr. Peter C. Raffalt for statistical advice and assistance. This project was funded by the Danish research Council (DFF-1333-00197), and the Elsass Foundation.

Author Contributions

All authors have contributed to this work and have approved the final version of the manuscript. All authors are designated as authors and are qualified for authorship, and are all listed as authors. Design and planning of the project: J.P., R.F., M.B., T.L. Applied for funding and ethical approval: J.P., J.B.N. Applied for Beam Time: J.P., R.F. Execution of rat experiments: J.P., I.T.A., T.A. Execution of synchroton experiments: J.P., M.S.N., T.L., K.R., M.B., R.F. Execution of data and tissue analysis: J.P., M.S.N., T.A., I.T.A., T.L. Writing of the first draft of the manuscript: J.P. Correcting and improving the first draft of the manuscript: J.P., M.S.N., T.L., K.R., M.B., T.A., I.T.A., J.B.N., R.F.

Additional Information

Supplementary information accompanies this paper at https://doi.org/10.1038/s41598-017-14997-3.

Competing Interests: The authors declare that they have no competing interests.

Publisher's note: Springer Nature remains neutral with regard to jurisdictional claims in published maps and institutional affiliations.

C Appendix C - The Lorentz oscillator model

In the Lorentz oscillator model the atoms in the solid in question is considered to be harmonic oscillators whit given natural resonant frequency. As a wave is propagating in the medium these oscillators are driven by the electric field of the wave $\mathcal{E}(t)$.

$$m_0 \frac{d^2y}{dt^2} + m_0\gamma\frac{dy}{dt} + m_0\nu_0^2 y = -e\mathcal{E}(t) \tag{C.1}$$

An illustration of this is seen in figure 3.1.a. Here m_0 is the electron mass as the electron mass is much smaller than the nuclear mass of any atom. Therefore it will only be the electrons of medium that oscillates. γ is the dampening term and ω_0 is the natural resonance frequency of the electrons. e is the elementary charge. To simplify model it is advantageous to consider a monochromatic wave. The electric field can then be described as:

$$\mathcal{E}(t) = E_0(\nu t + \Phi) = \mathcal{E}_0 e^{-i\nu t} \tag{C.2}$$

An electron driven by an electric field of a frequency ν will be displaced from its equilibrium state given by the amplitude and the frequency of the driving field. Notice that $\mathcal{E}_0$ is complex and thus contains the phase. It then makes sense to look at solutions for eq. 3.2 on the same form as the electric field:

$$x(t) = \mathcal{X}_0 e^{-i\nu t} \tag{C.3}$$

A time varying dipole moment is created $p(t) = -ex(t)$, as the electron is displaced from the equilibrium. The macroscopic interpretation is then the amount of dipole

moments per volume. This is known as the resonant polarization $P_r = Np$. Substituting equation eq. C.2 and C.3 in eq. C.1 and applying this in the resonant polarization the following is obtained:

$$P_r = \frac{Ne^2}{m_0} \cdot \frac{\mathcal{E}}{(\nu_0^2 - \nu^2 - i\gamma\nu)} \tag{C.4}$$

Finally as the medium can be polarized the electric displacements field should be introduced. This is defined as:

$$\mathbf{D} = \epsilon_0 \mathbf{E} + \mathbf{P} \tag{C.5}$$

Here ϵ_0 is the is the electric permittivity of free space. In dielectric materials $\mathbf{D}$ is here equivalent to $\mathbf{E}$ in vacuum as described by Maxwell's 1^{st} equation. $\mathbf{P}$ is the polarization vector which must align with $\mathbf{E}$. For isotropic material this is given as, $\mathbf{P} = \epsilon_0 \chi \mathbf{E}$. Here a monochromatic wave is considered which is so it make sense to rewrite $\mathbf{D}$ as:

$$\mathbf{D} = \epsilon_0 \mathcal{E} + \mathbf{P}_b + \mathbf{P}_r = \epsilon_0 \mathcal{E} + \epsilon_0 \mathcal{E} \chi + \mathbf{P}_r \tag{C.6}$$

Here χ is the electric susceptibility and it accounts for all polarizability options of an atom. This just means that there are a finite number of resonant polarization options and these only contributes as background, thus the background polarization P_b. By the assumption that the medium in question is isotropic $\mathbf{D}$ can be defined as:

$$\mathbf{D} = \epsilon_0 \epsilon_r \mathbf{E} = \epsilon_0 \epsilon_r \mathcal{E} \tag{C.7}$$

Here the relative dielectric constant ϵ_r is introduced. An expression for ϵ_r can then be achieved by using eq. C.4, C.6 and C.7:

$$\epsilon_r(\nu) = 1 + \chi + \frac{Ne^2}{\epsilon_0 m_0} \cdot \frac{1}{(\nu_0^2 - \nu^2 - i\gamma\nu)} \tag{C.8}$$

Here it is seen that the relative dielectric constant is complex which is why it is also called the complex dielectric constant and can be written as $\tilde{\epsilon}_r(\nu) = \epsilon_1(\nu) + i\epsilon_2(\nu)$, where $\epsilon_1(\nu)$ and $\epsilon_2(\nu)$ is given as:

$$\epsilon_1(\nu) = 1 + \chi + \frac{Ne^2}{\epsilon_0 m_0} \frac{\nu_0^2 - \nu^2}{(\nu_0^2 - \nu^2)^2 + (\gamma\nu)^2} \tag{C.9}$$

$$\epsilon_2(\nu) = \frac{Ne^2}{\epsilon_0 m_0} \frac{\gamma\nu}{(\nu_0^2 - \nu^2)^2 + (\gamma\nu)^2} \tag{C.10}$$

The form of $\tilde{\epsilon}_r(\nu)$ is interesting as it is very similar to the way the complex refractive is often presented $\tilde{n} = n + i\kappa$. Indeed n, κ, ϵ_1 and ϵ_2 are not independent variables. From Maxwells equations the relation between the refractive index and relative dielectric

constant of a given medium is given as $\sqrt{\tilde{\epsilon}_r} = \tilde{n}$. The following relationship can then be achieved:

$$n = \frac{1}{\sqrt{2}} \left(\epsilon_1 + \sqrt{\epsilon_1^2 + \epsilon_2^2} \right)^{\frac{1}{2}} \tag{C.11}$$

$$\kappa = \frac{1}{\sqrt{2}} \left(\sqrt{\epsilon_1^2 + \epsilon_2^2} - \epsilon_1 \right)^{\frac{1}{2}} \tag{C.12}$$

To fully connect Beers law to the Lorentz oscillator model a wave propagating in a

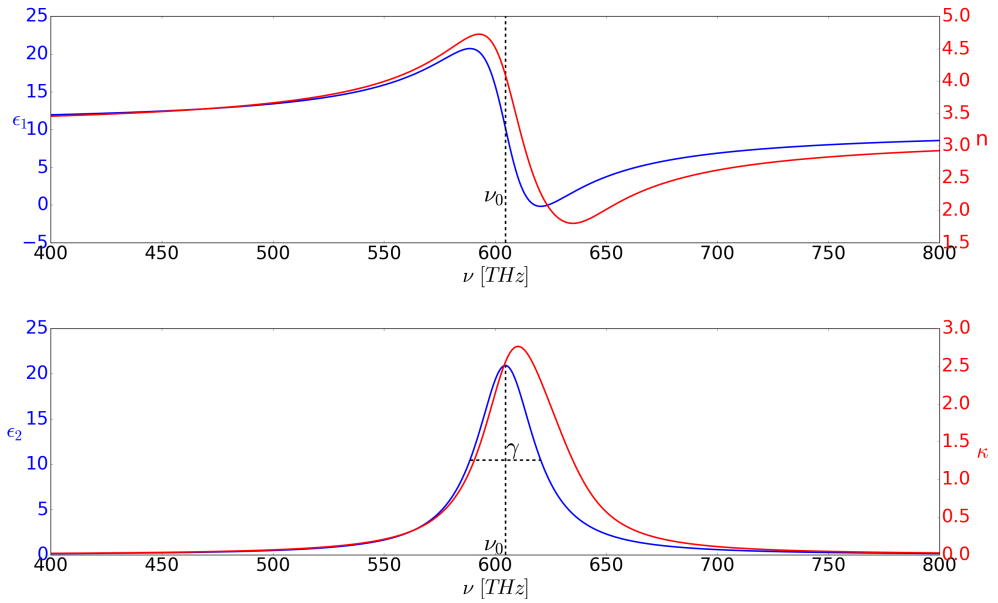

Figure C.1: Two attenuation illustrations of electromagnetic radiation where **a** illustrates the mechanism of a solid absorbing optical light and **b** the mechanism of the solid absorbing x-rays. **a**) Here a electromagnetic wave is propagation in tree regimes. An air regime before an absorbing material. The absorbing material, which attenuate the wave as it propagates. Finally, another air regime after the absorbing material. **b**) Here the electromagnetic radiation is illustrated as an ensemble of photons which propagates trough tree equivalent regimes as in **a**. This time the electromagnetic radiation is attenuated as the single photons encounter absorbing atoms.

medium can be considered. Because the interaction between matter electromagnetic radiation is coursed be the electric field modulation, the Maxwell's differential equation describing the electrical field is of interest. Here the variation considering matter propagation is given by:

$$\nabla^2 \mathcal{E} = \frac{1}{v^2} \frac{\partial^2 \mathcal{E}}{\partial t^2} \tag{C.13}$$

Where v is the velocity of the wave or just the phase velocity, given by:

$$v = \frac{c}{n} \tag{C.14}$$

The time and propagation direction dependent solution to eq. C.13 is well known:

$$\mathcal{E}(z,t) = \mathcal{E}_p e^{i(kz-2\pi\nu t)} \tag{C.15}$$

Here k is the wave vector or wave number as the direction is defined by z and ν is again the frequency. Dy definition we know that:

$$k = \frac{2\pi}{\lambda} = \frac{2\pi\nu}{v} = \frac{n2\pi\nu}{c} \tag{C.16}$$

If n is only real the medium of propagation must be non absorbing. If the medium do absorb the wave number must be complex through refractive index n:

$$k = \tilde{n}\frac{2\pi\nu}{c} = (n + i\kappa)\frac{2\pi\nu}{c} \tag{C.17}$$

Substituting this into the propagating electrical field one gets:

$$\mathcal{E}(z,t) = \mathcal{E}_p e^{i((n+i\kappa)2\pi\nu z/c-2\pi\nu t)} = \mathcal{E}_p e^{2\pi(-\kappa\nu z/c)} e^{i2\pi((n\nu z/c-\nu t)} \tag{C.18}$$

The intensity of an electromagnetic field is proportional to the square:

$$I(z) \propto \mathcal{E}(z,t)\mathcal{E}(z,t)* = \mathcal{E}_p^2 e^{4\pi(-\kappa\nu z/c)} = \mathcal{E}_p^2 e^{-\alpha z)} \tag{C.19}$$

Here $\alpha = 4\pi(-\kappa\nu z/c)$. Note that these results is exactly what was stated concerning beers law and the absorption coefficient in eq. 3.1 and 3.3 respectively.

D Appendix D - Suplementary material to x-ray Absorption

D.1 Calculating the density of states of the ejected electron

The Standard method for calculating the density of states assumes that the full system x-rays and sample is confined in a box of volume V. Furthermore by assuming periodic boundary conditions the density of states defined by the wave vector of the ejected electron must be uniform:

$$\rho(\mathbf{q}_f) = 2 \cdot \left(\frac{V}{(2\pi)^3} \right) \tag{D.1}$$

The Factor 2 contribution is due to the two degenerate electron spin states. By definition $\rho(\mathcal{E}_f)d\mathcal{E}_f$ must be the total number of energy states between $\mathcal{E}_f$ and $\mathcal{E}_f + d\mathcal{E}_f$ which is the equal to the number of vector states:

$$\rho(\mathcal{E}_f)d\mathcal{E}_f = \rho(\mathbf{q}_f)d\mathbf{q}_f \tag{D.2}$$

The absorption process is obvious inelastic but the energy is still conserved. All the energy of the photon is transferred to an electron in two contributions. First of all the photon energy $\mathcal{E}_p$ converted must be at least be equal to the binding energy of electron $\mathcal{E}_b$ any excess energy is transferred to the, now called, photoelectron as kinetic energy

$\mathcal{E}_{pe}$. Through energy conservation the following is obtained:

$$\mathcal{E}_i = \mathcal{E}_f \Rightarrow \mathcal{E}_p = \mathcal{E}_b + \mathcal{E}_{pe} \Rightarrow 2\pi\hbar\nu = \mathcal{E}_b + \frac{\hbar^2 q^2}{2m_0} \tag{D.3}$$

This also means that $\rho(\mathcal{E}_f)d\mathcal{E}_f$ must be equal to $\rho(\mathcal{E}_{pe})d\mathcal{E}_{pe}$. By substituting this and eq. D.1 into eq. D.2 the following is obtained:

$$\rho(\mathcal{E}_{pe})d\mathcal{E}_{pe} = 2 \cdot \left(\frac{V}{(2\pi)^3}\right) d\mathbf{q}_f \tag{D.4}$$

The next step is then to introduces the restrictions defined above to Fermi's Golden Rule seen in eq. 3.20. This is done including a delta function which ensures energy conservation and then integrating over all final states:

$$W = \int \frac{2\pi}{\hbar} |M_{if}|^2 \rho(\mathcal{E}_{pe}) \delta(\mathcal{E}_{pe} - (\mathcal{E}_p - \mathcal{E}_b)) d\mathcal{E}_{pe} \tag{D.5}$$

Substituting eq. D.4 into eq. D.5:

$$W = \int \frac{4\pi}{\hbar} \frac{V}{(2\pi)^3} |M_{if}|^2 \delta(\mathcal{E}_{pe} - (\mathcal{E}_p - \mathcal{E}_b)) d\mathbf{q}_f \tag{D.6}$$

Considering a system of spherical coordinates the volume element $\mathbf{q}_f$ can be replaced with $q^2 \sin(\theta) dq d\theta d\varphi$ and as the the ejected photoelectron can be ejected in all directions the integration must be over the full solid angle which is 4π. The flux is here defined as $\Phi_0 = c/V$. Inserting this and eq. D.5 into eq. 3.19 the following in achieved:

$$\sigma_a = \frac{1}{\Phi_0} W = \frac{V}{c} \int \frac{4\pi}{\hbar} \frac{V}{8\pi^3} |M_{if}|^2 \delta(\mathcal{E}_{pe} - (\mathcal{E}_p - \mathcal{E}_b)) d\mathbf{q}_f \tag{D.7}$$

$\Downarrow$

$$\sigma_a = \frac{V}{c} \frac{4\pi}{\hbar} \frac{V}{8\pi^3} \int |M_{if}|^2 \delta(\mathcal{E}_{pe} - (\mathcal{E}_p - \mathcal{E}_b)) q^2 \sin(\theta) dq d\theta d\varphi \tag{D.8}$$

$\Downarrow$

$$\sigma_a = \frac{V^2}{2\pi^2 \hbar c} \int |M_{if}|^2 \delta(\mathcal{E}_{pe} - (\mathcal{E}_p - \mathcal{E}_b)) q^2 \sin(\theta) dq d\theta d\varphi \tag{D.9}$$

D.2 Quantifying the vector potential

Like the classical approach of the Lorentz oscillator model, only the electrical field of the radiation is of consequence. Here however both the magnetic- and the electric field is indirectly account for. This is because the interaction Hamiltonian $\mathcal{H}_I$ is a

function of the vector potential $\mathbf{A}(\mathbf{r},t)$ which relates to both electric- and magnetic field through:

$$\mathbf{E}(\mathbf{r},t) = -\frac{\delta \mathbf{A}(\mathbf{r},t)}{\delta t} \tag{D.10}$$

$$\mathbf{B}(\mathbf{r},t) = \bigtriangledown \times \mathbf{A}(\mathbf{r},t) \tag{D.11}$$

The vector potential $\mathbf{A}$ is often described as a superposition of planar waves:

$$\mathbf{A}(\mathbf{r},t) = \sum_{\mathbf{k}p} \boldsymbol{\varepsilon}_{\mathbf{k}p} \left(A_{\mathbf{k}p}(t) e^{i(\mathbf{k}\cdot\mathbf{r})} + A^*_{\mathbf{k}p(t)} e^{-i(\mathbf{k}\cdot\mathbf{r})} \right) \tag{D.12}$$

$\boldsymbol{\varepsilon}$ is the polarization unit vector and $A_{\mathbf{k}p}(t)$ is a time dependent complex amplitude given by:

$$A_{\mathbf{k}p}(t) = A_{\mathbf{k}p} e^{-i2\pi\nu t} \tag{D.13}$$

The vector potential must undergoes quantization which in turn convert $\mathbf{A}(\mathbf{r},t)$ into an operator $\hat{\mathbf{A}}(\mathbf{r},t)$ and therefore also $A_{\mathbf{k}p}(t)$ into $\hat{A}_{\mathbf{k}p}(t)$. This is quantum mechanical excises which here is skipped. For the full explanation i recommend (ref Chapter 2 Quantum optics). $\hat{A}_{\mathbf{k}p}(t)$ is now given by:

$$\hat{A}_{\mathbf{k}p}(t) = A_0 \hat{a}_{\mathbf{k}p}(t), \quad \textbf{where} \quad A_0 = \sqrt{\frac{\hbar}{4\pi\nu\varepsilon_0 V}} \tag{D.14}$$

A_0 is a conveniently chosen normalization factor. The vector potential then becomes:

$$\hat{\mathbf{A}}(\mathbf{r},t) = \sum_{\mathbf{k}p} \boldsymbol{\varepsilon}_{\mathbf{k}p} \sqrt{\frac{\hbar}{4\pi\epsilon_0 V\nu}} \left[\hat{a}_{\mathbf{k}p} e^{i\mathbf{k}\cdot\mathbf{r}} + \hat{a}^\dagger_{\mathbf{k}p} e^{-i\mathbf{k}\cdot\mathbf{r}} \right] \tag{D.15}$$

With the vector potential operator the concept of the creation- and annihilation operator is introduced. These are mathematical operators that are used to increase or lower the number of particles in a quantum mechanical system. The creation operator is denoted $\hat{a}^\dagger_{\mathbf{k}p}$ and the annihilation operator is denoted $\hat{a}_{\mathbf{k}p}$.

D.3 Calculating the absorption matrix element of Fermi's Golden Rule

The starting point of this calculation is eq. 3.27.

$$M_{if} = \langle 1|_{pe} \langle 0|_{x-p} \frac{e}{m} \mathbf{p}\cdot\mathbf{A} \, |1\rangle_{x-p} |0\rangle_{pe} \tag{D.16}$$

To further simplify the system two assumptions of the vector potential must be made. First of all we only consider a single photon which mean that the sum over different wave vectors is discarded. Secondly as in the classical case we assume that the electron only interacts with the electrical field the of the photon. This means that the polarization sum also can be discarded. Substituting the vector potential of eq. D.15 into the matrix element the following is obtained:

$$M_{if} = {}_{pe}\langle 1|_{x-p}\langle 0|\frac{e}{m}\mathbf{p}\cdot\boldsymbol{\varepsilon}\sqrt{\frac{\hbar}{4\pi\epsilon_0 V\nu}}\left[\hat{a}e^{i\mathbf{k}\cdot\mathbf{r}}+\hat{a}^\dagger e^{-i\mathbf{k}\cdot\mathbf{r}}\right]|1\rangle_{x-p}|0\rangle_{pe} \tag{D.17}$$

$\Downarrow$

$$M_{if} = \mathcal{K}\left[{}_{pe}\langle 1|_{x-p}\langle 0|(\mathbf{p}\cdot\boldsymbol{\varepsilon})\hat{a}e^{i\mathbf{k}\cdot\mathbf{r}}+(\mathbf{p}\cdot\boldsymbol{\varepsilon})\hat{a}^\dagger e^{-i\mathbf{k}\cdot\mathbf{r}}|1\rangle_{x-p}|0\rangle_{pe}\right] \tag{D.18}$$

Where $\mathcal{K}$ is:

$$\mathcal{K} = \frac{e}{m}\sqrt{\frac{\hbar}{4\pi\epsilon_0 V\nu}} \tag{D.19}$$

Here the operation is done to the left. Furthermore the electron is considered to be free (the free electron approximation)in which case the final state of the photoelectron is a eigenfunction of the momentum operator $\mathbf{p}$ with the corresponding eigenvalue $\hbar\mathbf{q}$, where $\mathbf{q}$ is the wave vector of the photoelectron. The matrix element becomes:

$$M_{if} = \mathcal{K}\left[(\hbar\mathbf{q}\cdot\boldsymbol{\varepsilon})_{pe}\langle 1|_{xp}\langle 1|e^{i\mathbf{k}\cdot\mathbf{r}}|1\rangle_{xp}|0\rangle_{pe}\right] \tag{D.20}$$

$\Downarrow$

$$M_{if} = \mathcal{K}\hbar(\mathbf{q}\cdot\boldsymbol{\varepsilon})_{pe}\langle 1|e^{i\mathbf{k}\cdot\mathbf{r}}|0\rangle_{pe} \tag{D.21}$$

Rewriting the notation to wavefunction notation:

$$M_{if} = \mathcal{K}\hbar(\mathbf{q}\cdot\boldsymbol{\varepsilon})\int\psi^*_{pe,f}e^{i\mathbf{k}\cdot\mathbf{r}}\psi_{pe,i}d\mathbf{r} \tag{D.22}$$

$\psi_{pe,f}$ is the wave function of the free electron, while $\psi_{pe,i}$ is chosen to be the 1s bound state of the k-shell:

$$\psi_{pe,i} = \psi_{1s}(\mathbf{r}) \tag{D.23}$$

$$\psi_{pe,f} = \frac{1}{\sqrt{V}}e^{i\mathbf{q}\cdot\mathbf{r}} \tag{D.24}$$

$\Downarrow$

$$M_{if} = \mathcal{K}\hbar(\mathbf{q}\cdot\boldsymbol{\varepsilon})\int\frac{1}{\sqrt{V}}e^{-i\mathbf{q}\cdot\mathbf{r}}e^{i\mathbf{k}\cdot\mathbf{r}}\psi_{1s}(\mathbf{r})d\mathbf{r} \tag{D.25}$$

Introduction the wavevector trasfer as $\mathbf{Q} = \mathbf{k} - \mathbf{q}$ the intergral of eq. D.25 denoted $\phi(\mathbf{Q})$ becomes:

$$\phi(\mathbf{Q}) = \int e^{i(\mathbf{k}-\mathbf{q})\cdot\mathbf{r}}\psi_{1s}(\mathbf{r})d\mathbf{r} = \int e^{i(\mathbf{Q})\cdot\mathbf{r}}\psi_{1s}(\mathbf{r})d\mathbf{r} \tag{D.26}$$

Talking a further look at eq. D.26 one realizes that this is simply the Fourier transformation of the initial state wavefunction of the electron. If a photoelectron is ejected in a given direction hence $\mathbf{q}\cdot\boldsymbol{\varepsilon} = q\sin(\theta)\cos(\varphi)$ where (θ,φ) is the polar angles. Then considering the modulus squired of the M_{if} the following can be obtained.

$$|M_{if}|^2 = \left(\frac{\mathcal{K}^2\hbar^2}{V}\right)\left(q^2\sin^2(\theta)\cos^2(\varphi)\right)\phi^2(\mathbf{Q}) \tag{D.27}$$

D.4 Calculating the absorption cross-section

Continuing from the previous section eq. D.27 is substituted into eq. D.9:

$$\sigma_a = \frac{V^2}{2\pi^2\hbar c}\left(\frac{\mathcal{K}^2\hbar^2}{V}\right)I_{3D} = \frac{V^2}{2\pi^2\hbar c}\left(\frac{e}{m}\sqrt{\frac{\hbar}{4\pi\epsilon_0 V\nu}}\right)^2\left(\frac{\hbar^2}{V}\right)I_{3D} \tag{D.28}$$

$\Downarrow$

$$\sigma_a = \left(\frac{V^2e^2}{2\pi^2\hbar cm^2}\frac{\hbar}{4\pi\epsilon_0 V\nu}\frac{\hbar^2}{V}\right)I_{3D} = \left(\frac{\hbar^2e^2}{8\pi^3\epsilon_0 cm^2\nu}\right)I_{3D} \tag{D.29}$$

Here I_{3D} is the tree dimensional integral given by:

$$I_{3D} = \int q^2\sin^2(\theta)\cos^2(\varphi)\phi^2(\mathbf{Q})\delta(\mathcal{E}_{pe} - (\mathcal{E}_p - \mathcal{E}_b))q^2\sin(\theta)dqd\theta d\varphi \tag{D.30}$$

The next step is calculate I_{3D}. To do this the wave function og the 1s bound state must be defined. For the sake of simplicity the 1s bound state hydrogen is considered, where the nuclear charge Z can be set to any given value.

$$\psi_{1s}(\mathbf{r}) = \frac{2}{\sqrt{4\pi}}\left(\frac{Z}{a_0}\right)^{\frac{3}{2}}e^{-\frac{Z}{a_0}r} = \frac{2}{\sqrt{4\pi}}\kappa^{\frac{3}{2}}e^{-\kappa r} \tag{D.31}$$

Here Z is the nuclear charge, a_0 is the Bohr radius. The effective radius is given by $\kappa = Z/a_0$. The definition of the Fourier transformation of $\psi_{1s}(\mathbf{r})$ is seen in eq. D.26.

$$\phi(\mathbf{Q}) = \int e^{i(\mathbf{Q})\cdot\mathbf{r}}\psi_{1s}(\mathbf{r})d\mathbf{r} = \frac{4\sqrt{4\pi\kappa^{\frac{5}{2}}}}{\left[Q^2+\kappa^2\right]^2} \tag{D.32}$$

A thorough evaluation of the Fourier Transformation is seen in appendix **??**. Before substituting eq. D.32 into eq. D.30, eq. D.30 is simplified and converted into a 1D integral. The integral over the variable φ is quit easy to handle as the the following is the case:

$$\int\cos^2(\varphi)d\varphi = \pi \tag{D.33}$$

Then considering the delta function of the integral using eq. D.3:

$$I_{3D} = \pi \int q^2 \sin^2(\theta)\phi^2(\mathbf{Q})\delta\left(\frac{\hbar^2 q^2}{2m_0} - 2\pi\hbar\nu - 2\pi\hbar\nu_K)\right) q^2 \sin(\theta) dq d\theta \tag{D.34}$$

Here the binding energy ε_b of the K electron is given as $2\pi\hbar\nu_K$. To proceed the integral variable q is exchange with τ. The relationship between these are given as $\tau = q^2$. Furthermore the $\cos(\theta)$ is substituted with μ. The integral then becomes:

$$I_{3D} = \pi \int (1-\mu^2)\phi^2(\mathbf{Q})\delta\left(\tau\frac{\hbar^2}{2m_0} - 2\pi\hbar\nu - 2\pi\hbar\nu_K\right) \frac{\tau^2}{2\sqrt{\tau}} d\tau d\mu \tag{D.35}$$

The integral over τ must be evaluated at:

$$\tau = \tau_0 = \frac{2m_e}{\hbar^2}\left[2\pi\hbar\nu - 2\pi\hbar\nu_K\right] \tag{D.36}$$

τ_0 is set to be the value of τ where the delta Dirac function is different from 0. This results is that the integral evaluation becomes a factor $(2m_e/\hbar^2)$. For the mathematical explanation see section D.5 of this appendix. The I_{3D} then becomes:

$$I_{3D} = \frac{\pi m_e}{\hbar^2} \int (1-\mu^2)\phi^2(\mathbf{Q})\tau_0^{3/2} d\mu \tag{D.37}$$

The square of $\phi(\mathbf{Q})$ is then calculated. The starting point here is Q^2 of eq. D.32. Remembering the definition of $\mathbf{Q}$ the square $\mathbf{Q}$ becomes:

$$Q^2 = k^2 + q^2 - 2\mathbf{k}\cdot\mathbf{q} = K^2 + \tau - 2k\sqrt{\tau}\mu \tag{D.38}$$

Applying this in eq. D.32 the square $\phi(\mathbf{Q})$ becomes:

$$\phi^2(\mathbf{Q}) = 64\pi \frac{\kappa^5}{\left(k^2 + \tau_0 - 2k\sqrt{\tau_0}\mu + \kappa^2\right)^4} \tag{D.39}$$

I_{3D} is at this point given as:

$$I_{3D} = 64\frac{\pi^2 m_o}{\hbar^2} \int \frac{\kappa^5 \tau_0^{3/2}(1-\mu^2)}{\left(k^2 + \tau_0 - 2k\sqrt{\tau_0}\mu + \kappa^2\right)^4} d\mu \tag{D.40}$$

The tree dimensional integral is now reduced to a factor and one dimensional integral given by:

$$I_{1D} = \int_{-1}^{1} \frac{\kappa^5 \tau_0^{3/2}(1-\mu^2)}{\left(k^2 + \tau_0 - 2k\sqrt{\tau_0}\mu + \kappa^2\right)^4} d\mu \tag{D.41}$$

The understand why the integral only "goes" from -1 to 1 it must be remembered that $\mu = sin(\theta)$ and therefore only have values between -1 and 1. The absorption cross-section can now be greatly simplified:

$$\sigma_a = \left(\frac{\hbar^2 e^2}{8\pi^3 \epsilon_0 \hbar c m_0^2 \nu}\right) I_{3D} = \left(\frac{\hbar^2 e^2}{8\pi^3 \epsilon_0 c m_0^2 \nu}\right) 64\frac{\pi^2 m_0}{\hbar^2} I_{1D} \tag{D.42}$$

$$\Downarrow$$

$$\sigma_a = 32\left(\frac{e^2}{4\pi\epsilon_0 c m_0 \nu}\right) I_{1D} = 32\left(\frac{ce^2}{4\pi\epsilon_0 c^2 m_0 \nu}\right) I_{1D} = 32 r_0 \frac{c}{\nu} I_{1D} \tag{D.43}$$

c/ν is off course equivalent to the wave length while r_0 which is called the Thomson scattering length is given by:

$$r_0 = \frac{e^2}{4\pi\epsilon_0 c^2 m_0} \tag{D.44}$$

This is given by universal constants which means that r_0 in it self is a universal constant. To finally finish the simple expression of the absorption cross-section the final 1D integral must be evaluated. To get a better overview some of the terms is exchange with a constants:

$$\begin{aligned} c_1 &= \tau_0^{3/2}\kappa^5 \\ c_2 &= 2k\sqrt{\tau_0} \\ c_3 &= k^2 + \kappa^2 + \tau_0 \end{aligned} \tag{D.45}$$

$$\Downarrow$$

$$I_{1D} = \int_{-1}^{1} \frac{c_1(1-\mu^2)}{(c_3 - c_2\mu)^4} d\mu = c_1 \int_{-1}^{1} \frac{1-\mu^2}{(c_3 - c_2\mu)^4} d\mu = \frac{4}{3}\frac{c_1}{(c_2^2 - c_3^2)^2} \tag{D.46}$$

This integral is calculated in matlab which is seen in appendix(matlab codes) Using the above in eq. D.43 the absorption cross-section becomes:

$$\sigma_a = \left(\frac{\hbar^2 e^2}{8\pi^3 \epsilon_0 c m^2 \nu}\right) \frac{4}{3}\frac{c_1}{(c_2^2 - c_3^2)^2} \tag{D.47}$$

The approach going forward is then to investigate what happens within the frequency range of interest:

$$2\pi\hbar\nu_k \ll 2\pi\nu\hbar \ll 2\pi\nu_c\hbar \tag{D.48}$$

The first part of low extreme case is the binding energy of the K electron. The range in between is the photon energy, while the high end extreme is the minimum required energy to achieve pair production defined as $2\pi\hbar\nu_c = 2 \cdot m_e \cdot c^2 = 2 \cdot 511$ keV. Here the different terms of the absorption cross-section is considered. Before this however another parameter is defined as $2\pi\hbar\nu_A \equiv \hbar c\kappa$, here $2\pi\hbar\nu_A$ just illustrates an energy which is related to the inverse effective radius (κ). In the case of c_1 the following must hold true:

$$c_1 = \tau_0^{3/2}\kappa^5 = c^{-3}\left[2\pi\nu_c(2\pi\nu - 2\pi\nu_K)\right]^{3/2} c^{-5}(2\pi\nu_A)^5 \tag{D.49}$$

$$c_1 \to c^{-8}(2\pi\nu_A)^5\left[2\pi\nu_c \cdot 2\pi\nu\right]^{3/2} \tag{D.50}$$

Considering c_2 with the assumption:

$$c_2 = 2k\sqrt{\tau_0} = 2c^{-2}2\pi\nu\left[2\pi\nu_c(2\pi\nu - 2\pi\nu_K)\right]^{1/2} \tag{D.51}$$

$$c_2 \to 2c^{-2}2\pi\nu \left[2\pi\nu_c \cdot 2\pi\nu\right]^{1/2} \tag{D.52}$$

Finally under the assumption c_3 becomes:

$$c_3 = k^2 + \kappa^2 + \tau_0 = c^{-2}\left[(2\pi\nu)^2 + 2\pi\nu_c(2\pi\nu - 2\pi\nu_K) + (2\pi\nu_A)^2\right] \tag{D.53}$$

$$c_3 \to c^{-2}\left[2\pi\nu_c \cdot 2\pi\nu\right] \tag{D.54}$$

With this the absorption cross-section is found to be:

$$\sigma_a = 32r_0\frac{c}{\nu}\frac{4}{3}\left[\frac{\nu_A^2}{(\nu \cdot \nu_c)}\right]^{5/2}, \quad \textbf{for} \quad 2\pi\hbar\nu_k \ll 2\pi\nu\hbar \ll 2\pi\nu_c\hbar \tag{D.55}$$

D.5 Delta Dirac Integration

The use of the the delta Dirac function is often in connection with integration. This is a useful tool when an integral needs to be evaluated at specific value variable . The delta Dirac function is define as:

$$\delta(x) = \begin{cases} +\infty & \textbf{for} \quad x = 0 \\ 0 & \textbf{for} \quad x \neq 0 \end{cases} \tag{D.56}$$

Furthermore it also satisfy:

$$1 = \int_{-\infty}^{\infty} \delta(x)dx \tag{D.57}$$

This means that the integral over the product between a given function and the delta Dirac function is given by:

$$f(0) = \int f(x)\delta(x)dx \tag{D.58}$$

In the case where the argument of δ is function of the integration variable as the case in eq. D.35 the integration becomes:

$$\int f(x)\delta(g(x))dx = \int f(g(x))\delta(g(x))\left(\frac{dg}{dt}\right)^{-1}dg = \left[f(t)\left(\frac{dg}{dt}\right)^{-1}\right]_{g=0} \tag{D.59}$$

This is the property of the delta Dirac function which is used to evaluate the integration over τ in eq. D.35. Considering only the τ related parts of I_{3d}:

$$I_\tau = \int \frac{\tau^2}{2\sqrt{\tau}}\delta\left(\tau\frac{\hbar^2}{2m_0} - 2\pi\hbar\nu - 2\pi\hbar\nu_K\right)d\tau \tag{D.60}$$

$$\Downarrow$$

$$I_\tau = \frac{1}{2}\int \tau^{3/2}\delta\left(\tau\frac{\hbar^2}{2m_0} - 2\pi\hbar\nu + 2\pi\hbar\nu_K\right)d\tau \tag{D.61}$$

In this specific case $g(\tau)$ is identified as:

$$g(\tau) = a\tau + b, \quad \textbf{where} \quad a = \frac{\hbar^2}{2m_0} \quad \textbf{and} \quad b = -2\pi\hbar\nu + 2\pi\hbar\nu_K \tag{D.62}$$

Furthermore $f(\tau)$ is recognized as:

$$f(\tau) = \tau^{3/2} \Rightarrow f(g(\tau)) = \left(\frac{g(\tau) - b}{a}\right)^{3/2} \tag{D.63}$$

The derivative of g is then:

$$\frac{dg}{d\tau} = \frac{\hbar^2}{2m_0} \tag{D.64}$$

Substituting eq. D.63 and D.64 into D.59, I_τ becomes:

$$I_\tau = \frac{1}{2}\left[\left(\frac{g(\tau) - b}{a}\right)^{3/2}\frac{\hbar^2}{2m_0}^{-1}\right]_{g=0} \tag{D.65}$$

$$\Downarrow$$

$$I_\tau = \frac{1}{2}\left(\frac{-b}{a}\right)^{3/2}\frac{2m_0}{\hbar^2} \tag{D.66}$$

Here the constants defined in D.62 is inserted:

$$I_\tau = \frac{1}{2}\left(\frac{2m_0}{\hbar^2}\left[2\pi\hbar\nu - 2\pi\hbar\nu_K\right]\right)^{3/2}\frac{2m_0}{\hbar^2} \tag{D.67}$$

The terms inside the parenthesis is quickly recognized as τ_0:

$$I_\tau = \frac{1}{2}\left(\tau_0\right)^{3/2}\frac{2m_0}{\hbar^2} = \frac{m_0}{\hbar^2}\left(\tau_0\right)^{3/2} \tag{D.68}$$

With this the evaluation of τ integral is completed.

E Appendix E - Suplementary material to x-ray Scattering Scattering

E.1 Calculating the differential scattering cross-section

The starting point is eq. 3.35 which describes the differential scattering cross-section. Like in the case of the absorption cross-section in appendix D.1, the density of final states most be calculated. Considering the inverse square law in same manner as in appendix D.1 the volume element can describe the density of states as:

$$\rho(\mathcal{E}_f) = \left(\frac{V}{(2\pi)^3}\right)\frac{d\mathbf{k}_f}{d\mathcal{E}_f} \tag{E.1}$$

Here $d\mathbf{k}_f$ is volume element which contains the number of possible states of scattered photons with the wave vector between k_f and $k_f + dk_f$. It should also be noted that because the photon is a boson it does not have a generate state. The factor 2 of the photoelectron discussed in the previous section is therefore not extended to this case. Considering the inverse square law the volume element can be described as:

$$d\mathbf{k}_f = \Delta\Omega \cdot k_f^2 dk_f \tag{E.2}$$

The density of final states then becomes:

$$\rho(\mathcal{E}_f) = \left(\frac{V}{(2\pi)^3}\right)\Delta\Omega k_f^2 \frac{dk_f}{d\mathcal{E}_f} \tag{E.3}$$

The energy of a photon is given by its wave number. The final energy states therefore implies the following:

$$\mathcal{E}_f = \hbar c k_f \Rightarrow k_f^2 \frac{dk_f}{d\mathcal{E}_f} = \left(\frac{\mathcal{E}_f}{\hbar c}\right)^2 \cdot \frac{1}{\hbar c} = \frac{\mathcal{E}_f^2}{\hbar^3 c^3} \tag{E.4}$$

The density of final states then becomes:

$$\rho(\mathcal{E}_f) = \left(\frac{V}{(2\pi)^3}\right) \Delta\Omega \frac{\mathcal{E}_f^2}{\hbar^3 c^3} \tag{E.5}$$

W in eq 3.20 is considered differently as only the scattering into $\Delta\Omega$ is of interest. W then becomes equivalent to W_d and eq. 3.20 then becomes:

$$W_d = \int \frac{2\pi}{\hbar} |M_{if}|^2 \rho(\mathcal{E}_f) \delta(\mathcal{E}_f - \mathcal{E}_i) d\mathcal{E}_f \tag{E.6}$$

Again the flux is defined as $\Phi_0 = c/V$. Then by substituting the definition of the flux as well as eq. E.5 into eq. E.6, Fermi's golden rule becomes:

$$\frac{d\sigma}{d\Omega} = \frac{V^2}{4\pi^2 \hbar^2 c^4} \int |M_{if}|^2 \mathcal{E}_f^2 \delta(\mathcal{E}_f - \mathcal{E}_i) d\mathcal{E}_f \tag{E.7}$$

E.2 Small angle scattering from simple systems

The simplest imaginable system which have a structure is two electrons that are so close that the incoming wave experiences the charge from both. For the sake of simplicity we assume that polarization is perpendicular to the scattering plane as it is illustrated in figure 3.9. This means that we avoid to consider the phase factor discussed in 3.2.1. To further simplify this the electron positions are considered fixed. The first electron is considered to be at the origin in which case the scattering amplitude is just given by the Thomson scattering length $-r_0$. The scattering amplitude contribution from the other electron is then defined by vector $\mathbf{r}$ between them due to different phases. The resulting phase difference is; $\varphi = (\mathbf{k}) - \mathbf{k}' \cdot \mathbf{r}$. Here the vector transfer is quickly recognized and the scattering amplitude can then be written as (Als-Nielsen and McMorrow 2010):

$$A(\mathbf{Q}) = -r_0 - r_0(e^{i\mathbf{Q}\cdot\mathbf{r}}) = -r_0(1 + e^{i\mathbf{Q}\cdot\mathbf{r}}) \tag{E.8}$$

The intensity is therefore:

$$I(\mathbf{Q}) = |A(\mathbf{Q})|^2 = A(\mathbf{Q})A(\mathbf{Q})^* = r_0^2(1 + e^{i\mathbf{Q}\cdot\mathbf{r}})(1 + e^{-i\mathbf{Q}\cdot\mathbf{r}}) \tag{E.9}$$

$$\Downarrow$$

$$I(\mathbf{Q}) = 2r_0^2(1 + \cos \mathbf{Q} \cdot \mathbf{r}) \tag{E.10}$$

The behavior of the vector transfer for this case is plotted in figure E.1. Here $\mathbf{r}$ and $\mathbf{Q}$ is parallel. In reality, it is impossible to have fixed electrons but such a measurement result is achievable with ultra fast measurements (snapshot). By inspecting this simplest of cases it is already seen that scattering becomes energy dependent as this simple 1d diffraction pattern oscillates when Q changes. In this case, the scattering angle, defined in eq. 3.58 and figure 3.9.c, is constant as is r. This means only the change in wavelength contributes to the oscillation of the scattering pattern. However, no system is fast enough to make a measurement where electrons can be considered stationary. If it is assumed that the distance between the electrons is constant so that the vector $\mathbf{r}$ only changes direction one can simply average over all orientations. Doing so, a generalized expression of the result in eq. E.9 is made:

$$I(\mathbf{Q}) = A(\mathbf{Q})A(\mathbf{Q})^* = f_1^2 + f_2^2 + f_1 f_2 e^{i\mathbf{Q}\cdot\mathbf{r}} + f_1 f_2 e^{i\mathbf{Q}\cdot\mathbf{r}} \tag{E.11}$$

This is called orientational averaging and is given by orientation of the phase factor so that:

$$\langle I(\mathbf{Q})\rangle = A(\mathbf{Q})A(\mathbf{Q})^* = f_1^2 + f_2^2 + 2f_1 f_2 \left\langle e^{i\mathbf{Q}\cdot\mathbf{r}}\right\rangle \tag{E.12}$$

The averaging over the full sphere is then given as:

$$\left\langle e^{i\mathbf{Q}\cdot\mathbf{r}}\right\rangle = \frac{\int e^{i\mathbf{Q}\cdot\mathbf{r}\cos\theta}\sin\theta d\theta d\varphi}{\int \sin\theta d\theta d\varphi} = \frac{\int e^{i\mathbf{Q}\cdot\mathbf{r}\cos\theta}\sin\theta d\theta d\varphi}{4\pi} \tag{E.13}$$

$$\Downarrow$$

$$\left\langle e^{i\mathbf{Q}\cdot\mathbf{r}}\right\rangle = \frac{2\pi\int_0^\pi e^{i\mathbf{Q}\cdot\mathbf{r}\cos\theta}\sin\theta d\theta}{4\pi} = \frac{2\pi\left(-\frac{1}{iQr}\right)\int_{iQr}^{-iQr} e^x dx}{4\pi} = \frac{\sin Qr}{Qr} \tag{E.14}$$

$$\Downarrow$$

$$\langle I(\mathbf{Q})\rangle = f_1^2 + f_2^2 + 2f_1 f_2 \frac{\sin Qr}{Qr} \tag{E.15}$$

This is easily generalized to N number of electrons using this format:

$$\langle I(\mathbf{Q}_N)\rangle = \left\langle \left| \sum_{j=1}^{N} f_j e^{i\mathbf{Q}\mathbf{r}_j} \right| \right\rangle \tag{E.16}$$

The blue lines in figure E.1 are calculated using equation E.15. Here an exponential decay going towards a constant value of two for the scattering intensity as the frequency of the incoming wave is increased. The next step is to consider a hydrogen like molecule which consists of two hydrogen atoms separated by a vector $\mathbf{r}$. The approach is simply to switch out the point charge of the two electrons with the scattering amplitude of

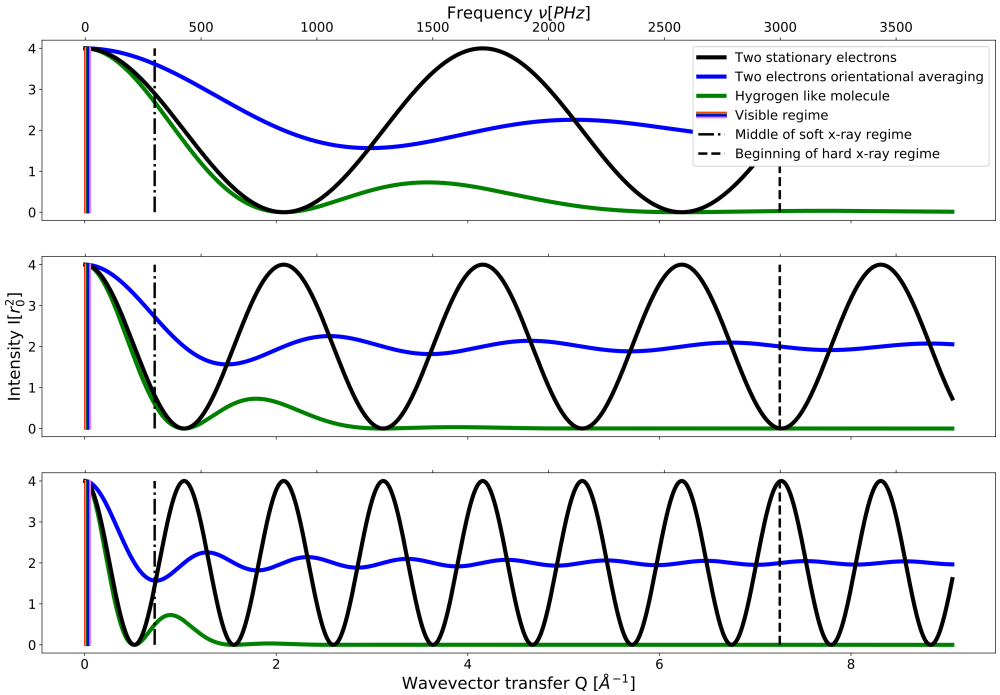

Figure E.1: Defining **Q**. 1D diffraction pattern as function of the scattering vector Q (bottom axis) with a constant scattering angle. As the scattering angle is constant only the frequency varies for different values of Q. An additional x-axis(top axis) is therefore added. a) The scattering intensity calculated for two stationary electrons (black line), two electrons under orientational averaging correction (blue line) and for a hydrogen like molecule. b) Equivalent to panel a where the values of a(in the molecules case) and r is doubled compared to panel a. Specifically these values of r and a are equivalents to a real hydrogen molecule. c) Equivalent to panel a and b. Here the values of a and r are 4 times that of a.

the hydrogen atom. The electron around the nuclei is considered an electron cloud with a charge density as function of position. $\rho(\mathbf{r})$ the charge in a volume element is therefore defined as $\rho(\mathbf{r})d\mathbf{r}$. The scattering amplitude is determined as the integration over r and a phase factor:

$$f_1 s(\mathbf{Q}) = \int \rho(\mathbf{r}) e^{i\mathbf{Q}\cdot\mathbf{r}} d\mathbf{r} \tag{E.17}$$

At this this point the scattering amplitude is renamed to be the atomic form factor. It should noticed here, that the form factor is the Fourier transform of the charge distribution which means that it very easy to go from the Form factor to charge distribution. This fact is exploited in experiments to determine structural information. In simple case where only the ground state of the K-shell electrons is considered. The

wave function is given as:

$$\psi_{1s} = \frac{1}{\sqrt{\pi a^3}} e^{-r/a}, \quad where \quad a = \frac{a_0}{Z - z_S} \tag{E.18}$$

For elements with Z greater than one, the effective radius a of the electron cloud is corrected. Z is the nuclear charge and z_S is a correction term due to the other 1s electrons. When Z is greater than one, an atom will contain two K-shell 1s electrons. The charge density is therefore $|\psi_{1s}^2|$. The atomic form factor then becomes:

$$f_{1s}(\mathbf{Q}) = \frac{1}{\pi a^3} \int e^{-2r/a} e^{i\mathbf{Q}\cdot\mathbf{r}} d\mathbf{r} \tag{E.19}$$

For convenience the coordinates are shifted to spherical

$$f_{1s}(\mathbf{Q}) = \frac{1}{\pi a^3} \int 2\pi r^2 e^{-2r/a} \int_0^\pi e^{iQr\cos\theta} \sin\theta d\theta dr = \frac{1}{[1 + (Qa/2)^2]^2} \tag{E.20}$$

Again, the directions of $\mathbf{Q}$ and $\mathbf{r}$ are considered parallel. Determining the scattering intensity is done by substituting the r_0 in eq. E.10 with the scattering amplitude of an atom. The scattering amplitude is defined by the electron wave function in eq. E.18:

$$I_{H_2}(\mathbf{Q}) = 2f_{1s}^2(1 + \cos\mathbf{Q}\cdot\mathbf{r}) = \left(\frac{1}{[1 + (Qa/2)^2]^2}\right)^2 (1 + \cos\mathbf{Q}\cdot\mathbf{r}) \tag{E.21}$$

The scattering intensity of this fixed hydrogen-like molecule is also seen in figure E.1 as the green lines. In figure E.1.b the value r is set to be four times the effective radius a, which is pretty close to the distance between the two hydrogen atoms. Figures E.1.a and -.c is the intensity two times and eighth times the effective radius respectively. these values of r also used in the stationary and oriental averaging calculations. Although it does not make any sense in the physical world just to change distances, it still gives a good idea on what effect sizes of scatters have on the diffraction pattern. The most interesting observation here is that a smaller structure means higher scattering power for higher frequencies when the wavelength is comparable to the scattering structure. As seen momentarily this is applicable for all energies including the visible regime where such scattering is called Mie-scattering. Atoms and small molecules are in the pm or Å area. The visible light have much longer wavelengths compared to these scales, hence the intensity of the scattering is $4r_0$ for all visible light. On the other hand, the very high x-ray/gamma regime has much smaller wavelengths and therefore no scattering intensity is observed in this regime.
Finally, one can investigate what happens to the diffraction pattern when different scattering angles are used in the calculations. This is done by considering 3 different gases. Hydrogen, Nitrogen and Oxygen. For easy comparison only one 1s K-shell electron is considered in all cases. Furthermore, the case of fixed r orientation as

well as orientational averaging is considered. The orientational averaging is done by substituting eq. E.18 into eq. E.18:

$$\left\langle I(\mathbf{Q}_{H_2,N_2,O_2})\right\rangle = f_1^2 + f_2^2 + 2f_1 f_2 \frac{\sin Qr}{Qr}, \tag{E.22}$$

where

$$f_1 = f_2 = \psi_{1s(H_2,N_2,O_2)} = \left(\frac{1}{[1+(Qa_{H_2,N_2,O_2}/2)^2]^2}\right) \tag{E.23}$$

In figure E.2 the calculations of the three molecules are displayed. r and a for hydrogen are the same as in the calculation already discussed. $r_{N_2} = 1.5$Å and $r_{O_2} = 1.21$Å are found as table values. Note that this is a shorter distance than the hydrogen case. a_{N_2} and a_{O_2} are calculated from E.18. Figures E.2.a and .b display the calculations for a fixed r while figures E.2.c and .d display the calculations for orientational averaging calculations. In both cases the calculations are performed for a large θ value seen in figures E.2.a and .c and small θ value seen in figures E.2.b and .d.

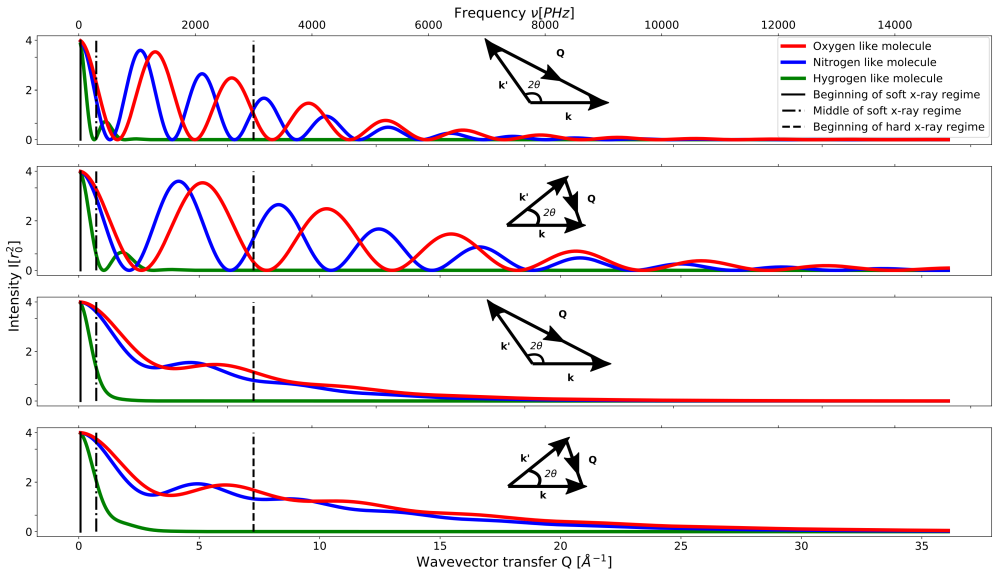

Figure E.2: Defining **Q**. Scattering intensity from K-shell electrons of dumbell like molecules. Two different scattering angles are considered. a) Wide angle scattering from k-shell electron in dumbell like molecules. Here the **r** is fixed and parallel to **Q** b) Small angle scattering from k-shell electron in dumbell like molecules. Here the **r** is fixed and parallel to **Q** c) Wide angle scattering from k-shell electron in dumbell like molecules. Here the orientational average of **r** and **Q** is included. d) Small angle scattering from k-shell electron in dumbell like molecules. Here the orientational average of **r** and **Q** is included.

Figure E.2 clearly illustrates the general tendency that the scattering intensity is higher at lower scattering angles. This feature is mostly evident in the regime where

the wavelength of the incident wave is comparable to the scatters. In figure E.2 the vertical line representing the middle of the soft x-ray regime is equivalent to a wavelength of 10Å . This is also the point where the size between the scatterers and the x-ray wavelength become really comparable. This is also the point where the diffraction pattern in figure E.2 is most sensitive to frequency changes.

In Dark Field imaging it is this small angles scattering effect that is exploited. This does not mean that it is possible to image sizes on molecule level. However, if the sample contains structures which scatters at even extremely small angles (which means relative large structures) this becomes measurable even on sub pixel level by applying a grating interferometer. This actually results in a completely unique image contrast method called Dark field imaging, which basically is a scattering contrast
It is impossible to obtain an analytical expression for every atom as the charge distribution in equation eq. E.17 becomes extremely complex for even the simplest atoms. However an analytical approximation have been calculated:

$$f(Q) = \sum_{j=1}^{4} = a_j e^{b_j (Q/4\pi)^2} + c \tag{E.24}$$

This trend becomes even more complicated with more complex structures with polyatomic molecules with different distances between the atoms. However when materials such as liquids or amorphous solids are considered, the scattering will start to be governed by two different regimes. One describes the inter-atomic structures, while the other much larger structures. As discussed earlier larger structures induce small scattering angles which is why this regime is called the small angle x-ray scattering(SAXS) regime. The scattering intensity in this regime is given by:

$$I^{SAXS}(Q) = \left| \int_V f \rho_{at} e^{i\mathbf{Q}\cdot\mathbf{r}} dV \right|^2 \tag{E.25}$$

ρ_{at} is the average areal number density of the atom or molecules composing the larger structure. f is again the atomic or molecular form factor of the smaller components of the structure. ρ_{at} and f is combined to scattering length density $\rho_{sl} = f\rho_{at}$. As mentioned in the beginning of the chapter small angle scattering is a huge field of science by itself and it is in no way the aim to go into depths to describes the science of this field. However, this effect is the contrast mechanism of Dark field imaging and to give an idea on structure sizes and angles in question, a final an simple consideration is shown here.

F Appendix F - Suplementary material to x-ray Refraction

F.1 The scattering approach to refraction

In this appendix E_D^P of eq. 3.77 is determined. Then the scattering approach is done the waves are considered to be spherical and only experience scattering as illustrated in figure 3.14.b. Then two contributions to the wave at P_D must be investigated. Observing the wave on exact path between P_S and P_D the wave looks plane although it is loosing amplitude as it propagates. The contribution is therefore:

$$E_0^P = \frac{e^{ik2R_0}}{2R_0} \tag{F.1}$$

In all other cases E_D^P is contributed by scattering in the material slab. One case is illustrated in figure 3.14.b. From some geometric considerations and performing the math as seen in appendix F, E_D^P

$$R = \sqrt{(R_0^2 + x^2)} \approx R_0 \left(1 + \frac{x^2}{2R_0^2}\right) \tag{F.2}$$

Here the direct path between P_S and P_D goes trough $x = 0$. It is assumed x is much smaller than R_0 which means that the approximation $\sqrt{k^2 + x^2} \approx k + x^2/2k$ can be used:

$$R \approx R_0 + \frac{x^2}{2R_0} = R_0 \left(1 + \frac{x^2}{2R_0^2}\right) \tag{F.3}$$

The second term in eq. F.2 accounts is the distance contributing to a phase lag compared to the direct path between P_S and P_D. Notice, as illustrated in figure 3.14.b, the total additional distance is two times that of the second term. The phase lag is therefore $2kx^2/2R_0^2$. A completely equivalent observation can be done in the y-direction. The phase difference of a wave scattered at a given xy-coordinate in the slab is therefore defined as:

$$e^{i\phi(x,y)} = e^{ix^2k/R_0} e^{iy^2k/R_0} \tag{F.4}$$

The number of scattering particles in the xy-element is determined to be $\rho\Delta dxdk$. The contribution to ψ_D^P from the waves scattered in (x,y) is therefore

$$dE_s^P \approx \left(\frac{e^{ikR_0}}{R_0}\right)(\rho\Delta dxdy)\left(-l\frac{e^{ikR_0}}{R_0}\right)e^{i\phi(x,y)} \tag{F.5}$$

Here l is the scattering length of the scatterers in the slab. By integrating over this wave element the scattering contribution in P_D is found:

$$E_s^P \approx \int dE_s^P = -\rho b\Delta\left(\frac{e^{i2kR_0}}{R_0^2}\right)\int_{-\infty}^{\infty} e^{i\phi(x,y)}dxdy = -\rho l\Delta\left(\frac{e^{i2kR_0}}{R_0^2}\right)I^2 \tag{F.6}$$

The integral defining I^2 can be shown have the following solution (Als-Nielsen and McMorrow 2010):

$$I^2 = \int_{-\infty}^{\infty} e^{i\phi(x,y)}dxdy = i\left(\frac{\pi R_0}{k}\right) \tag{F.7}$$

Substituting eq. F.7 into F.6 determines ψ_s^P:

$$E_s^P = -\rho l\Delta\left(\frac{e^{i2kR_0}}{R_0^2}\right)i\left(\frac{\pi R_0}{k}\right) = -i\rho l\Delta\left(\frac{\pi e^{i2kR_0}}{R_0 k}\right) \tag{F.8}$$

With this the full wave in P_D can be described as the sum of eq. 3.76 and F.8:

$$E_D^P = \psi_0^P + E_s^P = \frac{e^{ik2R_0}}{2R_0} - i\rho l\Delta\left(\frac{\pi e^{i2kR_0}}{R_0 k}\right) = \frac{e^{ik2R_0}}{2R_0}\left(1 - i\frac{2\pi\rho l\Delta}{k}\right) \tag{F.9}$$

$$\Downarrow$$

$$E_D^P = E_0^P\left(1 - i\frac{2\pi\rho l\Delta}{k}\right) \tag{F.10}$$

If a material slab consists of a uniform distribution of well known particles, for instance atom l and ρ is just switched with the atomic number density ρ_{at}, and its corresponding form factor f_{at}, both discussed in the previous section:

$$E_D^P = \psi_0^P\left(1 - i\frac{2\pi\rho_{at}f_{at}r_0\Delta}{k}\right) \tag{F.11}$$

If E_D^P and E_d^P is recognized as the same, $2\pi\rho_{at}f_{at}r_0\Delta/k$ is the phase shift denoted ϕ_0. If ϕ_0 is small the following approximation can be implemented which emphasizes that ϕ_0 is a phase shift:

$$E_D^P = E_0^P\,(1 - i\phi_0) \approx E_0^P e^{-i\phi_0} \tag{F.12}$$

In the previous, if the path of P_S and P_D does not have 90°, the parameter Δ is changed with $\Delta/\sin\theta$ and ϕ_0 is then denoted:

$$\phi_0 = \frac{\lambda\rho_{at}f_{at}r_0\Delta}{sin\theta} \tag{F.13}$$

Effectively this is a change in the thickness of the slab which again induces a larger phase shift. Considering the density of scatters or as here the atomic density the scattering length δ_{at} is easiest recognized by considering 3.75. Here the scattering length δ_{at} is (1-n). By multiplying the numerator and the denominator of last term in eq. F.11, E_D^P will appear on the following form:

$$E_D^P = E_0^P\left(1 - i\frac{2\pi\rho_{at}f_{at}r_0}{k^2}k\Delta\right) = E_0^P\,(1 - i\delta_{at}k\Delta) \tag{F.14}$$